nanomaterials

Modeling of Complex Interfaces

From Surface Chemistry to Nano Chemistry

Edited by

Frederik Tielens

Printed Edition of the Special Issue Published in *Nanomaterials*

www.mdpi.com/journal/nanomaterials

MDPI

Modeling of Complex Interfaces

Modeling of Complex Interfaces

From Surface Chemistry to Nano Chemistry

Special Issue Editor

Frederik Tielens

MDPI • Basel • Beijing • Wuhan • Barcelona • Belgrade • Manchester • Tokyo • Cluj • Tianjin

Special Issue Editor
Frederik Tielens
Vrije Universiteit Brussel
Belgium

Editorial Office
MDPI
St. Alban-Anlage 66
4052 Basel, Switzerland

This is a reprint of articles from the Special Issue published online in the open access journal *Nanomaterials* (ISSN 2079-4991) (available at: https://www.mdpi.com/journal/nanomaterials/special_issues/nano_modeling_interfaces).

For citation purposes, cite each article independently as indicated on the article page online and as indicated below:

LastName, A.A.; LastName, B.B.; LastName, C.C. Article Title. *Journal Name* **Year**, *Article Number*, Page Range.

ISBN 978-3-03936-194-6 (Pbk)
ISBN 978-3-03936-195-3 (PDF)

Contents

About the Special Issue Editor

Frederik Tielens graduated in Chemistry at the Free University of Brussels, Belgium (1996) and earned his PhD degree in Theoretical Chemistry with cum laude at the Free University of Brussels, Belgium (2000). His doctoral work on the study of adsorption and catalytic properties of zeolites was awarded the Solvay Prize and the second prize of the prestigious international DSM contest. After a post doc in collaboration with ExxonMobil Research he then moved to industry. In November 2003, he reintegrated university. During that period he obtained a Marie Curie Post Doc grant at the Universitat Jaume I (Spain), and was postdoctoral researcher at the Université Pierre et Marie Curie (UPMC, Paris, France) in collaboration with Yara, where he worked on the reactivity of metal and metal oxide catalysts. In September 2006, he was made contractual Assistant Professor at the UPMC. From 2007–2013, he was Assistant Professor in charge of theoretical chemistry at Surface Reactivity Laboratory (UPMC). In January 2013, he joined the Laboratory of Condensed Matter of Paris (UPMC). Since September 2017, he has been appointed Professor at the Vrije Universiteit Brussel, led the group of materials modeling, and became Maître de Conferences ”hors classe” of the Sorbonne University. He specializes in three families of materials: Silica, SAMs/noble metals, and biocalcifications. Frederik Tielens has authored over 130 peer reviewed scientific publications.

nanomaterials

MDPI

Editorial

Modeling of Complex Interfaces: From Surface Chemistry to Nano Chemistry

Jelle Vekeman and Frederik Tielens *

General Chemistry (ALGC), Materials Modelling Group, Vrije Universiteit Brussel (Free University Brussels-VUB), Pleinlaan 2, 1050 Brussel, Belgium; Jelle.Vekeman@vub.be

* Correspondence: Frederik.Tielens@vub.be

Received: 3 March 2020; Accepted: 12 March 2020; Published: 17 March 2020

For a few years now, quantum chemical modeling of materials has experienced a tremendous boost due to the increasing computational power. However, regardless of whether Moore's law is respected or not, the difficulty of modeling has now shifted to the construction of the model itself. Of course, the accuracy of the calculations can still be improved, but the main chemical properties and their trends are relatively well reproduced today, especially when they are combined with experiments. One can say that density functional theory (DFT) is now at a mature age and that it can be used as a reliable prediction tool in material science applications, although some work can be done on accuracy. Nevertheless, DFT is especially efficient in describing chemical phenomena at the molecular level, whereby the studied systems increase continuously in size and complexity. Indeed, the size of the system is directly related to the computation power, and the complexity is related to the quality of the calculation method and the representation of the chemical environment in the model. It is the latter property that brings the computational chemist's chemical intuition and general chemistry knowledge at the forefront. In this Special Issue, we wanted to focus on the construction of pertinent models that are able to describe and predict, as accurately as possible with the available computational power, the chemistry of materials.

This Special Issue contains 10 articles on the topic of modeling of complex interfaces whereby the depth of the field is nicely reflected in the wide variety of systems that is investigated in this issue. Indeed, studies are included on titanium dioxide, silicon/silicon dioxide, carbide- and graphene-based systems, sulfides, and metals such as tin and ruthenium.

In a first paper, the role of rutile TiO_2 surface orientation and the associated surface termination on molecular hydrogen activation is systematically investigated at the DFT level by Wei et al. [1]. More specifically, four different orientations were considered, and the activation barriers for the heterolytic dissociation of H_2 and the subsequent H transfer from Ti to O were calculated.

The second paper, by Hessou et al. [2], discusses the adsorption of dibenzyl disulfide adsorption in faujasite zeolites, a major cause of copper corrosion in electrical transformer oil. After carefully comparing different MY zeolites at the DFT+D level, they found that CsY, AgY and CuY are the most promising adsorbents. Indeed, these materials exhibit a good compromise between high interaction energies and limited S–S bond activation.

In addition to this, there is a paper describing a study of the thermal boundary characteristics of homo- and heterogeneous, reactive, and nonreactive interfaces between two solids by Heijmans et al. [3]. Via a connection between reactive force field molecular dynamics and phenomenological theory, a continuous temperature profile was found for the homogeneous nonreactive interface, while a temperature jump was found for the heterogeneous nonreactive interface. Furthermore, it was found that the thermal boundary resistance was twice as large for reactive interfaces than for nonreactive interfaces.

This issue also includes an article by Black et al. [4] on the investigation of the impact of cross-polymerization on the frictional properties of chemisorbed alkylsilane monolayers on silica

surfaces. Using molecular simulations, it was demonstrated that crosslinking, together with a fraction of chemisorbed chains, affects the monolayer structure slightly without significantly impacting the frictional performance. It was the first time the effect of this specific property was isolated.

A Raman spectroscopy investigation by Chong et al. [5] of the strain relaxation from grain boundaries in epitaxial graphene is also presented, whereby the graphene was grown via chemical vapor deposition in SiC. The study shows that multiple boundary-like effects are present in the graphene film, while compressive strain in the film shifts the 2D-band frequency downwards due to strain relaxation. A detailed analysis of the phenomenon is given.

In second study on graphene by Lee et al. [6], the effect of N- and S-doping on the electronic structure was investigated using DFT. It was found that N-doping gives rise to p-type defects, while N/S-doping leads to n-type defects. It is thus suggested that by varying the S concentration, the material can switch between p-type and n-type behavior. This is interesting as both types of doping are shown to lead to different unique electronic properties.

Lu et al. [7] contributed with a study on a single tunnel field-effect transistor. They boosted the performance of the model device via energy-band engineering of the InAs/Si heterojunction and a novel device structure of the source-pocket concept. The model showed and improved the tunnel-on state current and subthreshold swing. Their protocol shows the ability to study Tunnel field-effect transistors-based circuit simulations in significantly less time than conventional methods, maintaining an acceptable accuracy.

A study towards the mitigation of hydrogen uptake in ruthenium aided by tin is presented by Onwudinanti et al. [8] as to avoid blistering of ruthenium-capped multilayer reflectors. DFT calculations and charge density analyses showed a significant drop in the energy barrier for hydrogen to penetrate the ruthenium surface when a tin atom was present. They show that the main reason is a charge transfer from tin to hydrogen and the ruthenium surface.

Friák et al. [9] studied the structural, thermodynamic, and elastic properties of nanocomposites such as transition-metal disilicides and magnetic phases containing Fe and Al. For both types, they used first-principles electronic structure calculations to study a range of different atom orderings and crystal structures and assess their interface energies and related properties.

Finally, tensile stress effects on the structure and stability of prototypical covalent and layered materials were studied and presented by Chorfi et al. [10] They used DFT calculations to quantify the response of selected covalent and layered materials and to find the ideal strength along their main crystallographic direction. With some exceptions, it was found that increasing transverse stress leads to a decrease of the critical strength. Furthermore, the calculated stress–strain curves were described by a newly proposed spinodal equation of state that is generally applicable.

With this, we hope that readers interested in nanomaterials will find in this Special Issue a nice overview of the field of modeling of complex interfaces: from surface chemistry to nano chemistry. Furthermore, we hope that the included works may inspire the scientific community to further push the boundaries of these interesting topics.

Funding: This research received no external funding.

Acknowledgments: The Guest Editor would like to thank all authors for considering this Special Issue for their publication as well as the reviewers for their contribution to the quality of the studies.

Conflicts of Interest: The authors declare no conflict of interest.

References

1. Wei, B.; Tielens, F.; Calatayud, M. Understanding the role of rutile TiO2 surface orientation on molecular hydrogen activation. *Nanomaterials* **2019**, *9*, 1199. [CrossRef] [PubMed]
2. Hessou, E.P.; Ponce-Vargas, M.; Mensah, J.B.; Tielens, F.; Santos, J.C.; Badawi, M. Dibenzyl disulfide adsorption on cationic exchanged faujasites: A DFT study. *Nanomaterials* **2019**, *9*, 715. [CrossRef] [PubMed]

3. Heijmans, K.; Pathak, A.D.; Solano-López, P.; Giordano, D.; Nedea, S.; Smeulders, D. Thermal boundary characteristics of homo-/heterogeneous interfaces. *Nanomaterials* **2019**, *9*, 663. [CrossRef] [PubMed]
4. Black, J.E.; Summers, A.Z.; Iacovella, C.R.; Cummings, P.T.; McCabe, C. Investigation of the impact of cross-polymerization on the structural and frictional properties of alkylsilane monolayers using molecular simulation. *Nanomaterials* **2019**, *9*, 639. [CrossRef] [PubMed]
5. Chong, L.; Guo, H.; Zhang, Y.; Hu, Y.; Zhang, Y. Raman study of strain relaxation from grain boundaries in epitaxial graphene grown by chemical vapor deposition on SiC. *Nanomaterials* **2019**, *9*, 372. [CrossRef] [PubMed]
6. Lee, J.H.; Kwon, S.H.; Kwon, S.; Cho, M.; Kim, K.H.; Han, T.H.; Lee, S.G. Tunable electronic properties of nitrogen and sulfur doped graphene: Density functional theory approach. *Nanomaterials* **2019**, *9*, 268. [CrossRef] [PubMed]
7. Lu, H.; Lu, B.; Zhang, Y.; Zhang, Y.; Lv, Z. Drain current model for double gate tunnel-FETs with InAs/Si heterojunction and source-pocket architecture. *Nanomaterials* **2019**, *9*, 181. [CrossRef] [PubMed]
8. Onwudinanti, C.; Tranca, I.; Morgan, T.; Tao, S. Tin, the enabler—Hydrogen diffusion into ruthenium. *Nanomaterials* **2019**, *9*, 129. [CrossRef] [PubMed]
9. Friák, M.; Holec, D.; Šob, M. Quantum-mechanical study of nanocomposites with low and ultra-low interface energies. *Nanomaterials* **2018**, *8*, 1057. [CrossRef] [PubMed]
10. Chorfi, H.; Lobato, Á.; Boudjada, F.; Salvadó, M.A.; Franco, R.; Baonza, V.G.; Recio, J.M. Computational modeling of tensile stress effects on the structure and stability of prototypical covalent and layered materials. *Nanomaterials* **2019**, *9*, 1483. [CrossRef] [PubMed]

nanomaterials

MDPI

Article

Computational Modeling of Tensile Stress Effects on the Structure and Stability of Prototypical Covalent and Layered Materials

Hocine Chorfi [1,2], Álvaro Lobato [1,3], Fahima Boudjada [2,4], Miguel A. Salvadó [1], Ruth Franco [1], Valentín G. Baonza [3,5] and J. Manuel Recio [1,*]

1 MALTA-Consolider Team and Departamento de Química Física y Analítica, Universidad de Oviedo, E-33006 Oviedo, Spain; zahraoviedo@gmail.com (H.C.); a.lobato@ucm.es (Á.L.); mass@uniovi.es (M.A.S.); ruth@uniovi.es (R.F.)
2 Physics Department, University of Constantine 1, Constantine 25017, Algeria; boudjadafahima@yahoo.fr
3 MALTA-Consolider Team and Departamento de Química Física, Universidad Complutense de Madrid, E-28040 Madrid, Spain; vgbaonza@ucm.es
4 Institut Lumiere Matiere, Université Claude Bernard Lyon 1, CNRS, F-69622 Villeurbanne, France
5 Instituto de Geociencias, IGEO, CSIC-UCM, E-28040 Madrid, Spain
* Correspondence: jmrecio@uniovi.es; Tel.: +34-985-103036

Received: 18 September 2019; Accepted: 14 October 2019; Published: 18 October 2019

Abstract: Understanding the stability limit of crystalline materials under variable tensile stress conditions is of capital interest for technological applications. In this study, we present results from first-principles density functional theory calculations that quantitatively account for the response of selected covalent and layered materials to general stress conditions. In particular, we have evaluated the ideal strength along the main crystallographic directions of 3C and 2H polytypes of SiC, hexagonal ABA stacking of graphite and 2H-MoS_2. Transverse superimposed stress on the tensile stress was taken into account in order to evaluate how the critical strength is affected by these multi-load conditions. In general, increasing transverse stress from negative to positive values leads to the expected decreasing of the critical strength. Few exceptions found in the compressive stress region correlate with the trends in the density of bonds along the directions with the unexpected behavior. In addition, we propose a modified spinodal equation of state able to accurately describe the calculated stress–strain curves. This analytical function is of general use and can also be applied to experimental data anticipating critical strengths and strain values, and for providing information on the energy stored in tensile stress processes.

Keywords: ideal strength; quantum-mechanical calculations; SiC; graphite; molybdenum disulfide; spinodal equation of state

1. Introduction

A clear understanding of the cohesive and mechanical properties of technological materials is of capital importance especially when applications are demanded in environments with hostile thermal, stress, and chemical conditions. Since the nature of the crystalline bonding networks is ultimately responsible for the response of the compounds to these external conditions, it is rewarding and necessary to investigate how macroscopic properties correlate with chemical interactions at an atomic level. Covalent and layered solids constitute two crystal families currently attracting interest in a variety of areas such as electronics and solar cell industries [1–3]. These compounds provide a good target to examine how changes in strong and weak interactions affect the observed elastic stability of materials. To this end, computer simulations constitute a practical research route to microscopically

analyze strained structures of solids since geometries optimized by minimizing the crystal energy can be accurately obtained from first-principles electronic structure calculations under different stress conditions (see for example, [4]).

Within the above two families of compounds, silicon carbide (SiC), graphite and molybdenum disulfide (MoS_2) are pertinent examples because, besides their genuine bonding networks, they are materials with a variety of applications in several technological sectors, such as new semiconductor devices, field effect transistors [1,2,5–8], lubricants [9,10], and components of solar cell panels [3]. In the manufacturing processes of these materials, mechanical failure may occur as a result of the stresses induced during the heating cycles to which the compounds are subjected. In addition, the simultaneous existence of covalent and van der Waals (vdW) interactions leads to preferential bi-dimensional and three-dimensional atomic arrangements in their crystalline structures that result in a high anisotropic response of these materials under variable stress conditions which is worth exploring.

The challenge consists in the accurate calculation of the limiting tension that these materials can support in particular directions. Considering perfect non-defective crystals, this maximum tension is known as the ideal or critical strength (σ_c) of the material for that direction. Both experimentally and theoretically, the evaluation of strain-stress curves constitutes the usual strategy to access this quantity, since after this critical point a catastrophic scenario emerges in the form of a crystal fracture or a phase transition. It then seems required to understand how the atomic level interactions correlate with the mechanism of failure in these environmental conditions and, if possible, anticipate the onset of the catastrophic scenario.

A number of theoretical studies using first-principles calculations, mainly employing density functional theory (DFT) [11,12], have permitted a quantitative evaluation of the critical strength of various materials (see [13–15] and references therein) showing that the effect of multi-axial stress obviously depends on the atomic species involved [16–18]. However, to the best of our knowledge, none of these studies have addressed the description of the observed or calculated stress–strain data by means of analytical functions as normally happens in high-pressure and related fields. Such equations of state would open the possibility of anticipating critical values for the strength and strain of materials without reaching the instability condition. In this regard, it is pertinent to recall the spinodal equation of state (SEOS) [19]. This analytical function was designed to describe the high-pressure behavior of condensed matter using as a reference state the onset of elastic instability. It has been successfully applied not only to the description of experimental and theoretical pressure-volume data, but also to the pressure evolution of one dimensional unit cell parameters [20]. Along with this fact, the SEOS is particularly well suited for the description of both experimental and theoretical stress–strain data derived from variable stress tensile conditions since, in the limit, these conditions precisely lead to the elastic instability of the material, i.e., the reference state for this analytical equation of state (EOS) .

In this study, we performed DFT calculations to obtain the critical strength of 3C and 2H polytypes of SiC, graphite and 2H-MoS_2 along their main crystallographic directions, with and without superimposed transverse stress conditions. The results are analyzed in terms of the density of chemical bonds and atomic interactions in the investigated directions of these materials. We are particularly interested in general analytical functions able to represent the behavior of different types of compounds under these tensile conditions and to reproduce the critical parameters. To this end, we propose a new SEOS form that uses the critical strain as the reference state, and that can be easily used to fit both the experimental and calculated stress–strain data.

Our paper is divided in three more sections. In the next section, we present the computational details of the electronic structure calculations and the algebra related with the new EOS. Section 3 contains the results and the discussion and is divided into three subsections, devoted, respectively, to the equilibrium properties of the four compounds, the stress–strain calculated curves, and the energetics and Young moduli derived from the proposed SEOS. The paper ends with a summary of our main findings.

2. Computational Details

2.1. Electronic Structure Calculations

First-principles electronic energy calculations and geometry optimizations under the Kohn–Sham DFT framework of 3C and 2H polytype structures of SiC, ABA stacking of graphite and hexagonal 2H-MoS_2 are carried out with the ABINIT code [21,22] using the Perdew–Burke–Ernzerhof (PBE) exchange-correlation functional [23]. In order to take into account van der Waals forces, the correction (DFT-D2) to the exchange-correlation term, as proposed by Grimme [24], is used for graphite and MoS_2. Although this pairwise approach does not capture many-body effects inherent to van der Waals interactions (see for example [25–27]), it has been proven to be accurate enough to determine optimized geometries involving the length scale (Å) of the tensile phenomena explored in this work. The so-called FHI atomic plane wave pseudopotentials [28] are adopted, while cut off energies and Monkhorst–Pack grids [29] are set to 1000 eV and $6 \times 6 \times 6$ and $6 \times 6 \times 4$ for 3C-SiC and 2H-SiC respectively, 1200 eV and $6 \times 6 \times 3$ for graphite, and 400 eV and $6 \times 6 \times 2$ for 2H-MoS_2. Atomic positions were optimized until the total energy converged within 0.1 meV. At the same time, all the strain components (except in the applied loading direction) were optimized so that the corresponding stress components turned out to be within 100 MPa from a predetermined value. The Broyden–Fletcher–Goldfarb–Shanno minimization scheme (BFGS) [22] was used. In this way, tensile-strain curves under controlled normal stress were obtained. Ideal strength (critical strength from now on) was determined as the maximum value of tensile stress before the lattice loses stability and the forces diverge. Multi-axial stress calculations have been performed superimposing a transverse stress to the chosen stress direction. Atomic positions and movements through the different paths are analyzed using the visualization program for structural models (VESTA code) [30].

For the cubic 3C-SiC polytype, we calculate how the stress increases along the [100], [110] and [111] symmetry directions. For the hexagonal 2H-SiC polytype, and graphite and 2H-MoS_2 layered crystals, calculations were performed along the inter-plane direction ([001]) perpendicular to the layers, and two in-plane directions, one containing nearest neighbors ([120], so-called zigzag direction) and the other connecting next nearest neighbors ([100], so-called armchair direction).

The stress tensor is calculated in ABINIT as the derivative of the total energy with respect to the strain tensor. The strain tensor, ϵ, can be calculated from the relation between the strain-free lattice vector of a given atom μ, $\vec{r_\mu}$, and its strained lattice vector, $\vec{r'_\mu}$, as follows [31]:

$$r'^{\alpha}_{\mu} = r^{\alpha}_{\mu} + \sum_{\beta=1}^{3} \epsilon_{\alpha\beta} r^{\beta}_{\mu}, \tag{1}$$

where the α and β symbols denote the Cartesian components.

In the calculation of the second-order elastic constants in these cubic and hexagonal lattices, we follow an energy–strain scheme (see [32,33]). The lattice was first relaxed to achieve a zero stress state and then strains were applied by multiplying the lattice vectors by the strain matrix. For a lattice initially under no stress, and using Voigt notation, the energy of the strained lattice can be expressed around the equilibrium position as:

$$E = E_0 + \frac{V_0}{2} \sum_{i,j} C_{ij} \epsilon_i \epsilon_j, \tag{2}$$

where E_0 and V_0 are, respectively, the energy and the volume of the unstrained lattice. There are three independent elastic constants for the cubic lattice (C_{11}, C_{12}, C_{44}) and five independent elastic constants (C_{11}, C_{12}, C_{33}, C_{13}, C_{44}) for the hexagonal one, thus three and five sets of finite strains were applied respectively. For each case, eleven equally-spaced strain values were applied between -0.05 and 0.05. The elastic constants were obtained from fitting a quadratic equation to the energy–strain calculated

data points. The bulk modulus B_0 for each structure was calculated using its relationship with the elastic constants.

2.2. Spinodal-Like Stress–Strain Equation of State

From a thermodynamic point of view, the elastic stability limit of a solid at athermal conditions is defined by the point where the second derivative of the internal energy with respect to the volume becomes zero. At the corresponding pressure, also named as the spinodal pressure (p_{sp}), the bulk modulus (B) of the substance tends to zero, and therefore any restoring force given by the chemical bonds is overcome, leading to a crystal rupture or a phase transition [34].

The spinodal locus has been considered as an excellent reference to describe the thermodynamic behavior of solids under high pressure conditions [19,35]. Polymers, metals, covalent and ionic crystals have been analyzed showing that their p-V data is accurately and universally represented through the spinodal constrain. This follows from the fact that along a given isotherm, the isothermal bulk modulus depends on the pressure through the following universal relation [36,37]:

$$B = B^{\star}(p - p_{sp})^{\beta}, \tag{3}$$

where $B^{\star}$ and β are, respectively, the amplitude and the pseudocritical exponent that characterize the pressure behavior of the isothermal bulk modulus.

The spinodal equation of state has not been used only in its volumetric form. For instance, Francisco et al. [20] studied the evolution under isotropic compression of the lattice parameters of rutile TiO_2, showing that a one dimensional (1D) spinodal equation of state (1D-SEOS) can reproduce accurately their pressure dependence. To that, the authors define a linear bulk modulus, or equivalently a directional Young modulus (Y_I, I specifies the direction), and applied the universal relation of Equation (3). Considering both the physical significance and the directional behaviour of this spinodal-like equation of state, in this article we introduce a 1D-SEOS to analytically describe the stress–strain curves associated with tensile stress phenomena. Indeed, under directional stretching, the critical strength attained along the stress–strain curve corresponds to the spinodal stress limit, σ_{sp}. The later parameter accounts for the maximum engineering stress at which the solid breaks, and therefore, represents the elastic limit of the material. Furthermore, at this spinodal point the directional Young modulus Y_I has a value of zero, pointing out that there is no material resistance to a phase transition or rupture. Notice that these two parameters (σ_{sp} and Y_I) are also the one-dimensional analogs of the spinodal pressure and the bulk modulus. Consequently, from this perspective, the spinodal constrain is clearly fulfilled. Accordingly, the stress dependence of Y_I can be accurately described with an amplitude factor $Y_I^{\star}$ and a pseudocritical exponent γ following an equivalent power law form as Equation (3), and taking into account the engeneering convention of signs (σ is positive for tensile and negative for compressive stress):

$$Y_I = Y_I^{\star}(\sigma_{sp} - \sigma)^{\gamma}. \tag{4}$$

Under these premises, an analytical stress–strain EOS can be derived. As the Young modulus is thermodynamically defined as the derivative of the stress with respect to the strain, the simple integration of Equation (4) leads to the following expression for a directional tensile curve:

$$\sigma = \sigma_{sp} - \{Y_I^{\star}(1 - \gamma)(\epsilon_{sp} - \epsilon)\}^{1/(1-\gamma)}. \tag{5}$$

Equation (5) provides an analytical relationship between the stress and the strain along a particular direction of a crystalline solid involving four characteristic parameters. However, it must be emphasized that only three are independent since the spinodal strength, the spinodal strain and the amplitude factor are related realizing that no strain is present at $\sigma = 0$:

$$Y_I^{\star}(1-\gamma) = \frac{\sigma_{sp}^{(1-\gamma)}}{\epsilon_{sp}}. \tag{6}$$

Using this expression in Equation (5), we arrive at our final stress–strain 1D-SEOS:

$$\sigma = \sigma_{sp}\left(1 - \left(\frac{\epsilon_{sp}-\epsilon}{\epsilon_{sp}}\right)^{\frac{1}{1-\gamma}}\right). \tag{7}$$

An interesting feature of the proposed stress–strain SEOS is that it can be also expressed analytically in its energy form. In fact, considering the isotherm at 0 K and neglecting zero point vibrational contributions, the stress is related to the internal energy E and the zero-pressure volume V_0 by means of [38]:

$$\sigma = \frac{1}{V_0}\frac{dE}{d\epsilon}. \tag{8}$$

Consequently, the integrated energy–strain SEOS is:

$$E_{sp} - E = V_0\sigma_{sp}(\epsilon_{sp}-\epsilon) - V_0\frac{(1-\gamma)}{(2-\gamma)}\frac{\sigma_{sp}}{\epsilon_{sp}}^{\frac{1}{1-\gamma}}(\epsilon_{sp}-\epsilon)^{\frac{2-\gamma}{1-\gamma}}, \tag{9}$$

where E_{sp} is the internal energy of the solid at the spinodal strain, or equivalently the spinodal energy. This quantity must be understood as the energy needed to separate the crystallographic planes perpendicular to the stress–strain direction, and therefore to overcome the interatomic forces. Moreover, the spinodal energy can be expressed in terms of the spinodal stress and spinodal strain once we set to zero, the internal energy at zero strain:

$$E_{sp} = V_0\epsilon_{sp}\left(\sigma_{sp} - \frac{1-\gamma}{2-\gamma}\right). \tag{10}$$

An important feature of our current spinodal stress–strain EOS is that the spinodal energy gives us the opportunity to connect the mechanical parameters along a given tensile direction with the cohesive interatomic interactions.

Some words of caution on the notation should be given. First, σ_c and σ_{sp} both represent the critical or ideal strength of the material along a given direction. The first symbol is obtained from (ϵ_i,σ_i) calculated or experimental data, whereas the second one comes from our 1D-SEOS fittings as we discuss later. The same applies to ϵ_c and ϵ_{sp}. Second, in our static simulations (zero temperature and zero point energy contributions neglected), the internal energy of the system E is reduced to the electronic energy obtained in our DFT calculations. Finally, the symbol E is often used in other works to design the Young modulus. To avoid confussion, here we have chosen Y_I for the directional Young modulus.

2.3. Spinodal Equation of State Fittings

The versatility of the proposed 1D-SEOS allows us to fit the Young modulus-stress (Equation (4)), stress–strain (Equation (7)), and energy–strain (Equation (10)) data. Since the spinodal hypothesis is based on the assumption that the universal relationship given in expression Equation (3) can accurately describe the stress dependence of the directional Young modulus, it becomes first necessary to examine if the proposed power law can fit the calculated data, in a reliable manner. To minimize numerical errors induced by the second strain derivative of the energy involved in the $Y_I - \sigma$ curves, a linear interpolation of the computed electronic energy has been performed. In all the cases, adjusted R-squares for the Y_I-σ curves lie in the range between 0.97 and 0.99 and residuals are equally distributed between negative and positive values with a percentage of deviation lower than 7%. In order to test the reliability of our proposed 1D-SEOS, the pseudocritical exponent and the critical strength and

critical strain have been used as fitting parameters to analytically construct the stress–strain curves and energy–strain curves for all the directions and materials studied in this work according to the expressions derived in Section 2.2. Successfully, we obtain that the differences between the analytical curves and the calculated data are always below 1%. A summary of the fitting parameters are presented in Table 1.

Table 1. One dimensional (1D) spinodal equation of state (1D-SEOS) parameters from the fittings to our computed stress–strain data. Units of σ_{sp} are GPa.

Material	Direction	γ	ϵ_{sp}	σ_{sp}
3C-SiC	[100]	0.29	0.35	90.5
	[110]	0.49	0.30	52.3
	[111]	0.36	0.15	45.1
2H-SiC	[001]	0.36	0.15	44.9
	[100]	0.46	0.29	58.0
	[120]	0.34	0.17	50.7
Graphite	[001]	0.35	0.99	0.06
	[100]	0.53	0.26	85.8
	[120]	0.37	0.11	78.3
2H-MoS_2	[001]	0.39	0.05	0.07
	[100]	0.38	0.27	21.4
	[120]	0.46	0.20	14.2

As we can see in Table 1, the γ parameter lies inside the 0.41 ± 0.12 interval, depending on the crystal and the direction considered. These γ values are much lower than the universal β value of 0.85 assumed by Baonza et al. for the volumetric compression of solids [19]. Such a difference is attributed to the fact that we are in the stretching region in this case . Indeed, Brosh et al. [39] studied the dependence of the pseudocritical exponent as a function of the reduced volume both in the compressive and expansive regimes. These authors conclude that while the universal pseudocritical exponent of 0.85 accurately describes the solid under high and moderate pressure, the exponent goes down to the value of 0.5 in the case of the negative pressure regime, which is within the range of the results obtained in our spinodal stress–strain equation of state.

3. 3C-SiC, 2H-SiC, Graphite and 2H-MoS_2: Results and Discussion

3.1. Bulk Properties

This subsection is restricted just to the summary of the equilibrium structural and elastic data of the four structures. Computed lattice constants, bulk moduli and elastic constants are collected in Table 2 along with experimental and other calculated values. Overall, our results are found to be in good agreement with the reported observed data, showing only slight differences due to the overestimation of the lattice constants and underestimation of the elastic constants inherent to the generalized gradient approximation (GGA) level of calculation. The introduction of the DFT-D2 correction, which is intended to take into account the vdW inter-layer interactions, leads our results for graphite and molybdenum disulfide to be in good agreement with the experiments and improves in general other previous local density approximation (LDA) or GGA results. In addition, the controversial C_{12} parameter in 2H-MoS_2, the higher discrepancy (less than 20%) is found in our calculation of C_{11} in graphite (see Table 2). We attribute this deviation to the above tendency of GGA results. Regarding C_{12} in 2H-MoS_2, the situation is different. The discrepancy between the negative value reported in the experimental paper of Feldman [40] and the positive one obtained when the D2 Grimme correction is included in the calculations was discussed by Peelaers and Van de Walle [10]. We only notice here that C_{12} was not directly measured but derived by Feldman using linear compressibilities reported in other

works. Further details can be found in [10]. Overall, our calculated equilibrium properties provide the necessary reliable basis to undertake tensile stress simulations.

Table 2. Zero pressure lattice and elastic constants of 3C- and 2H-SiC polytypes, graphite and 2H-MoS_2. All B_0 values calculated using Voigt elastic constants relationship.

		This Work	Calculated	Experimental
3C-SiC	a(Å)	4.39	4.34 [41], 4.38 [42]	4.34 [43]
	C_{11}(GPa)	341	390 [41], 385 [42]	352 [44]
	C_{12}(GPa)	130	134 [41], 128 [42]	140 [44]
	C_{44}(GPa)	224	253 [41], 264 [42]	233 [44]
	B_0(GPa)	200	219, 213	211
2H-SiC	a(Å)	3.085	3.05 [45], 3.09 [42]	3.076[46]
	c(Å)	5.060	5.00 [45], 5.07 [42]	5.224 [46]
	C_{11}(GPa)	528	541 [45], 536 [42]	501 ± 4 [47]
	C_{12}(GPa)	112	117 [45], 78 [42]	111 ± 5 [47]
	C_{33}(GPa)	565	586 [45], 573 [42]	553 ± 4 [47]
	C_{13}(GPa)	52	61 [45], 31 [42]	52 ± 9 [47]
	C_{44}(GPa)	156	162 [45], 164 [42]	163 ± 4 [47]
	B_0(GPa)	228	238, 214	220
Graphite	a(Å)	2.521	2.451 [48]	2.464 [49]
	c(Å)	7.067	6.582 [50]	6.712 [49]
	C_{11}(GPa)	892	1118 [51]	1109 ± 16 [49]
	C_{12} (GPa)	163	235 [51]	139 ± 36 [49]
	C_{33} (GPa)	31	29 [51]	38.7 ± 7 [49]
	C_{13} (GPa)	5	8.5 [51]	0 ± 3 [49]
	C_{44} (GPa)	6	−2.8 [51]	5 ± 3 [49]
	B_0 (GPa)	240	307	281
2H-MoS_2	a(Å)	3.19	3.16 [52]	3.163 [53]
	c(Å)	12.56	12.296 [52]	12.341 [53]
	C_{11} (GPa)	220	218 [52]	238 [40]
	C_{12} (GPa)	45	38 [52]	−54 [40]
	C_{33} (GPa)	40	35 [52]	52 [40]
	C_{13} (GPa)	16	17 [52]	23 [40]
	C_{44} (GPa)	26	15 [52]	19 [40]
	B_0 (GPa)	75	68	57

3.2. Ideal Strength with and without Transverse Stress

This subsection is devoted to the calculation of the strain-stress curves of the four structures considered in this study. First, we collect in Figure 1 the results under vanishing transverse stress. For 3C-SiC and 2H-SiC, calculated points are very similar to those reported by Umeno, Kubo, and Nagao [42]. For graphite, our in-plane stress–strain curves show maxima at similar strain values to those reported by Liu et al. [48] for graphene, although we compute critical strengths along these directions around 25 GPa lower than in their work. This is due in part to differences between LDA (Liu et al.) and GGA (ours) levels of calculation, and on the other hand, to differences in the system, single sheet (graphene) and the bulk (graphite). To the best of our knowledge, the corresponding curve for the c direction has not been reported so far. Analogously, we have not found previous strain-stress curves along this direction for bulk 2H-MoS_2, whereas for the in-plane directions the previous reported studies refer to single- or few-layer 2H-MoS_2 [54,55]. These results indicate a noticeable decreasing of σ_c as the size of the slab increases, which is also the expected trend according to our calculations.

It is usual to refer to the chemical bonding network to interpret, at an atomic level, the differences in the strain-stress curves between compounds and/or directions. Without being strictly quantitative, while keeping the basic chemical meaning, a simple and practical indicator able to account for the majority of these differences is proposed as follows. Each chemical bond in the unit cell is described

by a vector connecting its two bound nearest-neighbor atoms. The projection of this vector along the corresponding tensile direction is evaluated and the sum calculated over all the bonds in the unit cell is defined as the total effective bond length (EBL) associated to that direction. The two main structural effects induced in the chemical bonds by the tensile strain (changes in bonding lengths and angles) are essentially captured in this parameter. EBL values exhibit the expected trend always increasing as the strain increases up to the stability limit.

Figure 1a shows that in 3C-SiC the slopes in the low strain region are nearly equal regardless of the direction. However, the maximum stress value strongly depends on the direction of the deformation with a critical strength nearly twice as large along the [100] axis (ϵ_c= 0.35 and σ_c = 91 GPa), as that found for [110] (ϵ_c = 0.30 and σ_c = 53 GPa) and [111] (ϵ_c = 0.15 and σ_c = 45 GPa). We notice that along [100] all tensile forces are equally distributed over the Si-C bonds. This is in contrast to the tension along the [110] and [111] directions. For example, in the latter, one of the four C nearest neighbors of a given Si atom stand along the same [111] direction and the corresponding Si-C bond suffers a pure stretching, whereas the stretching of the other three Si-C bonds is not so effective and involves bond angle modifications upon the tensile strain along the [111] direction. At zero strain, the previously defined EBL parameter already has a value roughly twice greater for the [100] direction (17.5 Å) than for the [110] (9.3 Å) and [111] (9.5 Å) directions. Thus, although the order between the [100] and [111] directions is not captured considering just the equilibrium structure, the EBL parameter catches the essential difference between the [100] direction and these two other directions.

The stress–strain curves during uniaxial tension with vanishing transverse stress in 2H-SiC are shown in Figure 1b. Slopes in the low strain (harmonic) region are almost exactly equal whereas the maximum stress value strongly depends on the direction of the deformation. The stress–strain relation in 2H-SiC [001] (ϵ_c = 0.15 and σ_c = 45 GPa) and 3C-SiC [111] are nearly identical. It is so because of the similarity of the lattice planes normal to the stress direction, and so are the curves of 2H-SiC [100] (ϵ_c = 0.29 and σ_c = 58 GPa) and 3C-SiC [110]. The stress–strain relation in 2H-SiC along [120] shows intermediate values (ϵ_c = 0.20 and σ_c = 50 GPa). Again, these values correlate with the effective Si-C bond lengths along the corresponding directions. Calculated EBL values in Å for the [100], [120] and [001] are, respectively, 21.3, 16.8, and 12.3, following the same trend as σ_c and in agreement also with previous interpretations in terms of next-nearest Si-C interactions by Umeno et al. [42].

In Figure 1c,d, the responses of graphite and 2H-MoS_2 to tensile stress along the [100], [120], and [001] directions are displayed. Here, the laminar nature of these two compounds is clearly revealed by the very low critical strength values along the *c* axis (ϵ_c = 0.13 and σ_c = 0.063 GPa in graphite and ϵ_c = 0.05 and σ_c = 0.069 GPa in 2H-MoS_2) which is in concordance with the weak van der Waals nature of the inter-layer interaction. At low strains, the in-plane graphite strains reveal an isotropic 2D elastic behavior in good agreement with previous DFT calculations [56]. At large in-plane strains, the lattice layers start to behave anisotropically and the critical stress along the next-nearest-neighbor [100] direction (ϵ_c = 0.26 and σ_c = 86 GPa in graphite and ϵ_c = 0.27 and σ_c = 22 GPa in 2H-MoS_2) becomes greater than that along the nearest-neighbor [120] direction (ϵ_c = 0.11 and σ_c = 78 GPa in graphite and ϵ_c = 0.20 and σ_c = 14 GPa in 2H-MoS_2). Expected differences between stronger C–C than Mo–S intralayer bonds are also clearly manifested when comparing these data.

For all directions and structures, we now analyze new results coming from the proposed analytical 1D-SEOS. All the curves in the four panels of Figure 1 were obtained from the 1D-SEOS fittings to the calculated strain-stress data. The performance of the 1D-SEOS is apparent and allows us to derive with confidence critical stress and critical strain values from the corresponding fitting parameters σ_{sp} and ϵ_{sp}, respectively. We have checked that the trends and specific values of these two key parameters compare with high accuracy with our first-principles computed numerical values (see Table 1). Thus, we arrive to this interesting conclusion: the 1D-SEOS of Equation (7) is an appropriate analytical function for describing stress–strain data.

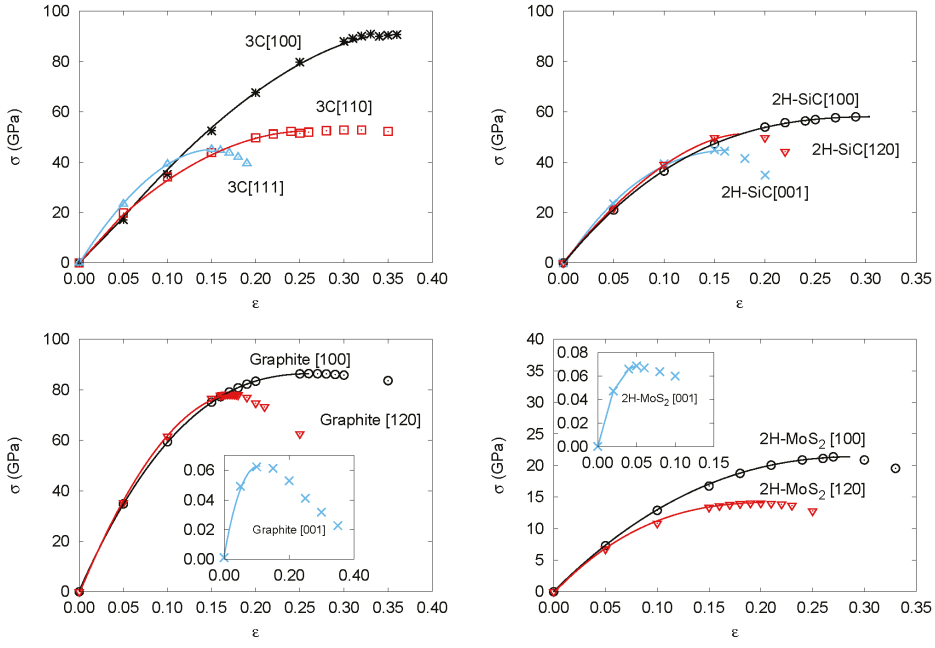

Figure 1. Calculated strain-stress curves without transverse stress for: 3C-SiC (**top left**), 2H-SiC (**top right**), Graphite (**bottom left**), and 2H-MoS_2(**bottom right**).

We noticed earlier that multi-load conditions may be present in manufacturing processes, combining thermal effects and epitaxial growth. As a particular situation of these conditions, in a second round of simulations, we have studied the effects of superimposing transverse stress (both compressive and tensile) on the previous tensile directions for the four structures. We detected convergence problems in some simulations that have hindered the calculations in the compressive (negative) transverse stress range in 2H-MoS_2, and also along the [100] direction in the positive range of this compound. Based on previous resuls in other covalent systems [42], the expected trend is a decreasing of the critical strength as we increase the superimposed transverse stress from negative to positive values. In fact, this is the computed behavior for the majority of situations we have studied. For example, the critical strength σ_c is lowered by the transverse stress σ_t in all the directions in 3C-SiC (except [110]), 2H-SiC (except [100]), graphite, and 2H-MoS_2. In this two laminar compounds, we obtain just one value at the most negative transverse stress breaking the decreasing trend along the [120] direction. All these results are displayed in Figure 2 and are in complete agreement with the computed data in 3C- and 2H-SiC reported by Umeno et al. [42]. In general, the unexpected positive slope in the critical strength-transverse stress curve appears at compressive transverse stress values. In the tensile regime, all the directions and structures show a modulated lowering of the critical strength as the transverse tension increases. This fact is compatible with the overall weakening of the compounds as multi-load conditions are enhanced, or, in Umeno et al. words as due to the higher strain energy stored in the material . However, we would like to notice that the opposite behavior was also found by Sestak et al. [15] and Cerný et al. [18]. The increasing of the critical strength under sumperimposed positive lateral tensile stress obtained in their calculations might be due to the different nature of the chemical bonding network. These authors deal with metallic materials where directional bonds are not identified, thus preventing the use for example of our EBL parameter that we introduce in what follows.

Interestingly enough, we observed an equivalent behavior when we analyzed the computed EBL parameters. In all but the cases where we have detected an exception, the calculated effective bond length parameter at the critical strain condition decreases monotonically as we superimpose the transverse stress on the corresponding tensile strain direction. Thus, we found that the decreasing of the critical strength value correlates with the decreasing in the EBL parameter. For example, along the [111] direction in 3C-SiC, EBL continuously decreases from 11.00 Å at $\sigma_t = -30$ GPa to 10.78 Å at $\sigma_t = +30$ GPa. The corresponding values at the same transverse stress conditions for the [100] direction are 24.71 Å and 21.18 Å. Similar trends are found for the EBL parameter along the [120] and [001] directions in 2H-SiC. On the contrary, in those cases where negative transverse stresses induce an unexpected behavior, this EBL parameter also shows as increasing as the transverse stress increases, up to the condition of vanishing transverse stress. Thus, along [110] in 3C-SiC and [100] in 2H-SiC, the values of EBL at $\sigma_t = -30$ GPa are, respectively, 10.94 Å and 26.08 Å, increasing up to 11.49 Å and 26.24 Å at $\sigma_t = 0$ GPa, and finally decreasing to 10.97 Å and 24.13 Å at $\sigma_t = +30$ GPa. The reason why a reduction in the critical strength occurs as compressive transverse is superimposed has been explained by the appearance of a thermodynamic competitive phase as the rock-salt structure in 3C-SiC [42]. Here, we also see that this reduction in the σ_c also correlates with the fact that the effective Si-C bond lengths along the [110] and [100] directions in 3C-SiC and 2H-SiC, respectively, show lower values at the critical conditions when the compressed transverse stress is increased, thus correlating with the trend followed by the critical strength.

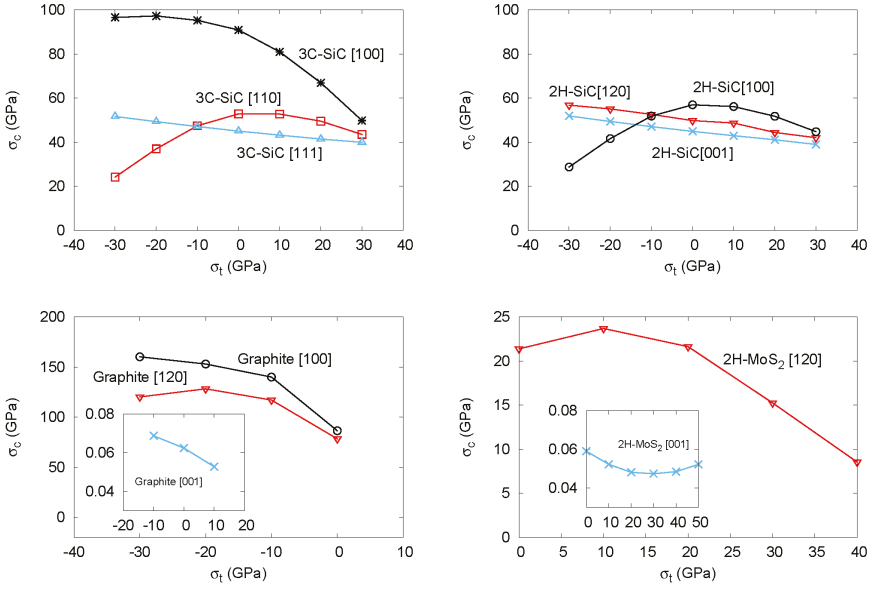

Figure 2. Calculated critical stress-transverse stress curves for: 3C-SiC (**top left**), 2H-SiC (**top right**), Graphite (**bottom left**), and 2H-MoS_2(**bottom right**).

Other Outcomes of the Stress–Strain SEOS: Energetics and Directional Young Moduli

As stated in Section 2.3, our analytical scheme allows us to gather information, not only on the critical parameters, but also on the energetics of crystalline materials and on the Young moduli along specific tensile directions. From an experimental point of view, stress–strain data can be directly measured for particular directions whereas the corresponding energy–strain curves remain only accessible once an equation of state is proposed. Equation (10) displays how, by simple integration

of our stress–strain 1D-SEOS, analytical energy–strain curves can be derived using data either from experiments or from computer simulations. In the previous subsection, we have shown that our calculated (ϵ_i,σ_i) data points are well described by the proposed 1D-SEOS. Here, the integrated SEOS for all the directions and materials studied in this work are represented in Figure 3. The symbols correspond to the energy minima at selected strains obtained from our first-principles calculations. The calculated parameters associated with the integrated forms are collected in Table 3.

The analytical energy curves clearly reflect the good quality of the fittings (see Figure 3). Two parameters define the shape of each of these curves, ϵ_{sp} and E_{sp}. The first one, previously discussed in relation to the stress–strain curves (see Table 1), identifies the abscissa of the inflexion point, where the directional Young modulus vanishes. The ordinate of this point is E_{sp} (see Table 3) and correlates quite well with the critical/spinodal strength calculated along each of the directions explored for the materials under study in this work. The higher the strength, the higher the energy required to induce an elastic instability in the material. Not surprising, the highest values are obtained in 3C-SiC along the [100] direction and graphite along the [100] direction, just the same systems and directions where we had found the greatest values for σ_c (and σ_{sp}). E_{sp} values provide also information on the energy stored in the material due to the tensile stretching. For example, along the last two directions the energy stored is expected to be higher than along other directions with flatter energy–strain curves, as [001] directions in graphite and 2H-MoS_2 (see Figure 3). Notice that for these two situations with the weakest cohesive interactions, values are so low (within the accuracy of the calculations) that only a limit value is given. Overall, we believe that these results evidence the utility of the energy–strain SEOS.

As regards the directional Young modulus, we can easily derive a simple expression at zero stress $Y_1(0)$ involving the three parameters of the stress–strain 1D-SEOS by evaluating Equation (4) at zero stress:

$$Y_1(0) = \frac{\sigma_{sp}}{\epsilon_{sp}(1-\gamma)}. \tag{11}$$

This parameter is discussed below.

Table 3. Energy and Young modulus parameters from the integrated stress–strain SEOS fittings.

Material	Direction	$Y_1(0)$ (GPa)	E_{sp} (kJ/mol)
3C-SiC	[100]	396	219
	[110]	407	110
	[111]	478	50
2H-SiC	[001]	481	50
	[100]	437	142
	[120]	450	66
Graphite	[001]	0.99	<1
	[100]	746	201
	[120]	746	113
2H-MoS_2	[001]	2.41	<1
	[100]	150	69
	[120]	140	153

In 3C-SiC, the directional Young moduli at zero stress are (in GPa) 396, 406, 478 GPa for the [100] [110] and [111] directions, respectively. These results are in concordance with the directional Young moduli calculated through the theory of representation surfaces [57]. For instance, in the case of the [111] direction

$$Y_{111} = \left(S_{11} - \frac{2}{3}\left(S_{11} - S_{12} - \frac{1}{2}S_{44} \right) \right)^{-1}, \tag{12}$$

where S_{11}, S_{12}, and S_{44} are the compliance constants related to the elastic constants by:

$$S_{11} = \frac{C_{11}+C_{12}}{(C_{11}-C_{12})(C_{11}+2C_{12})}, S_{12} = \frac{-C_{12}}{(C_{11}-C_{12})(C_{11}} + 2C_{12}), S_{44} = \frac{1}{C_{44}}. \tag{13}$$

According to the data from Table 2, and using the above equations, the calculated value for $Y_{111}(0)$ is 489 GPa in good agreement with the parameter obtained from our 1D-SEOS.

In this case, the elastic behavior of the cubic SiC polytype is not enterely isotropic and $Y_1(0)$ slightly increases along the sequence [100] [110] and [111]. $Y_1(0)$ provides a quantitative measure of the initial slope of the stress–strain curve, thus representing the resistance of the material to a tensile distortion along a particular direction at equilibrium. Under this perspective, the values of $Y_1(0)$ in the [100], [110] and [111] series of 3C-SiC inform that the direction [111] offers the highest resistance to a strain stretching at zero stress. In 2H-SiC, the values of $Y_1(0)$ point out that all the directions studied present similar resistance to distortion. Here, the solid behaves less anisotropically than in the case of the cubic polytype, expanding a narrower range of values, although both polytypes display similar zero stress Young moduli.

Let us finally conclude by analyzing these zero stress directional Young moduli in graphite and 2H-MoS_2. Layered materials constitute a severe test for our model since weak and covalent interactions are simultaneously present. In both compounds, the van der Waals nature of the inter-layer interactions is revealed through the values of the directional Young modulus provided by the spinodal parameters. $Y_{001}(0)$ values (in GPa) are as low as 0.99 and 2.40 for graphite and 2H-MoS_2, respectively, in contrast with the values along the [100] and [120] directions which are, respectively, 748 and 728 for graphite, and 150 and 140 for 2H-MoS_2. The latter values can be compared with the intra-layer Young modulus reported for graphite and MoS_2 by other authors. For instance, for graphite goes from 700 to 1100 GPa ([56] and references therein), whereas for 2H-MoS_2 the values range between 130 and 220 GPa [58–60] showing a good agreement with the results obtained in this work. At this point, it must also be emphasized that our Young modulus values reflect the expected different intralayer bond strengths between the C–C and Mo–S bonds, as we previously detected in the analysis of the 1D-SEOS parameters (see Section 3.2).

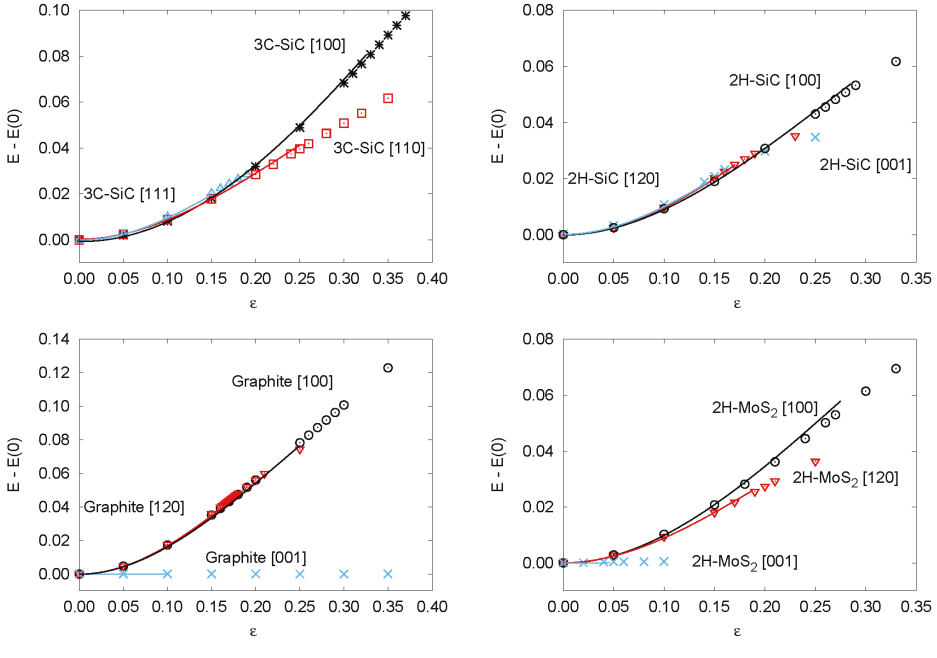

Figure 3. Calculated energy–strain curves for: 3C-SiC (**top left**), 2H-SiC (**top right**), Graphite (**bottom left**), and 2H-MoS_2(**bottom right**).

4. Conclusions

The critical strength of 3C- and 2H-SiC, graphite, and 2H-MoS_2 were evaluated by means of first principles quantum-mechanical methodologies based on the DFT approximation. Both vanishing and superimposed transverse stress over uniaxial tensile strains were considered in order to evaluate the critical (ideal) strength of the four crystalline structures. The critical strength is found to depend on the particular crystallographic direction revealing the expected stronger mechanical anisotropy in the layered compounds. In graphite and molybdenum disulfide layers, after an isotropic behavior at the low strain regime, we observe a different behavior along the two in-plane directions, the critical tensile strength being smaller in the nearest-neighbor than in the next-nearest-neighbor direction. In these crystals, the lowest value of σ_c is obtained in the c-direction as expected given the weak inter-layer vdW interactions. The critical tensile strength is generally decreased by the transverse tension. Reduction in the critical strength by large transverse compression occurs in some structures and orientations in concordance with an increase in the effective bond lengths in those conditions.

We present a new 1D-SEOS analytical function that was successfully applied to the computed strain-stress data points, and which can be also used to describe results from tensile stress experiments. The spinodal strain ϵ_{sp} along with the corresponding spinodal stress σ_{sp} fitting parameters have been calculated for the two covalent and the two layered compounds. These parameters are identified with the critical strength and strain values provided they appear at the instability elastic limit. In addition, the integrated energy–strain SEOS reveals an interesting equation, enclosing information on the energy stored in the material along tensile processes and providing data on the required energy to reach the instability elastic limit .

Author Contributions: Conceptualization, J.M.R., M.A.S., Á.L., V.G.B. and F.B.; methodology, H.C., M.A.S. and Á.L.; investigation, C.H., Á.L. and R.F.; writing–original draft preparation, C.H., J.M.R. and Á.L.; writing–review and editing, J.M.R.; Á.L., R.F.; supervision, V.G.B., J.M.R., F.B. and M.A.S.; project administration, R.F.; funding acquisition, V.G.B., J.M.R. and M.A.S.

Funding: This research was funded by the EU (FEDER) and Spanish institutions MINECO and MICINN under the projects CTQ2015-67755-C2-R and PGC2018-094814-B-C22, and Principado de Asturias-FICYT, project GRUPIN14-049.

Acknowledgments: Special thanks are due to the colleague A.H. Meziani for useful discussions. Computer facilities of MALTA-Computer center at the Universidad de Oviedo are gratefully acknowledged.

Conflicts of Interest: The funders had no role in the design of the study; in the collection, analyses, or interpretation of data; in the writing of the manuscript, or in the decision to publish the results.

References

1. Asano, K.; Hayashi, T.; Takayama, D.; Sugawara, Y.; Ryu, S.H.; Palmour, J.W. Temperature dependence of On-state characteristics, and Switching characteristics of 5 kV class 4H-SiC SEJFET. *IEEE Trans. Ind. Appl.* **2005**, *125*, 147–152. [CrossRef]
2. Peña-Álvarez, M.; del Corro, E.; Morales-García, Á.; Kavan, L.; Kalbac, M.; Frank, O. Single Layer Molybdenum Disulfide under Direct Out-of-Plane Compression: Low-Stress Band-Gap Engineering. *Nano Lett.* **2015**, *15*, 3139–3146. [CrossRef] [PubMed]
3. Tsai, M.-L.; Su, S.-H.; Chang, J.-K.; Tsai, D.-S.; Chen, C.-H.; Wu, C.-I.; Li, L.-J.; Chen, L.-J.; He, J.-H. Monolayer MoS_2 heterojunction solar cells. *ACS Nano* **2014**, *8*, 8317–8322. [CrossRef] [PubMed]
4. Recio, J.M.; Menéndez, J.M.; Otero-de-la-Roza, A. (Eds.) *An Introduction to High-Pressure Science and Technology*; CRC-Press: Boca Raton, FL, USA, 2016.
5. Radisavljevic, B.; Radenovic, A.; Giacometti, V.; Kis, A. Single-layer MoS_2 transistors. *Nat. Nanotechnol.* **2011**, *6*, 147–150. [CrossRef]
6. Wang, H.; Yu, L.; Lee, Y.H.; Shi, Y.; Hsu, A.; Chin, M.L.; Li, L.J.; Dubey, M. Kong, J.; Palacios, T. Integrated circuits based on bilayer MoS_2 transistors. *Nano Lett.* **2012**, *12*, 4674–4680. [CrossRef]
7. Fiori, G.; Szafranek,B.N.; Iannaccone, G.; Neumaier, D. Velocity saturation in few-layer MoS_2 transistor. *Appl. Phys. Lett.* **2013**, *103*, 233509(1)–233509(4). [CrossRef]

8. Kim, S.; Konar, A.; Hwang, W.S.; Lee, J.H.; Yang, J.; Jung, C.; Kim, H.; Yoo, J.B.; Choi, J.Y. High-mobility and low-power thin-film transistors based on multilayer MoS_2 crystals. *Nat. Commun.* **2012**, *3*, 1011–1017. [CrossRef]
9. Bollmann, W.; Spreadborough, J. Action of Graphite as a Lubricant. *Nature* **1960**, *186*, 29–30. [CrossRef]
10. Peelaers, H.; Van de Walle, C.G. Elastic Constants and Pessure-Induced Effects in MoS_2. *J. Phys. Chem.* **2014**, *118*, 12073–12076.
11. Kohn, W.; Sham, L.J. Self-Consistent Equations Including Exchange and Correlation Effects. *Phys. Rev.* **1965**, *140A*, 1133–1138. [CrossRef]
12. Argaman, N.; Markov, G. Density functional theory: An introduction. *Am. J. Phys.* **2000**, *68*, 69–79. [CrossRef]
13. Umeno, Y.; Kitamura, T. Ab Initio Simulation on Ideal Shear Strength of Silicon. *Mater. Sci. Eng.* **2002**, *88*, 79–84. [CrossRef]
14. Cerný, M.; Rehák, P.; Umeno, Y.; Pokluda, J. Stability and strength of covalent crystals under uniaxial and triaxial loading from first principles. *J. Phys. Condens. Matter* **2013**, *25*, 35401–35408. [CrossRef] [PubMed]
15. Sesták, P.; Friák, M.; Holec, D.; Vsianská, M.; Sob, M. Strength and brittleness of interfaces in Fe-Al superalloy nanocomposites under multiaxial loading: An ab initio and atomistic study. *Nanomaterials* **2018**, *8*, 873. [CrossRef]
16. Umeno, Y.; Cerný, M. Effect of normal stress on the ideal shear strength in covalent crystals. *Phys. Rev. B* **2008**, *77*, 100101–100104. [CrossRef]
17. Umeno, Y.; Cerný, M. Ideal shear strength under compression and tension in C, Si, Ge, and cubic SiC: An ab initio density functional theory study. *J. Phys. Condens. Matter* **2011**, *23*, 385401(1)–385401(7). [CrossRef]
18. Cerný, M.; Rehák, P.; Pokluda, J. The origin of lattice instability in bcc tungsten under triaxial loading. *Philos. Mag.* **2017**, *97*, 2971–2984. [CrossRef]
19. Baonza, V.G.; Cáceres, M.; Núñez, J. Universal compressibility behavior of dense phases. *Phys. Rev. B* **1995**, *51*, 28–37. [CrossRef]
20. Francisco, E.; Bermejo, M.; García Baonza, V.; Gerward, L.; Recio, J.M. Spinodal equation of state for rutile TiO_2. *Phys. Rev. B* **2003**, *67*, 064110(1)–064110(8). [CrossRef]
21. Gonze, X.; Beuken, J.M.; Caracas, R.; Detraux, F.; Fuchs, M.; Rignanese, G.M.; Sindic, L.; Verstraete M.; Zerah, G.; Jollet, F.; et al. First-principles computation of material properties: The ABINIT software project. *Comput. Mater. Sci.* **2002**, *25*, 478–492. [CrossRef]
22. Gonze, X.; Amadon, B.; Anglade, P.-M.; Beuken, J.-M.; Bottin, F.; Boulanger, P.; Bruneval, F.; Caliste, D.; Caracas, R.; Côté, M.; et al. ABINIT: First-principles approach to material and nanosystem properties. *Comput. Phys. Commun.* **2009**, *180*, 2582–2615. [CrossRef]
23. Perdew, J.P.; Burke, K.; Ernzerhof, M. Generalized Gradient Approximation Made Simple. *Phys. Rev. Lett.* **1996**, *77*, 3865–3868. [CrossRef] [PubMed]
24. Grimme, S. Semiempirical GGA-Type Density Functional Constructed with a Long-Range Dispersion Correction. *J. Comput. Chem.* **2006**, *27*, 1786–1799. [CrossRef] [PubMed]
25. Ambrosetti, A.; Ferri, N.; Di Stasio, R.A., Jr.; Tkatchencko, A. Wavelike charge density fluctuations and van der Waals interactions in the nanoscale. *Science* **2016**, *351*, 1171–1176. [CrossRef]
26. Ambrosetti, A.; Silvestrelli, P.L. Hidden by graphene—Towards effective screening of interface van der Waals interactions vian monolayer coating. *Carbon* **2018**, *139*, 486–491. [CrossRef]
27. Ambrosetti, A.; Silvestrelli, P.L. Faraday-like Screening by Two-Dimensional Nanomaterials: A Scale Dependent Tunable Effect. *J. Phys. Chem. Lett.* **2019**, *10*, 2044–2050. [CrossRef]
28. Trouillier, N.; Martins, J.L. Efficient pseudopotentials for plane-wave calculations. *Phys. Rev. B* **1991**, *43*, 1993–2006. [CrossRef]
29. Monkhost, H.J.; Pack, J.D. Special points for Brillouin-zone integrations. *Phys. Rev. B* **1976**, *13*, 5188–5192. [CrossRef]
30. Momma, K.; Izumi, F. VESTA 3 for three-dimensional visualization of crystal, volumetric and morphology data. *J. Appl. Crystallogr.* **2011**, *44*, 1272–1276. [CrossRef]
31. Born, M.; Huang, K. *Dynamical Theory of Crystal Lattice*; Oxford Clarendon Press: London, UK, 1966.
32. Zeina M.J.; Servio, P.; Rey A.D. Ideal Strength of Methane Hydrate and Ice Ih from First-Principles. *Cryst. Growth. Des.* **2015**, *15*, 5301–5309.
33. Otero de la Roza, A.; Luaña, V. Runwien: A text-based interface for the WIEN package. *Comput. Phys. Commun.* **2009**, *180*, 800–812. [CrossRef]

34. Baonza, V.G.; Taravillo, M.; Cáceres, M.; Núñez, J. Universal features of the equation of state of solids from a pseudospinodal hypothesis. *Phys. Rev. B* **1996**, *53*, 5252–5258. [CrossRef] [PubMed]
35. Taravillo, M.; Baonza, V.G.; Núñez, J.; Cáceres, M. Simple equation of state for solids under compression. *Phys. Rev. B* **1996**, *54*, 7034–7045. [CrossRef] [PubMed]
36. Baonza, V.G.; Cáceres, M.; Núñez, J. High-pressure compressibility behavior of liquids referred to a pseudospinodal curve. *Chem. Phys. Lett.* **1994**, *228*, 137–143. [CrossRef]
37. Baonza, V.G.; Cáceres, M.; Núñez, J. Universal Behavior of Compressed Liquids. *J. Chem. Phys.* **1994**, *19*, 4955–4958. [CrossRef]
38. Ogata, S.; Li, J.; Shibutant, N.; Yip, S. Ideal shear strain of metals and ceramics. *Phys. Rev. B* **2004**, *70*, 104104(1)–104104(7). [CrossRef]
39. Brosh, E.; Makov, G.; Shneck, R.Z. The spinodal constraint on the equation of state of expanded fluids. *J. Phys. Condens. Matter* **2003**, *19*, 2991–3001. [CrossRef]
40. Feldman, J.L. Elastic constants of 2H-MoS_2 and 2H-$NbSe_2$ extracted from measured dispersion curves and linear compressibilities. *J. Phys. Chem. Solids* **1976**, *37*, 1141–1144. [CrossRef]
41. Karch, K.; Pavone, P.; Windl, W.; Schuelt, O.; Strauch, D. Ab initio calculation of structural and lattice-dynamical properties of silicon carbide. *Phys. Rev. B* **1994**, *50*, 17054–17063. [CrossRef]
42. Umeno, Y.; Kubo, A.; Nagao, S. Density functional theory calculation of ideal strength of SiC and GaN: Effect of multi-axial stress. *Comput. Mater. Sci.* **2015**, *109*, 105–110. [CrossRef]
43. Ioffeinstitut. 2003. Available online: http://www.ioffe.ru/SVA/NSM (accessed on 18 August 2019).
44. Li, Z.; Brandt, R.C. The single-crystal elastic constants of cubic (3C) SiC to 1000 °C. *J. Mater. Sci.* **1987**, *22*, 2557–2559. [CrossRef]
45. Saramasak, K.; Limpijumnong, S.; Lambrecht, W.R.L. First principles calculations of elastic properties under pressure in SiC. *Comput. Mater. Sci.* **2010**, *49*, S43–S46.
46. Villard, P.; Calvert, L.D. *Pearson's Handbook of Crystallographic Data for intermetallic Phases*; ASM international: Cleveland, OH, USA, 1991.
47. Kamitani, K.; Grimsditch, M.; Nipko, J.C.; Loong, C.K.; Okada, M.; Kimura, I. The elastic constants of silicon carbide: A Brillouin-scattering study of 4H and 6H SiC single crystals. *J. Appl. Phys.* **1997**, *82*, 3152–3154. [CrossRef]
48. Liu, F.; Ming, P.; Li, J. Ab initio calculation of ideal strength and phonon instability of graphene under tension. *Phys. Rev. B* **2007**, *76*, 064120(1)–064120(7). [CrossRef]
49. Bosak, A.; Krisch, M.; Mohr, M.; Maultzsch, J.; Thomsen, C. Elasticity of single-crystalline graphite: Inelastic x-ray scattering study. *Phys. Rev. B* **2007**, *75*, 153408(1)–153408(4). [CrossRef]
50. Ooi, N.; Rairkar, A.; Adams, J.B. Density functional study of graphite bulk and surface properties. *Carbon* **2006**, *44*, 231–242. [CrossRef]
51. Mounet, N.; Marzari, N. First-principles determination of the structural, vibrational and thermodynamic properties of diamond, graphite, and derivatives. *Phys. Rev. B* **2005**, *71*, 205214(1)–205214(14). [CrossRef]
52. Alexiev, V.; Prins, R.; Weber, T. Ab initio study of MoS_2 and Li adsorbed on the (10-10) face of MoS_2. *Phys. Chem. Chem. Phys.* **2000**, *2*, 1815–1827. [CrossRef]
53. Fan, D.; Xu, J.; Ma, N.; Liu, J.; Xie, H. P-V-T Equation of state of molibdenite (MoS_2) by a diamond anvil cell and in situ synchrotron angel-dispersive X-ray diffraction. *Phys. B* **2014**, *451*, 53–57. [CrossRef]
54. Li, T. Ideal strength and phonon instability in single-layer MoS_2. *Phys. Rev. B* **2012**, *85*, 235407(1)–235407(5). [CrossRef]
55. Li, P.; Jiang, C.; Xu, S.; Zhuang, Y.; Gao, L.; Hu, A.; Wang, H.; Lu, Y. In situ nanomechanical characterization of multi-layer MoS_2 membranes: from intraplanar to interplanar fracture. *Nanoscale* **2017**, *9*, 9119–9128. [CrossRef] [PubMed]
56. Abbasi-Pérez, D.; Menéndez, J.M.; Recio, J.M.; Otero-de-la-Roza, A.; del Corro, E.; Taravillo, M.; Baonza, V.G.; Marqués, M. Modeling graphite under stress: Equations of state, vibrational modes, and interlayer friction. *Phys. Rev. B* **2014**, *90*, 054105(1)–054105(10). [CrossRef]
57. Nye, J.F. *Physical Properties of Crystals*; Oxford University Press: New York, NY, USA, 2004.
58. Bertolazzi, S.; Brivio, J.; Kis, A. Stretching and Breaking of Ultrathin MoS_2. *ACS Nano* **2011**, *5*, 9703–9709. [CrossRef]

59. Lorenz, T.; Teich, D.; Joswig, J.O.; Seifert, G. Theoretical Study of the Mechanical Behavior of Individual TiS_2 and MoS_2 Nanotubes. *J. Phys. Chem. C* **2012**, *116*, 11714–11721. [CrossRef]
60. Cooper, R.C.; Lee, C.; Marianetti, C.A.; Wei, X.; Hone, J.; Kysar, J.W. Nonlinear elastic behavior of two-dimensional molybdenum disulfide. *Phys. Rev. B* **2013**, *87*, 035423-1–035423-11. [CrossRef]

nanomaterials

MDPI

Article

Understanding the Role of Rutile TiO_2 Surface Orientation on Molecular Hydrogen Activation

Baohuan Wei [1], Frederik Tielens [2] and Monica Calatayud [1,*]

[1] Sorbonne Université, CNRS, Laboratoire de Chimie Théorique, LCT, F. 75005 Paris, France
[2] General Chemistry (ALGC), Materials Modelling Group, Vrije Universiteit Brussel (Free University Brussels-VUB), Pleinlaan 2, 1050 Brussel, Belgium
* Correspondence: calatayu@lct.jussieu.fr

Received: 23 June 2019; Accepted: 16 August 2019; Published: 26 August 2019

Abstract: Titanium oxide (TiO_2) has been widely used in many fields, such as photocatalysis, photovoltaics, catalysis, and sensors, where its interaction with molecular H_2 with TiO_2 surface plays an important role. However, the activation of hydrogen over rutile TiO_2 surfaces has not been systematically studied regarding the surface termination dependence. In this work, we use density functional theory (PBE+U) to identify the pathways for two processes: the heterolytic dissociation of H_2 as a hydride–proton pair, and the subsequent H transfer from Ti to near O accompanied by reduction of the Ti sites. Four stoichiometric surface orientations were considered: (001), (100), (110), and (101). The lowest activation barriers are found for hydrogen dissociation on (001) and (110), with energies of 0.56 eV and 0.50 eV, respectively. The highest activation barriers are found on (100) and (101), with energies of 1.08 eV and 0.79 eV, respectively. For hydrogen transfer from Ti to near O, the activation barriers are higher (from 1.40 to 1.86 eV). Our results indicate that the dissociation step is kinetically more favorable than the H transfer process, although the latter is thermodynamically more favorable. We discuss the implications in the stability of the hydride–proton pair, and provide structures, electronic structure, vibrational analysis, and temperature effects to characterize the reactivity of the four TiO_2 orientations.

Keywords: hydrogen activation; rutile TiO_2; hydrogen transfer

1. Introduction

Titanium oxide (TiO_2) has been widely used in numerous fields, from everyday applications (paint, inks, toothpaste, makeup) to technological devices, such as dye-sensitized solar cells (DSSCs) [1,2], photoelectrochemical cells [3], photocatalysts [4], catalysis [5,6], sensors [7,8], biomedical treatments [9], lithium ion batteries [10], or photovoltaics [11,12]. The interaction of hydrogen with TiO_2 surfaces plays an important role in many reaction processes [13–20] and has been widely studied [21–27]. Despite the high interest generated by hydrogen-titania interfaces, the nature of the species involved is still poorly understood—protons are generally reported as being stable in hydrogenated rutile (110) [28], atomic surface hydrogen has been found to prevent electron-hole recombination on an Au-TiO_2 photocatalyst [14], and very recently hydride species have been characterized as being stable on its surface [29,30]. In this work, we investigate the role of the surface termination in the H_2 dissociation and migration on rutile surfaces. We focus on the characterization of the stability of surface Ti-H species formed by interaction with H_2 and their subsequent transfer to neighboring oxygen sites in order to provide a comprehensive picture of the adsorption, desorption, and diffusion mechanisms occurring at H-TiO_2 interfaces.

In recent years, H_2 dissociation over metal oxides has attracted great interest [31–38]. Two main mechanisms are proposed: homolytic and heterolytic dissociation [39]. It is widely thought that non-reducible metal oxides follow the heterolytic pathway forming MH/OH pairs, while reducible

metal oxides proceed homolytically forming OH/OH pairs together with the metal site reduction. However, in recent years deviations from this rule have been proposed to explain experimental observations. Thus, García-Melchor et al. and Fernandez-Torre et al. reported that H_2 dissociation on CeO_2 (111) follows a heterolytic path, with H being transferred from Ce to a neighboring O, generating the homolytic product [34,40]. Chen and Pacchioni reported that on nanostructured MgO (001), the dissociation pathway depends on the choice of the support—on MgO/Ag (001), the heterolytic pathway is preferred, while with Au support, it follows the homolytic dissociation [31]. Very recently, Liu et al. reported the surface characteristics of anatase TiO_2 after reduction with H_2. In their study, they proposed that H_2 can dissociate on oxygen vacancies—one H atom binds with a Ti to form the Ti-H bond, whereas the other one bonds with O to form Ti–OH [41]. Moreover, Hu et al. reported H_2 dissociation on three TiO_2 polymorphs [35], which showed that homolytic activation barriers are all high (1.48–1.68 eV), with rutile showing the highest activity.

It is well known that the surface properties strongly vary with different crystallographic orientations, which can greatly affect their reactivity [42–46]. For rutile TiO_2, the main exposed low energy surface is the (110) surface, which is also the most studied [23,28,47–51]. There are also other terminations of rutile TiO_2 that are experimentally accessible, such as (100) facet [52–55], (001) facet [56–62], (101) facet [8,60,63,64], and (011) facet [65–67]. Herein, we systematically study the hydrogen dissociation over four rutile TiO_2 facets (001), (100), (110), and (101) by using density functional theorywith PBE+U(Perdew–Burke–Erzenhof functional with the Hubbard U correction). We consider a two-step mechanism for H_2 dissociation: first, heterolytic dissociation to form TiH/OH pairs, and second, H transfer from Ti to O to form OH, accompanied by a two-electron transfer of the hydride to the Ti sites. We provide the structures of the reaction intermediates, the energetic profile of the two steps, the electronic structure of the systems involved, and the temperature effects to evaluate the barriers at room temperature for stoichiometric slab models. Vibrational frequencies for TiH and OH are also reported as a guide to identify relevant species on the different terminations.

2. Materials and Methods

Density functional theory (DFT) calculations were performed using the Vienna ab initio simulation package (VASP) version 5.4.4 [68]. Projector-augmented wave (PAW) pseudopotential was used to describe the core electron representation with 1, 4, and 6 valence electrons for H, Ti, and O, respectively [69,70]. The generalized gradient approximation (GGA) approach was used for the exchange and correlation potential with the Perdew–Burke–Erzenhof (PBE) functional [71,72]. The GGA+U approach of Dudarev et al. was used to treat the 3d orbital electrons of Ti with the effective Hubbard on-site Coulomb interaction parameter (U′ = U − J) [73]. We chose U′ = 4 according to the proposed value from previous works [24,28,74], referred herein as *U*. A 400 eV cutoff energy for the plane-wave basis set was found to correctly treat the rutile surface [28]. The dissociation of hydrogen on rutile TiO_2 surfaces was investigated in the 1×1 unit cell for (001), (100), and (101) and in the 2×2 unit cell for the (110) surface. The open shell systems were treated with spin polarized calculations. The energy convergence was set to 3.0×10^{-2} eV for the ionic loop and 1.0×10^{-4} eV for the electronic loop. The slab models were cut from the optimized structure of bulk rutile (Figure 1). A vacuum layer of 20 Å was employed. The slab thickness used is given in Table 1. The lower-half layers of the slab were kept frozen and the upper-half layers were allowed to relax. We used the Monkhorst–Pack scheme to sample the Brillouin zone, and the distance between each k-point was 0.033 $Å^{-1}$ [18,35]. The constrained minimization and climbing-image nudged elastic band (CI-NEB) methods were used to locate transition states (TS) [75,76]. In this work, the minimum energy pathway for each elementary reaction was discretized by a total of four images between the initial and final states. The imaginary frequency of every transition state was checked to connect initial and final states. The zero point energy (ZPE) vibration energy was calculated from vibrational frequencies as one-half of the sum of real-valued harmonic vibrational frequencies [77].

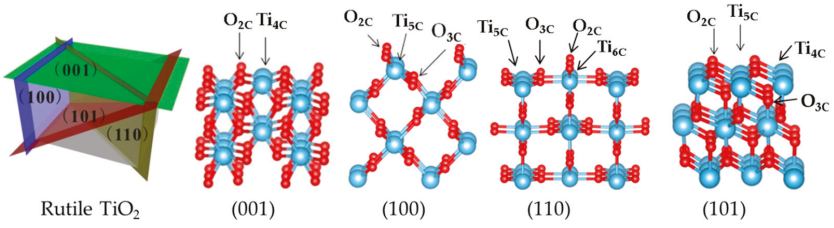

Figure 1. Side views of rutile TiO_2 (001), (100), (110), and (101) surfaces. Note: Ti, blue; O, red.

Table 1. Size, composition, layers, and coordination numbers of atomic surface.

Surface	(001)	(100)	(110)	(101)
Supercell	1 × 1	1 × 1	2 × 2	1 × 1
Composition (TiO_2 units)	8.00	8.00	32.00	8.00
TiO_2 layers (frozen/relaxed)	8 4/4	8 4/4	4 2/2	8 4/4
Coordination	O(2) Ti(4)	O(2,3) Ti(5)	O(2,3) Ti(5,6)	O(2,3) Ti(4,5)
Parameter: *a*, *b* in Å	*a* = 4.661 *b* = 4.661	*a* = 4.661 *b* = 2.962	*a* = 6.018 *b* = 13.096	*a* = 5.522 *b* = 4.661
Automatic k-point = 1/30 $Å^{-1}$	5 × 5 × 1	5 × 8 × 1	4 × 2 × 1	5 × 5 × 1
E_{surf} (J nm^{-2})	1.30	0.73	0.55	1.07

We also consider the effect of temperature by calculating the Gibbs free energy at room temperature (298 K); in the solid system, the pressure volume term pV can be ignored, thus:

$$G(T) = H - TS = U + pV - TS \approx U(T) - TS(T) \quad (1)$$

It is reasonable to only consider the vibrational contributions, therefore:

$$U(T) = E_{DFT} + E_{ZPE} + U_{vib}(T) \quad (2)$$

$$S(T) = S_{vib}(T) \quad (3)$$

For vibrational spectra, the density-functional perturbation theory (DFPT) linear response approach was used [78,79]. The matrix of Born effective charges (BEC) is obtained and indicates the change of involved atom's polarizabilities. The infrared intensity can be described as in the following formula containing Born effective charges and the eigenvectors $e_\beta(s|\upsilon)$:

$$f(\upsilon) = \sum_\alpha \left| \sum_{s\beta} Z^*_{\alpha\beta}(s) e_\beta(s|\upsilon) \right|^2 \quad (4)$$

where α and β are Cartesian polarization, $e_\beta(s|\upsilon)$ indicates the normalized vibrational eigenvector, and $Z^*_{\alpha\beta}$ indicates the effective charge tensor. To assess how the frequencies obtained depend on the computational setting, the performance of four different density functionals (PBE, Local Density Approximation (LDA), Perdew-Wang (PW91), Perdew-Burke-Ernzerhof revised for solids (PBESOL)), cut-off (300, 400, 500, 600, and 700 eV), choice of U (3, 4, 5, 6, and 7 eV), and the inclusion of dipole corrections were tested (see Supplementary Tables S1–S4 and Figures S7–S10). Although the numerical values are affected by computational settings, the trends between the different orientations are maintained.

Dispersion effects were evaluated for the heterolytic path for the intermediates and TS1 (the latter as a single-point calculation) by means of dispersion corrections (Grimme D3) (zero) [80] and the results are displayed in Supplementary Table S7 and Figure S12. Dispersion corrections were found to slightly stabilize adsorbates with respect to the non-corrected calculation and significantly decrease the barriers. However, they did not significantly alter the trends of the terminations, nor the vibrational frequencies (Supplementary Table S7 and Figure S12).

No dipole correction was used to account for the asymmetry of the slabs in the perpendicular direction. As our work is mainly based on the comparison of terminations, and as all of them should be affected in a similar manner by the spurious dipole, we do not expect it to have a significant impact on the conclusions. As can be seen in Supplementary Table S6 and Figure S11, the inclusion of dipole corrections did not have a significant effect in the vibrational frequencies.

Slab Model

We optimized the bulk TiO_2 rutile unit cell obtaining values of a = b = 4.661 Å and c = 2.961 Å, in agreement with experimental parameters of a = 4.593 Å and c = 2.958 Å [23]. The calculated lattice parameters for bulk rutile TiO_2 were overestimated by 1.46% for a and only 0.10% for c with respect to the experimental value, and the optimized values were used to build the slab models.

The four rutile TiO_2 surface (001), (100), (110), and (101) stoichiometric terminations are represented in Figure 1 and the main structural parameters are reported in Table 1. As we can see, the facets (001) and (110) are roughly flat, while (100) and (101) facets are uneven. On the surfaces, the coordination number of titanium sites vary from 4 to 6(001) has only Ti_{4C}; (101) possesses Ti_{4C} and Ti_{5C}; (100) has only Ti_{5C}; and (110) has Ti_{5C} and Ti_{6C}. Regarding oxygen, the surface coordination varies from two- to three-fold—(001) has only O_{2C}, while the other three exhibit O_{2C} and O_{3C}. The surface energy E_{surf}, calculated as the difference in energy between the slab and the bulk divided by twice the area, follows the trend of coordination—the lower the surface atomic coordination, the higher the surface energy. Thus, (001), where Ti and O are poorly coordinated, shows E_{surf} 1.30 J nm^{-2}, whereas (110), where the atoms are more coordinated, shows E_{surf} 0.55 J nm^{-2}.

3. Results and Discussion

3.1. H_2 Dissociation

Firstly we investigated the heterolytic pathway for H_2 dissociation on the four selected rutile TiO_2 selected. In the first step, the H_2 molecule physisorbs on the surface forming the adduct H_2*. Then, the heterolytic H_2 dissociation takes place between the Ti site and a neighboring O atom through a transition structure (TS1), generating a pair of O–H and Ti–H bonds (H^+-H^- species). The second step involves the transfer of the hydride (H^-) on the Ti site to a nearby O, leading to 2 O-H hydroxyl groups (H^+-H^+) and a two-electron transfer to surface titanium sites that become reduced. The transition state associated with this step is labeled as TS2. The reaction pathway involving these two steps is schematized in Figure 2, and the calculated energies are reported in Table 2. The energy profile of H_2 dissociation over the four surfaces is shown in Figure 3.

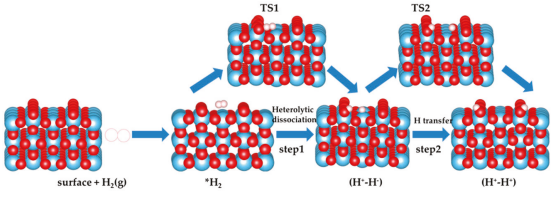

Figure 2. Schematic two-step mechanism considered in the present work. The heterolytic dissociation pathway of H_2 over TiO_2 surface (step 1) and sequential H transfer from Ti to near O (step 2). Ti, O, and H atoms are depicted by blue, red, and white spheres, respectively.

Table 2. Reaction energy (ΔE), dissociation activation energy (E_{act}^{forw}), and backward activation energies (E_{act}^{back} eV) for step 1, and the H transfer barrier of step 2 ($E_{act}2$). Values in brackets are energies without U correction (see below and Supplementary Information). All energies are referred to the physisorbed TiO_2-H_2 system. * indicates adsorption state.

	(001)	(100)	(110)	(101)
H_2 *	0.00 (0.00)	0.00 (0.00)	0.00 (0.00)	0.00 (0.00)
TS1	0.56 (0.63)	1.08 (1.15)	0.50 (0.70)	0.79 (1.10)
(H^+-H^-)	−0.08 (0.15)	0.68 (0.98)	0.12 (0.50)	−0.08 (0.28)
TS2	1.78 (1.98)	2.38 (2.52)	1.80 (1.86)	1.22 (1.50)
(H^+-H^+)	−0.61 (0.03)	0.15 (0.78)	−1.32 (−0.79)	−1.56 (−0.22)
ΔE_1	−0.08 (0.15)	0.68 (0.98)	0.12 (0.68)	−0.08 (0.28)
E_{act}^{forw}	0.56 (0.63)	1.08 (1.15)	0.50 (0.70)	0.79 (1.10)
E_{act}^{back}	0.64 (0.48)	0.40 (0.17)	0.38 (0.20)	0.87 (0.82)
ΔE_2	−0.53 (−0.12)	−0.53 (−0.20)	−1.44 (−1.47)	−1.48 (−0.50)
$E_{act}2$	1.86 (1.83)	1.70 (1.54)	1.68 (1.18)	1.40 (1.22)

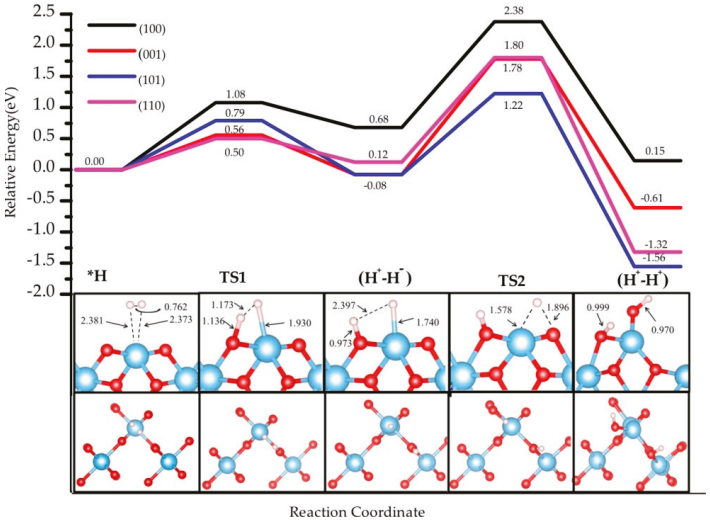

Figure 3. The energy profile of hydrogen dissociation and H transfer from Ti to near O on four rutile TiO_2 surfaces, namely (001), (100), (101), and (110). Inset images show the pathway (side view and top view) on TiO_2 (001); the three other pathways are depicted in Supplementary Figures S1–S3. The bond distance is in Å.

Here, all adsorption energies are referred to the energy of physisorbed TiO_2-H_2. The path for the TiO_2 (001) surface is illustrated, and those corresponding to the other three terminations are provided in Supplementary Figures S1–S3. Several pathways were considered involving different surface sites. For the heterolytic step, on (001) there is a unique possible pathway with only one kind of O_{2c} site and one Ti_{4c} site on the surface. On (100), besides the pathway reported in Supplementary Figure S1, there is also one additional combination of Ti_{5C} and O_{2C} sites (Supplementary Figure S6a), in which the direction of the OH bond is almost perpendicular to the direction of the TiH bond, which makes this combination less stable than the one selected. For (101), two other possible structures involving Ti_{5C} and O_{2C} (Supplementary Figure S6b) and Ti_{4C} and O_{3C} (Supplementary Figure S6c) resulted in less stable systems than the one retained. The model structures retained are stabilized as a consequence of the saturation of poorly coordinated sites of $Ti_{4C,}$ Ti_{5C}, and O_{2C} upon hydrogenation, and in some cases the formation of hydrogen bonds.

The stability of the (H^+, H^-) intermediate is slightly exothermic for the (001) and (101) terminations (−0.08 eV), whereas it is slightly endothermic for the (110) by 0.12 eV, and for the (100) by 0.68 eV. Hydrogen bonds between TiH and OH species form in all the terminations except (101). Whereas the terminations showing the poorest coordination exhibit the most exothermic adsorption energy for the (H^+, H^-) intermediate, the most highly coordinated slabs show less exothermic values. However, the most highly coordinated (110) slab exhibits a significantly lower adsorption energy than (100). The activation barriers of heterolytic H_2 dissociation on the four TiO_2 surfaces follow the trend (110) 0.50 eV < (001) 0.56 eV < (101) 0.79 eV < (100) 1.08 eV. As for the adsorption energy, a trend appears between coordination and kinetic barriers for (001), (101), and (100), whereas (110) presents lower values than expected (its higher coordination should lead to the most endothermic values). Our results are consistent with previous studies. For the (001) surface, our activation energy (0.56 eV) is consistent with the one reported previously (0.68 eV) [14]. The difference comes from the use of a different Hubbard parameter (U = 7 eV) and unit cell (2 × 1). Our activation energy for the (110) surface, 0.50 eV, is larger than the 0.37 eV reported for a much narrower slab (3-TiO_2-layer thick slab model [34]), highlighting the important role of slab thickness in the construction of a model.

According to our results, the (H^+, H^-) intermediate is more likely to be formed on (001) and (101) terminations, however the poor stability and the low barriers could induce the inverse reaction, i.e., the recombination and desorption as H_2 (see below). These results suggest that the rutile TiO_2 (001) exhibits the most likely H_2 heterolytic dissociation path in the series, with the lowest activation energy and a slight stabilization of the product. This specific reactivity could be associated with the low coordination of the surface titanium site—the four-fold coordinated Ti site in the (001) termination stabilizes the hydride Ti-H species to increase the number of neighbors. In the transition structure 1 (TS1) displayed in Figure 3, the Ti-H distance is 1.93 Å (1.74 Å in the intermediate), and the species appears in interaction with the OH group (H-H distance of 1.17 Å) with an imaginary frequency of 992.39 cm^{-1}. The charge density difference analysis shows that there exists a tight ion pair in TS1 where the H on Ti gains electronic density and the H on O is deprived, forming a H^+-H^- pair (Figure 4). This is consistent with a moderate polarization of the H_2 moiety, as shown in the Bader analysis discussed below. In this TS1 structure, the four atoms involved Ti-H … H-O are coplanar.

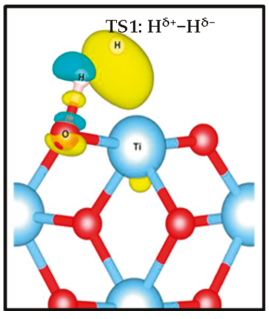

Figure 4. Charge density difference of transition state 1(TS1)illustrating the formation of the $H^{\delta+}$-$H^{\delta-}$ tight ion pair on the (001) surface. Yellow and green iso-surfaces show an electronic density gain and depletion, respectively.

For the other three facets, similar structures are found for TS1 involving coplanar Ti-H … O-H geometries. For the (100) termination, the transition state of this dissociation process shows −1106.91 cm^{-1} Ti-H vibration mode, with 1.83 Å for Ti−H and 1.10 Å for the H-H distance. For the (110) and (101) facets, the Ti-H vibration modes are −704.20 cm^{-1} and −1289.80 cm^{-1}, respectively. The Ti-H bond distances are both 1.95 Å, and the O-H distances are 1.22 Å and 1.33 Å, respectively.

The second step in the mechanism is the transfer of the H^- on the Ti site to the nearest two-fold-coordinated O site, finally yielding two hydroxyls on the surface and a reduction of the Ti sites. The final products (H^+-H^+) are thermodynamically the most stable ones in the path: (001) −0.61 eV, (110) −1.56 eV, (101) −1.09 eV, and (100) 0.15 eV. H-bonds are formed in some of the structures, which results in larger stabilization. In the cases of (001) and (100), the final products involve a rearrangement of the surface bonds—a Ti-O-Ti breaks to form a Ti-OH moiety. The activation barriers are significantly higher than for the first step, ranging from 1.30 to 1.80 eV. These results indicate an unfavorable evolution to the homolytic product from the heterolytic intermediate. Thus, the hydride TiH species could be kinetically stabilized on TiO_2 surfaces with a possible recombination to regenerate and desorb H_2 at low temperatures, whereas the reduction step would require much higher energies to occur. Nevertheless, the most thermodynamically stable product is found for step 2 and involves the presence of two hydroxyl groups and two Ti^{3+} sites; the latter originate from the electron transfer from the hydride to two titanium sites. This transfer results in open-shell systems that can be characterized by the presence of two unpaired electrons.

We have looked for correlations between adsorption energy, barrier heights, and geometry (TiH, HH, and OH distances), as well as Bader charges in TSs, and our results indicate no clear relationship. This is very interesting, as for CeO_2 those correlations do appear [81]. This might point to an ionocovalent character of Ti-O bond compared to the more ionic Ce-O bond, which would facilitate the formation of the H^+-H^- ionic pair, or to the important role of the local topology in stabilizing intermediates and transition structures. As a general trend, the activation barriers seem related to the coordination numbers of Ti and O on the surfaces, with the (110) termination behaving in a different way than is expected from its highly coordinated surface sites.

3.2. Electronic Structure

In order to characterize in more detail the electronic structure of the structures involved in the hydrogenation mechanisms, we have computed the *density of states* (DOS); Figure 5 and Supplementary Figure S4) for step 1 and step 2 of the four terminations considered. As unpaired electrons are involved, especially in H transfer process step 2, spin up and spin down are represented. The features of these four facets are similar and only the (001) and (100) facets are displayed in Figure 5. The other two facets are shown in Supplementary Figure S4. At the bottom of the plot a hydrogen molecular band appears as a sharp narrow peak in the valence region due to H_2 physical adsorption. In TS1, we observe a splitting in two bands associated with H^+ and H^- species that overlap with the slab levels. For the product of heterolytic dissociation (H^+-H^-), the H^- band is the highest occupied energy level, with a sharp peak at the Fermi level. For the TS2 of subsequent H transfer from Ti to nearby O, there still exists one H^+ band and one H^- band, but the intensity decreases. The existence of wide, weak peaks in the gap indicates an early reduction of the Ti site in TS2 on (100) and (110) facets, while no corresponding peak appears on (001) and (101). For the H transfer process product (H^+-H^+) species, we observe the H^+ levels corresponding to OH groups in O-H bonds in the valence band, which appear as two distinct peaks if they correspond to inequivalent hydroxyl groups. Also, Ti states appear in the gap below the Fermi level, indicating the reduction of the Ti sites. This is consistent with the picture of the spin density plots (Figure 6 and Supplementary Figure S5), indicating that the unpaired electrons from the hydride transfer are trapped by two Ti ions that get reduced, confirming the nature of Ti^{3+} sites. Note that the approach used in the present work does not allow one to state unambiguously which Ti sites are reduced—it only confirms qualitatively that two distinct Ti sites are involved.

Bader charge analysis [82] was carried out to complement the characterization of the electronic structure of the systems studied. In Table 3, we can follow the electronic charges during the two processes, whereas Table 4 shows the Bader analysis for the spin density. In step 1, the adsorbed hydrogen species shows a slightly polarized H-H bond. In TS1, the H-H bond is more polarized,

generating a tight ion pair with charges in the range 0.35-0.48 |e| for the H^+ and −0.31 to −0.41 |e| for the H^- species. The intermediate (H^+, H^-) species is characterized by charges in the range 0.65–0.70 |e| and −0.30 to −0.41 |e| for H^+ and H^-, respectively. Moreover, the oxygen involved in this hydrogen transfer process shows electron gain of about +0.15–0.30|e| compared to the same O in the slab. The Bader charge of the products (H^+-H^+) show values from 1.78 to 1.87 |e| for the surface Ti sites carrying the electrons. Actually, based on our spin density results (see Figure 6, Supplementary Figure S5 and Table 4) two Ti are reduced for every facet. For the TS2, one of the Ti on the surface partially decreases its positive charge, indicating partial reduction. Finally, in the H^+-H^+ species the two H are characterized as protons, whereas two Ti sites decrease their positive charge, indicating that they host the reduction electrons, and the integrated spin density varies from 0.90 to 1.05 |e| (See Table 4). It is worth stating that the O site involved in the H transfer process also contains a small amount of unpaired electrons of 0.24 |e| for TS2 of both (001) and (101) facets, as can be seen in Figure 6 for the (001) case.

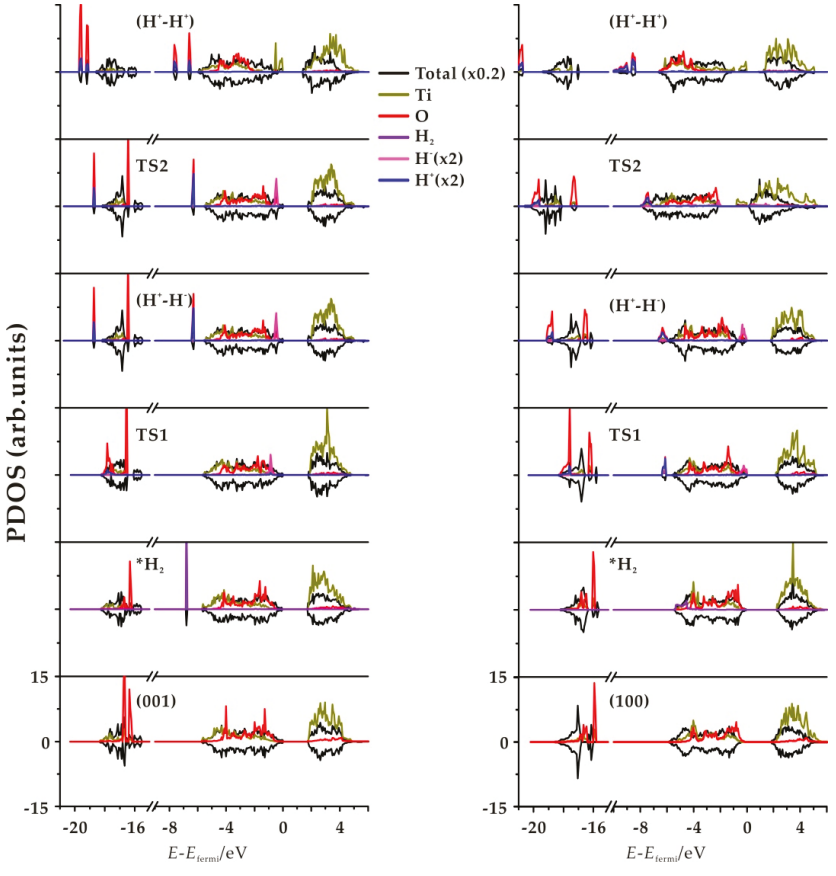

Figure 5. Total and projected densities of state (PDOS) of the TiO_2 slab, $*H_2$, TS, *(H^+, H^-), and *(H^+-H^+) for the (001) (**left**) and (100) (**right**) surfaces. For the PDOS, only the Ti and O involved in the two processes are projected. Positive *density of states* (DOS) correspond to spin up and negative to spin down.

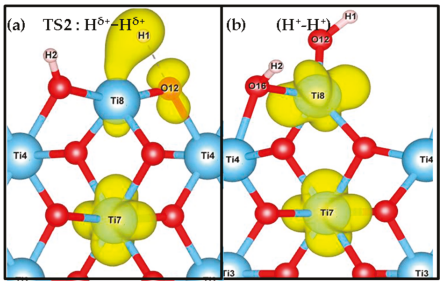

Figure 6. Spin density of TS2 (**a**) and (H^+-H^+) species (**b**) indicating the distribution of unpaired electrons on the (001) facet. The spin densities for TS2 and (H^+-H^+) species on the other three facets are shown in Supplementary Figure S5.

Table 3. Bader charges (|e|) of H and involved Ti and O_a in the H_2 dissociation process, and involved H, Ti, and O_b in subsequent H transfer from Ti to O process for H_2 *, TS and (H^+-H^-), and (H^+-H^+). For step 1, the O involved was labeled O_a, and O_b in step 2.

	qTi^+ /qO^-		**qH^+/qH^- qTi^+/qO_a^-**			**qH^+/qH^- qTi^+/qO_b^-**		**qH^+/qH^+ $/qTi^+/qO_b^-$**
	Slab	**H_2 ***	**TS1**	**(H^+-H^-)-O_a**	**(H^+-H^-)-O_b**	**TS2**	**(H^+-H^+)**
(001)	1.98/−1.00	0.02/−0.01 /1.98/−1.00	0.48/−0.41 /1.97/−1.02	0.67/−0.42 /1.95/−1.22	0.67/−0.42 /1.95/−0.98	0.63/−0.10 /1.90/−0.97	0.65/0.61 /1.79/−1.26
(100)	2.03/−1.07	0.04/−0.02 /2.01/−1.07	0.43/−0.32 /1.96/−1.12	0.65/−0.30 /1.90/−1.24	0.65/−0.30 /1.90/−0.98	0.64/−0.01 /1.77/−1.10	0.60/0.60 /1.78/−1.27
(110)	2.01/−0.90	0.04/−0.02 /2.04/−0.92	0.35/−0.31 /2.01/−0.97	0.70/−0.34 /1.93/−1.22	0.70/−0.34 /1.93/−0.91	0.67/0.00 /1.95/−0.92	0.64/0.62 /1.87/−1.15
(101)	1.99/−0.96	0.04/−0.03 /1.98/−0.96	0.38/−0.40 /1.97/−1.03	0.67/−0.40 /1.96/−1.20	0.67/−0.40 /1.96/−0.93	0.60/−0.10 /1.90/−1.25	0.60/0.66 /1.83/−1.30

Table 4. The number of unpaired electrons of TS2 and (H^+-H^+) species. Only involved atoms are shown.

Slab	**(001)**	**(100)**	**(110)**	**(101)**	**Slab**	**(001)**	**(100)**	**(110)**
Species	**TS2**	**(H^+-H^+)**	**TS2**	**(H^+-H^+)**	**TS2**	**(H^+-H^+)**	**TS2**	**(H^+-H^+)**
Total	1.70	2.00	1.90	2.00	1.92	2.00	1.70	2.00
Ti	0.80	0.97	0.99	0.91	0.24	0.90	0.80	0.99
Ti	0.16	1.00	0.11	1.05	0.24	0.90	0.16	0.99
O	0.24	0.00	0.02	0.00	0.00	0.00	0.24	0.00
H1	0.44	0.00	0.87	0.00	0.97	0.00	0.44	0.00
H_2	0.00	0.00	0.00	0.00	0.10	0.00	0.00	0.00

3.3. Effect of the Hubbard Correction U

The values without U correction were considered to analyze the effect of U in the energetic profile, which is reported in Table 2. The profile is similar to the one obtained for U = 4 eV (see Figure 7 for the (001) case and Supplementary Materials for the others). In step 1, the heterolytic dissociation leads to (H^+-H^-) products stable at 0.15 eV (001), 0.28 eV (101), 0.98 eV (101), and 0.50 eV (110), and barriers of 0.63 eV, 1.10 eV, and 1.15 eV, 0.70 eV, respectively, which is ~0.20 eV higher in energy than for the U = 4 eV case (Table 2, Figure 3). The increase in the values is significantly higher in step 2, where the (H^+-H^+) product is higher in energy by ~0.60 eV in the absence of U correction, and is associated with the stabilization of the localized solution favored by the U = 4 eV term with respect to the U = 0 eV case. In general, the activation barriers are not significantly affected by the U value, with the exception of (110) and (100) in step 1 (formation of H^+-H^-), where the U = 0 eV leads to a TS1 very close in energy to the H^+-H^- intermediate. The backward reaction i.e., recombination desorption of H_2, would thus be barrierless and the intermediate would not be stable at all. The overall profile and the trend of the activity for H_2 dissociation and subsequent H transfer for the four TiO_2 surfaces is maintained.

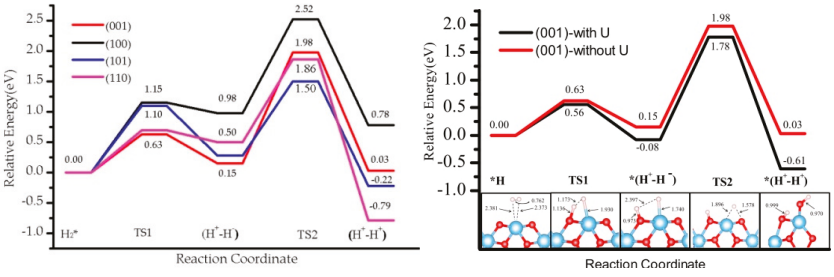

Figure 7. Comparison of energy profile on four facets without U correction (**left**). Comparison of energy profile on (001) when U is 4.0 eV and without U (**right**).

3.4. Vibrational Spectrum

We computed the vibration frequency and IR spectra of H_2 heterolytic dissociation products (H^+-H^-) for the four terminations. No scaling factor was applied. The vibration modes are shown in Table 5 and Figure 8, and present three main regions: Ti−H and O−H bending modes at low frequencies (below 1000 cm^{-1}); the vibration frequencies of Ti−H lie in the range of 1500–1800 cm^{-1}; the stretching OH modes are characterized by higher frequencies (between 2900 cm^{-1} and 3800 cm^{-1}). Ti−H stretching modes of the four species are seen in the calculated spectrum at 1644 cm $^{-1}$ (001), 1768 cm^{-1} (100), 1653 cm^{-1} (110), and 1577 cm^{-1} (101), corresponding to the expected Ti−H IR spectral region (around 1600 cm^{-1}) [83].The hydrides of (001) and (101) facets are Ti_{4C}-H, while they are Ti_{5c}-H on (100) and (110) surfaces, as displayed in Figure 9. Previous studies using electron-stimulated desorption (ESD) [84] and low-energy ion scattering (LEIS) [85] reported that the annealed TiO_2 surface is compensated by H, which is bonded in the Ti−H as well as O−H with bridging O or a subsurface, but no specific frequencies were provided. Recently, Yan et.al indicated the formation of Ti-H species on the P25 TiO_2 surface [86].

Table 5. Computed IR wavenumbers (cm^{-1}) and intensities (in brackets) of Ti−H and O−H stretching modes of (H^+, H^-) species for the four terminations studied.

Stretching Modes	(001)	(100)	(110)	(101)
(Ti-H)	1644.78 (0.39)	1768.74 (0.52)	1653.87 (0.32)	1577.45 (0.76)
(O-H)	3742.87 (0.05)	2976.54 (1.56)	3606.59 (0.22)	3622.37 (0.44)

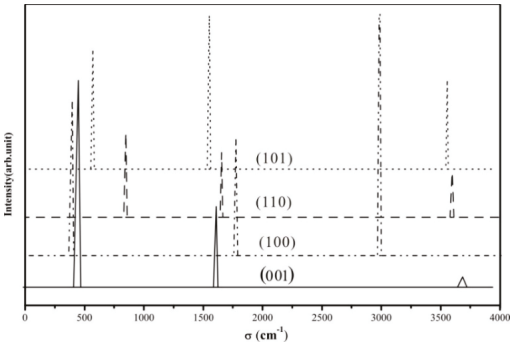

Figure 8. Computed IR spectra of the TiO_2-(H^+, H^-) species for the four selected terminations. Intensities are given in arbitrary units.

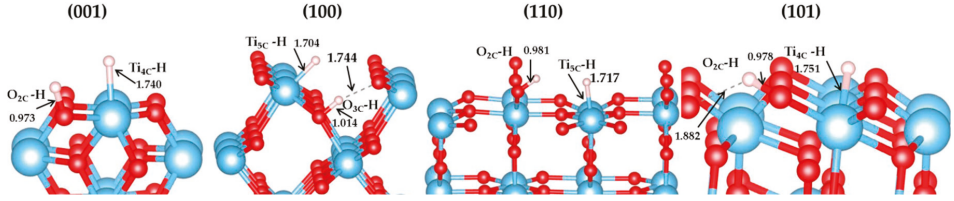

Figure 9. Structures of (H^+-H^-) species on (001), (100), (110), and (101) surfaces (bond distance in Å).

For the (O-H) vibrations, there are many experimental reports by various authors (see selected ones in Supplementary Table S5), showing that the vibrations can be greatly influenced by the nature of the site, the surface topology, the presence of defects and coverage [87], as well as the polymorph [88]. In the present work, we perform an analysis of OH vibrations for the four terminations considered (see Table 5, Figure 9) as a guide for qualitative assignment. It is found that the OH stretching vibrations are different between these four facets. The calculated IR results of TiO_2 (100) surface (2976.54 cm^{-1}) correspond to a Ti_{5C}-O_{3C}H exhibiting an H bond with one O site nearby. An experimental value of 3550 cm^{-1} for OH on (100) [89] was reported for the adsorption of water on the surface, most likely assigned to terminal hydroxyl groups. Our value is consistent with a higher coordination of the hydroxyl group (three-fold in our case), as well as with the presence of a hydrogen bond, both blue-shifting the vibration with respect to the experimental value. For the TiO_2 (101) surface (3622.37 cm^{-1}) it corresponds to a Ti_{4C}-O_{2C}H. Experimentally, the OH stretching vibrations from water adsorption are observed at 3680 and 3610 cm^{-1} [89]. For the TiO_2 (110) surface (3606.59 cm^{-1}) the vibration corresponds to Ti_{6C}-O_{2C}H, which is lower than in a previous theoretical study by Wöll (3700 cm^{-1}) [90]. Note that the model used in the work of Wöll et al. involves a hydroxyl perpendicular to the slab, whereas in our work the hydroxyl is tilted. Other experimental works report 3665 and 3690 cm^{-1} measured by High-Resolution Electron Energy Loss Spectroscopy (HREELS) [91,92], and 3711 cm^{-1} by IR [93] on systems obtained by H_2O adsorption on a clean single-crystal TiO_2 surface.

As a general remark, the lack of experimental data in well-controlled structures and conditions make an assessment of the vibrational spectra of surface hydroxyl and hydride species difficult, although several trends can be observed. First, the vibrations are dependent on the surface topology due to specific local chemical environments. Second, the coordination of oxygen and titanium sites seems to play a role, as well as hydrogen bonds formed between TiH/OH pairs and neighboring O sites. Overall, our results are consistent with previous experimental and theoretical data published in the literature and provide a set of spectra to stimulate the search of TiH/OH species on different rutile terminations.

3.5. The H_2 Recombination-Desorption Reaction

We studied the energy barriers for hydride TiH/OH species recombination to regenerate and desorb H_2 on four facets (Figure 10, Table 2). The corresponding barrier for that process, E_{act}^{back}, requires 0.64 eV for (001), 0.87 eV for (101), 0.38 eV for the (110), and 0.40 eV for the (100) slabs. The backward activation energies for the facets (001) and (101) are larger than those found for facets (110) and (100), probably due to the higher stability of the (H^+-H^-) species. Contrary to the dissociation process, the desorption of H_2 is slightly endothermic for the (001) and (101) terminations (0.08 eV), whereas it is exothermic for the (110) by −0.12 eV, and for the (100) by −0.68 eV. On (101) and (001) facets, hydrogen dissociation, and therefore (H^+-H^-) formation, is slightly more favorable than H_2 desorption: 0.79 eV vs. 0.56 eV for (101), 0.87 eV vs. 0.64 eV for (001). H_2 dissociation and desorption occur with similar barriers on (110), with 0.50 eV and 0.40 eV, respectively. Thus, it is expected that the (H^+-H^-) intermediate involving Ti-H species is more likely to be observed in (001), and to a lesser extent (101), where the (100) and (110) would lead to recombination and desorption.

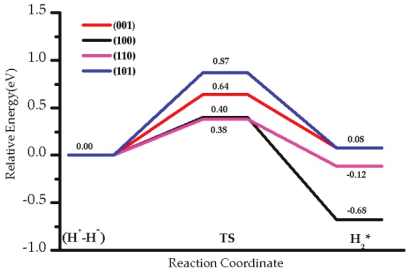

Figure 10. The energy profile of hydrides TiH (H^+-H^-) species recombination with OH to desorb H_2 on four facets at 0 K, U = 4 eV.

3.6. Zero-Point Energy Correction and Effect of Temperature

The energy profiles with Zero Point Energy (ZPE) correction are also studied together with the Gibbs free energies for T = 298 K (Figure 11). With ZPE correction, the energy for these two steps increases, while it does not affect the kinetic barriers. Temperature has almost no effect on this reaction profile.

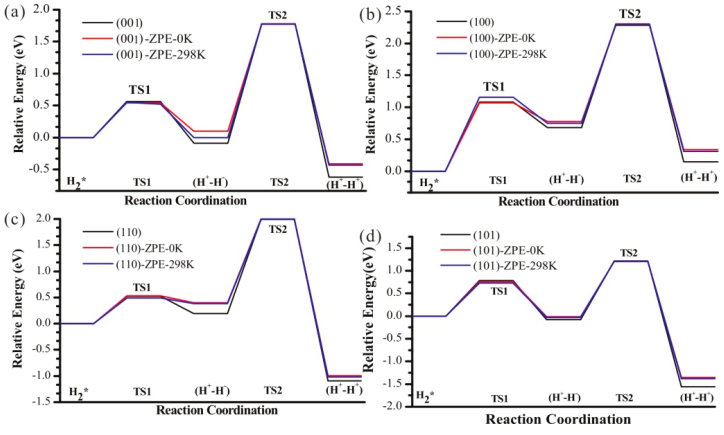

Figure 11. The heterolytic pathway of H_2 dissociation and subsequent H transfer from Ti to O nearby on four (**a**–**d**) TiO_2 facets, considering zero point energy (red lines). Blue lines indicate the profiles for T = 298 K.

As a final remark, many other factors may have a deep influence on the behavior of TiO_2 regarding hydrogenation—the presence of surface and subsurface defects [94], the nature of the bulk phase [95], nanostructuring [96,97], interfacial water [98], or reduction [99]. More fundamental works to elucidate the structure of hydrogenated surfaces are needed to build a robust scenario for the complex behavior observed [100].

4. Conclusions

The mechanisms of H_2 dissociation on four different rutile TiO_2 facets by means of density functional theory (PBE+U) calculations have been investigated. The results showed that the topology of the surface has a moderate effect on H_2 dissociation on TiO_2 kinetically and also thermodynamically. We found that for all four surfaces, the heterolytic dissociation pathway towards hydride–hydroxyl surface pairs is kinetically more favorable than the H transfer process towards substrate reduction, although the reduction product, with only surface hydroxyl groups, is thermodynamically more

favorable. On (110) and (100), the hydride–hydroxyl pair formed can recombine and desorb as molecular dihydrogen, whereas the (001), and to a lesser extent (101), stabilize the hydride–hydroxyl pair. The energetics of the reaction seems related to the coordination numbers of Ti and O on the surfaces, although (110) shows a specific behavior. No clear trend relating adsorption energies and barriers with local geometry or charges was found. The electronic structure analysis allows characterization of charge and electron transfers. The IR spectra of the (H^+-H^-) pair species were also computed indicating the vibrational region of Ti-H species on TiO_2 facets in the range of 1550–1750 cm^{-1}. The frequencies are found to depend on the facet exposed and could be used as a qualitative guideline to identify them experimentally.

Supplementary Materials: The following are available online at http://www.mdpi.com/2079-4991/9/9/1199/s1. Figure S1: H_2 dissociation on rutile TiO_2 (100) facets with U = 4 eV and U = 0 eV. Figure S2: H_2 dissociation on rutile TiO_2 (110) facets with U = 4 eV and U = 0 eV. Figure S3: H_2 dissociation on rutile TiO_2 (101) facets with U = 4 eV and U = 0 eV. Figure S4: Projected Density of State (PDOS) of the TiO_2 slab, H_2*, TS, and (H^+, H^-), (H^+-H^+) for the (110) (left) and (101) (right) surfaces. Figure S5: Spin Density of TS2 and (H^+-H^+). Figure S6: Structures of (H^+-H^-) for the other adsorption modes considered. Tables S1–S6 and Figures S7–S11 IR frequencies. Tables S7 and S12: Grimme D3 corrections. Geometric structures for the intermediates and transition structures used in this work (POSCAR - VASP input files- format).

Author Contributions: Investigation, B.W. and M.C.; software, M.C.; supervision, M.C.; writing—original draft, B.W.; writing—review and editing, F.T. and M.C.

Funding: This research was funded by China Scholarship Council (CSC).

Acknowledgments: This study was supported by China Scholarship Council (CSC). Authors acknowledge Scienomics for the MAPS program used in the construction of the slab models for a courtesy license. B. Diawara is acknowledged for the Modelview program. O. Matz is warmly acknowledged for his technical support. This work was performed using HPC resources from GENCI- CINES/IDRIS (Grant numbers 2018-x2018082131 and 2019-x2019082131), and the PER-SU iDROGEN project.

Conflicts of Interest: The authors declare no conflict of interest. The funders had no role in the design of the study; in the collection, analyses, or interpretation of data; in the writing of the manuscript, or in the decision to publish the results.

References

1. Bach, U.; Lupo, D.; Comte, P.; Moser, J.E.; Weissortel, F.; Salbeck, J.; Spreitzer, H.; Gratzel, M. Solid-state dye-sensitized mesoporous TiO_2 solar cells with high photon-to-electron conversion efficiencies. *Nature* **1998**, *395*, 583–585. [CrossRef]
2. Crossland, E.J.W.; Noel, N.; Sivaram, V.; Leijtens, T.; Alexander-Webber, J.A.; Snaith, H.J. Mesoporous TiO_2 single crystals delivering enhanced mobility and optoelectronic device performance. *Nature* **2013**, *495*, 215–219. [CrossRef] [PubMed]
3. Fujishima, A.; Honda, K. Electrochemical photolysis of eater at a semiconductor electrode. *Nature* **1972**, *238*, 37. [CrossRef] [PubMed]
4. Tada, H.; Fujishima, M.; Kobayashi, H. Photodeposition of metal sulfide quantum dots on titanium (IV) dioxide and the applications to solar energy conversion. *Chem. Soc. Rev.* **2011**, *40*, 4232–4243. [CrossRef] [PubMed]
5. Chen, M.S.; Goodman, D.W. The structure of catalytically active gold on titania. *Science* **2004**, *306*, 252–255. [CrossRef] [PubMed]
6. Maeda, Y.; Iizuka, Y.; Kohyama, M. Generation of oxygen vacancies at a Au/TiO_2 perimeter interface during CO oxidation detected by in situ electrical conductance measurement. *J. Am. Chem. Soc.* **2013**, *135*, 906–909. [CrossRef]
7. Varghese, O.K.; Gong, D.W.; Paulose, M.; Ong, K.G.; Dickey, E.C.; Grimes, C.A. Extreme changes in the electrical resistance of titania nanotubes with hydrogen exposure. *Adv. Mater.* **2003**, *15*, 624–627. [CrossRef]
8. Zhou, X.Y.; Wang, Z.; Xia, X.H.; Shao, G.S.; Homewood, K.; Gao, Y. Synergistic cooperation of rutile TiO_2 {002}, {101}, and {110} facets for hydrogen sensing. *ACS Appl. Mater. Interfaces* **2018**, *10*, 28199–28209. [CrossRef]
9. Sugita, Y.; Ishizaki, K.; Iwasa, F.; Ueno, T.; Minamikawa, H.; Yamada, M.; Suzuki, T.; Ogawa, T. Effects of pico-to-nanometer-thin TiO_2 coating on the biological properties of microroughened titanium. *Biomaterials* **2011**, *32*, 8374–8384. [CrossRef]

10. Bruce, P.G.; Scrosati, B.; Tarascon, J.M. Nanomaterials for rechargeable lithium batteries. *Angew. Chem. Int. Ed.* **2008**, *47*, 2930–2946. [CrossRef]
11. Linsebigler, A.L.; Lu, G.Q.; Yates, J.T. Photocatalysis on TiO_2 surface—Principles, mechanisma, and selected results. *Chem. Rev.* **1995**, *95*, 735–758. [CrossRef]
12. Etgar, L.; Zhang, W.; Gabriel, S.; Hickey, S.G.; Nazeeruddin, M.K.; Eychmuller, A.; Liu, B.; Gratzel, M. High efficiency quantum dot heterojunction solar cell using anatase (001) TiO_2 nanosheets. *Adv. Mater.* **2012**, *24*, 2202–2206. [CrossRef] [PubMed]
13. Sun, C.H.; Jia, Y.; Yang, X.H.; Yang, H.G.; Yao, X.D.; Lu, G.Q.; Selloni, A.; Smith, S.C. Hydrogen incorporation and storage in well-defined nanocrystals of anatase titanium dioxide. *J. Phys. Chem. C* **2011**, *115*, 25590–25594. [CrossRef]
14. Wang, Z.; Xia, X.H.; Guo, M.L.; Shao, G.S. Fundamental pathways for the adsorption and transport of hydrogen on TiO_2 Surfaces: Origin for effective sensing at about room temperature. *ACS Appl. Mater. Interfaces* **2016**, *8*, 35298–35307. [CrossRef] [PubMed]
15. Chen, X.B.; Liu, L.; Yu, P.Y.; Mao, S.S. Increasing solar absorption for photocatalysis with black hydrogenated titanium dioxide nanocrystals. *Science* **2011**, *331*, 746–750. [CrossRef] [PubMed]
16. Kudo, A.; Miseki, Y. Heterogeneous photocatalyst materials for water splitting. *Chem. Soc. Rev.* **2009**, *38*, 253–278. [CrossRef] [PubMed]
17. Wang, G.M.; Wang, H.Y.; Ling, Y.C.; Tang, Y.C.; Yang, X.Y.; Fitzmorris, R.C.; Wang, C.C.; Zhang, J.Z.; Li, Y. Hydrogen-treated TiO_2 nanowire arrays for photoelectrochemical water splitting. *Nano Lett.* **2011**, *11*, 3026–3033. [CrossRef]
18. Woll, C. Hydrogen adsorption on metal oxide surfaces: A reinvestigation using He-atom scattering. *J. Phys. Condes. Matter* **2004**, *16*, S2981–S2994. [CrossRef]
19. Zheng, Z.K.; Huang, B.B.; Lu, J.B.; Wang, Z.Y.; Qin, X.Y.; Zhang, X.Y.; Dai, Y.; Whangbo, M.H. Hydrogenated titania: Synergy of surface modification and morphology improvement for enhanced photocatalytic activity. *Chem. Commun.* **2012**, *48*, 5733–5735. [CrossRef]
20. Joo, J.B.; Dillon, R.; Lee, I.; Yin, Y.D.; Bardeen, C.J.; Zaera, F. Promotion of atomic hydrogen recombination as an alternative to electron trapping for the role of metals in the photocatalytic production of H_2. *Proc. Natl. Acad. Sci. USA* **2014**, *111*, 7942–7947. [CrossRef]
21. Aschauer, U.; Selloni, A. Hydrogen interaction with the anatase TiO_2(101) surface. *Phys. Chem. Chem. Phys.* **2012**, *14*, 16595–16602. [CrossRef] [PubMed]
22. Calatayud, M.; Minot, C. Effect of relaxation on structure and reactivity of anatase (100) and (001) surfaces. *Surf. Sci.* **2004**, *552*, 169–179. [CrossRef]
23. Diebold, U. The surface science of titanium dioxide. *Surf. Sci. Rep.* **2003**, *48*, 53–229. [CrossRef]
24. Islam, M.M.; Calatayud, M.; Pacchioni, G. Hydrogen adsorption and diffusion on the anatase TiO_2(101) surface: A first-principles investigation. *J. Phys. Chem. C* **2011**, *115*, 6809–6814. [CrossRef]
25. Liu, L.L.; Wang, Z.; Pan, C.X.; Xiao, W.; Cho, K. Effect of hydrogen on O_2 adsorption and dissociation on a TiO_2 anatase (001) surface. *ChemPhysChem* **2013**, *14*, 996–1002. [CrossRef]
26. Nadeem, I.M.; Treacy, J.P.W.; Selcuk, S.; Torrelles, X.; Hussain, H.; Wilson, A.; Grinter, D.C.; Cabailh, G.; Bikondoa, O.; Nicklin, C.; et al. Water dissociates at the aqueous interface with reduced anatase TiO_2 (101). *J. Phys. Chem. Lett.* **2018**, *9*, 3131–3136. [CrossRef] [PubMed]
27. Vittadini, A.; Casarin, M.; Selloni, A. Hydroxylation of TiO_2-B: Insights from density functional calculations. *J. Mater. Chem.* **2010**, *20*, 5871–5877. [CrossRef]
28. Yin, X.L.; Calatayud, M.; Qiu, H.; Wang, Y.; Birkner, A.; Minot, C.; Woll, C. Diffusion versus desorption: Complex behavior of H atoms on an oxide surface. *ChemPhysChem* **2008**, *9*, 253–256. [CrossRef]
29. Ma, S.C.; Huang, S.D.; Fang, Y.H.; Liu, Z.P. TiH hydride formed on amorphous black titania: Unprecedented active species for photocatalytic hydrogen evolution. *ACS Catal.* **2018**, *8*, 9711–9721. [CrossRef]
30. Chen, H.Y.T.; Giordano, L.; Pacchioni, G. From heterolytic to homolytic H_2 dissociation on nanostructured MgO(001) Films as a function of the metal support. *J. Phys. Chem. C* **2013**, *117*, 10623–10629. [CrossRef]
31. Coluccia, S.; Boccuzzi, F.; Ghiotti, G.; Mirra, C. Evidence for heterolytic dissociation of H_2 on the surface of thermally activated MgO powders. *Z. Fur Phys. Chem. Wiesb.* **1980**, *121*, 141–143. [CrossRef]
32. Di Valentin, C.; Pacchioni, G.; Selloni, A. Electronic structure of defect states in hydroxylated and reduced rutile TiO_2(110) surfaces. *Phys. Rev. Lett.* **2006**, *97*. [CrossRef] [PubMed]

33. Garcia-Melchor, M.; Lopez, N. Homolytic products from heterolytic paths in H_2 dissociation on metal oxides: The example of CeO_2. *J. Phys. Chem. C* **2014**, *118*, 10921–10926. [CrossRef]
34. Hu, G.X.; Wu, Z.L.; Jiang, D.E. First principles insight into H_2 activation and hydride species on TiO_2 Surfaces. *J. Phys. Chem. C* **2018**, *122*, 20323–20328. [CrossRef]
35. Joubert, J.; Salameh, A.; Krakoviack, V.; Delbecq, F.; Sautet, P.; Coperet, C.; Basset, J.M. Heterolytic splitting of H_2 and CH_4 on gamma-alumina as a structural probe for defect sites. *J. Phys. Chem. B* **2006**, *110*, 23944–23950. [CrossRef] [PubMed]
36. Menetrey, M.; Markovits, A.; Minot, C. Reactivity of a reduced metal oxide surface: Hydrogen, water and carbon monoxide adsorption on oxygen defective rutile TiO_2(110). *Surf. Sci.* **2003**, *524*, 49–62. [CrossRef]
37. Panayotov, D.A.; Yates, J.T. n-Type doping of TiO_2 with atomic hydrogen-observation of the production of conduction band electrons by infrared spectroscopy. *Chem. Phys. Lett.* **2007**, *436*, 204–208. [CrossRef]
38. Calatayud, M.; Markovits, A.; Menetrey, M.; Mguig, B.; Minot, C. Adsorption on perfect and reduced surfaces of metal oxides. *Catal. Today* **2003**, *85*, 125–143. [CrossRef]
39. Fernandez-Torre, D.; Carrasco, J.; Ganduglia-Pirovano, M.V.; Perez, R. Hydrogen activation, diffusion, and clustering on CeO_2(111): A DFT+U study. *J. Chem. Phys.* **2014**, *141*. [CrossRef]
40. Liu, Y.P.; Li, Y.H.; Yang, S.Y.; Lin, Y.; Zuo, J.L.; Liang, H.; Peng, F. Revealing the relationship between photocatalytic properties and structure characteristics of TiO_2 reduced by hydrogen and carbon monoxide treatment. *ChemSusChem* **2018**, *11*, 2766–2775. [CrossRef]
41. Batzill, M. Fundamental aspects of surface engineering of transition metal oxide photocatalysts. *Energy Environ. Sci.* **2011**, *4*, 3275–3286. [CrossRef]
42. Farneth, W.E.; Hotsenpiller, P.A.M.; Bolt, J.D.; Lowekamp, J.B.; Rohrer, G.S. Orientation dependence of photochemical reactions on TiO_2 thin film surfaces. *Abstr. Pap. Am. Chem. Soc.* **1998**, *216*, U747.
43. Han, X.G.; Kuang, Q.; Jin, M.S.; Xie, Z.X.; Zheng, L.S. Synthesis of titania nanosheets with a high percentage of exposed (001) facets and related photocatalytic properties. *J. Am. Chem. Soc.* **2009**, *131*, 3152–3153. [CrossRef]
44. Kislov, N.; Lahiri, J.; Verma, H.; Goswami, D.Y.; Stefanakos, E.; Batzill, M. Photocatalytic degradation of methyl orange over single crystalline ZnO: Orientation dependence of photoactivity and photostability of ZnO. *Langmuir* **2009**, *25*, 3310–3315. [CrossRef]
45. Ohno, T.; Sarukawa, K.; Matsumura, M. Crystal faces of rutile and anatase TiO_2 particles and their roles in photocatalytic reactions. *New J. Chem.* **2002**, *26*, 1167–1170. [CrossRef]
46. Calatayud, M.; Yin, X.L.; Qiu, H.; Wang, Y.; Birkner, A.; Minot, C.; Woll, C. Comment on "Imaging of the hydrogen subsurface site in rutile TiO_2". *Phys. Rev. Lett.* **2010**, *104*. [CrossRef]
47. Kowalski, P.M.; Meyer, B.; Marx, D. Composition, structure, and stability of the rutile TiO_2(110) surface: Oxygen depletion, hydroxylation, hydrogen migration, and water adsorption. *Phys. Rev. B* **2009**, *79*. [CrossRef]
48. Sasahara, A.; Murakami, T.; Tomitori, M. XPS and STM study of TiO_2(110)-(1 x 1) surfaces immersed in simulated body fluid. *Surf. Sci.* **2018**, *668*, 61–67. [CrossRef]
49. Yu, X.J.; Zhang, Z.R.; Yang, C.W.; Bebensee, F.; Heissler, S.; Nefedov, A.; Tang, M.R.; Ge, Q.F.; Chen, L.; Kay, B.D.; et al. Interaction of formaldehyde with the Rutile TiO_2(110) Surface: A combined experimental and theoretical study. *J. Phys. Chem. C* **2016**, *120*, 12626–12636. [CrossRef]
50. Zhang, D.Y.; Yang, M.N.; Dong, S. Hydroxylation of the rutile TiO_2(110) surface enhancing its reducing power for photocatalysis. *J. Phys. Chem. C* **2015**, *119*, 1451–1456. [CrossRef]
51. Imanishi, A.; Tsuji, E.; Nakato, Y. Dependence of the work function of TiO_2 (Rutile) on crystal faces, studied by a scanning auger microprobe. *J. Phys. Chem. C* **2007**, *111*, 2128–2132. [CrossRef]
52. Lu, Y.; Jaeckel, B.; Parkinson, B.A. Preparation and characterization of terraced surfaces of low-index faces of anatase, rutile, and brookite. *Langmuir* **2006**, *22*, 4472–4475. [CrossRef]
53. Raza, H.; Pang, C.L.; Haycock, S.A.; Thornton, G. Evidence of discrete bond breaking steps in the 1 x 1 to 1 x 3 phase transition of TiO_2(100). *Phys. Rev. Lett.* **1999**, *82*, 5265–5268. [CrossRef]
54. Warschkow, O.; Wang, Y.; Subramanian, A.; Asta, M.; Marks, L.D. Structure and local-equilibrium thermodynamics of the c(2 × 2) reconstruction of rutile TiO_2 (100). *Phys. Rev. Lett.* **2008**, *100*. [CrossRef]
55. Lindberg, F.; Heinrichs, J.; Ericson, F.; Thomsen, P.; Engqvist, H. Hydroxylapatite growth on single-crystal rutile substrates. *Biomaterials* **2008**, *29*, 3317–3323. [CrossRef]

56. Muscat, J.; Harrison, N.M. The physical and electronic structure of the rutile (001) surface. *Surf. Sci.* **2000**, *446*, 119–127. [CrossRef]
57. Norenberg, H.; Dinelli, F.; Briggs, G.A.D. Network-like (7 root 2 x root 2) R45 degrees surface reconstruction on rutile TiO_2(001) by non-equilibrium self-organization. *Surf. Sci.* **1999**, *436*, L635–L640. [CrossRef]
58. Poirier, G.E.; Hance, B.K.; White, J.M. Identification of the facet planes of phase I TiO_2(001) rutile by scanning tunneling tunneling microscopy and low-energy electron-diffraction. *J. Vac. Sci. Technol. B* **1992**, *10*, 6–15. [CrossRef]
59. Sosnowchik, B.D.; Chiamori, H.C.; Ding, Y.; Ha, J.Y.; Wang, Z.L.; Lin, L.W. Titanium dioxide nanoswords with highly reactive, photocatalytic facets. *Nanotechnology* **2010**, *21*. [CrossRef]
60. Thibado, P.M.; Bonnell, D.A. Metal-oxide interactions on copper-segregated and copper-deposited TiO_2 rutile (001) surfaces. *J. Am. Ceram. Soc.* **1997**, *80*, 1267–1273. [CrossRef]
61. Yang, M.H.; Chen, T.T.; Wang, Y.S.; Chiu, H.T.; Lee, C.Y. Electrochromism of rutile nanowires, vertically aligned along the 001 direction, due to alkali metal ion intercalation. *J. Mater. Chem.* **2011**, *21*, 18738–18743. [CrossRef]
62. Yamamoto, Y.; Matsumoto, Y.; Koinuma, H. Homo-epitaxial growth of rutile TiO_2 film on step and terrace structured substrate. *Appl. Surf. Sci.* **2004**, *238*, 189–192. [CrossRef]
63. Yang, X.F.; Jin, C.J.; Liang, C.L.; Chen, D.H.; Wu, M.M.; Yu, J.C. Nanoflower arrays of rutile TiO_2. *Chem. Commun.* **2011**, *47*, 1184–1186. [CrossRef]
64. Di Valentin, C.; Tilocca, A.; Selloni, A.; Beck, T.J.; Klust, A.; Batzill, M.; Losovyj, Y.; Diebold, U. Adsorption of water on reconstructed rutile TiO_2(011)-(2x1): Ti=O double bonds and surface reactivity. *J. Am. Chem. Soc.* **2005**, *127*, 9895–9903. [CrossRef]
65. Dulub, O.; Di Valentin, C.; Selloni, A.; Diebold, U. Structure, defects, and impurities at the rutile TiO_2(011)-(2 x 1) surface: A scanning tunneling microscopy study. *Surf. Sci.* **2006**, *600*, 4407–4417. [CrossRef]
66. Kubo, T.; Orita, H.; Nozoye, H. Surface structures of rutile TiO_2 (011). *J. Am. Chem. Soc.* **2007**, *129*, 10474–10478. [CrossRef]
67. Kresse, G.; Hafner, J. Ab initio molecular-dynamics for liquid-metals. *Phys. Rev. B* **1993**, *47*, 558–561. [CrossRef]
68. Kresse, G.; Hafner, J. Ab initio molecular-dynamics simulation of the liquid-metal amorphous-semiconductor transition in germantion in germanium. *Phys. Rev. B* **1994**, *49*, 14251–14269. [CrossRef]
69. Blochl, P.E. Projector augmented-wave method. *Phys. Rev. B* **1994**, *50*, 17953–17979. [CrossRef]
70. Kresse, G.; Joubert, D. From ultrasoft pseudopotentials to the projector augmented-wave method. *Phys. Rev. B* **1999**, *59*, 1758–1775. [CrossRef]
71. Perdew, J.P.; Burke, K.; Ernzerhof, M. Generalized gradient approximation made simple. *Phys. Rev. Lett.* **1996**, *77*, 3865–3868. [CrossRef]
72. Perdew, J.P.; Chevary, J.A.; Vosko, S.H.; Jackson, K.A.; Pederson, M.R.; Singh, D.J.; Fiolhais, C. Atoms, moleculars, solids, and surfaces: Application of the generalized gradient approximation for exchange and correlation. *Phys. Rev. B* **1993**, *48*, 4978. [CrossRef]
73. Dudarev, S.L.; Botton, G.A.; Savrasov, S.Y.; Humphreys, C.J.; Sutton, A.P. Electron-energy-loss spectra and the structural stability of nickel oxide: An LSDA+U study. *Phys. Rev. B* **1998**, *57*, 1505–1509. [CrossRef]
74. Finazzi, E.; Di Valentin, C.; Pacchioni, G.; Selloni, A. Excess electron states in reduced bulk anatase TiO_2: Comparison of standard GGA, GGA plus U, and hybrid DFT calculations. *J. Chem. Phys.* **2008**, *129*. [CrossRef]
75. Henkelman, G.; Jonsson, H. Improved tangent estimate in the nudged elastic band method for finding minimum energy paths and saddle points. *J. Chem. Phys.* **2000**, *113*, 9978–9985. [CrossRef]
76. Henkelman, G.; Uberuaga, B.P.; Jonsson, H. A climbing image nudged elastic band method for finding saddle points and minimum energy paths. *J. Chem. Phys.* **2000**, *113*, 9901–9904. [CrossRef]
77. Kyriakou, G.; Davidson, E.R.M.; Peng, G.W.; Roling, L.T.; Singh, S.; Boucher, M.B.; Marcinkowski, M.D.; Mavrikakis, M.; Michaelides, A.; Sykes, E.C.H. Significant quantum effects in hydrogen activation. *ACS Nano* **2014**, *8*, 4827–4835. [CrossRef]
78. Baroni, S.; de Gironcoli, S.; Dal Corso, A.; Giannozzi, P. Phonons and related crystal properties from density-functional perturbation theory. *Rev. Mod. Phys.* **2001**, *73*, 515–562. [CrossRef]
79. Giannozzi, P.; Baroni, S. Vibrational and dielectric-properties of C_{60} from density-functional perturbation theory. *J. Chem. Phys.* **1994**, *100*, 8537–8539. [CrossRef]

80. Grimme, S.; Antony, J.; Ehrlich, S.; Krieg, S. A consistent and accurate ab initio parametrization of density functional dispersion correction (DFT-D) for the 94 elements H-PuJ. *Chem. Phys.* **2010**, *132*, 154104. [CrossRef]
81. Matz, O.; Calatayud, M. Breaking H_2 with CeO_2: Effect of Surface Termination. *ACS Omega* **2018**, *11*, 16063–16073. [CrossRef]
82. Sanville, E.; Kenny, S.D.; Smith, R.; Henkelman, G. Improved grid-based algorithm for Bader charge allocation. *J. Comput. Chem.* **2007**, *28*, 899–908. [CrossRef]
83. Coperet, C.; Estes, D.P.; Larmier, K.; Searles, K. Isolated surface hydrides: Formation, structure, and reactivity. *Chem. Rev.* **2016**, *116*, 8463–8505. [CrossRef]
84. Knotek, M.L. Characterization of hydrogen species on TiO_2 by electron-stimulated desorption. *Surf. Sci.* **1980**, *91*, L17–L22. [CrossRef]
85. Pan, J.M.; Maschhoff, B.L.; Diebold, U.; Madey, T.E. Interaction of water, oxigen, and hydrogen with TiO_2 surfaces having different defect densities. *J. Vac. Sci. Technol. A Vac. Surf. Films* **1992**, *10*, 2470–2476. [CrossRef]
86. Yan, Y.; Shi, W.D.; Yuan, Z.; He, S.G.; Li, D.M.; Meng, Q.B.; Ji, H.W.; Chen, C.C.; Ma, W.H.; Zhao, J.C. The formation of Ti-H Species at interface is lethal to the efficiency of TiO_2-based dye-sensitized devices. *J. Am. Chem. Soc.* **2017**, *139*, 2083–2089. [CrossRef]
87. Tsyganenko, A.; Filimonov, V. Infrared spectra of surface hydroxyl groups and crystalline structure of oxides. *Spectrosc. Lett.* **1972**, *5*, 477–487. [CrossRef]
88. Arrouvel, C.; Digne, M.; Breysse, M.; Toulhoat, H.; Raybaud, P. Effects of morphology on surface hydroxyl concentration: A DFT comparison of anatase–TiO_2 and γ-alumina catalytic supports. *J. Catal.* **2004**, *222*, 152–166. [CrossRef]
89. Jones, P.; Hockey, J. Infra-red studies of rutile surfaces. Part 2—Hydroxylation, hydration and structure of rutile surfaces. *Trans. Faraday Soc.* **1971**, *67*, 2679–2685. [CrossRef]
90. Buchholz, M.; Wöll, C. Interaction of carboxylic acids with rutile TiO_2(110): IR-investigations of terephthalic and benzoic acid adsorbed on a single crystal substrate. *Surf. Sci.* **2016**, *643*, 117–123. [CrossRef]
91. Henderson, M.A. An HREELS and TPD study of water on TiO_2(110): The extent of molecular versus dissociative adsorption. *Surf. Sci.* **1996**, *355*, 151–166. [CrossRef]
92. Henderson, M.A.; Epling, W.S.; Peden, C.H.F.; Perkins, C.L. Insights into photoexcited electron scavenging processes on TiO_2 obtained from studies of the reaction of O_2 with OH groups adsorbed at electronic defects on TiO_2(110). *J. Phys. Chem. B.* **2003**, *107*, 534–545. [CrossRef]
93. Petrik, N.G.; Kimmel, G.A. Reaction kinetics of water molecules with oxygen vacancies on rutile TiO_2(110). *J. Phys. Chem. C* **2015**, *119*, 23059–23067. [CrossRef]
94. Hameeuw, K.; Cantele, G.; Ninno, D.; Trani, F.; Iadonisi, G. Influence of surface and subsurface defects on the behavior of the rutile TiO_2(110) surface. *Phys. Status Solidi A Appl. Mater.* **2006**, *203*, 2219–2222. [CrossRef]
95. Kim, W.J.; Han, M.H.; Lebegue, S.; Lee, E.K.; Kim, H. Electronic Structure and Band Alignments of Various Phases of Titania Using the Self-Consistent Hybrid Density Functional and DFT plus U Methods. *Front. Chem.* **2019**, *7*. [CrossRef]
96. Iacomino, A.; Cantele, G.; Ninno, D.; Marri, I.; Ossicini, S. Structural, electronic, and surface properties of anatase TiO_2 nanocrystals from first principles. *Phys. Rev. B* **2008**, *78*. [CrossRef]
97. Iacomino, A.; Cantele, G.; Trani, F.; Ninno, D. DFT Study on Anatase TiO_2 Nanowires: Structure and Electronic Properties as Functions of Size, Surface Termination, and Morphology. *J. Phys. Chem. C* **2010**, *114*, 12389–12400. [CrossRef]
98. Han, F.S.; Zhou, Z.H.; Huang, Z.X.; Li, M.T.; Guo, L.J. Effect of Water Adsorption on the Interfacial Structure and Band Edge Alignment of Anatase TiO_2(001)/Water by First-Principles Molecular Dynamics. *J. Phys. Chem. C* **2018**, *122*, 26965–26973. [CrossRef]
99. Zhang, D.Y.; Yang, M.N.; Dong, S. Improving the photocatalytic activity of TiO_2 through reduction. *RSC Adv.* **2015**, *5*, 35661–35666. [CrossRef]
100. Kunat, M.; Burghaus, U.; Woll, C. The adsorption of hydrogen on the rutile TiO_2(110) surface. *Phys. Chem. Chem. Phys.* **2004**, *6*, 4203–4207. [CrossRef]

nanomaterials

MDPI

Article

Dibenzyl Disulfide Adsorption on Cationic Exchanged Faujasites: A DFT Study

Etienne Paul Hessou [1,2], Miguel Ponce-Vargas [3], Jean-Baptiste Mensah [2], Frederik Tielens [4,*], Juan Carlos Santos [5,*] and Michael Badawi [1,*]

1 Laboratoire de Physique et Chimie Théoriques, Faculté des Sciences et Technologies, CNRS, Université de Lorraine, Boulevard des Aiguillettes, 54500 Vandoeuvre-lès-Nancy, France; tiganahess@gmail.com
2 Laboratoire de Chimie Théorique et de Spectroscopie Moléculaire, Université d'Abomey-Calavi, 03 BP 3409 Cotonou, Benin; menfolben@yahoo.fr
3 Institut de Chimie Moléculaire de Reims, Université de Reims Champagne-Ardenne, 51687 Reims, France; miguel.ponce-vargas@univ-reims.fr
4 Chemistry (ALGC), Vrije Universiteit Brussel, Pleinlaan 2, B-1050 Brussel, Belgium
5 Laboratorio de Corrosión, Departamento de Ciencias Químicas, Facultad de Ciencias Exactas, Universidad Andres Bello, Av. República 330, 8370186 Santiago, Chile
* Correspondence: frederik.tielens@vub.be (F.T.); jsantos@unab.cl (J.C.S.); michael.badawi@univ-lorraine.fr (M.B.); Tel.: +333-7274-9867 (M.B.)

Received: 13 April 2019; Accepted: 30 April 2019; Published: 8 May 2019

Abstract: Although dibenzyl disulfide (DBDS) is used as a mineral oil stabilizer, its presence in electrical transformer oil is associated as one of the major causes of copper corrosion and subsequent formation of copper sulfide. In order to prevent these undesirable processes, MY zeolites (with M = Li, Na, K, Cs, Cu or Ag) are proposed to adsorb molecularly DBDS. In this study, different MY zeolites are investigated at the DFT+D level in order to assess their ability in DBDS adsorption. It was found that CsY, AgY and CuY exhibit the best compromise between high interaction energies and limited S-S bond activation, thus emerging as optimal adsorbents for DBDS.

Keywords: ab initio; zeolite; faujasite; copper; silver; alkali metals; sulfur compounds; DBDS

1. Introduction

Mineral insulating oil, which is conventionally divided in aliphatic, naphthenic and aromatic hydrocarbons, is widely used in transformers, circuit breakers and other electrical equipment. However, there is usually still a small amount of sulfur containing compounds present, which are obtained from the refining technique or that have been added as antioxidants, which could cause the corrosion of copper coils within the transformers [1–9]. Dibenzyl disulfide (DBDS) is one of the most abundant and representative of these sulfur species. Thus, the development of new adsorbents to improve the DBDS selective removal is of paramount importance. In this regard, various types of adsorbents, such as, metal oxides, clays, activated carbon and zeolites have been used as adsorbents for organic compounds [10–13]. Among them, cation-exchanged zeolites are attractive for this application due to their thermal stability, facility to be separated from the reaction products, ability to be regenerated, high surface area, size-selective adsorption property and capacity to include a large variety of cationic sites. These materials have also been evaluated as adsorbents for sulfur compounds [11–13].

Particularly, ion exchanged faujasites (type Y zeolite) have proven to be efficient adsorbents for dimethyl disulfide (DMDS) [14], hydrogen sulfide (H_2S) [15–18], tetrahydrothiophene (THT) and t-butyl mercaptan (TBM) [19,20]. In the same vein, systems using Ag^+, Cu^{2+} and Ce^{3+} exchanged Y zeolites have been employed for adsorption of thiophenes from organic liquid medium [21]. Moreover,

adsorbent systems based on Cu-Y, Ag-Y and Ce-Y have been used for DBDS removal from insulating oil with good performance [1]. Indeed, AgY was able to remove 76% of DBDS, 80% of CeY and 97% of CuY. However, adsorption enthalpies were not measured, and these results deserve to be explained at a molecular level. Therefore, for the sake of this study the faujasite zeolite was retained to examine the DBDS adsorption.

The adsorption efficiency of the cation exchanged zeolites had been attributed to an adsorption mechanism involving π complexation of cations in zeolites with sulfides after ion exchange, but some questions have not been answered yet, such as the structural effect of the adsorbent (type of zeolite), the amount and type of metal exchanged on the zeolite. As the time required to perform cationic exchange can be very long, here we propose to undertake a theoretical screening of all monovalent cations that can be experimentally incorporated in the Y zeolite.

Density functional theory (DFT) is one of the most effective tools to elucidate adsorption processes at molecular level, and is conveniently employed to investigate such processes in various cation-exchanged zeolites [22–29]. Therefore, in the present work a systematic DFT investigation will be performed in order to evaluate the use of metal-exchanged faujasites as adsorbents of dibenzyl disulfide (DBDS). The paper is organized as follows. Section 2 contains the computational details. In Section 3, the DBDS properties are analyzed, first in gas phase and then adsorbed in NaY, and finally, the interaction is studied in different exchanged zeolites LiY, NaY, KY, CsY, Cu(I)Y and Ag(I)Y. In Section 4, the main conclusions are summarized.

2. Methodology

In this study, density functional theory was used applying the augmented plane wave method (PAW) [30] to describe the electron-ion interactions with a cut-off energy of 450 eV. The functional of Perdew Burke Ernzerhof (PBE) [31] was employed, and the Kohn–Sham equations were solved self-consistently until the energy difference of the cycles is less than 10^{-6} eV. The atomic positions were fully optimized until all forces were smaller than 0.01 eV/Å per atom. Due to the large size of the unit cell, all computations were performed only at the Γ-point. The computations were performed using the Vienna Ab initio Simulation Package (VASP) [32].

To accurately describe the adsorption process of DBDS molecule in the zeolite, van der Waals (vdW) interactions, which are not included in the PBE functional were taken into account [23,28,33,34] using two correction schemes, D2 and TS/HI, with each method representing a different degree of complexity in the correction formulation. In the D2 correction of Grimme [35–37] the vdW interactions are described as an atom-pairwise correction and the C_6 coefficients are defined for each atomic species irrespective of the system. On the other hand, in the Tkatchenko–Scheffler scheme with iterative Hirshfeld partitioning (TS/HI) [38–40], the C_6 coefficients are dependent on the electron density and the ionic character of the system. Both methods were recently implemented in VASP code [37,39,40]. Once the total energy of the different systems has been computed with either of the two dispersion correction schemes, the interaction energies of DBDS over cation-exchanged FAU at 0 K are obtained using Equation (1) below.

$$\Delta E_{int} = E_{FAU-X} - E_{FAU} - E_X , \quad (1)$$

where

- E_{FAU-X}: the energy of the system containing faujasite with DBDS;
- E_{FAU}: the energy of the faujasite alone;
- E_X: the energy of the isolated DBDS in gaseous phase.

In a similar fashion, the contribution of dispersion forces ΔE_{disp} to the interaction energy was computed as:

$$\Delta E_{disp} = E_{disp\ FAU-X} - E_{disp\ FAU} - E_{disp\ X} . \quad (2)$$

Finally, a Noncovalent Interactions Analysis (NCI), as proposed by Yang and coworkers, was conducted by using the NCI code [41,42] to describe more precisely the different types of noncovalent interactions such as π-cation. The suitability of this methodology to explain host-guest interactions in metal-containing systems has been reported previously [42,43].

The faujasite is a three dimensional network belonging to the family of large pore zeolites. Its framework is composed of sodalite cages also named β cages with diameter of 6.6 Å connected to supercages also named α cages and having a diameter of 12.4 Å. These two units are interconnected by hexagonal prisms whose opening is of 2.3 Å (D6R). These supercages are linked together by a 12MR ring with diameter of 7.4 Å, forming the porous accessible network.

The siliceous structure of faujasite crystallizes within the *Fd*3*m* symmetry space group [44]. The lattice parameters of the standard cubic cell (576 atoms, $Si_{192}O_{384}$) are: a = b = c = 25.028 Å [45,46]. In the present study, in order to reduce the computational cost, we consider the primitive rhombohedral cell containing 144 atoms (Figure 1). The primitive cell of faujasite contains two supercages and eight hexagonal windows connecting the sodalite with the supercage. In this work, we exchange 14 Si by Al atom inside this primitive cell (see Figure 1), resulting in a Si/Al ratio of 2.43 which corresponds to Y zeolite [47]. Therefore, the molecular formulas of the investigated cells are $M_{14}Al_{14}Si_{34}O_{96}$, with M = Li^+, Na^+, K^+, Cs^+, Cu^+ or Ag^+. As the cation volumes influence the cell parameters, we carried out a full relaxation of the cells for each system investigated at the PBE+D2 level of theory.

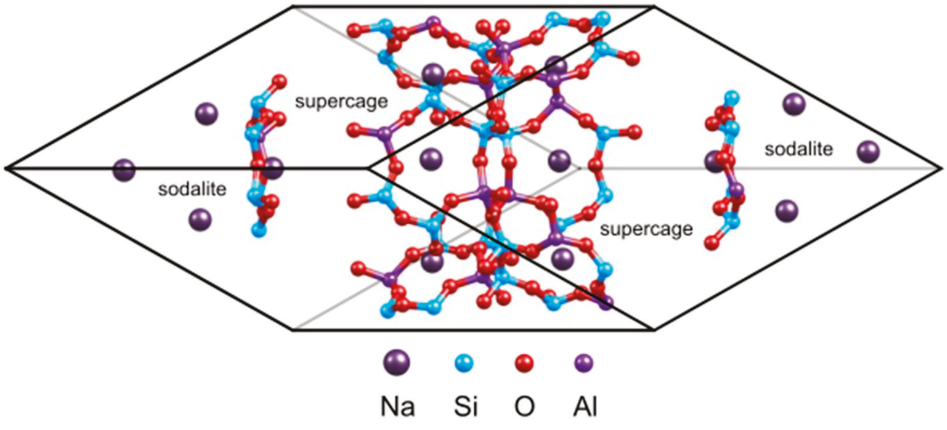

Figure 1. Unit cell of the sodium exchange faujasite.

3. Results

3.1. DBDS in Gas Phase

The conformation analysis of DBDS in the gas phase reveals that the conformer I is the most stable one followed by conformer II, III, IV and V (see Figure 2). These results are in agreement with those obtained by Saavedra et al. [7] who also found a series of closely related conformers with a C-S-S-C dihedral angle of about 90°. The main difference between the most stable and the least stable conformer is the relative orientation of the aromatic rings described by this C-S-S-C dihedral angle. In conformer I the aromatic rings are almost perpendicular to each other whereas in conformer V they are almost parallel. Conformer V was found to be the least stable (see Table 1) and it will not be further considered in this work. Another plausible difference between the conformers is the disulfide bond length, which varies within 0.7 Å (see Table 1). The energy difference between the different conformers I to IV was calculated to be within a range of around 13 kJ mol^{-1} at both PBE+D2 (Table S1) and PBE+TS/HI (Table 1) levels of theory. Both approaches predict conformer I (C-S-S-C dihedral angle of about 90°) to be the most stable of the five DBDS conformers. Conformer II, less stable than

conformer I by 10.3 kJ mol^{-1} was found in solid phase by Lee et al. [48] while conformer IV, less stable than conformer I by 13.4 kJ mol^{-1} was obtained by Meichning et al. [49]. At this point we can conclude that there is no significant difference in structural parameters obtained at both levels of theory, i.e., PBE+D2 (Table S1 after the references) and PBE+TS/HI (see Table 1).

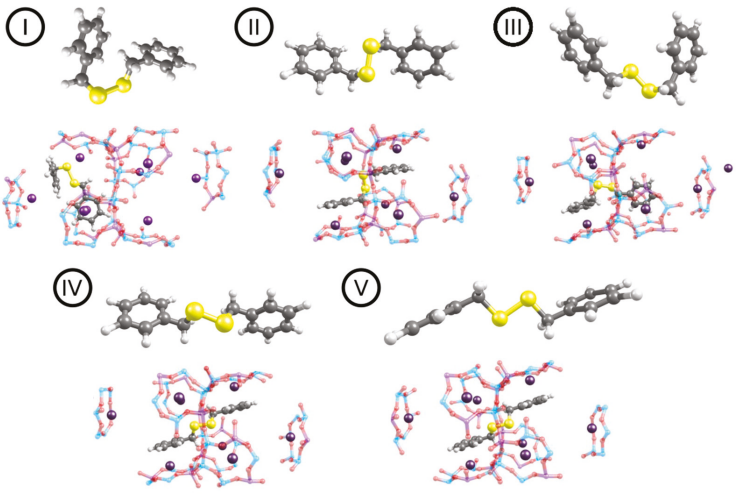

Figure 2. For each DBDS conformer **I–V**: Optimized DBDS structure before (up)/after (down) the incorporation in the Y zeolite (here shown for the case of NaY). In I and II, the DBDS phenyl rings keep the gas configuration inside the cell, whereas in II, IV and V they adopt a parallel configuration. Given its higher energy, structure V is not further considered in this work.

Table 1. Selected structural parameters and energies of the dibenzyl disulfide (DBDS) structures optimized with PBE+TS/HI. Energies in kJ mol^{-1}, distances in Å, and dihedral angles in degrees.

Dibenzyl Disulfide Conformers	Structural Parameters in Gas Phase		ΔE_{rel} (kJ mol^{-1})
	d(S-S) (Å)	ang(C-S-S-C) (°)	
I	2.030	90.9	0.0
II	2.025	85.5	10.3
III	2.028	84.7	11.1
IV	2.031	86.5	13.4
V	2.104	179.9	46.7

3.2. DBDS Adsorbed in NaY (Si/Al = 2.43)

Subsequently, the four most stable DBDS gas phase conformations (I to IV) were considered for the study of DBDS adsorption in the NaY zeolite. In almost all cases, the conformation geometries were altered after adsorption, as a consequence of the rise of π-cation interactions between the sodium cations and the aromatic rings, except for I where the initial conformation already allowed an effective DBDS-zeolite coupling (Figure 2).

In order to investigate the adsorption of DBDS within the Y zeolite, a NCI analysis was carried out. This enables to clarify the role of cation-π interactions between the DBDS molecule and the exchangeable cations in the faujasite structure. This analysis is based on a 2D plot of the reduced density gradient s, and the electron density ρ, where s can be expressed as:

$$s = \frac{1}{2(3\pi^2)^{1/3}} \frac{|\nabla\rho|}{\rho^{4/3}}. \quad (3)$$

A noticeable variation in *s* generates density critical points leading to an isosurface which reveals the presence of non-covalent interactions. The second eigenvalue of the electronic density Hessian (λ_2) enables us to determine the nature of such interactions; hence, intense stabilizing forces are characterized by $\lambda_2 < 0$, steric repulsion by $\lambda_2 > 0$, and weak interactions by $\lambda_2 \approx 0$. These λ_2 values are represented by using a color scale.

The NCI results for the conformer I of DBDS embedded in NaY and CuY systems are presented in Figure 3. In the DBDS-NaY structure an isosurface is clearly observed between one DBDS aromatic ring and a Na^+ ion, revealing an efficient cation-π interaction in this case. Conversely, the absence of this isosurface in the analog DBDS-CuY, along with a shorter distance between the second aromatic ring and a Cu^+ (2.350 Å) in comparison to DBDS-NaY (3.815 Å) suggest that a covalent character interaction is the main factor governing the DBDS inclusion in CuY, prior to the rise of noncovalent forces. Remarkably, neither of the two systems exhibits an isosurface between the cation and sulphur, suggesting a negligible interaction between the disulfide bridge and the Na^+/Cu^+ ions. Hence, the DBDS-CuY adsorption complex formation is an advantageous situation in order to avoid the copper sulfide generation.

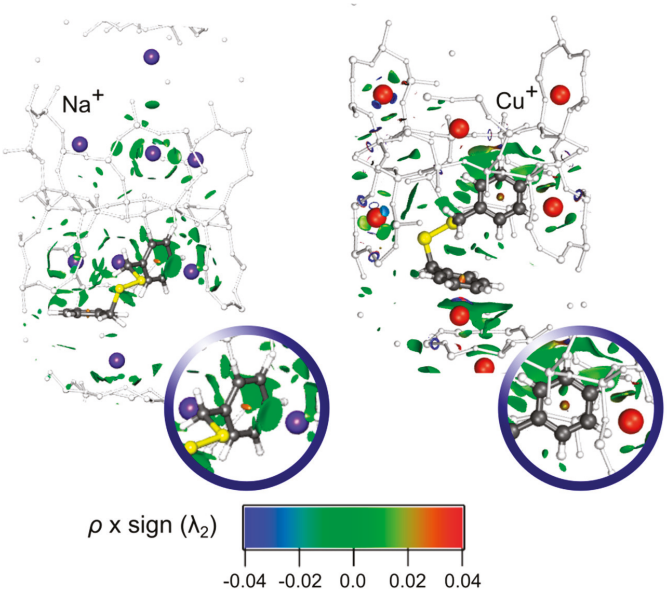

Figure 3. Noncovalent Interactions Analysis (NCI) analysis for the conformer I of the NaY and CuY faujasites containing DBDS. An isosurface of 0.01 a.u. was considered.

3.3. Cationic Screening Results for DBDS Adsorption in Cu(I)-Exchanged Y Zeolites

The interaction energies of the DBDS conformers (I to IV) with LiY, NaY, KY, CsY, Cu(I)Y and Ag(I)Y were computed at the PBE+D2 (Table S3) and PBE+TS/HI (Table 2) levels of theory.

Both methods give similar trends. However, it can be noticed that the use of D2 leads to higher interaction energies (in absolute value) for zeolites containing large cations such as CsY—around 100 kJ mol^{-1} higher in absolute value—in comparison to those obtained using the TS/HI dispersion method. Remarkably, for other small molecules in the same zeolite structure [28], D2 was found to overestimate the adsorption enthalpies compared to TS/HI.

It is clear from the interaction energies that the most stable gas phase conformation does not adsorb stronger to MY (see Table 2). This is in line with the fact that most stable structures are the least reactive. Conformer II was found the best starting conformation for adsorption for Na^+, K^+, Cs^+, Ag^+ cations and conformer IV for Li^+ and Cu^+ cations. The adsorption conformation does not differ

significantly from the gas phase conformations II or IV. Conformer II is always the most favorably adsorbed, except in LiY and Cu(I)Y where IV exhibits the highest interaction energy. The interaction energies range between −170 and −275 kJ mol^{-1} for LiY and CuY, respectively.

Table 2. Computed (PBE+TS/HI) total interaction energies ΔE_{int} and the corresponding contributions of dispersion energies of the four conformers of DBDS with LiY, NaY, KY, CsY, CuY and AgY. Energies in kJ mol^{-1}.

	CONFORMERS							
	I		II		III		IV	
	ΔE_{int}	ΔE_{disp}	ΔE_{int}	ΔE_{disp}	ΔE_{int}	ΔE_{disp}	ΔE_{int}	ΔE_{disp}
LiY	−144.5	−84.8	−158.2	−91.5	−159.2	−95.4	−170.0	−126.7
NaY	−180.4	−130.5	−194.7	−128.6	−160.9	−129.2	−187.1	−130.1
KY	−188.6	−133.4	−207.8	−137.6	−184.8	−135.3	−189.6	−134.4
CsY	−210.9	−170.5	−236.9	−180.7	−210.6	−160.2	−230.1	−167.6
CuY	−217.2	−110.8	−262.0	−123.8	−238.9	−123.6	−275.1	−127.2
AgY	−234.0	−131.5	−251.3	−131.2	−222.7	−123.5	−236.3	−163.3

The interaction energy between DBDS and MY for M = alkali metal increases with the cation softness and decreases with their electronegativity, in agreement with the chemical concepts developed by Pearson et al. [50,51]. The interaction energy also increases in line with the cation radius. Remarkably, the trends for the group X ions (Cu and Ag) are opposite to those observed for the alkali cations, as in this case the interactions are not only electrostatic.

3.4. Evaluation of the Regenerability of the Materials

Formation of byproducts is undesirable and can lead to the deactivation of the sorbent [52,53]. Therefore, a molecular adsorption of DBDS is targeted, and its dissociation into two benzylsulfides must be prevented. To this end, the stretching of the S-S bond of DBDS upon adsorption in the MY zeolites was evaluated. The results obtained are reported in Figure 4 and Table S5.

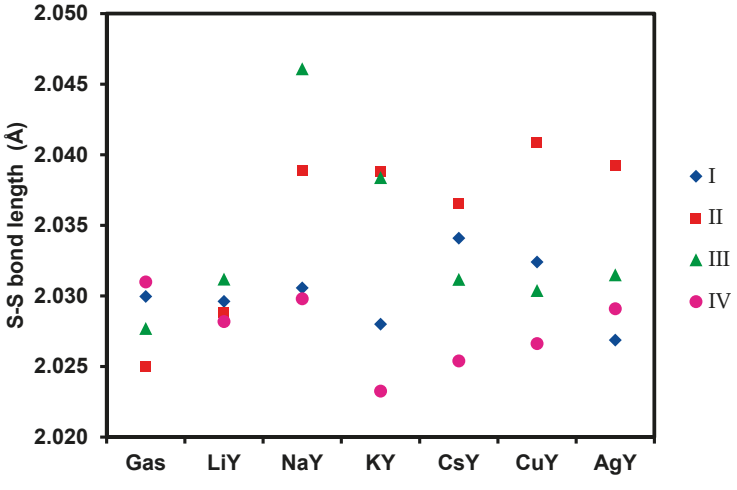

Figure 4. S-S bond length of DBDS conformers in gas phase and upon adsorption.

Regarding the conformer I, the analysis of the S-S bond lengths before and after adsorption reveals an almost negligible evolution of the S-S bond upon adsorption (less than 0.02 Å). Hence, conformer I

is not expected to dissociate upon adsorption over cationic-exchanged faujasites, except for CsY. In the case of the conformer II, an elongation of the S-S bond is observed for all cations. With regard to the variation of the S-S bond after adsorption of the conformer III, one can notice a lengthening of the S-S bond with all the cations, which is more pronounced in NaY.

Regarding the conformer IV, the least stable of the four conformers studied, one can observe a shortening of the S-S bond for all cations, making them good candidates for DBDS removal. We highlight the fact that Li^+ and Cu^+ exchanged zeolites give the highest interaction energies with values of −170.0 and −275.1 kJ mol^{-1}, respectively.

As the proportion of each conformer cannot be controlled experimentally, especially under the conditions of electric transformers, we have to select a Y zeolite formulation where the S-S bond activation would be the most limited as possible. According to this criterion, NaY has to be rejected because it could decompose the conformers II and III quite easily, while LiY appears as an ideal candidate. Hence, CsY, AgY and CuY can be selected as a compromise between high interaction energies and limited S-S bond activation. These recommendations are partially supported or in agreement with the experimental results obtained by Wan et al. [1], who found that CuY was an efficient material to remove DBDS (97% of removal after 2 h), followed by AgY (76%). Unfortunately, we do not have other elements of comparison as adsorption enthalpies were not measured in this study [1].

4. Conclusions

The adsorption of DBDS on MY zeolites (with M = Li, Na, K, Cs, Cu or Ag) was investigated using periodic DFT including dispersion corrections in order to propose an efficient DBDS adsorbent for its removal from mineral insulating oils. From the different MY structures herein studied, it was clear that DBDS adsorbs via its phenyl moieties instead of forming a sulfur bond. Among the five conformers, conformer I is recognized as the most stable one followed by conformers II, III and IV that are less stable however equivalent, while conformer V is the least stable and was not considered in this study. The interaction energies of the four considered conformers range from −170 to −275 kJ mol^{-1} in the cationic-exchanged Y zeolites investigated in the present work.

In the case of DBDS-CuY, the comparative NCI analysis with the analog DBDS-NaY, and the shorter distance between the DBDS phenyl group and a Cu(I) belonging the supercage, suggest a covalent character interaction, explaining the high calculated adsorption energies found for this system. Remarkably, neither DBDS-NaY nor DBDS-CuY exhibit NCI isosurfaces between the cation and sulphur, suggesting a negligible interaction between them.

In general, one can conclude that the adsorption complex (DBDS/MY) displays an advantageous geometry in order to avoid copper sulfide formation. Moreover, CsY, AgY and CuY can be selected as a compromise between high interaction energies and limited S-S bond activation, and are predicted to be optimal adsorbents for molecular DBDS, avoiding the formations of dissociated species. In the future we plan to extend our study on other zeolites and MOFs, still on the DBDS molecule, but also its sub-species and other sulfated species that may be present in the oil, such as C_6H_5-CH_2-SH and SH_2 in the frame of ab initio molecular dynamics.

Supplementary Materials: The following are available online at http://www.mdpi.com/2079-4991/9/5/715/s1, Figure S1. Dibenzyil disulfide (DBDS) structures optimized with Gaussian (starting from the DBDS structures optimized with Vienna Ab initio Simulation Package (VASP)). Figure S2. Evolution of the interaction energy as a function of the variation of the S-S distance after adsorption. Table S1. Selected structural parameters of the optimized dibenzyil disulfide structures. Energies in kJ mol^{-1}, distances in Å and angles in degrees. Table S2. Selected structural parameters and energies of the DBDS structures optimized with Gaussian (starting from the DBDS structures optimized with PBE+D2). Energies in kJ mol^{-1}, distances in Å and angles in degrees. Table S3. Computed (PBE+D2) total interaction energies ΔEint of the four conformers of DBDS with LiY, NaY, KY, CsY, CuY and AgY. The contributions of dispersion energies to the interaction energies ΔEdis are reported in this table in parentheses. Energies in kJ mol^{-1}. Table S4. Selected structural parameters of dibenzyil disulfide inside the Na-faujasite cell. Energies in kJ mol^{-1}, and distances in Å. Table S5. S-S bond (Å) before and after adsorption upon LiY, NaY, KY, CsY, CuY and AgY.

Author Contributions: Conceptualization, F.T. and J.C.S.; Methodology, M.B. and M.P.-V.; Formal Analysis, F.T., J.C.S., M.B., M.P.-V., J.-B.M. and E.P.H.; Investigation, E.P.H. and M.P.-V.; Writing-Original Draft Preparation, M.B., E.P.H. M.P.-V. and F.T.; Writing—Review & Editing, F.T., J.C.S., M.B., M.P.-V., J.-B.M. and E.P.H.; Visualization, E.P.H. and M.P.-V.; Supervision, F.T., M.B., J.-B.M.; Project Administration, F.T., J.C.S., and M.B.; Funding Acquisition, F.T.

Funding: This research received no external funding.

Acknowledgments: E.P.H thanks VUB for funding a short stay in the framework of his Thesis. Computational resources and services were provided by the Shared ICT Services Centre funded by the Vrije Universiteit Brussel, the Flemish Supercomputer Center (VSC) and FWO.

Conflicts of Interest: The authors declare no conflict of interest.

References

1. Wan, T.; Feng, B.; Zhou, Z.; Qian, H.; Gong, S.K. Removal of corrosive sulfur from insulating oil with adsorption method. *IEEE Trans. Dielectr. Electr. Insul.* **2015**, *22*, 3321–3326. [CrossRef]
2. Amimoto, T.; Hosokawa, N.; Nagao, E.; Tanimura, J.; Toyama, S. Concentration dependence of corrosive sulfur on copper-sulfide deposition on insulating paper used for power transformer insulation. *IEEE Trans. Dielectr. Electr. Insul.* **2009**, *16*, 1489–1495.
3. Amimoto, T.; Nagao, E.; Tanimura, J.; Toyama, S.; Fujita, Y.; Kawarai, H.; Yamada, N. Identification of affecting factors of copper sulfide deposition on insulating paper in oil. *IEEE Trans. Dielectr. Electr. Insul.* **2009**, *16*, 265–272. [CrossRef]
4. Lewand, L.R. *The Negative Effects of Corrosive Sulfur on Transformer Components*; Doble Engineering Company/NETA World: Watertown, MA, USA, 2004; pp. 1–4.
5. Lukic, J.M.; Milosavljevic, S.B.; Orlovic, A.M. Degradation of the insulating system of power transformers by copper sulfide deposition: Influence of oil oxidation and presence of metal passivator. *Ind. Eng. Chem. Res.* **2010**, *49*, 9600–9608. [CrossRef]
6. Griffin, P.J.; Lewand, L.R. Understanding corrosive sulfur problems in electric apparatus. In Proceedings of the Seventy-Forth Annual Conference of Doble Clients, Boston, MA, USA, 29–30 March 2007. Insulating Materials Session 1.
7. Saavedra-Torres, M.; Jaque, P.; Tielens, F.; Santos, J.C. Theoretical study of dibenzyl disulfide adsorption on Cu 7 cluster as a first approximation to sulfur-induced copper corrosion process. *Theor. Chem. Acc.* **2015**, *134*, 73. [CrossRef]
8. Scatiggio, F.; Tumiatti, V.; Maina, R.; Tumiatti, M.; Pompili, M.; Bartnikas, R. Corrosive Sulfur in Insulating Oils: Its Detection and Correlated Power Apparatus Failures. *IEEE Trans. Power Deliv.* **2008**, *23*, 508–509. [CrossRef]
9. Tumiatti, V.; Maina, R.; Scatiggio, F.; Pompili, M.; Bartnikas, R. In service reduction of corrosive sulfur compounds in insulating mineral oils. In Proceedings of the Conference Record of the 2008 IEEE International Symposium on Electrical Insulation (ISEI 2008), Vancouver, BC, Canada, 9–12 June 2008; pp. 284–286.
10. Huang, C.; Sun, R.; Lu, H.; Yang, Q.; Hu, J.; Wang, H.; Liu, H. A pilot trial for fast deep desulfurization on MOF-199 by simultaneous adsorption-separation via hydrocyclones. *Sep. Purif. Technol.* **2017**, *182*, 110–117. [CrossRef]
11. Dehghan, R.; Anbia, M. Zeolites for adsorptive desulfurization from fuels: A review. *Fuel Process. Technol.* **2017**, *167*, 99–116. [CrossRef]
12. García, H.; Roth, H.D. Generation and reactions of organic radical cations in zeolites. *Chem. Rev.* **2002**, *102*, 3947–4008. [CrossRef]
13. Miao, G.; Ye, F.; Wu, L.; Ren, X.; Xiao, J.; Li, Z.; Wang, H. Selective adsorption of thiophenic compounds from fuel over TiO2/SiO2 under UV-irradiation. *J. Hazard. Mater.* **2015**, *300*, 426–432. [CrossRef] [PubMed]
14. Lv, L.; Zhang, J.; Huang, C.; Lei, Z.; Chen, B. Adsorptive separation of dimethyl disulfide from liquefied petroleum gas by different zeolites and selectivity study via FT-IR. *Sep. Purif. Technol.* **2014**, *125*, 247–255. [CrossRef]
15. Sung, C.-Y.; Al Hashimi, S.; McCormick, A.; Tsapatsis, M.; Cococcioni, M. Density Functional Theory Study on the Adsorption of H2S and Other Claus Process Tail Gas Components on Copper- and Silver-Exchanged Y Zeolites. *J. Phys. Chem. C* **2012**, *116*, 3561–3575. [CrossRef]

16. Sung, C.-Y.; Al Hashimi, S.; McCormick, A.; Cococcioni, M.; Tsapatsis, M. A DFT study on multivalent cation-exchanged Y zeolites as potential selective adsorbent for H2S. *Microporous Mesoporous Mater.* **2013**, *172*, 7–12. [CrossRef]
17. Chen, X.; Shen, B.; Sun, H. Ion-exchange modified zeolites X for selective adsorption desulfurization from Claus tail gas: Experimental and computational investigations. *Microporous Mesoporous Mater.* **2018**, *261*, 227–236. [CrossRef]
18. Kumar, P.; Sung, C.-Y.; Muraza, O.; Cococcioni, M.; Al Hashimi, S.; McCormick, A.; Tsapatsis, M. H2S adsorption by Ag and Cu ion exchanged faujasites. *Microporous Mesoporous Mater.* **2011**, *146*, 127–133. [CrossRef]
19. Duan, L.; Gao, X.; Meng, X.; Zhang, H.; Wang, Q.; Qin, Y.; Zhang, X.; Song, L. Adsorption, co-adsorption, and reactions of sulfur compounds, aromatics, olefins over Ce-exchanged Y zeolite. *J. Phys. Chem. C* **2012**, *116*, 25748–25756. [CrossRef]
20. Lee, D.; Kim, J.; Lee, H.C.; Lee, K.H.; Park, E.D.; Woo, H.C. Adsorption properties of organosulfur compounds on zeolite clusters: A density functional theory calculation study. *J. Phys. Chem. C* **2008**, *112*, 18955–18962. [CrossRef]
21. Xue, M.; Chitrakar, R.; Sakane, K.; Hirotsu, T.; Ooi, K.; Yoshimura, Y.; Feng, Q.; Sumida, N. Selective adsorption of thiophene and 1-benzothiophene on metal-ion-exchanged zeolites in organic medium. *J. Colloid Interface Sci.* **2005**, *285*, 487–492. [CrossRef]
22. Bucko, T.; Hafner, J. The role of spatial constraints and entropy in the adsorption and transformation of hydrocarbons catalyzed by zeolites. *J. Catal.* **2015**, *329*, 32–48. [CrossRef]
23. Chibani, S.; Chebbi, M.; Lebègue, S.; Bučko, T.; Badawi, M. A DFT investigation of the adsorption of iodine compounds and water in H-, Na-, Ag-, and Cu- mordenite. *J. Chem. Phys.* **2016**, *144*, 244705. [CrossRef]
24. Chibani, S.; Medlej, I.; Lebègue, S.; Ángyán, J.G.; Cantrel, L.; Badawi, M. Performance of CuII-, PbII-, and HgII-Exchanged Mordenite in the Adsorption of I_2, ICH_3, H_2O, CO, $ClCH_3$, and Cl_2: A Density Functional Study. *ChemPhysChem* **2017**, *18*, 1642–1652. [CrossRef]
25. Chebbi, M.; Chibani, S.; Paul, J.-F.; Cantrel, L.; Badawi, M. Evaluation of volatile iodine trapping in presence of contaminants: A periodic DFT study on cation exchanged-faujasite. *Microporous Mesoporous Mater.* **2017**, *239*, 111–122. [CrossRef]
26. Bučko, T.; Chibani, S.; Paul, J.-F.; Cantrel, L.; Badawi, M. Dissociative iodomethane adsorption on Ag-MOR and the formation of AgI clusters: An ab initio molecular dynamics study. *Phys. Chem. Chem. Phys.* **2017**, *19*, 27530–27543. [CrossRef]
27. Chibani, S.; Badawi, M.; Loiseau, T.; Volkringer, C.; Cantrel, L.; Paul, J.-F. A DFT study of RuO4 interactions with porous materials: Metal–organic frameworks (MOFs) and zeolites. *Phys. Chem. Chem. Phys.* **2018**, *20*, 16770–16776. [CrossRef]
28. Hessou, E.P.; Kanhounnon, W.G.; Rocca, D.; Monnier, H.; Vallières, C.; Lebègue, S.; Badawi, M. Adsorption of NO, NO_2, CO, H_2O and CO_2 over isolated monovalent cations in faujasite zeolite: A periodic DFT investigation. *Theor. Chem. Acc.* **2018**, *137*, 161. [CrossRef]
29. Khalil, I.; Jabraoui, H.; Maurin, G.; Lebègue, S.; Badawi, M.; Thomas, K.; Maugé, F. Selective Capture of Phenol from Biofuel Using Protonated Faujasite Zeolites with Different Si/Al Ratios. *J. Phys. Chem. C* **2018**, *122*, 26419–26429. [CrossRef]
30. Kresse, G.; Joubert, D. From ultrasoft pseudopotentials to the projector augmented-wave method. *Phys. Rev. B* **1999**, *59*, 1758–1775. [CrossRef]
31. Perdew, J.P.; Burke, K.; Ernzerhof, M. Generalized gradient approximation made simple. *Phys. Rev. Lett.* **1996**, *77*, 3865. [CrossRef]
32. Kresse, G.; Hafner, J. Ab initio molecular dynamics for liquid metals. *Phys. Rev. B* **1993**, *47*, 558–561. [CrossRef]
33. Göltl, F.; Grüneis, A.; Bučko, T.; Hafner, J. Van der Waals interactions between hydrocarbon molecules and zeolites: Periodic calculations at different levels of theory, from density functional theory to the random phase approximation and Møller-Plesset perturbation theory. *J. Chem. Phys.* **2012**, *137*, 114111. [CrossRef]
34. Ramalho, J.P.P.; Gomes, J.R.; Illas, F. Accounting for van der Waals interactions between adsorbates and surfaces in density functional theory based calculations: Selected examples. *RSC Adv.* **2013**, *3*, 13085–13100. [CrossRef]

35. Grimme, S. Accurate description of van der Waals complexes by density functional theory including empirical corrections. *J. Comput. Chem.* **2004**, *25*, 1463–1473. [CrossRef]
36. Grimme, S. Semiempirical GGA-type density functional constructed with a long-range dispersion correction. *J. Comput. Chem.* **2006**, *27*, 1787–1799. [CrossRef]
37. Bučko, T.; Hafner, J.; Lebègue, S.; Ángyán, J.G. Improved Description of the Structure of Molecular and Layered Crystals: Ab Initio DFT Calculations with van der Waals Corrections. *J. Phys. Chem. A* **2010**, *114*, 11814–11824. [CrossRef]
38. Tkatchenko, A.; Scheffler, M. Accurate molecular van der Waals interactions from ground-state electron density and free-atom reference data. *Phys. Rev. Lett.* **2009**, *102*, 073005. [CrossRef]
39. Bučko, T.; Lebègue, S.; Hafner, J.; Ángyán, J.G. Improved Density Dependent Correction for the Description of London Dispersion Forces. *J. Chem. Theory Comput.* **2013**, *9*, 4293–4299. [CrossRef]
40. Bučko, T.; Lebègue, S.; Ángyán, J.G.; Hafner, J. Extending the applicability of the Tkatchenko-Scheffler dispersion correction via iterative Hirshfeld partitioning. *J. Chem. Phys.* **2014**, *141*, 034114. [CrossRef]
41. Contreras-García, J.; Johnson, E.R.; Keinan, S.; Chaudret, R.; Piquemal, J.-P.; Beratan, D.N.; Yang, W. NCIPLOT: A Program for Plotting Noncovalent Interaction Regions. *J. Chem. Theory Comput.* **2011**, *7*, 625–632. [CrossRef]
42. Ponce-Vargas, M. Metallacycles Capabilities in Host–Guest Chemistry. *ChemistryOpen* **2015**, *4*, 656–660. [CrossRef]
43. Ponce-Vargas, M.; Muñoz-Castro, A. Tiara-like Complexes acting as Iodine Encapsulating Agents: The Role of M···I Interactions in $[M(\mu\text{-}SCH_2CO_2Me)_2]_8 \subset I_2$ (M = Ni, Pd, Pt) Inclusion Compounds. *J. Phys. Chem. C* **2016**, *120*, 23441–23448. [CrossRef]
44. Baur, W.H. On the cation and water positions in faujasite. *Am. Mineral. J. Earth Planet. Mater.* **1964**, *49*, 697–704.
45. Dempsey, E.; Kuehl, G.H.; Olson, D.H. Variation of the lattice parameter with aluminum content in synthetic sodium faujasites. Evidence for ordering of the framework ions. *J. Phys. Chem.* **1969**, *73*, 387–390. [CrossRef]
46. Porcher, F.; Souhassou, M.; Dusausoy, Y.; Lecomte, C. The crystal structure of a low-silica dehydrated NaX zeolite. *Eur. J. Mineral.* **1999**, 333–344. [CrossRef]
47. Fitch, A.N.; Jobic, H.; Renouprez, A. Localization of benzene in sodium-Y-zeolite by powder neutron diffraction. *J. Phys. Chem.* **1986**, *90*, 1311–1318. [CrossRef]
48. Lee, J.D.; Bryant, M.W.R. The crystal and molecular structure of dibenzyl disulphide. The refinement of a structure with high correlation coefficients. *Acta Crystallogr. Sect. B* **1969**, *25*, 2497–2504. [CrossRef]
49. Meicheng, S.; Genpei, L.; Youqi, T.; Pinzhe, L.; Yuguo, F.; Dongyao, G. The crystal structure of a novel inclusion compound tetrakis (-n, n-diethyldithiocarbamato-s,s)-Mo (V).(tetrachloro-Fe(III)) with included dibenzyl-disulfide. *Sci. China Ser. B Chem. Biol. Agric. Med. Earth Sci.* **1982**, *25*, 576–586.
50. Parr, R.G.; Pearson, R.G. Absolute hardness: Companion parameter to absolute electronegativity. *J. Am. Chem. Soc.* **1983**, *105*, 7512–7516. [CrossRef]
51. Pearson, R.G. Hard and soft acids and bases—The evolution of a chemical concept. *Coord. Chem. Rev.* **1990**, *100*, 403–425. [CrossRef]
52. Brändle, M.; Sauer, J. Combining ab initio techniques with analytical potential functions. A study of zeolite-adsorbate interactions for NH_3 on H-faujasite. *J. Mol. Catal. A Chem.* **1997**, *119*, 19–33.
53. Li, C.Y.; Rees, L.V.C. Ion exchange, thermal stability and water desorption studies of faujasites with different Si/Al ratios. *React. Polym. Ion Exch. Sorbents* **1988**, *7*, 89–99. [CrossRef]

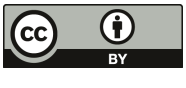

nanomaterials

MDPI

Article

Thermal Boundary Characteristics of Homo-/Heterogeneous Interfaces

Koen Heijmans [1], Amar Deep Pathak [1], Pablo Solano-López [2], Domenico Giordano [3], Silvia Nedea [1,*] and David Smeulders [1]

[1] Energy Technology, Department of Mechanical Engineering, Eindhoven University of Technology, 5600 MB Eindhoven, The Netherlands; k.heijmans@tue.nl (K.H.); simplyamar06@gmail.com (A.D.P.); d.m.j.smeulders@tue.nl (D.S.)

[2] Departmento de Fisica Aplicada, ETSIAE, Universidad Politécnica de Madrid, 28040 Madrid, Spain; Pablo.Solano@upm.es

[3] ESA—Estec, Keplerlaan 1, 2201 AZ Noordwijk, The Netherlands; dg.esa.retired@gmail.com

* Correspondence: s.v.nedea@tue.nl

Received: 15 March 2019; Accepted: 19 April 2019; Published: 26 April 2019

Abstract: The interface of two solids in contact introduces a thermal boundary resistance (TBR), which is challenging to measure from experiments. Besides, if the interface is reactive, it can form an intermediate recrystallized or amorphous region, and extra influencing phenomena are introduced. Reactive force field Molecular Dynamics (ReaxFF MD) is used to study these interfacial phenomena at the (non-)reactive interface. The non-reactive interfaces are compared using a phenomenological theory (PT), predicting the temperature discontinuity at the interface. By connecting ReaxFF MD and PT we confirm a continuous temperature profile for the homogeneous non-reactive interface and a temperature jump in case of the heterogeneous non-reactive interface. ReaxFF MD is further used to understand the effect of chemical activity of two solids in contact. The selected Si/SiO_2 materials showed that the TBR of the reacted interface is two times larger than the non-reactive, going from 1.65×10^{-9} to 3.38×10^{-9} m^2K/W. This is linked to the formation of an intermediate amorphous layer induced by heating, which remains stable when the system is cooled again. This provides the possibility to design multi-layered structures with a desired TBR.

Keywords: ReaxFF; interface; thermal boundary resistance; Kapitza resistance

1. Introduction

Molecular characteristics of solids in contact play a key role in various fundamental studies related to heat transfer [1], mechanical behavior [2], micro/nano-fluidics [3], and catalysis [4]. Besides, it plays an important role in applications related to semiconductors [5], microelectronics [6,7] and heat-shielding in re-entry vehicles for aerospace applications [8]. In the latter case, insight into the thermal resistance at an interface of a multilayer structure is crucial for prediction and control of overheating of the thermal protection system used for the re-entry shuttle. The non-equilibrium effects of a hypersonic flow impinging on a solid interface requires detailed investigation of the boundary processes. Mass, momentum, energy transfer and chemical reactions on the interface are critical under these extreme conditions [9]. These processes can change the interfacial properties significantly compared to initial bulk properties. Furthermore, in case of chemical reactions at the interface (as shown in Figure 1), insight into the heat transfer in a small layer of material (a few molecular layers) is required.

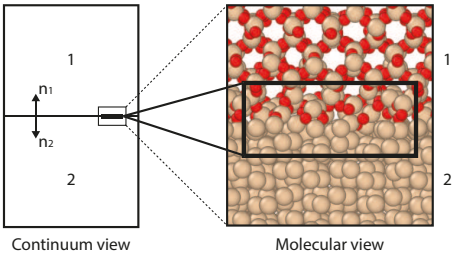

Figure 1. A schematic representation of continuum and molecular view of a system chosen for the present study.

The influence of the solid interfaces on thermal properties can be analyzed by the local temperature profiles on a molecular level. Experimental measurement of a temperature profile at the molecular level is extremely challenging. Therefore, computational models can be useful accurate tools to provide thermal insight and to establish the interfacial thermal correlations. In the context of building up a macroscopic theory of gas–surface interactions targeting the hypersonic re-entry flows, Giordano et al. [8] have proposed a Phenomenological-Theory (PT) to study heat transfer between two solids in contact. Another tool is Molecular Dynamics (MD) simulations, which has been used before to investigate thermal transport across solid interfaces [10–16], and significant influences of the solid interface on the thermal conduction are reported. A schematic representation of these two methods is shown in Figure 1, with a continuum view for PT, and a molecular view for ReaxFF.

Though temperature profiles at the solid interface are investigated before, these studies and methods focus mainly on non-reactive interfaces. However, chemical activity at the interfaces can influence the thermal behavior of solids in contact. Therefore, reactive force field Molecular Dynamics (ReaxFF [17,18]) is used, which is able to capture the chemical reaction and its influence on the surface transformation and temperature profile on molecular level.

In this study, we first consider the characterization of material properties like thermal expansion, thermal conductivity, and elastic properties using ReaxFF, to validate the force field. Thereafter, we build a generic non-reactive system, in which an interface is created based on the same material, for this, we considered two Platinum slabs (homogeneous Pt/Pt interface). Further, we create an interface between two different materials in contact, a non-reactive heterogeneous Platinum-Nickel interface (Pt/Ni). Accordingly, the temperature profiles from the ReaxFF MD simulations are compared with the macroscopic level PT based model of Giordano et al. [8]. For the computation of the temperature profile with PT, relevant material properties are computed with ReaxFF MD and upscaled, to be used as input in the PT model. Platinum and Nickel were selected because they are well studied, non-reactive, monatomic, and have similar lattice size.

After we analyzed this generic model, we created the reactive heterogeneous interface of Silicon and Silicon-oxide (Si/SO_2). This Si/SiO_2 interface is of relevance for many applications in the semiconductor industry, as well as aerospace engineering [19]. Because of its relevance, the Si/SiO_2 interface is studied numerous times before [20], including the thermal boundary resistance (TBR) based on experiments [21], or numerical methods like MD [12–14], acoustic and diffusive mismatch models (AMM, DMM) [22], and phonon wave-package method [12]. With ranging values between 0.4–3.5 $\times 10^{-9}$ m^2K/W, depending on the method and composition of the materials. Furthermore, Chen et al. showed a strong correlation between the coupling between the materials and the TBR. These coupling can be directly related to reactions happening at the interface. However, to our knowledge no systematic studies has been done on the influence of a reactive interface on the TBR. Therefore, we used ReaxFF to study the influence of the reactive interface. The Si/SiO_2 system is kept at various temperatures, within the ReaxFF simulations, to increase/decrease the chemical activity. Accordingly, the TBR is computed. The TBR is defined as the temperature discontinuity at the interface (ΔT) divided

by the heat flux (Q) that crosses the interface, see Equation (1). The TBR is often referred as the Kapitza resistance [23], however, we kept the analogy of Peterson et al. [24]:

$$TBR = R = \Delta T / Q \tag{1}$$

2. Methodology & Material Properties Estimation

2.1. Phenomenological-Theory (PT)

To study the heat transfer between two solids in contact, Giordano et al. [8] have proposed a Phenomenological-Theory (PT). With the aim of building up a macroscopic theory of gas–surface interactions targeting the hypersonic re-entry flows. They have remarked the lack of a physical principle justifying the standard temperature-continuity boundary conditions as a replacement of temperature-continuity, and have introduced tension continuity:

$$\mathbf{n}_1 \cdot \tau_{U,1}(P,t) + \mathbf{n}_2 \cdot \tau_{U,2}(P,t) = 0 \tag{2}$$

where, $\mathbf{n}_1$ and $\mathbf{n}_2$ are normal unit vectors at a point of contact P and time t. This macroscopic theory is founded on momentum conservation and represents a more physically motivated boundary condition. For the mathematical formulation of the phenomenological-theory and further details, readers can refer to the original paper [8]. This method is used to compare the temperature profile non-reactive interfaces studied with MD. For the input of required material properties, the MD calculated values are used.

2.2. Reactive Force Field Molecular Dynamics

Molecular Dynamics (MD) is a computational method to obtain macroscopic and microscopic properties from approximated trajectories of individual particles. These approximated trajectories, obtained from Newton's equations of motion, form an ensemble from which macroscopic properties of materials can be obtained [25]. To capture the chemical change during a reaction, Reactive force field (ReaxFF) [17] is used. ReaxFF is computationally more expensive than the non-reactive force field, however, it allows bond formation and bond breaking during the simulations, which makes simulations of chemical reactions possible. According to ReaxFF the bond order between a pair of atoms can be obtained directly from the inter-atomic distance, which relation is used to mimic chemical change. The feature of bond formation and breaking allows the user not to give predefined reactions pathways, these should present themselves given the right temperatures and chemical environment. However, the accuracy of this relies directly on the training set and the weights that are used to parameterize the reactive force field. Therefore, we tested several available ReaxFF on their ability to predict relevant material characteristics for our study. ReaxFF is widely used in studying chemical activities at a molecular level [18,26], including many Si/SiO_2 systems [19,20,27–35].

For the in-silico characterization using ReaxFF MD methodology, we compute the material properties of relatively simple systems of Platinum (Pt), Nickel (Ni), Silicon (Si) and Silicon dioxide (SiO_2). Furthermore, the elastic properties, thermal expansion coefficient, and thermal conductivity of the materials are important parameters for the phenomenological-theory, and thus the computed values are used as input parameters to upscale the molecular results up to the macroscopic level.

2.2.1. Force Field Selection

Selection of an appropriate force field is very important for in-silico characterization. The calculations of elastic properties, thermal expansion coefficients and the radial distribution function (RDF), guide as a selection criterion for the appropriate force fields. Supercells of $(5 \times 5 \times 5)$ Pt, $(5 \times 5 \times 5)$ Ni, $(3 \times 3 \times 3)$ Si and $(4 \times 4 \times 4)$ SiO_2 are created, containing approximately 400–800 atoms, with initial volumes of 7547, 5469, 7890, and 10,913 $Å^3$, respectively. Periodic Boundary Conditions

(PBC) are applied in all directions. The unit cells of Pt [36], Ni [37], Si [38] and SiO_2 [39] are taken from experimental crystallographic information files.

We have chosen three reactive force fields [4,29,40] available for Pt and Ni and nine force fields for Si and SiO_2 [19,29–35]. These force fields are tested by deforming the crystals in the range of 0.86 to 1.16 times their initial volume. The resulting increase in potential energy is shown in Figure 2.

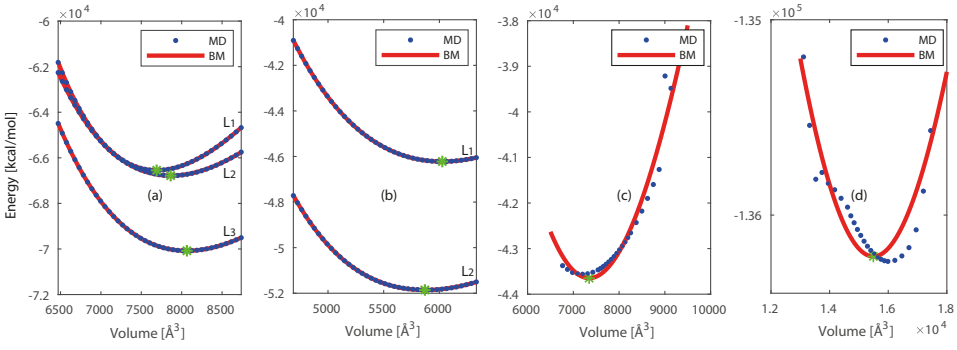

Figure 2. The energy of system obtained from selected force fields as a function of volume and the fitted BM-eos for: (**a**) 5 × 5 × 5 Pt, (**b**) 5 × 5 × 5 Ni, (**c**) 3 × 3 × 3 Si, and (**d**) 4 × 4 × 4 SiO_2. The '⋆' represents the minimum energy point (E_0, V_0) on each curve.

For clarity only the best performing force field is shown for Si and SiO_2. The relation between volume and energy is found by integration of the pressure in the third order Birch-Murnaghan equation of state (BM-eos) [41–43], this relation is fitted to the results of the deformed crystal. The resulting parameters (B_0 and V_0) are given in Appendix A and compared with the literature.

The force field developed by J.E. Mueller et al. [4] showed the best results, and was therefore chosen for further use including Pt and Ni. This force field was parameterized for studying hydrocarbon reactions on nickel surfaces. They included the equation of state (EOS) for different Ni bulk structures in the training. Both our and their calculations predicted the EOS, together with the lattice parameters, in close agreement with quantum mechanical calculations. We predicted the equilibrium volume (V_0) of Pt [36] and Ni [37] unit cells within 1.9% and 7.0% deviations from their experimentally observed crystal structures. The deviations for the bulk modulus (B_0) of Pt and Ni are 9.8% [44] and 16.0% [45] respectively. Furthermore, Mueller et al. computed cohesive energies in close agreement with experimental values. The force field developed by Kulkarni et al. [19] was chosen for further use including Si and SiO_2. This force field is an extension to include gas–surface reactions between oxygen and silica into an existed force field developed by van Duin et al. [20]. This original force field was parametrized to include the chemistry of silicon and silicon oxides, and the interface between these materials. Previous work of Tian et al. [46] also indicated that this original force field predicts the thermal conductivity of vitreous SiO_2 in close agreement with experimental values. The force field of Kulkarni et al. is able to predict the equilibrium volume (V_0) within 7.5% [38] and 30% [39] deviations for Si and SiO_2, respectively. The bulk modulus (B_0) is within 22.9% [47] and 5.7% [48] deviations for Si and SiO_2, respectively. Therefore, this force field is selected for the study that includes Si and SiO_2. These force fields are chosen for further investigation.

To validate further the applicability of the chosen force fields, we have obtained the Radial Distribution Functions (RDFs) of Pt–Pt, Ni–Ni, Si–Si (Si and SiO_2) and Si–O (SiO_2) pairs from ReaxFF MD simulations in periodic solid supercells as shown in Figure 3.

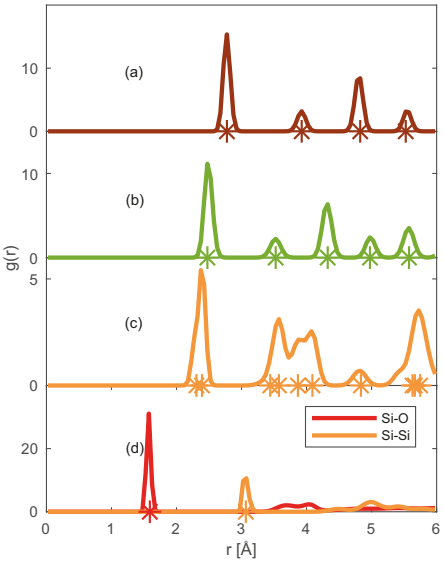

Figure 3. Radial distribution functions for: (**a**) Pt–Pt, (**b**) Ni–Ni, (**c**) Si–Si and (**d**) Si–O pairs present in studied solid crystals obtained from the ReaxFF MD simulations. The '$*$' represents the neighboring atomic distances inside the solid crystal. For clarity, only the nearest neighbor '$*$' is shown in SiO_2.

The sharp peaks in RDF elucidate the extent of ordering in the supercell, thus representing the solid phase. The locations of the peaks coincide with the position of neighboring atoms (represented by '$*$') in the experimentally observed solid crystal [36–39]. Concluding that the selected force fields [4,19] can capture the crystalline phase of Pt, Ni, Si, and SiO_2.

The volumetric thermal expansion coefficient (α_v) can be obtained from the slope of the natural logarithm of the volume ($\ln V$) versus imposed temperature (T) [49]:

$$\alpha_v = \frac{1}{V}\left(\frac{\partial V}{\partial T}\right)_p = \left[\frac{\partial ln(V)}{\partial T}\right]_p \quad (3)$$

where α_v is the volumetric thermal expansion coefficient at constant pressure. We have varied the temperature over 250–500 K at atmospheric pressure in an NPT ensemble. The thermal expansion coefficients for Pt and Ni computed from ReaxFF MD and existing literature values are given in Table 1. The results on the molecular scale are in reasonable agreement with the bulk experimental value [50,51].

Table 1. Comparison of volumetric expansion coefficients (α_v) obtained from the present ReaxFF MD simulations, and reported from literature (in parentheses).

Element	$\alpha_v \times 10^{-5}$ (m^3/m^3K)
Pt	2.0 (2.7 [50])
Ni	3.2 (3.9 [51])

2.2.2. Thermal Conductivity with Steady State NEMD Method

The thermal conductivity of a solid can be computed from Steady State Non-Equilibrium Molecular Dynamics (ss-NEMD). This method has been previously used [16,46,52–55], and it is based

on imposing a temperature gradient over a system to estimate the thermal conductivity. A schematic view of this method is shown in Figure 4.

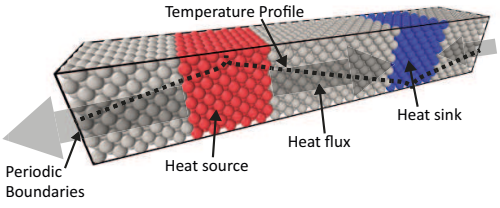

Figure 4. Schematic representation of the chosen system for steady state NEMD simulations. The heat source and sink are coupled to different temperatures with a damping constant of 100 fs. This will induce a heat flux through the intermediate zone, which is weakly coupled with a damping constant of 100.000 fs.

Two strongly coupled regions (using a Berendsen thermostat with damping constant τ = 100 fs) are created, one hot zone (red zone, T_H = 330 K) and one cold zone (blue zone, T_C = 300 K), which act as the heat source and sink, respectively. In between these two zones, there are weakly coupled regions (gray zone, $\tau = 10^5$ fs), this damping constant proved to have a negligible low influence on the system. This results in a steady state temperature gradient (dT/dx) and an energy flux (q), in the weakly coupled regions between heat source and sink.

From the energy flux and the temperature gradient, the thermal conductivity (k) can be computed, following Fourier's law. This intuitive principle makes NEMD well suited to study thermal conductivity of different matter, and investigate the influence of structural defects and solid interfaces [52]. According to the kinetic theory, the thermal conductivity (k) is related to the mean free path (λ) of energy carriers (Equation (4)). If the characteristic length of the system is larger than the mean free path of carriers, thermal energy is transferred by multiple collisions. In this diffusive regime, the Fourier law is still valid. In cases when the characteristic length of the system is in the order of the mean free path, the energy carriers may travel ballistically between source and sink. This scattering in the heat source and sink introduces an extra limiting effect on the mean free path, and thus a reducing effect on the conductivity (Equation (4)). Thus, the conductivity equation must be corrected for the enhanced scattering effect [56]:

$$k = \frac{1}{3} C_v v \lambda_L \tag{4}$$

where C_v is the heat capacity, v the energy carrier velocity, and λ_L the corrected mean free path for a system of size L. This can be estimated from Matthiessen's rule [57], which states that the corrected resistivity is the sum of the intrinsic scattering and the scattering due to impurity. Thus, the corrected mean free path can be expressed as a combined effect of the mean free path of bulk (λ_∞) and length of the system (L) as:

$$\frac{1}{\lambda_L} = \frac{1}{\lambda_\infty} + \frac{4}{L} \tag{5}$$

In a system with periodic boundary conditions, the average distance for an energy carrier to scatter with the heat source or sink is $L/4$ [16]. Combining Equations (4) and (5), the thermal conductivity (k_L) of system size L can be expressed as:

$$\frac{1}{k_L} = \frac{12}{C_v v} \frac{1}{L} + \frac{1}{k_\infty} \tag{6}$$

In this equation, $\frac{1}{k_\infty}$ is the thermal conductivity of the bulk material. Bulk thermal conductivity (k_∞) can be estimated by extrapolating the effective thermal conductivity obtained for small system sizes (k_L).

The thermal conductivities of Pt and Ni are computed using the ss-NEMD method for different system sizes. The total length of the systems varied from $3 \times 3 \times X$ (with X from 24 to 156), including $3 \times 3 \times 6$ zones as the heat source and sink. The energy flux is taken from the average of the heat flux added and extracted by the two strongly coupled regions. The temperature gradient is computed over the weakly coupled region, and the system is equilibrated up to 1 ns with time steps (Δt) of 0.25 fs. The by ss-NEMD computed thermal conductivity values are presented in Table 2, and increases with system size for both Pt and Ni systems.

Table 2. Thermal conductivities for different system sizes of Pt and Ni.

System	Conductivity Pt (W/mK)	Conductivity Ni (W/mK)
$3 \times 3 \times 24$	4.0 ± 0.4	7.7 ± 0.5
$3 \times 3 \times 36$	5.9 ± 0.3	—
$3 \times 3 \times 60$	—	17.2 ± 0.6
$3 \times 3 \times 84$	10.4 ± 0.3	21.7 ± 0.6
$3 \times 3 \times 108$	15.0 ± 0.5	24.4 ± 0.5
$3 \times 3 \times 132$	16.3 ± 0.3	—
$3 \times 3 \times 156$	19.2 ± 0.5	—
Extrapolated	49.8 ± 10.5	74.4 ± 9.2
Literature	71.6 [58]	90.7 [58]

The thermal conductivities are extrapolated for long length by fitting the linear expression between $1/L$ and $1/k$ (Equation (6)) as shown in Figure 5. The fitted lines intersect the Y axis at $1/k_{\mathrm{Pt}} = 0.021$ mK/W and $1/k_{\mathrm{Ni}} = 0.013$ mK/W, which results in a bulk thermal conductivity of $k_{\mathrm{Pt}} = 49.8 \pm 10.5$ W/mK and $k_{\mathrm{Ni}} = 74.4 \pm 9.2$ W/mK. The small deviations in an individual system result in large deviations in the bulk thermal conductivity, due to the extrapolation [59]. The computed thermal conductivities are approximately 35 % and 18 % lower than literature [58] values for Pt and Ni, respectively. This was expected because the ReaxFF formalism we used does not describe free electrons. The difference with experimental values can be explained by limitations of the ReaxFF method we used. ReaxFF MD is not able to model free electrons, thereby we underestimate the thermal conductivity. However, our aim is to compare models and confirm the temperature jump, not to compute exactly the thermal conductivities of Pt and Ni. There is a ReaxFF expansion including free electrons (e-ReaxFF) developed by Islam et al. [60]. At the moment of writing this e-ReaxFF concept does not include the studied materials, nonetheless, this might be interesting for future research.

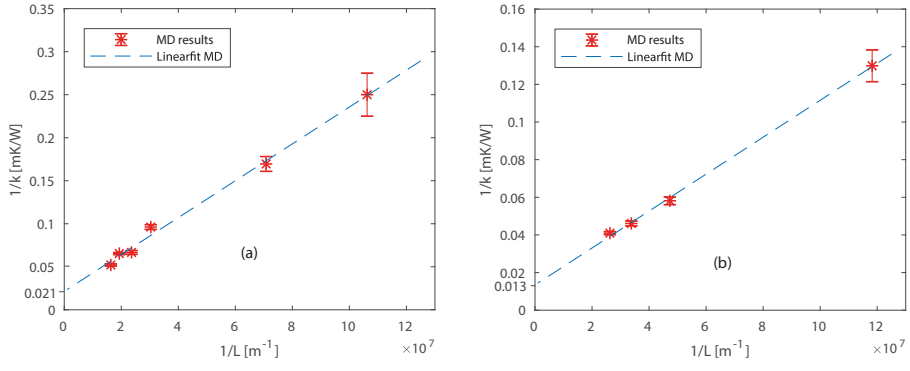

Figure 5. Extrapolation of thermal conductivities for different sizes of (**a**) Pt and (**b**) Ni.

The gradients of the extrapolated curve (Figure 5) obtained from ReaxFF MD simulations are 2.1×10^{-9} m^{2}K/W and 1.0×10^{-9} m^{2}K/W for Pt and Ni, respectively. The gradient should be equal to the theoretical gradient $12/C_v v$ (Equation (6)) obtained from the kinetic theory. By assuming a specific heat of $C_{v,\mathrm{Pt}} = 29 \times 10^5$ J/m^{3}K, and $C_{v,\mathrm{Ni}} = 40 \times 10^5$ J/m^{3}K [58], the computed velocities of thermal transport carriers are $v_{\mathrm{Pt}} \approx 2 \times 10^3$ m/s, $v_{\mathrm{Ni}} \approx 3 \times 10^3$ m/s. These values are found to be in agreement with the speed of sound in the lateral direction through Pt and Ni from literature [58]. We also studied the final size effects perpendicular to the heat flow for platinum systems, see Appendix B. However, no finite size effects were observed for perpendicular directions, corresponding to the findings of Zhou et al. [54].

2.2.3. Building the Interfacial Molecular System

Schematic diagrams of the studied Pt/Pt, Pt/Ni and Si/SiO_2 systems are given in Figure 6. The crystal structures of Pt [36], Ni [37], Si, and SiO_2 [39] are used to build the interfaces. For Si the bc8 form given by Kasper et al. [38] is used, and we used the cristobalite SiO_2 of Nieuwenkamp et al., these two where specifically chosen to closely match each-others crystal lattice. The top and bottom sections ($9 \times 9 \times 6$ Pt, $10 \times 10 \times 6$ Ni, $3 \times 3 \times 2$ Si and $4 \times 4 \times 2$ SiO_2), are attached to strongly coupled thermostats ($\tau = 100$ fs) and act as a heat source and heat sink. The intermediate regions ($9 \times 9 \times 9$ Pt, $10 \times 10 \times 10$ Ni, $3 \times 3 \times 25$ Si and $4 \times 4 \times 24$ SiO_2) are weakly coupled ($\tau = 10^5$ fs). The supercells are initially placed at a small distance and approach each other during an energy minimization to form the interface. From these energy minimized (merged) systems, the simulations are started. In the non-reactive systems, the top sections are kept at $T_H = 330$ K and bottom sections are kept at $T_C = 300$ K. In the reactive systems temperature values are varied to trigger a chemical reaction at the interface. To calculate the TBR, all the simulations are done over 1 ns, from which the last 0.75 ns are considered to obtain the data.

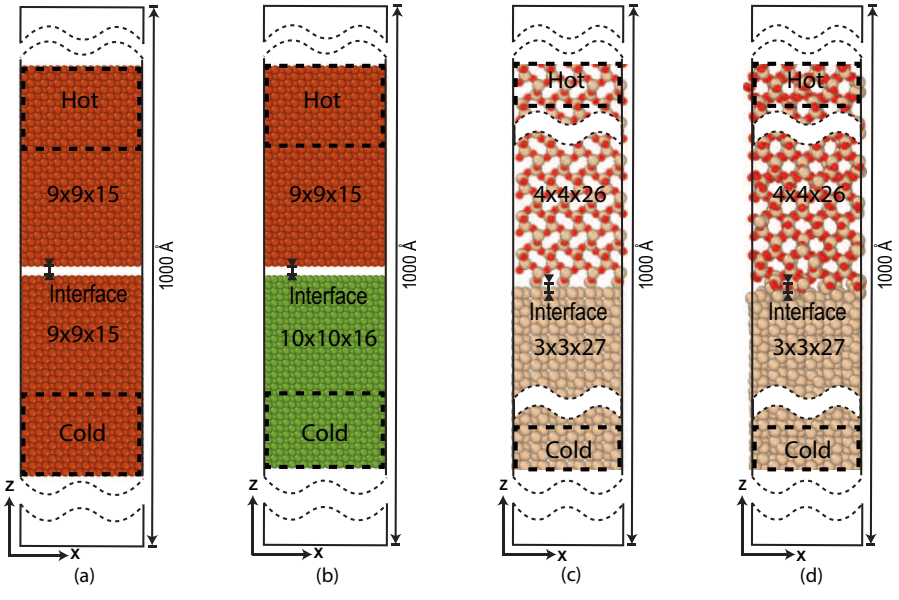

Figure 6. Schematic representation of systems: (**a**) non-reactive Pt/Pt interface, (**b**) non-reactive Pt/Ni interface, (**c**) initial reactive Si/SiO_2 interface, and (**d**) the merged reactive Si/SiO_2 interface. The particles in the dashed area are the strongly coupled sections, which acts as a heat source and heat sink.

When an interface between two different materials is created artificial mechanical stresses are introduced by fitting the different lattice constants in one single periodic box. To restrict this to a minimum we carefully selected the materials, supercells, and orientation to create the interface. Thereby, the deformation of the crystals is limited to 0.1% compared to their literature value. Furthermore, we studied the influence of 1% deformation of Platinum on the thermal conductivity. The thermal conductivity for a compressed, as well as, a stretched crystal was lower, however for both cases within the standard deviation of the original system. The deformation of the crystals, and the study towards the thermal conductivity can be found in Appendix C.

3. Results

ReaxFF MD simulations are carried out to understand the temperature discontinuity across the solid interfaces of homogeneous (Pt/Pt), heterogeneous (Pt/Ni) and heterogeneous reactive materials (Si/SiO_2). The computed material properties from the previous section are used to upscale the results from the molecular level to macroscopic phenomenological-theory level. For the thermal conductivity, the extrapolated value is used. A comparison is made between both methods for the non-reactive interfaces.

3.1. Non-Reactive Interfaces

In realistic experimental conditions, the thermostat takes time to set the desired temperature, thus the temperature of the heat source evolves with time. To study this effect on the final temperature profile in ReaxFF MD, we compared two different settings to increase the temperature of the heat source. One with a gradual temperature increase to T_H, and one with an instantaneously high temperature at T_H. See Appendix D, and Figure A1, for the result of the comparison between the two cases. We observe that the final temperature profile is almost the same for both cases. Thus in the following cases, we have initialized the temperature of the heat source instantaneously at high temperature (instant ΔT).

For the non-reactive ReaxFF MD interface investigation, the systems given in Figure 6a,b are studied. The temperature profile evolution across the solid interfaces of Pt/Pt and Pt/Ni systems with ReaxFF MD is plotted in gray-scale after every 200 ps, which can be seen in Figure 7a,b. The light-gray to black lines represents respectively the earlier and later time periods.

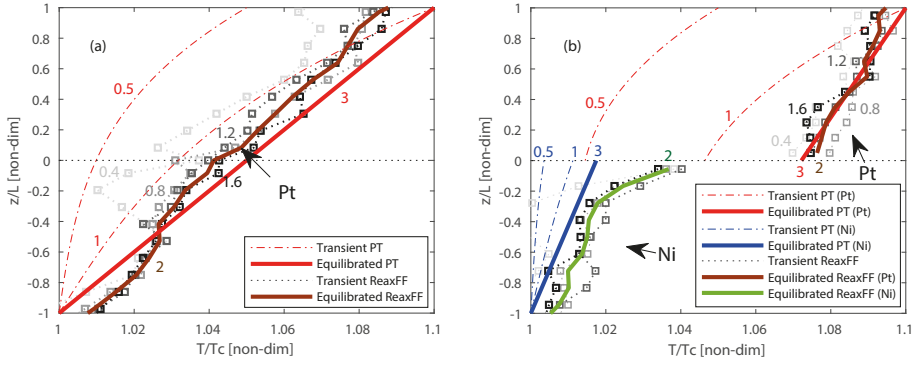

Figure 7. Comparison of temperature profile computed from PT based model and ReaxFF MD simulation for: (**a**) Pt/Pt interface. (**b**) Pt/Ni interfaces. The solid lines represent the equilibrated, and the dashed/dotted lines the transient temperature profiles. The dashed-dotted lines are intermediate transient temperature profiles for PT, and the dotted lines with square markers represent intermediates from ReaxFF MD simulations. The corresponding numbers at the lines represent $t_{\text{non-dim}}$.

The equilibrated temperature is represented by the solid brown and green lines, respectively Platinum and Nickel. The temperature profiles developed over time obtained from ReaxFF MD are compared with the temperature profile from phenomenological-theory as shown in Figure 7. The molecular level ReaxFF MD simulations and macroscopic level phenomenological-theory have a different time scale, thus to compare them, a non-dimensional time ($t_{\text{non-dim}}$) is defined as:

$$t_{\text{non-dim}} = t/t_{eq} \tag{7}$$

where t is the actual time and t_{eq} is the time assumed the system is in steady state. An steady state time of 0.5 ns is assumed for the MD simulations. The red, blue and gray numbers in the figures represent these different transient $t_{\text{non-dim}}$ states. The temperature profile obtained from the phenomenological-theory evolves slowly with time when compared with the ReaxFF MD simulations, where the transient states are quickly converging and fluctuation around the equilibrium state. In the ReaxFF MD results, a continuous temperature profile is observed at the Pt/Pt interface while a temperature jump (discontinuity) is observed at the Pt/Ni interface as shown in Figure 7a,b, respectively. Similar temperature profiles are also observed from the phenomenological-theory. The ReaxFF MD method shows a temperature jump of approximately 39%, where the phenomenological-theory results in a 55% jump of the imposed temperature difference of 30 K. Since one method is based on molecular level and another one is based on macroscopic level theory, a slight discrepancy in the magnitude of the temperature jump can be expected. These results confirm that the temperature jump is observed at the solid interface between different materials for both molecular level and macroscopic level modeling.

3.2. Reactive Interfaces

At the surface of re-entry vehicles chemical reactions can occur, these reactions contribute to the heating of such vehicles [8,19]. Furthermore, these reactions form a small layer, and influence the heat and mass transport at the surface. To gain more fundamental knowledge of such a surface, we studied a reactive solid Si/SiO_2 interface (see Figure 6c,d). The building of the physical system is similar to the two previous systems (Pt/Pt and Pt/Ni). The length between the heat source and sink is approximately 327 Å, and temperatures of the heat source and sink are varied to increase/decrease the chemical reaction at the solid interface [61]. Four different cases are studied, for the first case (Case 1) the set temperatures for heat source (T_H) and sink (T_C) are 150 and 100 K, respectively. For the second case (Case 2), the temperatures are T_H = 350 K and T_C = 300 K, and for the third case (Case 3) the temperatures are T_H = 850 K and T_C = 800 K. These cases have an interface temperatures of approximately 125, 325, and 825 K. In the fourth case (Case 4) the complete system was heated to a high temperature (1700 K) for 3.5 ns to create a reactive region, and thereafter, cooled back to T_C = 100 K, and T_H = 150 K to stop the chemical activity completely again. After the cooling, a new steady state simulation was done at T_C = 100 K, and T_H = 150 K. From Figure A2 in Appendix E, one can see that the major part of the interface formation takes place within the first nanosecond. In terms the thickness of the interface, as well as, the depth of the oxygen penetration into the silicon surface only little changes are observed after the first nanosecond. Therefore, it was not needed to go for longer simulations to create the interface. This fourth case was chosen to get a distinct comparison between the non-reacted and reacted interface, at the same temperature (Case 1 and 4).

The resulted temperature profiles for Case 1–3 are plotted in Figure 8a. The temperature is made non-dimensional by taking 100–150 K as reference and divide by 100. The thick solid lines are fitted to the data, and extrapolated to the interface, to get the temperature jump. The initial interface is positioned at z = 0 Å in the figures. A temperature jump is observed between Si and SiO_2 for all the cases. It reiterates that there is a temperature discontinuity at the reactive heterogeneous solid interface as well. Case 1 (100–150 K) shows a clear jump, with a sharp temperature profile. When the temperature is increased to 300–350 K (case 2), the jump remains, however, it is less sharp. This is

caused by some small deformation at the interface induced by the temperature. Moving to even higher temperatures 800–850 K (case 3), not only a temperature jump but also a drop of the temperature profile over the entire system is observed. This suggests a heat sink at the interface, due to energy consumption by the deformation of the crystals at the interface. This deformation has an impact on the heat transfer and results in an intermediate region between the Silicon and Silica crystals of a few ångströms.

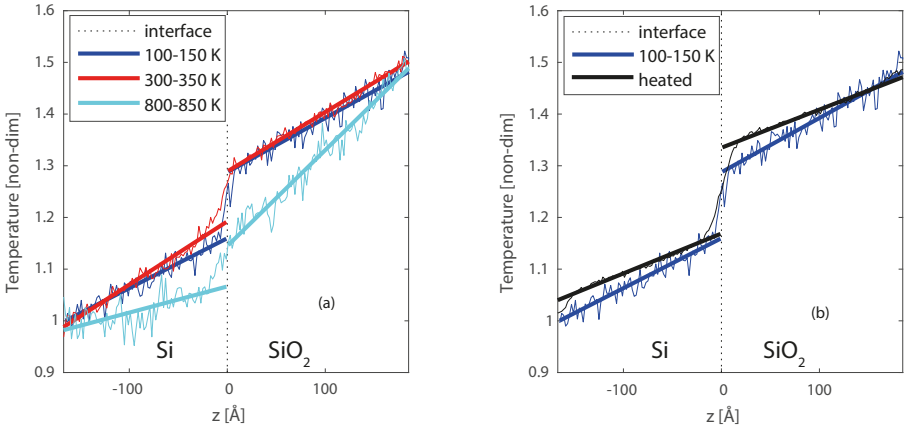

Figure 8. Temperature profiles for the Si/SiO_2 interfaces, with (**a**) case 1, case 2, and case 3, and (**b**) case 1, and case 4. The dotted line indicates the location of the interface, the dark blue lines represent case 1 (T_H = 150 and T_C = 100 K), the red lines represent case 2 (T_H = 350 and T_C = 300 K), the light blue lines represent case 3(T_H = 850 and T_C = 800 K), and the black line represents case 4 (first heated to 1700 K, and then a steady state at T_H = 150 and T_C = 100 K).

To better study the effect and size of the intermediate region, the entire Si/SiO_2 system was heated up to 1700 K to increase the reactivity and advance the formation of the intermediate region. Higher temperatures were also tested, however, these resulted in melting of the Silicon crystal, and separation of the two slabs. Lower temperatures would require more time to create a similar intermediate region. The heating process results in a larger intermediate amorphous region, where oxygen diffused up to 5 Å into the Silicon crystal, and deformation of both materials is visible up to 10 Å from the interface. After the heating, the system was cooled back to 100–150 K, this temperature was chosen to stop the chemical activity as far as possible. The final equilibrated temperature profile is compared with the temperature profile of case 1, where no reactive region is had been present at the interface. This comparison shown in Figure 8b, and a closer profile around the interface is shown in Figure 9a–c. From Figure 9c, the thicker interfacial region for the reacted interface can be clearly observed, compared to the non-reacted clean interface (Figure 9b). For the heated interface (case 4), the temperature jump (ΔT) is larger, however, is has become less sharp than case 1 and smoothed over the formed intermediate region.

The thermal boundary resistances (TBR) are given in Table 3. The calculated value for the low temperature (case 1) is in good agreement with Deng et al. [12], who found a value of 1.48 ($\pm$0.46) $\times$ 10^{-9} m^2K/W using NEMD, and 1.37 ($\pm$0.42) $\times$ 10^{-9} m^2K/W using phonon wave-package dynamics approach. The higher temperatures (case 2,3) approach the experimental results of Hurley et al. [21], who measured a resistance of 2.3 $\times$ 10^{-9} m^2K/W. The reacted interface, which includes an amorphous SiO_2 region, is in good agreement with the DMM results of Hu et al.[22], who found a resistance of 3.5 $\times$ 10^{-9} m^2K/W, for amorphous SiO_2 with Si. The temperature jump at the interface for the 300–350 K and 800–850 K temperatures (case 2,3) is smaller, however, the calculated TBR is higher, caused by the deformation of the interface which acts as an extra heat sink. The TBR for

the reacted interface (case 4) is more than twice the TBR of the non-reacted clean interface (case 1) at the same temperature, caused by the amorphous Si–SiO_2 intermediate region.

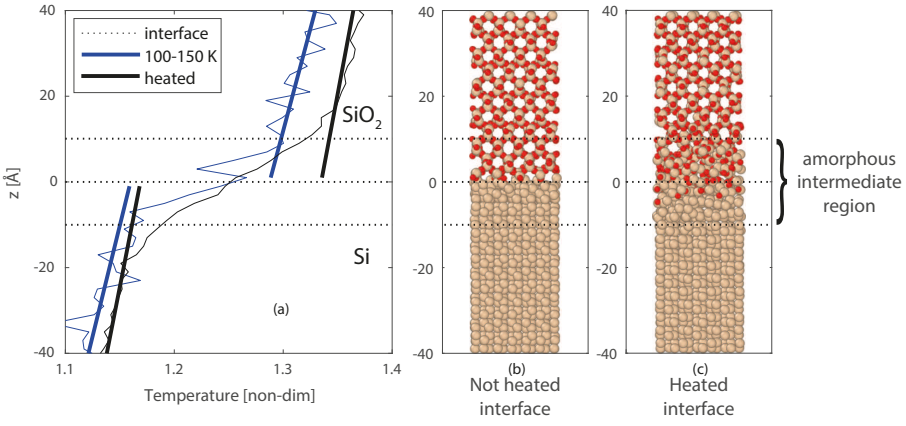

Figure 9. (**a**) zoom of Figure 8b, with the temperature profiles for case 1 (T_H = 150 and T_C = 100 K), and case 4 (first heated to 1700 K, and then a steady state at T_H = 150 and T_C = 100 K). The final molecular structures of the interfaces are given in (**b**) for case 1, and (**c**) for case 4.

Table 3. Thermal Boundary Resistance (TBR) of Si/SiO_2 systems, with T_C and T_H (K) as thermostatted temperature for the heat sink and source respectively.

Case	T_C (K)	T_H (K)	Temperature Jump, ΔT (K)	TBR $\left(\frac{\mathbf{m^2K}}{\mathbf{W}}\right)$
1	100	150	12.8	1.65×10^{-9}
2	300	350	9.7	2.40×10^{-9}
3	800	850	7.8	2.34×10^{-9}
4	$1700 \rightarrow 100$	$1700 \rightarrow 150$	16.6	3.38×10^{-9}

4. Conclusions

ReaxFF MD is known to capture the physical and chemical phenomena under various conditions [18,26]. We have chosen various force fields for Pt/Ni and Si/SiO_2 systems, which can mimic their material properties. The selected force fields predict the equilibrium volumes [36–39] and bulk modulus [44,45,47,48] of respectively Pt, Ni, Si and SiO_2 in close agreement with experiments/theory. To validate further, thermal expansion and thermal conductivity coefficients of Pt and Ni are estimated using ReaxFF MD. The thermal expansion coefficients are found to be in reasonable agreement with experiments. The thermal conductivity of a solid material is size-dependent on the molecular level. Thus, we have obtained the thermal conductivity of Pt and Ni for various system sizes and extrapolated to a very long length to determine the bulk thermal conductivity.

The elastic and thermal properties, obtained from ReaxFF MD, served as input parameters for the macroscopic level phenomenological-theory (PT) [8]. Temperature profiles of non-reactive interfaces, obtained from both methods, are compared. In this comparison, we have reported the temperature profiles across a homogeneous (Pt/Pt), and heterogeneous (Pt/Ni) interface. Temperature continuity is observed at the solid homogeneous interface of Pt/Pt. The temperature profile of the molecular level simulation is faster at equilibrium than the phenomenological-theory. The temperature profiles between Pt/Ni has a discontinuity at the interface observed in both molecular and macroscopic level. The temperature jump obtained from the molecular level calculation is 18% lower than the one obtained from PT calculations. The discrepancy between the two models in the temperature jump for Pt/Ni is minimal, and can be explained by the fact that the length- and time-scale for both calculations

are different, and/or the length dependence of the thermal conductivity. We can conclude that both models, the molecular level ReaxFF MD simulations and the PT, predict a temperature discontinuity across the solid boundary if the materials are not the same.

The ReaxFF MD methodology can capture chemical reactions, therefore, interesting insights could be obtained for solid pairs which can form a reactive interface. For this purpose, the Si/SiO_2 pair was chosen and the heat source and heat sink were varied to increase/decrease the chemical reaction at the interface. Three distinct solids (Si, amorphous reacted Si–SiO_2 interface, and SiO_2) have been observed. The thermal boundary resistance (TBR) is computed at the Si/SiO_2 interface for the different systems, providing us with information of the TBR over interfaces with different chemical activity. It can be concluded that the reacted amorphous region at the interface introduces extra resistivity, compared to the non-reactive clean interface. Showing the opportunity to control the thermal resistivity of a multi-layered system by controlling the interfacial reactive regions.

Author Contributions: Conceptualization, S.N. and D.G.; methodology, S.N. and D.G.; validation, K.H., A.P. and P.S.; investigation, K.H., A.P. and P.S.; resources, D.S.; writing–original draft preparation, K.H., A.P. and S.N.; writing–review and editing, K.H., A.P., S.N., P.S., D.G. and D.S.; supervision, S.N., D.G. and D.S.; funding acquisition, D.S.

Funding: This research received no external funding.

Acknowledgments: The authors would like to thank the Netherlands Organization for Scientific Research (NWO) for access to the national high performance computing facilities (Dossiernr: 17092 6026).

Conflicts of Interest: The authors declare no conflict of interest.

Appendix A. Birch-Murnaghan Equation of State Fitting Si & SiO_2

To select the correct force field, a BM-EOS study is done. The results of the fitting are presented in Table A1, with r^2 as correlation coefficient of the fitting. The results are compared with literature, which gives $V_{0,Pt} = 60.38$ Å^3 [36], $V_{0,Ni} = 43.76$ Å^3 [37], $V_{0,Si} = 292$ Å^3 [38], $V_{0,SiO_2} = 171$ Å^3 [39], $B_{0,Pt} = 266$ GPa [44], $B_{0,Ni} = 185$ GPa [45], $B_{0,Si} = 98$ GPa [62], and $B_{0,SiO_2} = 36$ GPa [48]. The ReaxFF of Mueller et al. [4] and Kulkarni et al. [19] proves to be the best applicable for respectively the Pt/Ni system and the Si/SiO_2 system.

Table A1. Results of BM-eos fitting to different ReaxFF.

	Reference Force Field	B_0 (GPa)	V_0 (Å^3)	E_0 (kcal/mol)	r^2	Figure
Pt	[4]	240	61.52	−532.4	1.0	Figure 2a L1
	[40]	179	62.91	−534.3	1.0	Figure 2a L2
	[29]	166	64.52	−560.6	1.0	Figure 2a L3
Ni	[4]	155	46.96	−414.9	1.0	Figure 2b L2
	[29]	167	48.21	−369.8	1.0	Figure 2b L1
Si	[19]	144	272.1	−1617	0.92	Figure 2c
	[30]	165	273.6	−1611	0.88	
	[31]	292	252.9	−1729	0.95	
	[35]	216	291.2	−1675	0.53	
	[29]	295	265.7	−2244	0.84	
	[63]	235	268.3	−2206	0.95	
	[34]	334	255.2	−1728	0.95	
	[33]	289	252.3	−1730	0.95	
	[32]	334	255	−1728	0.95	

Table A1. *Cont.*

	Reference Force Field	B_0 (GPa)	V_0 (Å^3)	E_0 (kcal/mol)	r^2	Figure
SiO_2	[19]	35	242.1	−2128	0.83	Figure 2d
	[30]	500	244.6	−1847	0.60	
	[31]	33	260.0	−1818.6	0.86	
	[35]	34	238.1	−1793	0.98	
	[29]	47	244.7	−1860	0.83	
	[63]	234	247.2	−1828	0.78	
	[34]	331	263.4	−1841	0.19	
	[33]	273	258.1	−1837	0.16	
	[32]	331	263.4	−1840	0.19	

Appendix B. Finite Size Effects, Perpendicular to the Heat Flow

Platinum systems ($3 \times 3 \times 32$, $5 \times 5 \times 32$, $10 \times 10 \times 32$) were used to study the finite size effects in perpendicular direction to the heat flow. The system are placed in vacuum in z-direction and have periodic boundary conditions in x- and y-direction, the given crystal sizes are including heat source and sink. No final size effects are observed in perpendicular direction to the heat flow.

Table A2. Thermal conductivity of Pt-systems in vacuum in z-direction, and different sizes in x- and y-direction.

System	Thermal Conductivity (W/mK)
$3 \times 3 \times 32$	9.7
$5 \times 5 \times 32$	8.0
$10 \times 10 \times 32$	10.7

Appendix C. Influence of Mechanical Deformation of Slabs

When a heterogeneous interface with two different materials, and thus different lattice parameters, is created the materials are compressed or stretched to fit both materials within the same periodic box. This introduces extra mechanical stresses in the crystals. To restrict this to a minimum we have chosen the materials and supercells in such a way that these artificial deformations are kept to a minimum. The lattice parameters are given in Tables A3 and A4 for the literature value, after an energy minimization in ReaxFF, after an energy minimization in ReaxFF with a vacuum in z direction, and the size used in this work. The lattice parameters are compared with the literature value and the error is given in the last column, this shows that the values are all within 3%, and there is only 0.1% deformation in this work compared to the lattice from literature.

Table A3. Lattice constant for Pt and Ni.

System	Lattice [a; b; c] (Å)	Deviation from Literature (%)
Pt-literature [36]	3.9231; 3.9231; 3.9231	-
Pt-EM ReaxFF	3.9473; 3.9473; 3.9473	+0.6
Pt-EM ReaxFF + vacuum in z-direction	3.9412 ; 3.9412 ; —	+0.5
Pt-interface	3.9192; 3.9192; —	−0.1
Ni-literature [37]	3.5238; 3.5238; 3.5238	—
Ni-EM ReaxFF	3.6122; 3.6122; 3.6122	+2.5
Ni-EM ReaxFF + vacuum in z-direction	3.6048 ; 3.6048 ; —	+2.3
Ni-interface	3.5273; 3.5273; —	+0.1

Table A4. Lattice constant for Si (bc8), and cristobalite SiO_2.

System	Lattice [a; b; c] (Å)	Deviation From Literature (%)
Si (bc8)-literature [38]	6.636; 6.636; 6.636	—
Si (bc8)-EM ReaxFF	6.4393; 6.4393; 6.4393	−2.9
Si (bc8)-EM ReaxFF + vacuum in z-direction	6.4383; 6.4046; —	−2.9; −43.5
Si (bc8)-interface	6.6273; 6.6273; —	−0.1
SiO_2-literature [39]	4.964; 4.964; 6.920	—
SiO_2-EM ReaxFF	5.0443; 5.0443; 7.0063	+1.0
SiO_2-EM ReaxFF + vacuum in z-direction	5.0443; 5.0443; —	+1.0
SiO_2-interface	4.9705; 4.9705; —	+0.1

Influence of Stress on Thermal Conductivity

To form an interface with different materials, the materials are slightly stressed to match each other lattice constants. One of the two materials was slightly compressed, and the other one slightly stretched to form the interface. In the Tables A3 and A4 amount of deformation is shown for the materials used in this work, which are within ±0.1%. To gain more knowledge on the effect of these stresses on the heat transport across the material, we computed the thermal conductivity for 3 × 3 × 132 Platinum structures with lattices corresponding to the literature value, 1% compressed structures, a 1% stretched structures. The computed thermal conductivities for the different deformation are given in Table A5, and are within each other's standard deviation. Thereby, we conclude that we can neglect the effect of stress in this study.

Table A5. Thermal conductivity of a 3 × 3 × 132 Platinum structure under different mechanically induced stresses.

Simulation	No Stress k (W/mK)	1% Compression k (W/mK)	1% Stretched k (W/mK)
1	15.2	14.6	13.4
2	17.8	13.9	14.6
3	16.7	15.3	17.4
4	15.6	16.5	16.5
Average	16.3 ± 1.2	15.1 ± 1.1	15.5 ± 1.8

Appendix D. Comparison of Gradual and Instant Induced Temperature

In realistic experimental conditions, the thermostat takes time to set the desired temperature, thus the temperature of the heat source evolves with time. To investigate the effect of heating the systems on the final temperature distribution in ReaxFF-MD, we have compared a gradual temperature increase to T_H and an instantaneously temperature at T_H. For the gradual temperature setting, we have increased the temperature of the heat source (T_H = 330 K) in the steps of 5 K per 0.1 million iterations (25 ps). After 0.6 million iterations (150 ps), the temperature profile of the gradual temperature rise system is compared with the system in which temperature of hot zone was instantaneously set at T_H = 330 K (instant ΔT) as shown in Figure A1, the comparison was done over a total range of 1 million iterations. We observe that the equilibrated temperature profile is almost the same for both cases. Thus in the following cases, we have initialized the temperature of the heat source instantaneously at high temperature (instant ΔT).

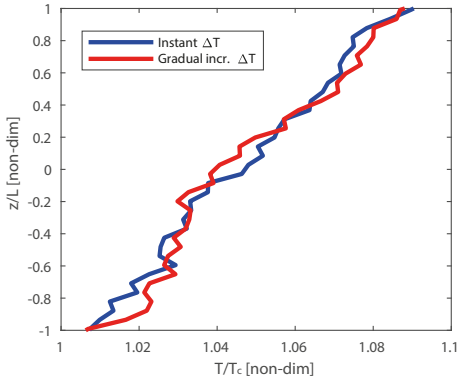

Figure A1. Comparison of temperature profiles (non-dim. T versus non-dim. x) obtained from ReaxFF-MD simulations for the Pt/Pt interface in the case where the heat source is immediately heated to T_H = 330 K (instant ΔT) and system in which the heat source is gradually heated to T_H = 330 K in steps of 5 K per 1×10^5 iterations (gradual ΔT).

Appendix E. Development of the Amorphous Si/SiO_2 Interface

To create a reactive formed interface between Si and SiO_2, the system was heated for to high temperatures (1700 K) for 3.5 ns. Thereafter, it was cooled back to T_C = 100 K, and T_H = 150 K to stop the chemical activity completely again. The development of the interface over the first 3 ns can be observed in the snapshots in Figure A2, also the number of oxygen atoms are counted for these snapshots.

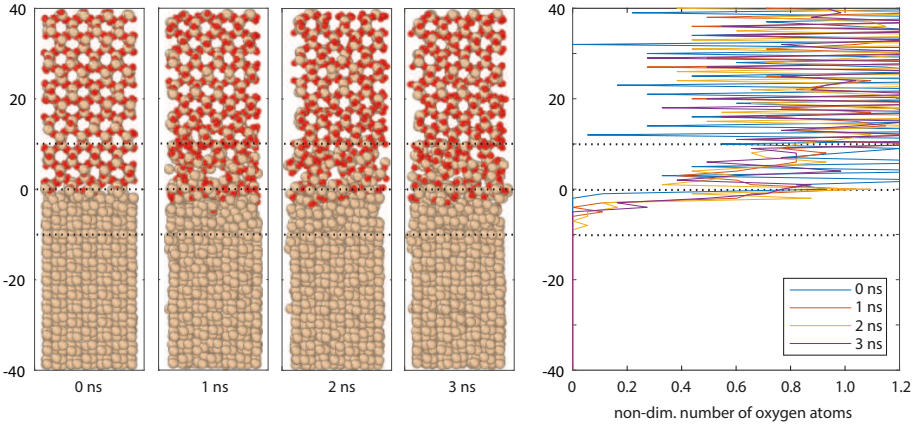

Figure A2. Snapshots of the Si/SiO_2 interface.

References

1. Samvedi, V.; Tomar, V. The role of interface thermal boundary resistance in the overall thermal conductivity of Si—Ge multilayered structures. *Nanotechnology* **2009**, *20*, 365701. [CrossRef]
2. Pilania, G.; Thijsse, B.J.; Hoagland, R.G.; Lazić, I.; Valone, S.M.; Liu, X.Y. Revisiting the Al/Al_2O_3 interface: Coherent interfaces and misfit accommodation. *Sci. Rep.* **2014**, *4*, 4485. [CrossRef] [PubMed]
3. Kim, J.; Frijns, A.J.H.; Nedea, S.V.; van Steenhoven, A.A. Molecular simulation of water vapor outgassing from silica nanopores. *Microfluid. Nanofluid.* **2015**, *19*, 565–576. [CrossRef] [PubMed]

4. Mueller, J.E.; van Duin, A.C.T.; Goddard, W.A., III. Development and validation of ReaxFF reactive force field for hydrocarbon chemistry catalyzed by nickel. *J. Phys. Chem. C* **2010**, *114*, 4939–4949. [CrossRef]
5. Majumdar, A.S.M.E. Microscale heat conduction in dielectric thin films. *J. Heat Transf.* **1993**, *115*, 7–16. [CrossRef]
6. Schutze, J.; Ilgen, H.; Fahrner, W.R. An integrated micro cooling system for electronic circuits. *IEEE Trans. Ind. Electron.* **2001**, *48*, 281–285. [CrossRef]
7. Nunzi, F.; Sgamellotti, A.; Coletti, C.; Re, N. Adsorption and Interfacial Chemistry of Pentacene on the Clean Si(100) Surface: A Density Functional Study. *J. Phys. Chem. C* **2008**, *112*, 6033–6048. [CrossRef]
8. Giordano, D.; Solano-López, P.; Donoso, J.M. Exploratory numerical experiments with a macroscopic theory of interfacial interactions. *CEAS Space J.* **2017**, *9*, 257–277. [CrossRef]
9. Dias, B.; Bariselli, F.; Turchi, A.; Frezzotti, A.; Chatelain, P.; Magin, T. Development of a melting model for meteors. *AIP Conf. Proc.* **2016**, *1786*, 160004.
10. Merabia, S.; Termentzidis, K. Thermal conductance at the interface between crystals using equilibrium and nonequilibrium molecular dynamics. *Phys. Rev. B* **2012**, *86*, 094303. [CrossRef]
11. Mahajan, S.S.; Subbarayan, G.; Sammakia, B.G. Estimating Kapitza Resistance Between Si–SiO_2 Interface Using Molecular Dynamics Simulations. *IEEE Trans. Compon. Packag. Manuf. Technol.* **2011**, *1*, 1132–1139. [CrossRef]
12. Deng, B.; Chernatynskiy, A.; Khafizov, M.; Hurley, D.H.; Phillpot, S.R. Kapitza resistance of Si/SiO_2 interface. *J. Appl. Phys.* **2014**, *115*, 084910.
13. Lampin, E.; Nguyen, Q.H.; Francioso, P.A.; Cleri, F. Thermal boundary resistance at silicon-silica interfaces by molecular dynamics simulations. *Appl. Phys. Lett.* **2012**, *100*, 131906. [CrossRef]
14. Chen, J.; Zhang, G.; Li, B. Thermal contact resistance across nanoscale silicon dioxide and silicon interface. *J. Appl. Phys.* **2012**, *112*, 064319. [CrossRef]
15. Zushi, T.; Ohmori, K.; Yamada, K.; Watanabe, T. Effect of a SiO_2 layer on the thermal transport properties of <100> Si nanowires: A molecular dynamics study. *Phys. Rev. B* **2015**, *91*, 115308.
16. Schelling, P.K.; Phillpot, S.R.; Keblinski, P. Comparison of atomic-level simulation methods for computing thermal conductivity. *Phys. Rev. B* **2002**, *65*, 144306. [CrossRef]
17. Van Duin, A.C.T.; Dasgupta, S.; Lorant, F.; Goddard, W.A. ReaxFF: A Reactive Force Field for Hydrocarbons. *J. Phys. Chem. A* **2001**, *105*, 9396–9409. [CrossRef]
18. Senftle, T.P.; Hong, S.; Islam, M.M.; Kylasa, S.B.; Zheng, Y.; Shin, Y.K.; Junkermeier, C.; Engel-Herbert, R.; Janik, M.J.; Aktulga, H.M.; others. The ReaxFF reactive force-field: Development, applications and future directions. *NPJ Comput. Mater.* **2016**, *2*, 15011. [CrossRef]
19. Kulkarni, A.D.; Truhlar, D.G.; Goverapet Srinivasan, S.; van Duin, A.C.T.; Norman, P.; Schwartzentruber, T.E. Oxygen interactions with silica surfaces: Coupled cluster and density functional investigation and the development of a new ReaxFF potential. *J. Phys. Chem. C* **2012**, *117*, 258–269. [CrossRef]
20. Van Duin, A.C.; Strachan, A.; Stewman, S.; Zhang, Q.; Xu, X.; Goddard, W.A. ReaxFFSiO reactive force field for silicon and silicon oxide systems. *J. Phys. Chem. A* **2003**, *107*, 3803–3811. [CrossRef]
21. Hurley, D.H.; Khafizov, M.; Shinde, S. Measurement of the Kapitza resistance across a bicrystal interface. *J. Appl. Phys.* **2011**, *109*, 083504. [CrossRef]
22. Hu, C.; Kiene, M.; Ho, P.S. Thermal conductivity and interfacial thermal resistance of polymeric low k films. *Appl. Phys. Lett.* **2001**, *79*, 4121–4123. [CrossRef]
23. Kapitza, P. Heat transfer and superfluidity of helium II. *Phys. Rev.* **1941**, *60*, 354. [CrossRef]
24. Peterson, R.; Anderson, A. The Kapitza thermal boundary resistance. *J. Low Temp. Phys.* **1973**, *11*, 639–665. [CrossRef]
25. Frenkel, D.; Smit, B. *Understanding Molecular Simulation: From Algorithms To Applications*, 2nd ed.; Academic Press: Cambridge, MA, USA, 2001.
26. Pathak, A.D.; Nedea, S.; van Duin, A.C.T.; Zondag, H.; Rindt, C.; Smeulders, D. Reactive force field development for magnesium chloride hydrates and its application for seasonal heat storage. *Phys. Chem. Chem. Phys.* **2016**, *18*, 15838–15847. [CrossRef]
27. Kim, J.; Iype, E.; Frijns, A.J.; Nedea, S.V.; van Steenhoven, A.A. Development of EEM based silicon–water and silica–water wall potentials for non-reactive molecular dynamics simulations. *J. Comput. Phys.* **2014**, *268*, 51–62. [CrossRef]

28. Suek, N.W.; Guillaume, M.C.; Delannoy, J.Y.P.; Tielens, F. Characterization of hydroxylated amorphous silica: A numerical approach. *Adsorption* **2018**, *24*, 267–278. [CrossRef]
29. Nielson, K.D.; van Duin, A.C.T.; Oxgaard, J.; Deng, W.Q.; Goddard, W.A., III. Development of the ReaxFF reactive force field for describing transition metal catalyzed reactions, with application to the initial stages of the catalytic formation of carbon nanotubes. *J. Phys. Chem. A* **2005**, *109*, 493–499. [CrossRef]
30. Fogarty, J.C.; Aktulga, H.M.; Grama, A.Y.; Van Duin, A.C.T.; Pandit, S.A. A reactive molecular dynamics simulation of the silica-water interface. *J. Chem. Phys.* **2010**, *132*, 174704. [CrossRef]
31. Narayanan, B.; van Duin, A.C.T.; Kappes, B.B.; Reimanis, I.E.; Ciobanu, C.V. A reactive force field for lithium–aluminum silicates with applications to eucryptite phases. *Model. Simul. Mater. Sci. Eng.* **2011**, *20*, 015002. [CrossRef]
32. Castro-Marcano, F.; van Duin, A.C.T. Comparison of thermal and catalytic cracking of 1-heptene from ReaxFF reactive molecular dynamics simulations. *Combust. Flame* **2013**, *160*, 766–775. [CrossRef]
33. Pitman, M.C.; Van Duin, A.C.T. Dynamics of confined reactive water in smectite clay–zeolite composites. *J. Am. Chem. Soc.* **2012**, *134*, 3042–3053. [CrossRef]
34. Zou, C.; Van Duin, A.C.T. Investigation of Complex Iron Surface Catalytic Chemistry Using the ReaxFF Reactive Force Field Method. *JOM* **2012**, *64*, 1426–1437. [CrossRef]
35. Newsome, D.A.; Sengupta, D.; Foroutan, H.; Russo, M.F.; van Duin, A.C.T. Oxidation of silicon carbide by O_2 and H_2O: A ReaxFF reactive molecular dynamics study, Part I. *J. Phys. Chem. C* **2012**, *116*, 16111–16121. [CrossRef]
36. Wyckoff, R.W. *Crystal Structures*; Interscience Publishers: New York, NY, USA, 1963; p. 1.
37. Swanson, H.E.; Tatge, E.; Fuyat, R.K. *Standard X-ray Diffraction Powder Patterns*; US Government Publishing Office: Washington, DC, USA, 1953.
38. Kasper, J.S.; Richards, S.M. The crystal structures of new forms of silicon and germanium. *Acta Crystallogr.* **1964**, *17*, 752–755. [CrossRef]
39. Nieuwenkamp, W. Die Kristallstruktur des Tief-Cristobalits SiO_2. *Z. Krist. Cryst. Mater.* **1935**, *92*, 82–88. [CrossRef]
40. Sanz-Navarro, C.F.; Åstrand, P.O.; Chen, D.; Rønning, M.; van Duin, A.C.T.; Jacob, T.; Goddard, W.A. Molecular dynamics simulations of the interactions between platinum clusters and carbon platelets. *J. Phys. Chem. A* **2008**, *112*, 1392–1402. [CrossRef] [PubMed]
41. Murnaghan, F.D. The compressibility of media under extreme pressures. *Proc. Natl. Acad. Sci. USA* **1944**, *30*, 244–247. [CrossRef]
42. Birch, F. Finite strain isotherm and velocities for single-crystal and polycrystalline NaCl at high pressures and 300 K. *J. Geophys. Res. Solid Earth* **1978**, *83*, 1257–1268. [CrossRef]
43. Colonna, F.; Fasolino, A.; Meijer, E.J. High-pressure high-temperature equation of state of graphite from Monte Carlo simulations. *Carbon* **2011**, *49*, 364–368. [CrossRef]
44. Holmes, N.C.; Moriarty, J.A.; Gathers, G.R.; Nellis, W.J. The equation of state of platinum to 660 GPa (6.6 Mbar). *J. Appl. Phys.* **1989**, *66*, 2962–2967. [CrossRef]
45. Chen, B.; Penwell, D.; Kruger, M.B. The compressibility of nanocrystalline nickel. *Solid State Commun.* **2000**, *115*, 191–194. [CrossRef]
46. Tian, Y.; Du, J.; Han, W.; Zu, X.; Yuan, X.; Zheng, W. Thermal conductivity of vitreous silica from molecular dynamics simulations: The effects of force field, heat flux and system size. *J. Chem. Phys.* **2017**, *146*, 054504. [CrossRef] [PubMed]
47. Bernstein, N.; Mehl, M.J.; Papaconstantopoulos, D.A.; Papanicolaou, N.I.; Bazant, M.Z.; Kaxiras, E. Energetic, vibrational, and electronic properties of silicon using a nonorthogonal tight-binding model. *Phys. Rev. B* **2000**, *62*, 4477–4487. [CrossRef]
48. Liu, L. Bulk moduli of SiO_2 polymorphs: Quartz, coesite and stishovite. *Mech. Mater.* **1993**, *14*, 283–290. [CrossRef]
49. Mashreghi, A. Determining the volume thermal expansion coefficient of TiO_2 nanoparticle by molecular dynamics simulation. *Comput. Mater. Sci.* **2012**, *62*, 60–64. [CrossRef]
50. Bolz, R.E. *CRC Handbook of Tables for Applied Engineering Science*; CRC Press:Boca Raton, FL, USA, 1973.
51. Kollie, T.G. Measurement of the thermal-expansion coefficient of nickel from 300 to 1000 K and determination of the power-law constants near the Curie temperature. *Phys. Rev. B* **1977**, *16*, 4872. [CrossRef]

52. Chantrenne, P.; Barrat, J.L. Finite size effects in determination of thermal conductivities: Comparing molecular dynamics results with simple models. *J. Heat Transf.* **2004**, *126*, 577–585. [CrossRef]
53. Stackhouse, S.; Stixrude, L. Theoretical methods for calculating the lattice thermal conductivity of minerals. *Rev. Mineral. Geochem.* **2010**, *71*, 253–269. [CrossRef]
54. Zhou, X.W.; Aubry, S.; Jones, R.E.; Greenstein, A.; Schelling, P.K. Towards more accurate molecular dynamics calculation of thermal conductivity: Case study of GaN bulk crystals. *Phys. Rev. B* **2009**, *79*, 115201. [CrossRef]
55. Heino, P.; Ristolainen, E. Thermal conduction at the nanoscale in some metals by MD. *Microelectron. J.* **2003**, *34*, 773–777. [CrossRef]
56. Chen, G. *Nanoscale Energy Transport and Conversion: A Parallel Treatment of Electrons, Molecules, Phonons, and Photons*; Oxford University Press: Oxford, UK, 2005.
57. Dames, C.; Chen, G. Theoretical phonon thermal conductivity of Si/Ge superlattice nanowires. *J. Appl. Phys.* **2004**, *95*, 682–693. [CrossRef]
58. Lide, D.R. *CRC Handbook of Chemistry and Physics*; CRC Press: Boca Raton, FL, USA, 2003.
59. Berendsen, H.J.C. *A Student's Guide to Data and Error Analysis*; Cambridge University Press: Cambridge, UK, 2011.
60. Islam, M.M.; Kolesov, G.; Verstraelen, T.; Kaxiras, E.; van Duin, A.C. eReaxFF: A pseudoclassical treatment of explicit electrons within reactive force field simulations. *J. Chem. Theory Comput.* **2016**, *12*, 3463–3472. [CrossRef] [PubMed]
61. Tromp, R.; Rubloff, G.W.; Balk, P.; LeGoues, F.K.; van Loenen, E.J. High-Temperature SiO_2 Decomposition at the SiO_2/Si Interface. *Phys. Rev. Lett.* **1985**, *55*, 2332. [CrossRef] [PubMed]
62. Hopcroft, M.A.; Nix, W.D.; Kenny, T.W. What is the Young's Modulus of Silicon? *J. Microelectromech. Syst.* **2010**, *19*, 229–238. [CrossRef]
63. Rahnamoun, A.; van Duin, A.C.T. Reactive Molecular Dynamics Simulation on the Disintegration of Kapton, POSS Polyimide, Amorphous Silica, and Teflon during Atomic Oxygen Impact Using the Reaxff Reactive Force-Field Method. *J. Phys. Chem. A* **2014**, *118*, 2780–2787. [CrossRef]

nanomaterials

MDPI

Article

Investigation of the Impact of Cross-Polymerization on the Structural and Frictional Properties of Alkylsilane Monolayers Using Molecular Simulation

Jana E. Black [1], Andrew Z. Summers [1], Christopher R. Iacovella [1], Peter T. Cummings [1] and Clare McCabe [2,*]

[1] Department of Chemical and Biomolecular Engineering, Vanderbilt University, Nashville, TN 37235, USA; jana.black@vanderbilt.edu (J.E.B.); andrew.z.summers@vanderbilt.edu (A.Z.S.); christopher.r.iacovella@vanderbilt.edu (C.R.I.); peter.cummings@vanderbilt.edu (P.T.C.)

[2] Department of Chemical and Biomolecular Engineering and Department of Chemistry, Vanderbilt University, Nashville, TN 37235, USA

* Correspondence: c.mccabe@vanderbilt.edu; Tel.: +1-615-322-6853

Received: 15 March 2019; Accepted: 12 April 2019; Published: 19 April 2019

Abstract: Cross-linked chemisorbed *n*-alkylsilane ($CH_3(CH_2)_{n-1}Si(OH)_3$) monolayers on amorphous silica surfaces have been studied and their structural properties and frictional performance were compared to those of equivalent monolayers without cross-linkages. The simulations isolated for the first time the effects of both siloxane cross-linkages and the fraction of chains chemisorbed to the surface, providing insight into a longstanding fundamental question in the literature regarding molecular-level structure. The results demonstrate that both cross-linkages and the fraction of chemisorbed chains affect monolayer structure in small but measurable ways, particularly for monolayers constructed from short chains; however, these changes do not appear to have a significant impact on frictional performance.

Keywords: molecular dynamics; tribology; surface science; self-assembled monolayers; cross-polymerization; adsorption; chemisorption; physisorption

1. Introduction

Micro- and nanoelectromechanical systems (MEMSs and NEMSs) have been used to develop smaller and more efficient sensors to detect chemical signals, stresses, vibrations, and forces at the atomic level [1,2]; examples include tips and cantilever beams in atomic force microscopy [3] and inertial navigation system accelerometers and gyroscopes [4]. MEMS/NEMS devices have small lateral dimensions and therefore large surface-area-to-volume ratios, which can result in significant surface interactions (e.g., adhesion and friction) that can lead to surface damage and eventual device failure [2,5,6]. An effective method to protect and lubricate contacting surfaces in such devices is to employ chemisorbed or physisorbed monolayers, which provide dense, two-dimensional sheets of surface-bound films that modify interfacial properties and reduce the risk of direct contact between surfaces [7–12]. The tribological properties of monolayer-coated surfaces primarily depend on the structure of the monolayer itself, which can be tailored by manipulating the composition of the precursor molecules (i.e., monomers) and/or the structure of the underlying surface [13–16]. Different types of monolayers assembled on a wide variety of surfaces have been shown to reduce static friction (i.e., stiction) and surface damage due to oxidation and wear [9–12].

Many MEMS/NEMS devices are fabricated from oxidized silicon (SiO_2) [11,17,18], and interest in lubrication schemes for such devices has led to numerous studies on the tribological behavior of organosilane monolayers, as they can bond to oxidized surfaces [17,19–27]. The most commonly used

organosilane molecules are monoalkylsilanes ($RSiX_3$, where "R" is a linear alkyl group and "X" is a hydrolyzable leaving group) [28]. The hydrolysis rate of "X" is known to play a significant role in both the formation and final structure of the monolayers. For example, Naik et al. compared monolayers constructed from octadecylsilane molecules with chloro, methoxy, and ethoxy leaving groups (i.e., $CH_3(CH_2)_{16}CH_2–SiX_3$, where "X" is Cl, OCH_3, or OCH_2CH_3); the trichloroalkylsilanes rapidly formed a densely packed, highly organized monolayer, whereas the other two monolayers remained sparse and disorganized following much longer immersion times [29]. The difference was primarily attributed to the much faster hydrolysis rate of Cl, as compared with methoxy and ethoxy groups. Note that high packing densities are crucial to the tribological performance of alkylsilane monolayers, and so they are generally prepared using trichloroalkylsilane monomers [9,17,19–21].

Although the exact mechanism by which alkylsilanes are adsorbed onto oxidized surfaces remains unclear, the most widely accepted model is illustrated in Figure 1 [28]. In the presence of water, alkylsilanes are hydrolyzed to form alkylsilanols, which react with each other to form Si–O–Si (siloxane) linkages and also with surface-bound hydroxyl groups via condensation reactions that release water. Although described sequentially, two or more of these steps may occur through a concerted mechanism [28]. Monolayer formation is thought to follow an "island growth" mechanism, whereby the first monomers that bond to the surface, the mobility of which is limited by surface attachment and cross-polymerization to neighboring monomers, serve as nucleation sites for the remainder of the monolayer to form [30,31]. This classical model of the reaction mechanism raises two fundamental questions regarding alkylsilane monolayer structure: to what degree do alkylsilanes (1) cross-polymerize via siloxane linkages and (2) form covalent bonds to surface-bound hydroxyl groups?

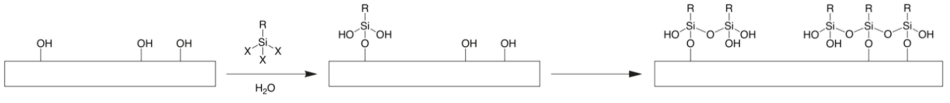

Figure 1. Proposed mechanism by which monoalkylsilanes ($RSiX_3$, where "R" is a linear alkyl group and "X" is a hydrolyzable leaving group) are adsorbed onto oxidized surfaces (e.g., silica, titania, and alumina). Although described sequentially, two or more of these steps may occur through a concerted mechanism as described in Ref. [28].

Alkylsilane monolayer stability and robustness are generally attributed to cross-polymerization via the siloxane linkages [30,32–39]. The degree to which alkylsilanes cross-polymerize has been previously studied, but the results are difficult to interpret because they appear to pose conflicting requirements on monolayer structure. Data obtained using several different methods (e.g., X-ray photoelectron spectroscopy [39], X-ray scattering [40], nuclear magnetic resonance [41], and infrared spectroscopy [29,40–45]) suggest that extensive cross-polymerization occurs; it is estimated that each monomer forms an average of ~1.5–2 siloxane linkages to other monomers [41]. The length of Si–O siloxane bonds varies between ~1.59 and 1.65 Å, so the largest possible distance between two Si atoms connected via a siloxane linkage is ~3.3 Å [40,46,47]. However, the average distance between neighboring monomers in densely packed alkylsilane monolayers is observed to be ~4.5 Å [47]. Note that parallel linear alkanes must be separated by a minimum distance of ~4.2 Å due to steric hindrance [48], so only minimal tilting/bending of the alkyl "R" groups can occur in dense monolayers. Under these conditions, cross-polymerization via siloxane linkages would be limited to a few small alkylsilane oligomers (two to six monomers) [40]. This apparent discrepancy could be explained if alkylsilane monolayers exist in a state of dynamic equilibrium involving the rapid breakage and reformation of siloxane Si–O bonds; at any instant, the monolayer would consist of monomers and small oligomers with the continuous redistribution of siloxane linkages creating the overall effect of an extensively cross-polymerized monolayer [40,49]. This idea is supported by the unusual observation that alkylsilane polar head groups are highly mobile about their equilibrium in-plane positions, while the alkyl "R" groups form a stable configuration [40]. Plueddemann asserted that continuous Si–O

bond breakage and reformation proceed via hydrolysis/condensation reactions (i.e., the addition/loss of water molecules) [49]; note that a submonolayer amount of water is expected to be physisorbed via hydrogen bonds with alkylsilanol and surface-bound hydroxyl groups [42]. Maoz et al. later proposed an alternate mechanism, where Si–O bonds are continuously redistributed among Si–O–Si (siloxane) and Si–O–H (silanol) groups; in this case, the activation energy required for Si–O bond breakage is thought to be supplied by simultaneous Si–O bond formation [40].

Alkylsilanes may be hydrogen bonded (physisorbed) or covalently bonded (chemisorbed) to the surface via surface-bound hydroxyl groups. Some experimental studies suggest these reactions compete near oxidized surfaces; if the density of surface-bound hydroxyl groups is high, monomers will readily form covalent bonds to the surface, but otherwise, they are more likely to form cross-linkages with other monomers and/or hydrogen bonds with surface oxygen atoms [28,39,43,44,47]. It is difficult to measure the fraction of monomers that become chemisorbed and is even more difficult to control due to the large number of variables involved as well as challenges related to understanding/regulating reactions with water molecules near the surface [37,39,50]. Some of the variables involved include alkylsilane structure (e.g., reactivity of hydrolyzable "X" groups) [28,45], surface structure (e.g., density of surface-bound hydroxyl groups) [28,39], and conditions during monolayer formation (e.g., temperature [41] and amount of water present [28,39]). The fraction of chemisorbed chains is expected to play a role in monolayer structure and durability [37,39,50]. For example, Allara et al. compared octadecylsiloxane monolayers on inert gold substrates to those on oxidized silicon (i.e., SiO_2) featuring a high density of surface-bound hydroxyl groups (~5 OH/nm^2), which are capable of reacting with hydrolyzed alkylsilane monomers. They found monolayers with few or no covalent bonds to the SiO_2 surfaces to be organized, smooth, and uniform (i.e., contain minimal defects), similar to those on gold. Since the reactive hydroxyl groups on amorphous SiO_2 surfaces are randomly distributed, increasing the fraction of monomers bonded to these sites is expected to force the monolayer into an increasingly disordered structure [37]. This study suggests that fully or partially physisorbed monolayers can be decoupled from their underlying surfaces to a degree, allowing for the in-plane lateral reorganization of monomers into a more ordered configuration; chemisorbed monolayer structure, however, is predominantly determined by surface structure. Thus, increasing the fraction of chemisorbed chains may lead to increased coefficients of friction and adhesion, as prior studies have reported a negative correlation between friction and monolayer ordering [16,23–25]. However, covalent bonds anchoring chains to the surface are thought to be necessary for durability/robustness [48], so decreasing the fraction of chemisorbed chains could cause the monolayer to degrade over shorter periods of time. Such behavior was observed by Booth et al., who compared the frictional properties of physisorbed *n*-alkanethiols on gold with chemisorbed *n*-alkylsilanes on oxidized silicon, finding that the physisorbed monolayers exhibited a threefold improvement in coefficient of friction at low normal loads, while the chemisorbed monolayers exhibited significantly improved durability and were able to withstand normal loads at least 30 times larger than those that damaged the physisorbed monolayers [17].

Direct control over surface morphology and decoupling of the numerous factors that influence friction and wear in monolayer systems is nearly impossible through a purely experimental approach. Computational methods, including molecular dynamics (MD) simulations, have emerged as an important tool to probe the molecular-level behavior of nanotribological systems, and recent improvements in computational speed and modeling methods have made simulations that closely mimic experimental systems possible. For example, MD simulations have been applied to improve our understanding of alkylsilane monolayers on oxidized surfaces [14,16,23,24,51–61], providing insight into the effects of various monolayer properties on frictional behavior, including monomer structure (e.g., backbone [14,55] and terminal group [13,16]) and surface structure (e.g., roughness and density of surface-bound hydroxyl groups) [53–55,57,60]. However, the simulations of alkylsilane monolayers performed to date have examined systems without siloxane cross-linkages. Furthermore, most have considered only fully chemisorbed monolayers; notable exceptions include the work of Chandross et al., who studied the behavior of fully and partially physisorbed monolayers under shear

by nanometer-scale tips in order to imitate the process by which atomic force microscopes measure forces between the tip and sample [57–59], and our previous work studying monolayer degradation under shear, in which interfacial Si–O bonds (i.e., those connecting chemisorbed monomers to the surface) were severed at random and the mobility of the broken chains examined [61]. While excluding cross-linkages seems like a reasonable assumption, it introduces an approximation compared to the experimental systems and is often cited as the reason for discrepancies observed in monolayer properties between the simulations and experiments. In its role as a stabilizer, cross-polymerization could potentially influence monolayer structure in measurable ways (e.g., packing density, orientational and/or conformational ordering, monomer tilt, monolayer surface roughness, or number of defects). Furthermore, does any observed effect depend on the fraction of monomers covalently bonded to the surface? For example, physisorbed monolayers can be somewhat decoupled from surfaces [37], possibly enabling cross-polymerization to play a more significant role than in their chemisorbed counterparts. These questions remain unanswered and are of particular concern given that previous studies have reported correlations between alkylsilane monolayers' structural properties and their frictional performance [23,25,53,60].

In an effort to address these fundamental questions regarding alkylsilane monolayer structure and cross-polymerization, we have developed two different simulation procedures to construct fully and partially chemisorbed *n*-alkylsilane ($CH_3(CH_2)_{n-1}Si(OH)_3$) monolayers featuring cross-linkages on amorphous silica surfaces. The structural properties and frictional performance of these cross-polymerized monolayers have been assessed and compared to those of equivalent monolayers without cross-linkages in order to isolate any effects of (1) siloxane cross-linkages and (2) the fraction of chains covalently bonded to the surface.

2. Simulation Methods

2.1. Initialization of Cross-Polymerized Monolayers

As discussed above, most previous simulations of alkylsilane monolayers on silica substrates have considered fully chemisorbed monolayers without siloxane cross-linkages [14,16,23,24,51–56,60]. Comparisons to equivalent cross-polymerized monolayers (i.e., those with all chains covalently bonded to the surface) would isolate any changes to structural properties and/or frictional performance that are directly correlated with cross-linkages. However, cross-polymerization is more likely to affect structure if fewer monomers are bonded to the surface; thus, monolayers in which not all chains are directly chemisorbed must also be considered. Here, two different approaches have been taken to create fully and partially chemisorbed *n*-alkylsilane monolayers featuring cross-linkages on amorphous silica surfaces. The methods used to initialize these systems were developed with the overall goal of creating monolayers that closely match those prepared experimentally. As such, they are essentially different implementations of the same underlying idea, guided by a common philosophy: cross-polymerized monolayers are assembled in a stepwise manner through random processes, restricted only by steric effects. Both methods yield packing densities that are consistent with experimental *n*-alkylsilane monolayers assembled on silica (~4.0–5.0 chains/nm^2) [47,52,62,63], as well as cross-linkages that are consistent with the proposed instantaneous structure of an alkylsilane monolayer in a state of dynamic equilibrium (i.e., small linear or cyclic oligomers of crosslinked monomers (≤6), most of which are dimers and trimers) [40].

2.1.1. Chemisorbed Monolayers

To facilitate direct comparison with previous simulations [14,16,23,24,51–56,60], cross-polymerized alkylsilane monolayers in which all monomers are covalently bonded to the surface have been created. Fully chemisorbed monolayers featuring cross-linkages have been constructed by the procedure summarized in Figure 2. A previously developed synthesis mimetic simulation (SMS) procedure was initially used to generate amorphous silica with a high density of surface-bound hydroxyl groups

and then to attach a chemisorbed alkylsilane monolayer without cross-linkages (see Figure 2a) [60]. The SMS procedure was designed to mimic the postsynthesis processing of silicon wafers with "piranha" solution (H_2SO_4/H_2O_2), which is done in experiments to encourage the chemisorption of alkylsilanes during monolayer formation [23]. The process results in surfaces with atomic-scale surface roughness (root-mean-squared roughness of ~0.13 nm) and a dense layer of surface-bound hydroxyl group bonding sites for chains (~5.8 OH/nm^2); root-mean-squared roughness was estimated by the standard deviation of the positions of oxygen atoms that are part of surface-bound hydroxyl groups in the direction normal to the surface plane (i.e., in the *z*-direction). Monolayers with varying densities (3.9–4.9 chains/nm^2) were then generated by varying the minimum cutoff distance between bonding sites from 2.0 to 2.5 Å and attaching monomers. Full details of the procedure can be found in the original paper [60]. To create the final cross-polymerized monolayers, siloxane (Si–O–Si) linkages were inserted between neighboring monomers (see Figure 2b). Cross-linkages are observed to have a length of ~2.8–3.3 Å [40], so monomers separated by ≤3.3 Å were considered eligible pairs for bonding. Cross-linkages were inserted to connect eligible pairs at random, with the restriction that each monomer can only bond with up to two neighbors. As an example, a system with 96 chains at a density of 4.9 chains/nm^2 is shown in Figure 2b. As can be seen from the figure, its 28 cross-linkages are scattered throughout the monolayer, creating small clusters of linked chains (i.e., 12 dimers, 6 trimers, and 1 linear oligomer of 5 chains). Note that this extent/organization of cross-linkages is consistent with the proposed instantaneous structure of an alkylsilane monolayer in a state of dynamic equilibrium (i.e., small oligomers of cross-linked monomers (≤6), most of which are dimers and trimers) [40].

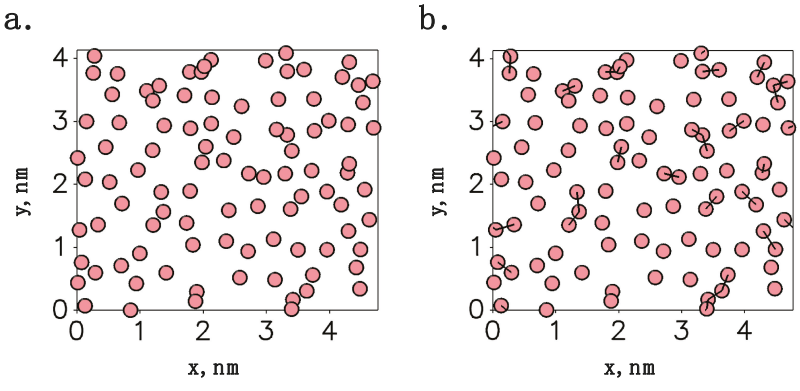

Figure 2. Chemisorbed monolayers with cross-linkages constructed using a two-stage procedure, whereby (**a**) a chemisorbed alkylsilane monolayer without cross-linkages is assembled on an amorphous silica surface with a high density of surface-bound hydroxyl groups (~5.8 OH/nm^2), and (**b**) cross-linkages are inserted at random between neighboring chains in the monolayer. Spheres represent the silicon atoms in alkylsilane head groups. These images and others in this work were generated using the Visual Molecular Dynamics (VMD) software (version 1.9.3, Theoretical and Computational Biophysics Group (University of Illinois at Urbana-Champaign), Urbana, IL, USA) [64].

2.1.2. Partially Chemisorbed Monolayers

As previously mentioned, cross-polymerization may play a more significant role in the behavior of alkylsilane monolayers if fewer monomer chains are bonded to the surface. To examine these effects, an additional set of monolayer systems has been studied in which only a fraction of chains is chemisorbed to the surface, while the remainder are bonded only via cross-linkages to other chains. Recall that these partially chemisorbed monolayers are more common in real systems than fully chemisorbed or physisorbed monolayers as a result of the island growth mechanism by which they form [30,31].

The procedure used to construct these systems features two stages, as shown in Figure 3, and is controlled purely by sterics.

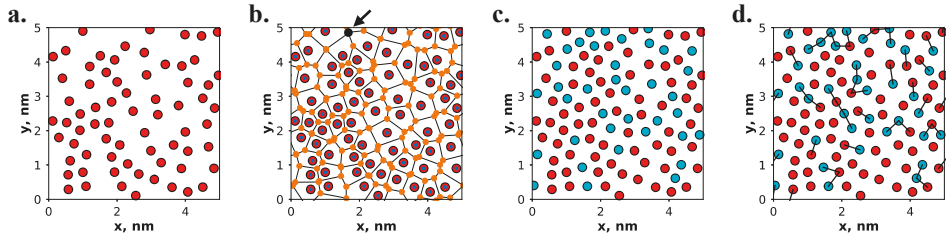

Figure 3. Partially chemisorbed monolayers are constructed using a multistage process whereby (**a**) chemisorbed chains are placed in an arrangement to fill all available surface sites without steric overlaps (using a van der Waals diameter of 0.42 nm per chain [65]), (**b**) Voronoi tessellation is used to determine locations for additional insertion of chains not bound to the surface (the arrow designates the site used for the first chain insertion), and this procedure is repeated until (**c**) no additional available locations exist and the monolayer is considered complete. Finally, (**d**) inserted chains that are not surface bound have bonds drawn to neighboring chains to create a cross-linked network. Red spheres represent the silicon atoms in chemisorbed chains and cyan spheres represent those in chains attached only via cross-linkages.

As with the fully chemisorbed monolayers, amorphous silica substrates were used to construct the partially chemisorbed monolayer systems. Using the mBuild toolkit [66], an analytical method was used to generate amorphous surfaces through carving from a bulk silica slab and adjusting the hydroxyl density to 5 OH/nm^2, to match expectations from experiment [37,39], by bridging neighboring surface oxygen atoms [67,68]. We note that the SMS procedure was not used for the partially chemisorbed monolayer systems since maximizing the density of surface-bound hydroxyl groups is not necessary for these systems, and so a more traditional, less computationally intensive approach to surface generation was taken. This method allows greater control over the initialization of the film structure needed to construct the partially chemisorbed monolayers. Substrates generated using this simpler approach featured a surface roughness of ~0.11 nm, thus closely approximating the structure of the SMS-generated surfaces. The initial stage of monolayer creation, as shown in Figure 3a, involved the placement of the chains that were directly bonded to the surface. Thus, only the discrete locations of surface hydroxyls on the substrate acted as available sites for attaching chains. In an iterative fashion, an available site was chosen at random, a chain was then placed at this location, and the list of available sites was updated to ensure that future chains would not overlap with existing chains. When no available sites remained, the chemisorbed portion of the monolayer was considered complete; however, if a desired number of chemisorbed chains was explicitly specified, then additional chains were added at locations that featured the furthest distance from existing chains. The second stage of monolayer construction, shown in Figure 3b,c, considered the placement of chains that were attached to the surface only through cross-linkages to other chains. To determine the locations for these chains, an iterative procedure was used whereby a 2D Voronoi tessellation was performed on the set of points representing the locations of existing monolayer chains. A new chain was placed at the site of the Voronoi vertex featuring the furthest distance from any existing monolayer chain. This process was repeated until either no locations exist, whereby overlap with existing chains occurred, or a desired total number of monolayer chains was reached. Each newly inserted chain was then attached via a cross-linkage to its nearest neighbor, which may be directly bonded to the surface or via a cross-linkage to another chain. The code used to construct these monolayers is available online (see Supplementary Materials). Constructing alkylsilane monolayers via this procedure yielded an average density of 3.9 ± 0.1 chains/nm^2 which was in close agreement with monolayer densities estimated from experiment (4.0–5.0 chains/nm^2) [47,52,62,63]. Additionally, this procedure resulted in

monolayers featuring roughly 65% chemisorbed chains, with the remaining 35% of chains attached via cross-linkages only. It is of importance to note that the monolayer density of the chemisorbed chains (2.5 chains/nm^2) agreed well with the density observed experimentally for alkanol molecules (which cannot form cross-linkages but feature a comparable van der Waals (VDW) diameter) attached to amorphous silica (2.65 chains/nm^2) [69].

2.2. Molecular Dynamics Simulations

Molecular dynamics simulations of fully and partially chemisorbed alkylsilane monolayers have been performed under equilibrium and nonequilibrium conditions. Postequilibration trajectory lengths ranged from 1–3 ns for equilibrium simulations and 5–10 ns for nonequilibrium simulations. These trajectory lengths were found to be sufficient in order for the simulations to converge to a steady state and to yield data with reasonably low uncertainty. Simulations were conducted using the optimized potentials for liquid simulations all-atom (OPLS-AA) force field [70]. The OPLS-AA parameters used for this work were taken from Lorenz et al. [54] for silica and Jorgensen et al. [70] for alkanes (see Supplementary Materials for details), in accordance with prior simulation studies of alkylsilane monolayers on silica [14,16,23,24,60,61]. All simulations were performed in the canonical, or *NVT*, ensemble (i.e., constant number of atoms, volume, and temperature) at a temperature of 298.15 K, with periodic boundary conditions in the surface plane (i.e., the *xy*-plane) in order to mimic the behavior of an infinite surface; simulations did not interact across the *z*-boundary. Shearing speeds of 10 m/s were used. While this speed is several orders of magnitude larger than those normally used in experiments (e.g., atomic force microscopy and tribometry, where shear rates are typically on the order of micrometers per second [17]), several studies report that shearing velocities of this magnitude and higher do occur between surfaces in nanotribological systems, including MEMSs/NEMSs [6,14,52–55,71]. Furthermore, prior studies have shown that frictional forces do not significantly depend on sliding velocity at moderate loads [14,52–55]. For these simulations, thermostatting was not performed in the direction of shear to allow for the possibility of viscous heating, although appreciable shear-induced heating has not been observed at the shear rates considered here [61]. Additional details regarding the simulation procedures are provided in the Supplementary Materials [72–81].

In order to quantify the structural properties of all monolayer systems considered in this work, the nematic order parameter (S_2), average tilt angle (θ), and gauche defect fraction were calculated under equilibrium and nonequilibrium conditions. The nematic order parameter was used to quantify global orientational ordering in each layer. A value of $S_2 = 1$ indicates perfect orientational ordering within a monolayer, and values of S_2 less than unity represent proportionately less ordering [82,83]. Here, values of S_2 below ~0.8 indicated a distinct loss of orientational ordering, as determined via visual inspection. Note that since these molecules are attached to a surface, the transition from well-ordered to disordered occurs at a higher value of S_2 than is typically seen for bulk nematic systems [83]. Average tilt angle is defined such that monolayers in perfect alignment with a vector normal to the silica surface yield a tilt angle of 0°. Monolayers' gauche defects were assessed via the gauche defect fraction; in this calculation, a dihedral angle (i.e., the twist of a C–C–C–C quadruplet in the monomer backbone) was considered to be in the trans state if it was between 90° and 270°, while angles outside this range were considered to be gauche defects [84]. A detailed description of the calculation of each of these metrics is provided in the Supplementary Materials [82–85]. To quantify frictional performance, the coefficient of friction (μ) and adhesion/force intercept (F_0) were determined for all monolayers undergoing shear. Specifically, μ and F_0 were calculated according to a modified form of Amontons's Law of Friction [20,86,87]:

$$F_f = \mu F_n + F_0 \tag{1}$$

where F_f represents the friction force, F_n represents the normal force, and F_0 represents the extrapolated friction force at zero load, or adhesion/force intercept. Simulations were conducted at several different normal loads, and μ and F_0 were approximated by the slope and *y*-intercept of the line generated by plotting friction force as a function of normal force, respectively.

3. Results and Discussion

To ascertain the impact of cross-polymerization and surface attachment on the structural properties of alkylsilane monolayers, equilibrium simulations have been performed for all systems. The nematic order parameter (S_2), average tilt angle (θ), and gauche defect fraction have been determined as a function of alkylsilane backbone length (6–22 carbon atoms) and compared for monolayers with or without cross-linkages. The results are summarized in Figure 4, with Figure 4a,c,e comparing S_2, θ, and the gauche defect fraction, respectively, for fully chemisorbed monolayers with cross-linkages (see Figure 2b) and identical chemisorbed monolayers without cross-linkages (see Figure 2a). The same comparisons are made in Figure 4b,d,f for partially chemisorbed monolayers with cross-linkages (see Figure 3d) and systems with all chains chemisorbed and no cross-linkages; note that this comparison also features the fraction of chains chemisorbed to the surface as a second variable. The four systems studied are summarized in Table 1. The transition from a disordered, liquid-like state to one that was well-ordered/solid-like occurred when S_2 increased to ~0.8, which was observed for all four monolayer systems as chain length increased from 14 to 16 carbon atoms (see Figure 4a,b). Thus, as highlighted in Figure 4, three chain-length-dependent regions appeared to exist: (I) a liquid-like region (chain length < 14), indicated by lower nematic order and more gauche defects per chain; (II) a transition region (14 ≤ chain length ≤ 16), where monolayers transitioned between liquid-like and solid-like states and may have featured local regions of order (indicated by larger error bars for global monolayer properties); and (III) a solid-like region (chain length > 16), indicated by high values of nematic order and a low number of gauche defects per chain.

As shown in Figure 4a,b, S_2 increased with monomer length for all systems with or without cross-linkages. A positive correlation between monolayer ordering and monomer length has been observed previously in experiments [23–25] and simulations [16,23,24,60]. This trend can be explained by an increase in stabilizing VDW forces between chains as the number of backbone carbon atoms was increased. Our initial expectation was that the addition of cross-linkages would increase orientational ordering, as neighboring monomers connected by siloxane linkages would be forced into closer proximity; furthermore, experimental results suggest that reducing the fraction of monomers that are chemisorbed to the surface also increases global ordering, as nonchemisorbed monomers are not coupled to the locations of surface-bound hydroxyl groups [37]. However, the results shown in Figure 4a,b suggest that both cross-linkages and the ratio of chemisorbed to physisorbed chains play a more complex role in monolayer ordering, which appears to vary as a function of monomer length. Figure 4b shows that the partially chemisorbed monolayers constructed from short chains (region I) had reduced ordering compared with the equivalent chemisorbed monolayers without cross-linkages. Although the same effect is observed in Figure 4a, the differences are not statistically significant, and thus, it is likely related specifically to the fraction of chains chemisorbed to the surface rather than cross-linkages. This observation is surprising, as reducing the number of chemisorbed chains is expected to result in a film that features greater in-plane fluidity (i.e., chains should be better able to rearrange themselves in the surface plane), thus allowing the chains to adopt a more uniform configuration. However, it is also known that the VDW forces that provide cohesiveness to monolayer films are weaker for shorter chains, and it appears that the lack of strong cohesive VDW forces takes precedence over the increase in surface plane mobility when determining monolayer ordering for these systems. In Figure 4b, the curves for partially chemisorbed monolayers and their fully chemisorbed counterparts have different slopes in regions I and II, and as a result, a transition occurs at a chain length of 14, whereby the partially chemisorbed monolayers exhibit higher ordering than their chemisorbed analogues. This phenomenon is not observed in Figure 4a, which once again suggests that it was related to the increase in surface plane mobility when fewer monomers were chemisorbed to the surface; at chain lengths of 14–16 (region II), the cohesive VDW forces were then strong enough that increased mobility did in fact lead to a more ordered monolayer. Figure 4a suggests that fully chemisorbed monolayers with cross-linkages were slightly less ordered than those without them for all chain lengths below 18 (regions I and II), which may have been due to the fact that

Si–O–Si cross-linkages were too short to allow the aliphatic tails to be parallel without overlapping; as a result, chains connected by cross-linkages would tilt or bend/twist away from each other, causing their tails to be splayed apart and leading to a slightly more disordered monolayer. As chain length increased to 18 and above (region III), all monolayer systems described in Figure 4a,b existed in a highly ordered, solid-like state ($S_2 > 0.95$), where neither cross-linkages nor the fraction of chemisorbed chains appeared to have a significant influence on nematic ordering.

Figure 4c,d indicate that there is a correlation between alkylsilane backbone length and average tilt angle, where θ is minimized for systems with intermediate monomer lengths just below the transition from a disordered to well-ordered state (10–14). This observation can be explained by referring back to the results for S_2 (Figure 4a,b). Monolayers with the shortest chain length of 6 backbone carbon atoms existed in a highly disordered state, where chains were allowed to adopt various tilted conformations with no preferred orientation. As chain length increased to 14, the cohesive VDW forces became stronger and caused the chains to stand more upright. When chain length exceeded 14, the chains once again adopted tilted conformations, except now with a preferred orientation (i.e., chains tilted in the same direction) in order to maximize film cohesivity. The inclusion of cross-linkages appeared to increase the average tilt angle at all chain lengths by ~1°–5° in chemisorbed monolayers (Figure 4c) and ~1°–10° in partially chemisorbed monolayers (Figure 4d). Since this effect is more pronounced in Figure 4d, it is likely related to both cross-linkages and the fraction of chains chemisorbed to the surface. Adding cross-linkages may have led to an increase in overall tilt because cross-linked chains must tilt away from each other to prevent their tails from overlapping, as previously mentioned. Any further increase in θ when fewer chains were bonded directly to the surface was likely related to the mobility of the nonchemisorbed chains in the surface plane.

Figure 4e,f suggest that all of the monolayer systems with or without cross-linkages featured most C–C–C–C dihedrals in the trans state, with only a few gauche defects. This observation is consistent with experimental results for densely packed alkylsilane monolayers on silica (≤4% gauche defects) [35,69]. The number of defects appeared to decrease with increasing chain length, a trend that has been observed previously in experiments [69] and simulations [51,52]. This effect can be explained by once again referring to the results for S_2 (Figure 4a,b). Monolayers with short chain lengths existed in a disordered state (region I), allowing both monomer tilting and gauche distortions (i.e., twisting about the C–C bond axis) to occur more easily. As chain length was increased and the monolayer became more well-ordered, fewer defects were able to form. The presence of cross-linkages did not appear to have a meaningful impact on the gauche defect fraction for systems in which all chains were chemisorbed to the surface (Figure 4e). Recall that adding cross-linkages to chemisorbed monolayers led to a small increase in average tilt angle at all chain lengths (Figure 4c). These results combined may indicate that cross-linked chains prefer to tilt away from each other rather than contort via gauche deformations when avoiding overlaps between their aliphatic tails. Partially chemisorbed monolayers constructed from chains with less than 14 backbone carbon atoms (region I) had a larger number of gauche defects than equivalent chemisorbed monolayers without cross-linkages (Figure 4f); this result is somewhat expected, given that the partially chemisorbed monolayer systems in region I also exhibited reduced nematic ordering (Figure 4b). The effect is most likely related to the fraction of chains bonded to the surface rather than cross-linkages (as it is not observed in Figure 4e), and more specifically, to the mobility of nonchemisorbed chains in the surface plane. Chains that are not directly coupled to bonding sites on the surface can more easily tilt and/or contort via gauche deformations, as discussed previously.

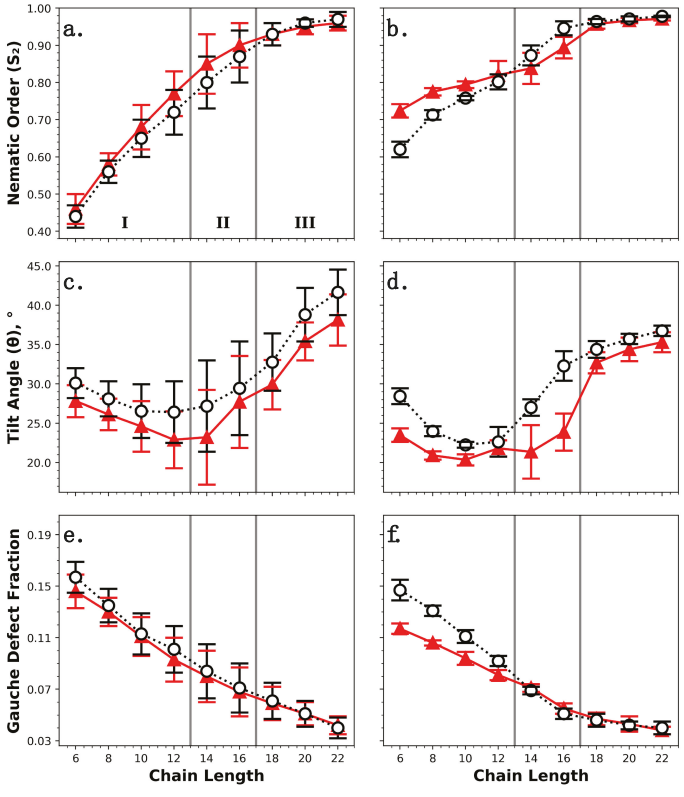

Figure 4. Structural properties of monolayers with or without cross-linkages (black circles and red triangles, respectively) as a function of chain length; the three chain-length-dependent regions described in the text are indicated by I, II, and III. Fully chemisorbed monolayers with or without cross-linkages are compared in (**a**,**c**,**e**) (error bars represent the standard deviation for three unique monolayer systems), and partially chemisorbed monolayers featuring cross-linkages are compared to equivalent fully chemisorbed monolayers without them in (**b**,**d**,**f**) (error bars represent the standard deviation for five unique monolayer systems). Structure was assessed via nematic order parameter (S_2) (**a**,**b**), average tilt angle (θ) (**c**,**d**), and gauche defect fraction (**e**,**f**). Lines connecting data points are provided only to guide the eye. This plot and the others included in this work were generated using the python plotting library matplotlib [88].

To assess the tribological impact of cross-linkages within alkylsilane monolayers, nonequilibrium molecular dynamics simulations have been performed to examine the frictional performance and structural properties of monolayers under shear. As discussed previously, experimental studies have attributed alkylsilane monolayers' tribological performance (i.e., robustness under harsh conditions and ability to protect underlying surfaces from damage) to their capacity to form strong covalent bonds with both the surface and each other [17,19]. The coefficient of friction (μ) and force intercept (F_0) have been calculated via Equation (1) to quantify frictional performance, and the nematic order parameter (S_2) and tilt angle (θ) have been calculated to assess structural properties; these metrics are again determined as a function of alkylsilane backbone length (6–22) and compared for monolayers with or without cross-linkages. The results are summarized in Figure 5. Chemisorbed monolayers with cross-linkages (see Figure 2b) are compared to identical chemisorbed monolayers without them (see Figure 2a) in Figure 5a,c,e,g, while partially chemisorbed monolayers with cross-linkages (see

Figure 3d) are compared to fully chemisorbed systems without cross-linkages in Figure 5b,d,f,h; once again, note that this comparison also features the fraction of chains chemisorbed to the surface as a second variable.

These results presented for the coefficient of friction (Figure 5a,b) and force intercept (Figure 5c,d) suggest that neither cross-linkages nor the fraction of chemisorbed/physisorbed chains play a noticeable role in frictional performance, as both the chemisorbed (Figure 5a,c) and partially chemisorbed (Figure 5b,d) monolayer systems yielded similar results compared with their analogues without cross-linkages. Partially chemisorbed monolayers did appear to yield slightly higher force intercepts than their chemisorbed counterparts without cross-linkages, but this result was not statistically significant at most chain lengths (Figure 5d). The results presented here suggest that excluding cross-linkages, as was done in prior simulations of alkylsilane monolayers, is a reasonable assumption, at least at short time scales; however, we note that both cross-linkages and covalent surface attachment are expected to play a more important role in frictional performance over longer periods of time than can be considered by simulation, especially under conditions that facilitate degradation and wear.

Figure 5a,b show that μ decreased with monomer chain length for all systems with or without cross-linkages, while Figure 5c,d show that F_0 also generally decreased, with the exception of partially chemisorbed monolayers with six to eight backbone carbon atoms (Figure 5d). Prior experiments [23–25] and simulations [16,23,24,60] have reported that adhesion and friction decrease with increasing chain length, a trend which was attributed to increased cohesivity (and thus a higher degree of ordering) in monolayers constructed from longer chains. This explanation is supported by Figure 5e,f, which show that S_2 increased with chain length for all systems with and without cross-linkages. Recall that a positive correlation between monomer length and S_2 was also observed for monolayer systems at equilibrium (see Figure 4a,b); however, the three chain-length-dependent regions which were present at equilibrium were not observed for the same monolayer systems under shear. S_2 increased under shearing conditions (as compared with equilibrium) for all of the fully chemisorbed monolayers, both with and without cross-linkages, and all partially chemisorbed monolayers except for the C_6 system; this observation is attributable to forced shear alignment of the chains.

Figure 5f indicates that partially chemisorbed monolayers constructed from chain lengths $\leq$ 10 had reduced ordering compared with equivalent chemisorbed systems without cross-linkages; this effect is not observed in Figure 5e, which suggests it is related specifically to the fraction of monomers chemisorbed to the surface and not cross-linkages. A more striking structural difference is visible in Figure 5h; partially chemisorbed monolayers with chain lengths $\leq$ 10 yielded tilt angles that were significantly higher than those of their fully chemisorbed counterparts, where the effect was most pronounced for the shortest backbone chain length of six carbon atoms. Again, this trend is not observed in Figure 5g, so it is likely related to the fraction of chemisorbed chains rather than cross-linkages. For all of the fully chemisorbed monolayer systems with and without cross-linkages shown in Figure 5g,h, the average tilt angle was higher under shearing conditions (as compared with equilibrium) and also increased with chain length; this trend was also observed for all of the partially chemisorbed systems with chain lengths > 10 (Figure 5h). These results seem to suggest a lack of shear alignment for the partially chemisorbed monolayer systems with short chain lengths (6–10), which would also explain the reduced nematic ordering for these systems (Figure 5f).

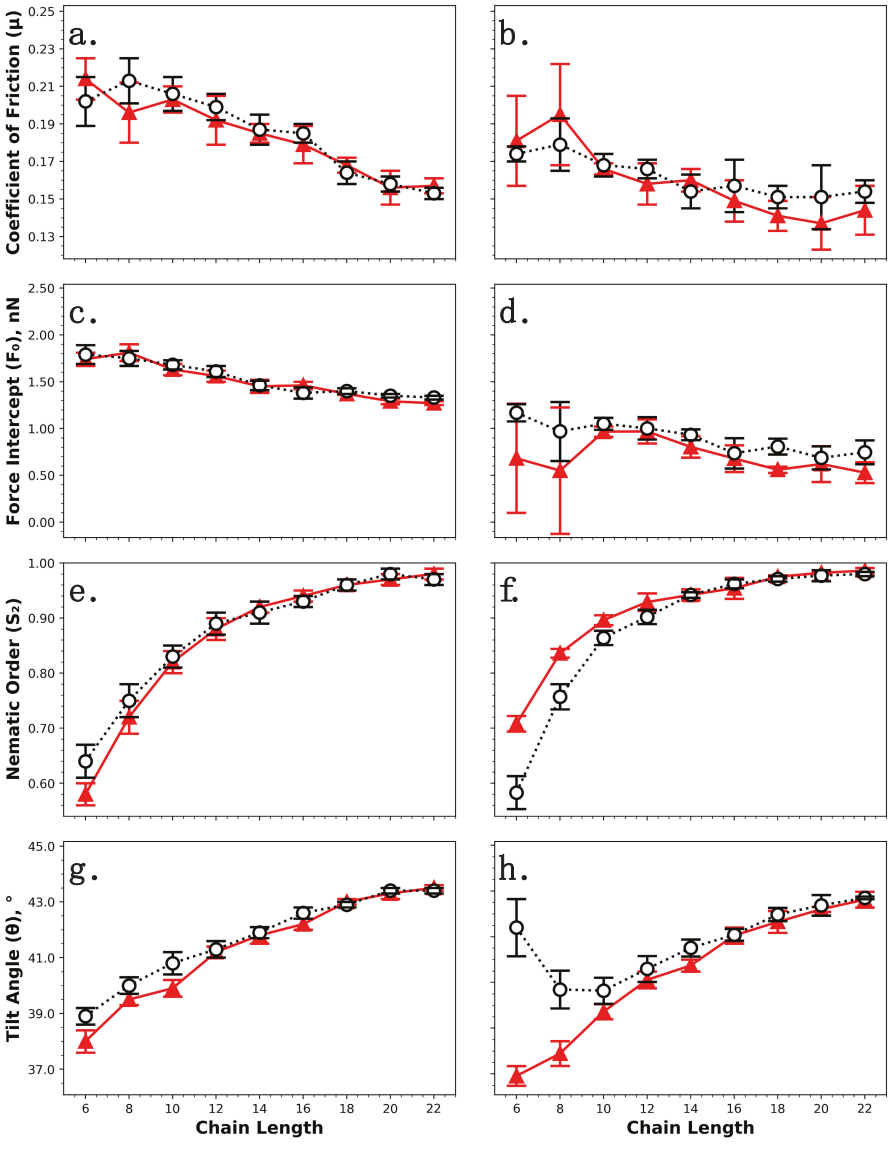

Figure 5. Tribological and structural properties of monolayers with or without cross-linkages (black circles and red triangles, respectively) under shear as a function of chain length. Fully chemisorbed monolayers with or without cross-linkages are compared in (**a**,**c**,**e**,**f**) (error bars represent the standard deviation for three unique monolayer systems), and partially chemisorbed monolayers featuring cross-linkages are compared to equivalent fully chemisorbed monolayers without them in (**b**,**d**,**f**,**h**) (error bars represent the standard deviation for five unique monolayer systems). Tribology is assessed via coefficient of friction (μ) (**a**,**b**) and force intercept (F_0) (**c**,**d**), and structure is assessed via nematic order parameter (S_2) (**e**,**f**) and average tilt angle (θ) (**g**,**h**). Lines connecting data points are provided only to guide the eye.

To further investigate the apparent discrepancy in structure between partially chemisorbed monolayers and their fully chemisorbed counterparts without cross-linkages at short chain lengths (≤10), fully and partially chemisorbed C_6 monolayer systems with varying numbers of cross-linkages have also been studied (Figure 6). We note that it is not possible to create fully chemisorbed monolayers with more than ~0.5 cross-linkages per chain due to the requirements that (1) chemisorbed chains must be coupled to hydroxyl groups on the silica surface that are separated by ≥2.0 Å to avoid steric hindrance [60], and (2) cross-linked chains must be separated by a maximum of 3.3 Å because siloxane (Si–O–Si) linkages are observed to have a length of ~2.8–3.3 Å [40]. As shown in Figure 6a,c, the number of cross-linkages did not appear to have a significant impact on S_2 or θ for C_6 monolayers in which all chains were chemisorbed to the surface; however, some structural differences were observed for the partially chemisorbed C_6 monolayers, as shown in Figure 6b,d. As the number of cross-linkages per chain increased (and thus the fraction of chemisorbed chains decreased), S_2 decreased dramatically and θ increased dramatically. These results combined indicate a lack of shear alignment for partially chemisorbed C_6 monolayers, which becomes more pronounced as the fraction of chains chemisorbed to the surface decreases. The values of S_2 and θ for partially chemisorbed C_6 monolayers reached those of analogous fully chemisorbed monolayers when the fraction of chemisorbed chains exceeded ~0.9 (i.e., the average number of cross-linkages per chain dropped below ~0.1) (see Figure 5b,d); at this point, the monolayers are expected to be in a forced orientation due to shear alignment.

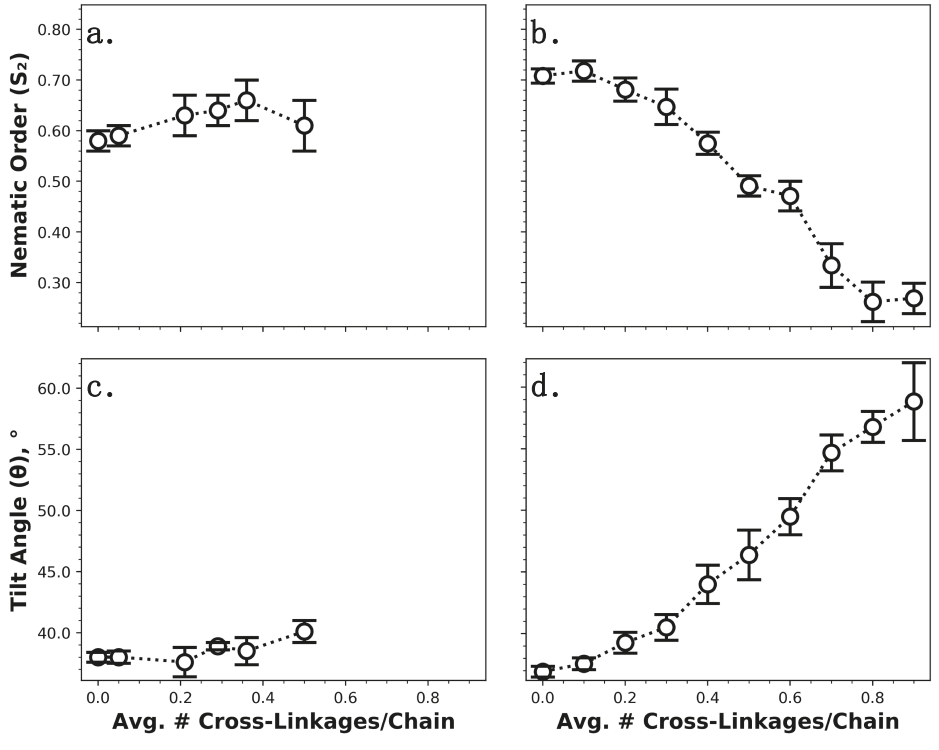

Figure 6. Structural properties of C_6 monolayers under shear as a function of the average number of cross-linkages per chain. Structure was assessed via nematic order parameter (S_2) (**a**,**b**) and average tilt angle (θ) (**c**,**d**). Fully chemisorbed monolayers with cross-linkages are compared in (**a**,**c**) and partially chemisorbed monolayers featuring cross-linkages are compared in (**b**,**d**). Lines connecting data points are provided only to guide the eye.

We note that about two-thirds of the chains in the partially chemisorbed monolayers described previously in Figure 5 were bonded to the surface, so given the results in Figure 6, it seems plausible that decreasing the fraction of chemisorbed chains has little impact on structural properties up to a certain point for monolayers constructed from longer chains (>10 backbone carbon atoms). To examine this idea, partially chemisorbed C_{18} monolayers with varying numbers of cross-linkages have been studied (Figure 7); note that C_{18} monolayers are also more commonly used in experimental systems and applications, as they are more stable and thus better able to reduce stiction and protect surfaces from wear [24,89]. As can be seen from Figure 7, the values of S_2 and θ for these systems reached those of analogous fully chemisorbed monolayers when the fraction of chemisorbed chains exceeded ~0.4 (i.e., the average number of cross-linkages per chain dropped below ~0.6, see Figure 5b,d), a value which was significantly lower than that for the C_6 systems. Furthermore, the overall changes in structure for the C_{18} systems were minimal compared with those in the C_6 systems (an overall spread of ~0.07 in S_2 compared with ~0.46, and ~1° in θ compared with ~22°). These results indicate that reducing the fraction of chains chemisorbed to the surface has a minimal effect on monolayer structure under shear until a certain threshold is reached, after which the chains become increasingly disordered and exhibit increasing average tilt due to a lack of shear alignment; this threshold appears to decrease with increasing chain length, and is below about two-thirds for chain lengths of >10 backbone carbon atoms. For C_{18} systems, which are most industrially relevant [24,89], neither cross-linkages nor the fraction of chemisorbed/physisorbed chains appear to play any significant role in monolayer structure under shearing conditions.

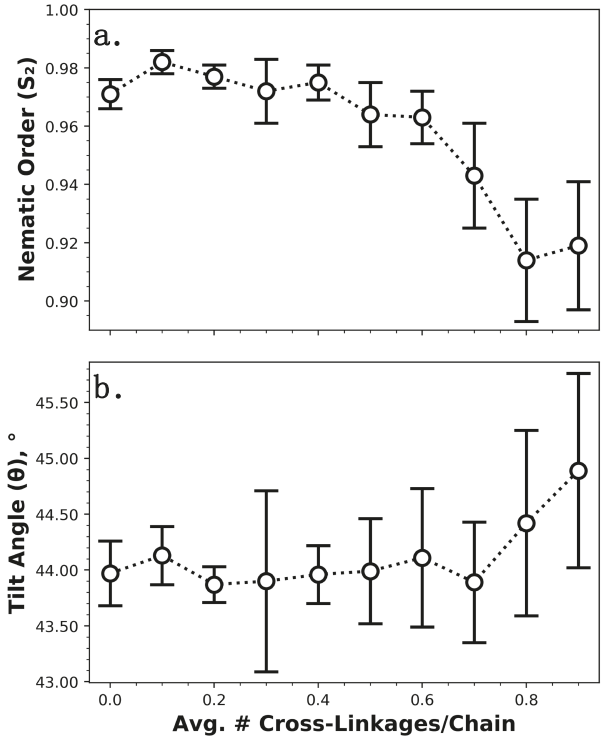

Figure 7. Structural properties of partially chemisorbed C_{18} monolayers under shear as a function of the average number of cross-linkages per chain. Structure was assessed via (**a**) nematic order parameter (S_2) and (**b**) average tilt angle (θ). Error bars represent the standard deviation for five trials (each with a unique monolayer configuration) and lines are provided only to guide the eye.

Table 1. Summary of the key structural properties of the fully and partially chemisorbed monolayer systems studied.

	Cross-Linkages	Average Number Cross-Linkages Per Chain	Fraction of Chemisorbed Chains
Fully Chemisorbed	Yes	0.334 ± 0.024	1.000
	No	0.000	1.000
Partially Chemisorbed	Yes	0.368 ± 0.015	0.632 ± 0.015
	No	0.000	1.000

4. Conclusions

In this work, fully and partially chemisorbed *n*-alkylsilane ($CH_3(CH_2)_{n-1}Si(OH)_3$) monolayers featuring cross-linkages on amorphous silica surfaces have been studied. The structural properties and frictional performance of these cross-polymerized monolayers have been assessed and compared to those of equivalent monolayers without cross-linkages in order to isolate the impact of (1) siloxane cross-linkages and (2) the fraction of chains covalently bonded to the surface.

Equilibrium simulations used to ascertain the effects of cross-polymerization on structural properties showed that both cross-linkages and the ratio of chemisorbed to physisorbed chains affect monolayer structure in small but measurable ways that vary based on chain length. Three chain-length-dependent regions were observed: (I) a liquid-like region (chain length < 14), (II) a transition region (14 ≤ chain length ≤ 16), and (III) a solid-like region (chain length > 16). Fully chemisorbed monolayers with cross-linkages exhibited slightly reduced nematic ordering compared with those without them in regions I and II, likely due to the cross-linked chains tilting or bending/twisting away from each other to prevent overlaps and causing their tails to be splayed apart, leading to a slightly more disordered monolayer. Chemisorbed monolayers with cross-linkages also yielded slightly higher average tilt angles than their counterparts without them, but cross-linkages did not play a meaningful role in the formation of gauche defects. These observations combined suggest that cross-linked chains prefer to tilt away from each other rather than contort via gauche deformations when avoiding overlaps. Partially chemisorbed monolayers in region I exhibited reduced nematic ordering compared with equivalent chemisorbed monolayers without cross-linkages. Albeit surprising, as reducing the number of chemisorbed chains is expected to result in greater in-plane fluidity, the VDW forces that provide monolayer cohesiveness are weaker for shorter chains and appear to take precedence over the increase in surface plane mobility for these systems. The partially chemisorbed monolayers did exhibit higher ordering than their chemisorbed analogues in region II, which suggests that the VDW forces were strong enough for increased mobility to lead to a more ordered monolayer for these systems. Partially chemisorbed monolayers in regions I and II yielded higher tilt angles than their chemisorbed counterparts, and in region I, they also had more gauche defects. These results can likely be explained by the increased mobility of nonchemisorbed chains in the surface plane; chains that are not directly coupled to bonding sites on the surface can more easily tilt into nonupright conformations and/or contort via gauche defects. In region III, all fully and partially chemisorbed monolayer systems with and without cross-linkages existed in a highly ordered state, where neither cross-linkages nor the fraction of chemisorbed chains appeared to have any significant influence on structural properties.

In the nonequilibrium simulations performed, neither cross-linkages nor the fraction of chemisorbed/physisorbed chains were found to play a noticeable role in frictional performance, as both the chemisorbed and partially chemisorbed monolayers yielded similar results for friction and adhesion compared to their analogues without cross-linkages. The results presented here therefore suggest that excluding cross-linkages, as was done in prior simulation studies, is a reasonable assumption at short time scales (i.e., before degradation and wear must be considered). Under shearing conditions, partially chemisorbed monolayers constructed from short chains (≤ 10 backbone carbon atoms) exhibited reduced nematic ordering and significantly increased chain tilt compared with equivalent chemisorbed

systems without cross-linkages. This observation suggests a lack of shear alignment for these systems, which was further investigated by studying partially chemisorbed C_6 and C_{18} monolayers with varying numbers of cross-linkages (and thus varying numbers of chemisorbed/physisorbed chains). These results indicated that decreasing the fraction of chemisorbed chains has little impact on structural properties up until a certain point that depends on chain length. The overall changes in structure for the C_{18} system were observed to be minimal over the entire range of average cross-linkages per chain considered, which indicates that neither cross-linkages nor the fraction of chemisorbed/physisorbed chains play a significant role in the structure of monolayers constructed from long chains under shear.

Supplementary Materials: Tabulated force field parameters (Tables S1 and S2), additional details of the simulation methods, and descriptions of the calculations performed to quantify the structural properties of monolayers (Equations (S1)–(S3)) are available online at http://www.mdpi.com/2079-4991/9/4/639/s1. The code used to construct partially chemisorbed monolayers is available online at https://github.com/summeraz/crosslinked_monolayer.

Author Contributions: J.E.B. and A.Z.S. performed the simulations; all authors conceived and designed the experiments, analyzed the data, and wrote the paper.

Funding: This research was funded by the National Science Foundation (NSF) through Grant ACI-1047828 and OAC-1835874. Jana E. Black also acknowledges funding from the U.S. Department of Education for Graduate Assistance in Areas of National Need (GAANN) Fellowship under Grant P200A090323.

Acknowledgments: Computational resources were provided by the National Energy Research Scientific Computing Center (NERSC), which is supported by the Office of Science of the Department of Energy under Contract DE-AC02-05CH11231.

Conflicts of Interest: The authors declare no conflict of interest.

References

1. Ventra, M.; Evoy, S.; Heflin, J.R. *Introduction to Nanoscale Science and Technology*, 1st ed.; Springer: New York, NY, USA, 2004.
2. Berman, D.; Krim, J. Surface science, MEMS and NEMS: Progress and opportunities for surface science research performed on, or by, microdevices. *Prog. Surf. Sci.* **2013**, *88*, 171–211. [CrossRef]
3. Willemsen, O.H.; Snel, M.M.E.; Cambi, A.; Greve, J.; Grooth, B.G.D.; Figdor, C.G. Biomolecular interactions measured by atomic force microscopy. *Biophys. J.* **2000**, *79*, 3267–3281.
4. Bush, B.G.; Rio, F.W.D.; Jaye, C.; Fischer, D.A.; Cook, R.F. Interfacial mechanical properties of *n*-alkylsilane monolayers on silicon substrates. *J. Microelectromech. Syst.* **2013**, *22*, 34–43. [CrossRef]
5. Maboudian, R. Surface processes in MEMS technology. *Surf. Sci. Rep.* **1998**, *30*, 207–269. [CrossRef]
6. Bhushan, B. Nanotribology and nanomechanics of MEMS/NEMS and BioMEMS/BioNEMS materials and devices. *Microelectron. Eng.* **2007**, *84*, 387–412. [CrossRef]
7. Allen, C.; Drauglis, E. Boundary layer lubrication: Monolayer or multilayer. *Wear* **1969**, *14*, 363–384. [CrossRef]
8. Deng, K.; Collins, R.J.; Mehregany, M.; Sukenik, C.N. Performance Impact of Monolayer Coating of Polysilicon Micromotors. *J. Electrochem. Soc.* **1995**, *142*, 1278–1285. [CrossRef]
9. Srinivasan, U.; Houston, M.R.; Howe, R.T.; Maboudian, R. Alkyltrichlorosilane-based self-assembled monolayer films for stiction reduction in silicon micromachines. *J. Microelectromech. Syst.* **1998**, *7*, 252–260. [CrossRef]
10. Maboudian, R.; Ashurst, W.R.; Carraro, C. Self-assembled monolayers as anti-stiction coatings for MEMS: Characteristics and recent developments. *Sens. Actuators* **2000**, *82*, 219–223.
11. Maboudian, R.; Ashurst, W.R.; Carraro, C. Tribological challenges in micromechanical systems. *Tribol. Lett.* **2002**, *12*, 95–100. [CrossRef]
12. Bhushan, B.; Liu, H. Micro/nanoscale tribological and mechanical characterization for MEMS/NEMS. *Proc. SPIE* **2004**, *5392*, 1–13.
13. Park, B.; Lorenz, C.D.; Chandross, M.; Stevens, M.J.; Grest, G.S. Frictional dynamics of fluorine-terminated alkanethiol self-assembled monolayers. *Langmuir* **2004**, *20*, 10007–10014. [CrossRef] [PubMed]
14. Lewis, J.B.; Vilt, S.G.; Rivera, J.L.; Jennings, G.K.; McCabe, C. Frictional properties of mixed fluorocarbon/hydrocarbon silane monolayers: A simulation study. *Langmuir* **2012**, *28*, 14218–14226. [CrossRef]

15. Kasai, T.; Bhushan, B.; Kulik, G.; Barbieri, L.; Hoffmann, P. Micro/nanotribological study of perfluorosilane SAMs for antistiction and low wear. *J. Vac. Sci. Technol. B* **2005**, *23*, 995–1003. [CrossRef]
16. Rivera, J.L.; Jennings, G.K.; McCabe, C. Examining the frictional forces between mixed hydrophobic-hydrophilic alkylsilane monolayers. *J. Chem. Phys.* **2012**, *136*, 244701. [CrossRef] [PubMed]
17. Booth, B.D.; Vilt, S.G.; McCabe, C.; Jennings, G.K. Tribology of monolayer films: Comparison between *n*-alkanethiols on gold and *n*-alkyl trichlorosilanes on silicon. *Langmuir* **2009**, *25*, 9995–10001. [CrossRef]
18. Merlijn van Spengen, W. MEMS reliability from a failure mechanisms perspective. *Microelectron. Reliab.* **2003**, *43*, 1049–1060. [CrossRef]
19. Bhushan, B.; Kasai, T.; Kulik, G.; Barbieri, L.; Hoffmann, P. AFM study of perfluoroalkylsilane and alkylsilane self-assembled monolayers for antistiction in MEMS/NEMS. *Ultramicroscopy* **2005**, *105*, 176–188. [CrossRef]
20. Clear, S.C.; Nealey, P.F. Chemical force microscopy study of adhesion and friction between surfaces functionalized with self-assembled monolayers and immersed in solvents. *J. Colloid Interface Sci.* **1999**, *213*, 238–250. [CrossRef] [PubMed]
21. Singh, R.A.; Yoon, E.-S.; Han, H.-G.; Kong, H. Friction behaviour of chemical vapor deposited self-assembled monolayers on silicon wafer. *Wear* **2007**, *262*, 130–137. [CrossRef]
22. Flater, E.E.; Ashurst, W.R.; Carpick, R.W. Nanotribology of octadecyltrichlorosilane monolayers and silicon: Self-mated versus unmated interfaces and local packing density effects. *Langmuir* **2007**, *23*, 9242–9252. [CrossRef] [PubMed]
23. Vilt, S.G.; Leng, Z.; Booth, B.D.; McCabe, C.; Jennings, G.K. Surface and frictional properties of two-component alkylsilane monolayers and hydroxyl-terminated monolayers on silicon. *J. Phys. Chem. C* **2009**, *113*, 14972–14977. [CrossRef]
24. Booth, B.D.; Vilt, S.G.; Lewis, J.B.; Rivera, J.L.; Buehler, E.A.; McCabe, C.; Jennings, G.K. Tribological durability of silane monolayers on silicon. *Langmuir* **2011**, *27*, 5909–5917. [CrossRef] [PubMed]
25. Lio, A.; Charych, D.H.; Salmeron, M. Comparative atomic force microscopy study of the chain length dependence of frictional properties of alkanethiols on gold and alkylsilanes on mica. *J. Phys. Chem. B* **1997**, *101*, 3800–3805. [CrossRef]
26. Escorihuela, J.; Sidharam, P.P.; Zuilhof, H. Organic monolayers by B(C6F5)3-catalyzed siloxanation of oxidized silicon surfaces. *Langmuir* **2017**, *33*, 2185–2193. [CrossRef]
27. Escorihuela, J.; Zuilhof, H. Rapid surface functionalization of hydrogen-terminated silicon by alkyl silanols. *J. Am. Chem. Soc.* **2017**, *139*, 5870–5876. [CrossRef] [PubMed]
28. Arkles, B. Tailoring surfaces with silanes. *Chem. Tech.* **1977**, *7*, 766–778.
29. Naik, V.V.; Städler, R.; Spencer, N.D. Effect of leaving group on the structures of alkylsilane SAMs. *Langmuir* **2014**, *30*, 14824–14831. [CrossRef]
30. Ulman, A. Formation and structure of self-assembled monolayers. *Chem. Rev.* **1996**, *96*, 1533–1554. [CrossRef]
31. Liu, Y.; Wolf, L.K.; Messmer, M.C. A study of alkyl chain conformational changes in self-assembled *n*-octadecyltrichlorosilane monolayers on fused silica surfaces. *Langmuir* **2001**, *17*, 4329–44335. [CrossRef]
32. Sagiv, J. Organized monolayers by adsorption. 1. Formation and structure of oleophobic mixed monolayers on solid surfaces. *J. Am. Chem. Soc.* **1980**, *102*, 92–98. [CrossRef]
33. Ulman, A. Self-assembled monolayers of alkyltrichlorosilanes: Building blocks for future organic materials. *Adv. Mater.* **1990**, *2*, 573–582. [CrossRef]
34. Parikh, A.N.; Allara, D.L.; Azouz, I.B.; Rondelez, F. An intrinsic relationship between molecular structure in self-assembled *n*-alkylsiloxane monolayers and deposition temperature. *J. Phys. Chem.* **1994**, *98*, 7577–7590. [CrossRef]
35. Hoffmann, H.; Mayer, U.; Krischanitz, A. Structure of alkylsiloxane monolayers on silicon surfaces investigated by external reflection infrared spectroscopy. *Langmuir* **1995**, *11*, 1304–1312. [CrossRef]
36. Ge, S.; Takahara, A.; Kajiyama, T. Phase separated morphology of an immobilized organosilane monolayer studied by a scanning probe microscope. *Langmuir* **1995**, *11*, 1341–1346. [CrossRef]
37. Allara, D.L.; Parikh, A.N.; Rondelez, F. Evidence for a unique chain organization in long chain silane monolayers deposited on two widely different solid substrates. *Langmuir* **1995**, *11*, 2357–2360. [CrossRef]
38. Zhao, X.; Kopelman, R. Mechanism of organosilane self-assembled monolayer formation on silica studied by second-harmonic generation. *J. Phys. Chem.* **1996**, *100*, 11014–11018. [CrossRef]
39. Rye, R.R.; Nelson, G.C.; Dugger, M.T. Mechanistic aspects of alkylchlorosilane coupling reactions. *Langmuir* **1997**, *13*, 2965–2972. [CrossRef]

40. Maoz, R.; Sagiv, J.; Degenhardt, D.; Möhwald, H.; Quint, P. Hydrogen-bonded multilayers of self-assembling silanes: Structure elucidation by combined Fourier transform infra-red spectroscopy and X-ray scattering techniques. *Supramol. Sci.* **1995**, *2*, 9–24. [CrossRef]
41. Soliveri, G.; Pifferi, V.; Annunziata, R.; Rimoldi, L.; Aina, V.; Cerrato, G.; Falciola, L.; Cappelletti, G.; Meroni, D. Alkylsilane-SiO_2 hybrids. A concerted picture of temperature effects in vapor phase functionalization. *J. Phys. Chem. C* **2015**, *119*, 15390–15400. [CrossRef]
42. Angst, D.L.; Simmons, G.W. Moisture absorption characteristics of organosiloxane self-assembled monolayers. *Langmuir* **1991**, *7*, 2236–2242. [CrossRef]
43. Tripp, C.P.; Hair, M.L. An infrared study of the reaction of octadecyltrichlorosilane with silica. *Langmuir* **1992**, *8*, 1120–1126. [CrossRef]
44. Tripp, C.P.; Hair, M.L. Direct observation of the surface bonds between self-assembled monolayers of octadecyltrichlorosilane and silica surfaces: A low-frequency IR study at the solid/liquid interface. *Langmuir* **1995**, *11*, 1215–1219. [CrossRef]
45. Naik, V.V.; Crobu, M.; Venkataraman, N.V.; Spencer, N.D. Multiple transmission-reflection IR spectroscopy shows that surface hydroxyls play only a minor role in alkylsilane monolayer formation on silica. *J. Phys. Chem. Lett.* **2013**, *4*, 2745–2751. [CrossRef]
46. Feher, F.J.; Newman, D.A.; Walzer, J.F. Silsesquioxanes as models for silica surfaces. *J. Am. Chem. Soc.* **1989**, *111*, 1741–1748. [CrossRef]
47. Stevens, M.J. Thoughts on the structure of alkylsilane monolayers. *Langmuir* **1999**, *15*, 2773–2778. [CrossRef]
48. Kenn, R.M.; Boehm, C.; Bibo, A.M.; Peterson, I.R.; Moehwald, H.; Als-Nielsen, J.; Kjaer, K. Mesophases and crystalline phases in fatty acid monolayers. *J. Phys. Chem.* **1991**, *95*, 2092–2097. [CrossRef]
49. Mittal, K.L.; Plueddemann, E.P. *Silanes and Other Coupling Agents*, 1st ed.; VSP: Utrecht, The Netherlands, 1992.
50. Tripp, C.P.; Veregin, R.P.N.; McDougall, M.N.V.; Osmond, D. Reaction of alkylchlorosilanes with silica: Importance of a surface attachment in defining the triboelectrification of the modified silica. *Langmuir* **1995**, *11*, 1858–1859. [CrossRef]
51. Mikulski, P.T.; Harrison, J.A. Packing-density effects on the friction of *n*-alkane monolayers. *J. Am. Chem. Soc.* **2001**, *123*, 6873–6881. [CrossRef]
52. Chandross, M.; Grest, G.S.; Stevens, M.J. Friction between alkylsilane monolayers: Molecular simulation of ordered monolayers. *Langmuir* **2002**, *18*, 8392–8399. [CrossRef]
53. Chandross, M.; Web, E.B., III; Stevens, M.J.; Grest, G.S. Systematic study of the effect of disorder on nanotribology of self-assembled monolayers. *Phys. Rev. Lett.* **2004**, *93*, 166103. [CrossRef] [PubMed]
54. Lorenz, C.D.; Web, E.B., III; Stevens, M.J.; Chandross, M.; Grest, G.S. Frictional dynamics of perfluorinated self-assembled monolayers on amorphous SiO_2. *Tribol. Lett.* **2005**, *19*, 93–99. [CrossRef]
55. Lorenz, C.D.; Chandross, M.; Grest, G.S.; Stevens, M.J.; Web, E.B., III. Tribological properties of alkylsilane self-assembled monolayers. *Langmuir* **2005**, *21*, 11744–11748. [CrossRef] [PubMed]
56. Kapila, V.; Deymier, P.A.; Raghavan, S. Molecular dynamics simulations of friction between alkylsilane monolayers. *Modell. Simul. Mater. Sci. Eng.* **2006**, *14*, 283–297. [CrossRef]
57. Chandross, M.; Lorenz, C.D.; Stevens, M.J.; Grest, G.S. Simulations of nanotribology with realistic probe tip models. *Langmuir* **2008**, *24*, 1240–1246. [CrossRef] [PubMed]
58. Lane, J.M.D.; Chandross, M.; Lorenz, C.D.; Stevens, M.J.; Grest, G.S. Water penetration of damaged self-assembled monolayers. *Langmuir* **2008**, *24*, 5734–5739. [CrossRef]
59. Chandross, M.; Lorenz, C.D.; Stevens, M.J.; Grest, G.S. Probe-tip induced damage in compliant substrates. *J. Manuf. Sci. Eng.* **2010**, *132*, 030916. [CrossRef]
60. Black, J.E.; Iacovella, C.R.; Cummings, P.T.; McCabe, C. Molecular dynamics study of alkylsilane monolayers on realistic amorphous silica surfaces. *Langmuir* **2015**, *31*, 3086–3093. [CrossRef] [PubMed]
61. Summers, A.Z.; Iacovella, C.R.; Billingsley, M.R.; Arnold, S.T.; Cummings, P.T.; McCabe, C. Influence of surface morphology on the shear-induced wear of alkylsilane monolayers: Molecular dynamics study. *Langmuir* **2016**, *32*, 2348–2359. [CrossRef] [PubMed]
62. Tidswell, I.M.; Rabedeau, T.A.; Pershan, P.S.; Kosowsky, S.D.; Folkers, J.P.; Whitesides, G.M. X-ray grazing incidence diffraction from alkylsiloxane monolayers on silicon wafers. *J. Chem. Phys.* **1991**, *95*, 2854–2861. [CrossRef]

63. Kojio, K.; Ge, S.; Takahara, A.; Kajiyama, T. Molecular aggregation state of *n*-octadecyltrichlorosilane monolayer prepared at an air/water interface. *Langmuir* **1998**, *14*, 3932–3936. [CrossRef]
64. Humphrey, W.; Dalke, A.; Schulten, K. VMD: Visual molecular dynamics. *J. Mol. Graph.* **1996**, *14*, 33–38. [CrossRef]
65. Kojio, K.; Takahara, A.; Omote, K.; Kajiyama, T. Molecular aggregation state of *n*-octadecyltrichlorosilane monolayers prepared by the langmuir and chemisorption methods. *Langmuir* **2000**, *16*, 3932–3936. [CrossRef]
66. Klein, C.; Sallai, J.; Jones, T.J.; Iacovella, C.R.; McCabe, C.; Cummings, P.T. *Foundations of Molecular Modeling and Simulation*, 1st ed.; Snurr, R.Q., Adjiman, C., Kofke, D.A., Eds.; Molecular Modeling and Simulation; Springer: Singapore, 2016; Chapter A Hierarchical, Component Based Approach to Screening Properties of Soft Matter; pp. 79–92.
67. Zhuravlev, L. The surface chemistry of amorphous silica. Zhuravlev model. *Colloids Surf. A* **2000**, *173*, 1–38. [CrossRef]
68. Hartkamp, R.; Siboulet, B.; Dufrêchec, J.-F.; Coasne, B. Ion-specific adsorption and electroosmosis in charged amorphous porous silica. *Phys. Chem. Chem. Phys.* **2015**, *17*, 24683–24695. [CrossRef]
69. Allara, D.L.; Parikh, A.N.; Judge, E. The existence of structure progressions and wetting transitions in intermediately disordered monolayer alkyl chain assemblies. *J. Chem. Phys.* **1994**, *100*, 1761–1764. [CrossRef]
70. Jorgensen, W.L.; Maxwell, D.S.; Tirado-Rives, J. Development and testing of the OPLS all-atom force field on conformational energetics and properties of organic liquids. *J. Am. Chem. Soc.* **1996**, *118*, 11225–11236. [CrossRef]
71. Transition to Advanced Format 4K Sector Hard Drives. Available online: https://www.seagate.com/tech-insights/advanced-format-4k-sector-hard-drives-master-ti/ (accessed on 2 February 2018).
72. Plimpton, S. Fast parallel algorithms for short-range molecular dynamics. *J. Comput. Phys.* **1995**, *117*, 1–19. [CrossRef]
73. Nosé, S. A unified formulation of the constant temperature molecular dynamics methods. *J. Chem. Phys.* **1984**, *81*, 511–519. [CrossRef]
74. Hoover, W.G. Canonical dynamics: Equilibrium phase-space distributions. *Phys. Rev. A* **1985**, *31*, 1695–1697. [CrossRef]
75. Klein, C.; Summers, A.Z.; Thompson, M.W.; Gilmer, J.; McCabe, C.; Cummings, P.T.; Sallai, J.; Iacovella, C.R. Formalizing atom-typing and the dissemination of force fields with foyer. *Comput. Mater. Sci.* **2018**, arXiv:1812.06779.
76. Abraham, M.J.; Murtola, T.; Schulz, R.; Páll, S.; Smith, J.C.; Hess, B.; Lindahl, E. GROMACS: High performance molecular simulations through multi-level parallelism from laptops to supercomputers. *SoftwareX* **2015**, *1–2*, 19–25. [CrossRef]
77. Hess, B.; Bekker, H.; Berendsen, H.J.C.; Fraaije, J.G.E.M. LINCS: A linear constraint solver for molecular simulations. *J. Comput. Chem.* **1998**, *18*, 1463–1472. [CrossRef]
78. Hockney, R.W.; Goel, S.P.; Eastwood, J.W. Quiet high-resolution computer models of a plasma. *J. Comput. Phys.* **1974**, *14*, 148–158. [CrossRef]
79. Darden, T.; York, D.; Pedersen, L. Particle mesh Ewald: An $N\cdot\log(N)$ method for Ewald sums in large systems. *J. Chem. Phys.* **1993**, *98*, 10089–10092. [CrossRef]
80. Essmann, U.; Perera, L.; Berkowitz, M.L. A smooth particle mesh Ewald method. *J. Chem. Phys.* **1995**, *103*, 8577–8593. [CrossRef]
81. Adorf, C.S.; Dodd, P.M.; Ramasubramani, V.; Glotzer, S.C. Simple data and workflow management with the signac framework. *Comput. Mater. Sci.* **2018**, *146*, 220–229. [CrossRef]
82. Eppenga, R.; Frenkel, D. Monte Carlo study of the isotropic and nematic phases of infinitely thin hard platelets. *Mol. Phys.* **1984**, *52*, 1303–1334. [CrossRef]
83. Wilson, M.R. Determination of order parameters in realistic atom-based models of liquid crystal systems. *J. Mol. Liq.* **1996**, *68*, 23–31. [CrossRef]
84. Knippenberg, M.T.; Mikulski, P.T.; Harrison, J.A. Effects of tip geometry on interfacial contact forces. *Model. Simul. Mater. Sci. Eng.* **2010**, *18*, 1–20. [CrossRef]
85. Blondel, A.; Karplus, M. New formulation for derivatives of torsion angles and improper torsion angles in molecular mechanics: Elimination of singularities. *J. Comput. Chem.* **1996**, *17*, 1132–1141. [CrossRef]
86. Bhushan, B. (Ed.) *Handbook of Micro/Nanotribology*, 2nd ed.; Mechanics and Materials Science; CRC Press: Boca Raton, FL, USA, 1998.

87. Schwarz, U.D.; Allers, W.; Gensterblum, G.; Wiesendanger, R. Low-load friction behavior of epitaxial C_{60} monolayers under Hertzian contact. *Phys. Rev. B* **1995**, *52*, 14976–14984. [CrossRef]
88. Hunter, J.D. Matplotlib: A 2D graphics environment. *Comput. Sci. Eng.* **2007**, *9*, 90–95. [CrossRef]
89. Ruehe, J.; Novotny, V.J.; Kanazawa, K.K.; Clarke, T.; Street, G.B. Structure and tribological properties of ultrathin alkylsilane films chemisorbed to solid surfaces. *Langmuir* **1993**, *9*, 2383–2388. [CrossRef]

nanomaterials

MDPI

Article

Raman Study of Strain Relaxation from Grain Boundaries in Epitaxial Graphene Grown by Chemical Vapor Deposition on SiC

Laiyuan Chong, Hui Guo *, Yuming Zhang, Yanfei Hu * and Yimen Zhang

The State Key Discipline Laboratory of Wide Band Gap Semiconductor Technology, School of Microelectronics, Xidian University, Xi'an 710071, China; chonglaiyuan@163.com (L.C.); zhangym@xidian.edu.cn (Y.Z.); ymzhang@xidian.edu.cn (Y.Z.)

* Correspondence: guohui@mail.xidian.edu.cn (H.G.); huyanfei@xidian.edu.cn (Y.H.)

Received: 27 January 2019; Accepted: 1 March 2019; Published: 5 March 2019

Abstract: Strains in graphene play a significant role in graphene-based electronics, but many aspects of the grain boundary effects on strained graphene remain unclear. Here, the relationship between grain boundary and strain property of graphene grown by chemical vapor deposition (CVD) on the C-face of SiC substrate has been investigated by Raman spectroscopy. It is shown that abundant boundary-like defects exist in the graphene film and the blue-shifted 2D-band frequency, which results from compressive strain in graphene film, shifts downward linearly as $1/L_a$ increases. Strain relaxation caused by grain boundary diffusion is considered to be the reason and the mechanism is analyzed in detail.

Keywords: Raman; strain relaxation; grain boundaries; epitaxial graphene

1. Introduction

The extraordinary electronic, optical and mechanical properties of pristine (strain-free and defect-free) graphene (e.g., excellent charge carrier mobility, optical transparency and mechanical strength) make it a promising material for semiconductor devices, effective Raman enhancement, and flexible and printable optoelectronics [1–5]. Strain can be used to dramatically modify the electronic structure and phonon dispersion of graphene and even introduce a band gap [6]. Thus, it is essential to investigate strained graphene for the realization of graphene-based electronics. In previous literatures to study strain property of graphene, the graphene samples were mainly mechanically exfoliated from highly oriented pyrolytic graphite (HOPG) and transferred onto polymer or SiO_2 substrates [6,7]. Although exfoliated graphene offers a large (10–100 μm) and high-quality single domain, the film size is too small for wafer-scale applications. Alternatively, chemical vapor deposition (CVD) on metal substrates and sublimation of silicon atoms from silicon carbide are promising routes for producing wafer-size graphene film [8,9]. However, polycrystalline graphene exists in the films grown by these two methods and the grain size is much smaller than exfoliated graphene, which results in the inevitable formation of grain boundaries [10]. Grain boundary is a common geometrical defect, and consists of repeated pentagon and heptagon pairs, and sometimes octagons [11]. Such kinds of defects can severely weaken the mechanical strength of graphene and have been observed in graphene grown on SiC substrate by scanning tunneling microscopy (STM) study [12–15]. However, there were very few investigations focused on the relationship between grain boundary and strain property of polycrystalline graphene, and many aspects of the grain boundary effects on strained graphene remain unclear.

Both the strain and grain size in materials can be probed by XRD and Raman spectroscopy [16–18]. However, XRD is unsuitable for probing few-layer graphene films grown on SiC substrate because

it needs constructive interference of x-rays reflected from a set of parallel atomic planes. Krishna et al. [18] have done a comparative study of the microstructural information extracted from the peaks of both Raman and XRD spectroscopy, and found that both techniques produced agreeable results for the graphite lattice strain and crystallite size, which proves the validity of deducing both strain and crystallite size from Raman spectra. So, Raman is used to analyze both strain and grain size in this paper. In Raman spectroscopy, the G-band (at about 1580 cm^{-1}) and 2D-band (at about 2680 cm^{-1}) are the fingerprints of pristine graphene. The G-band originates from in-plane vibration of sp^2 carbon atoms and is a doubly degenerate (TO and LO) phonon mode at the Brillouin zone center. The 2D-band is the second order overtone of the D-band and originates from a two-phonon double resonance Raman process where momentum conservation is satisfied by two phonons with opposite wave vectors. In Raman spectra of strained graphene, the G-band and 2D-band peak frequencies shift due to phonon hardening or softening. Typically, compressive strain leads to phonon hardening (frequency upshift), while tensile strain results in phonon softening (frequency downshift). For defective graphene there will appear another two disorder-induced peaks at about 1350 cm^{-1} (D-band) and 1620 cm^{-1} (D'-band). The D-band involves an iTO phonon around the K-point and is an intervalley process, and the D'-band is an intravalley process connecting two points belonging to the same cone around K (or K').

In this work, Raman spectra of polycrystalline graphene, grown by CVD method on the C-face of SiC substrate (CVD-EG) using propane as the carbon source [8,19], are investigated. This method can provide precise graphene layer number control by adjusting the mass transport of the carbon precursor because the carbon atoms in graphene come from the decomposition of propane molecule [8]. The effect of grain boundaries on the strain property of CVD-EG is studied. A nonuniform crystallite size and 2D-band frequency distribution are observed and the blue-shifted 2D-band frequency shifts back with decreasing crystallite size.

2. Materials and Methods

After ultrasonic cleaning by ethanol and acetone, the 2×2 cm^2 semi-insulating C-face 4H-SiC substrate was loaded into a commercial horizontal CVD hot-wall reactor (Aixtron VP508). The chamber was pumped down for 3 h to reach the pressure of 1×10^{-6} kPa for venting oxygen. Then the temperature was raised up to 1250 °C under an argon flow of 20 L/min. After temperature stabilized, 6 SCCM of propane was added to the argon to grow graphene. The growth time was 20 minutes and the growth pressure was kept at 40 kPa. After growth, the chamber was self-cooled down to room temperature under argon ambient.

The Raman measurements were carried out at room temperature using a HORIBA LabRAM HR800 system. The excitation laser energy was 2.41 eV (514.5 nm) and the laser spot size was about in diameter of 1 μm focused by a 100× objective lens. Backscattering configuration was applied with low power of 1 mW to avoid laser induced heating. The atomic force microscopy (AFM) measurements were carried out using a Bruker Dimension Edge system and the AFM images were obtained in tapping-mode.

3. Results and Discussion

Raman spectra were recorded at five different positions on the surface of the CVD-EG sample. Figure 1 plots the typical Raman spectrum with curve fitting. When fitting the spectrum, the contribution of the buffer layer [20,21] to the G-band is not contained because the buffer layer is not observed for graphene samples grown on the C-face of SiC substrate [22,23]. The spectrum consists of three strong peaks at 1352 cm^{-1} (D-band), 1586 cm^{-1} (G-band) and 2704 cm^{-1} (2D-band) and one weak peak at 1620 cm^{-1} (D'-band). The appearance of significant D-band and weak D'-band proves the presence of plenty of defects in the CVD-EG sample. Blue-shifts of G-band position (6 cm^{-1} shifted from 1580 cm^{-1} observed for monolayer exfoliated graphene at a laser wave-length of 514.5 nm) [24] and especially of 2D-band position (24 cm^{-1} shifted from 2680 cm^{-1}) are observed, which are attributed

to compressive strain in graphene layer generated during the cooling down period, because of the large thermal expansion coefficient difference between SiC and graphene [25,26].

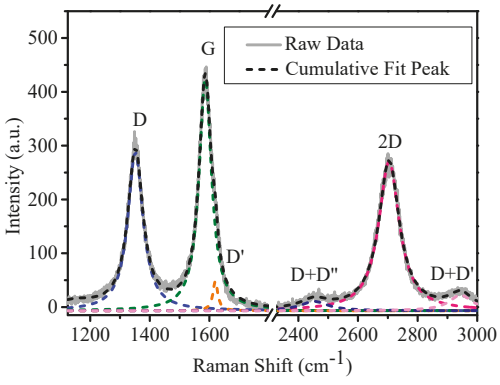

Figure 1. Raman spectrum and fitting peaks of polycrystalline graphene grown by chemical vapor deposition on the C-face of SiC substrate (CVD-EG).

Figure 2 presents the AFM topography image of the sample. The graphene film grows along the terraces of the SiC substrate and preserves the SiC surface morphology. Thus, the variation of terrace width in the SiC substrate leads to non-uniform grain size, which is shown in Figure 2.

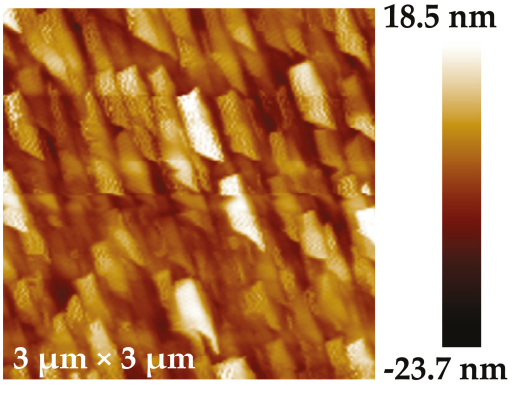

Figure 2. Atomic force microscopy (AFM) 3 μm × 3 μm topography image of CVD-EG.

The full width at half-maximum (FWHM) of the D-band (FWHM(D)), G-band (FWHM(G)) and 2D-band (FWHM(2D)) as a function of $1/L_a$ are presented in Figure 3. L_a is the crystallite size of the grown graphene film, and can be calculated using the ratio of the D-band intensity (I_D) to that of the G-band (I_G) according to Equation (1) [18].

$$L_a(\mathrm{nm}) = 2.4 \times 10^{-10} \lambda^4 \left(\frac{I_D}{I_G} \right)^{-1}, \quad (1)$$

where λ is the excitation laser wavelength in nm used in the Raman measurements. The linear behavior between FWHM and $1/L_a$ can be explained as follows [27]: If the crystallite size is smaller than the phonon mean free path, the phonon lifetime τ will be proportional to the crystallite size L_a. Since the FWHM is determined by lifetime effects in Raman bands involving resonance conditions, it can be assumed that FWHM is proportional to $1/\tau$ and consequently FWHM is proportional to $1/L_a$.

The intercept for the FWHM(2D) is 44 cm^{-1}, which means FWHM(2D) has a value of 44 cm^{-1} when the crystallite size of epitaxial graphene is large. This is consistent with the FWHM(2D) of single layer graphene epitaxially grown on SiC substrate observed by Lee et al. [28]. To identify the thickness of graphene epitaxially grown on SiC substrate unambiguously, the number of Lorentzian function numbers for fitting the 2D band should be used [28,29]. A single Lorentzian fit can identify monolayer graphene, four Lorentzians are necessary for bilayers, and two Lorentzians for three-layers [30,31]. The 2D-band of all the Raman spectra can be fitted quite well by one Lorentzian peak (as shown in Figure 1), therefore, the graphene obtained in our experiment is monolayer.

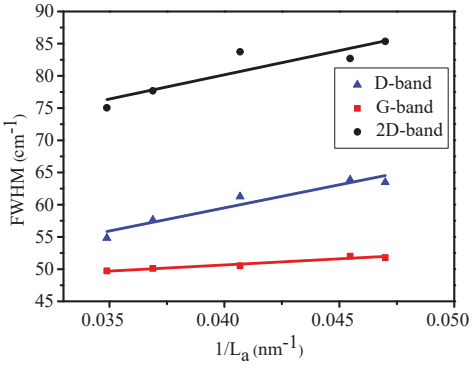

Figure 3. Peak widths of D, G and 2D bands as a function of $1/L_a$.

Eckmann et al. [32] found that the intensity ratio of the D and D′ peak could be used experimentally to obtain the information on the type of defects in graphene, in which it is about 7:1 for vacancy-like defects and decreases to about 7:2 for the boundaries. The ratio in our sample is around 5:1, so the defects mainly consist of boundary-like defects.

Ferrari and Robertson [33] defined a three-stage amorphization trajectory ranging from graphite to tetrahedral amorphous carbon, including graphite to nanocrystalline graphite (stage one), nanocrystalline graphite to low sp^3 amorphous carbon (stage two) and low sp^3 amorphous carbon to high sp^3 amorphous carbon (stage three). The evolution of the Raman spectrum in stage one is as follows: (a) D-band appears and I_D/I_G increases following Equation (1); (b) D′-band appears at about 1620 cm^{-1}; (c) each FWHM for all bands is broadened due to disorder; (d) D+D′ appears. The transition between stage one and two usually occurs at $I_D/I_G \approx 3$ (corresponding to $L_a \approx 5.5$ nm) using excitation laser energy of 2.41 eV [32].

L_a in our graphene sample is about 25 nm, and it is believed that our CVD-EG sample is in stage one, according to the three-stage amorphization trajectory and the peak characteristics shown in Figures 1 and 3. Eckmann et al. [34] reported a detailed Raman study of defective exfoliated graphene and observed that the positions of G-band and 2D-band were constant in this low disorder stage. However, as shown in Figure 4a, the G-band frequency shifts upward as the crystallite size decreases, and the blue-shifted 2D-band behaves in the opposite way and shifts back with increasing defects.

Although both charge and strain could affect the positions of G and 2D bands, the unintentional electron doping of epitaxial graphene on SiC substrate was found previously to be only about 1×10^{13} cm^{-2} [35]. Such order of magnitude shows negligible influence on the 2D-band frequency [29,36]. Thus, the down-shift of the 2D-band frequency is attributed to the reduction of compressive strain. The mode-dependent relation between peak shift $\Delta\omega$ and strain tensor ε is given by Equation (2) [26].

$$\frac{\Delta\omega}{\omega} = -\gamma_m \mathrm{Tr}(\varepsilon_{ij}), \quad (2)$$

where γ_m is the mode Grüneisen parameter. For 2D-band of graphene $\gamma_{2D} \approx 2.7$.

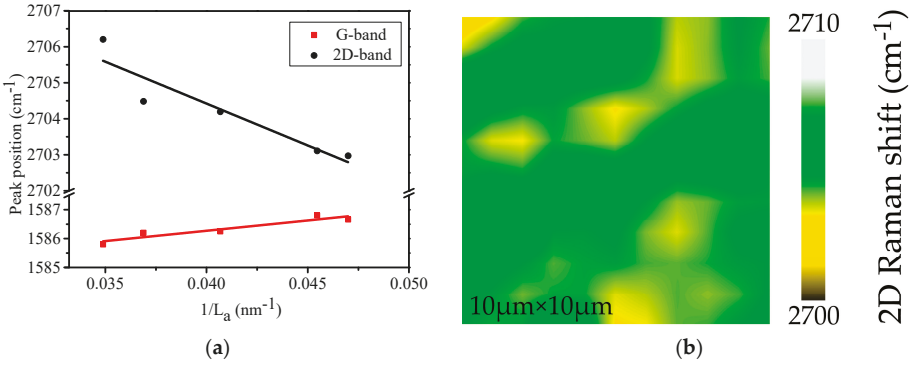

Figure 4. (**a**) Peak positions of G-band and 2D-band as a function of $1/L_a$, (**b**) scanning Raman map of 2D-band frequency.

Figure 4b plots the scanning Raman map of 2D-band frequency, and the homogeneous frequency distribution proves the uniformity of strain and doping across the 10 μm × 10 μm spatial region. It is noted that the five positions in Figure 4a are separated from each other by several millimeters. Thus, the big difference in 2D-band frequency between different positions and the homogeneous frequency distribution across the 10 μm × 10 μm spatial region near each position prove the robustness of the result in Figure 4a.

Figure 5 presents the positions of G and 2D bands as a function of strain using 2D peak shift for strain calibration. It can be seen that the slope of G-band (21.5 $cm^{-1}/\%$) has opposite sign comparing with that of 2D-band (-72.4 $cm^{-1}/\%$). This phenomenon is interesting, since the lattice deforms and the G-band and 2D-band positions should shift in the same way as a consequence of phonon hardening or softening when strain occurs in single domain graphene. Bissett et al. [16] also observed the same anomalous behavior when studying the polycrystalline graphene with the crystallite size of 1 μm and they concluded that the anomalous behavior resulted from the presence of grain boundaries in graphene with small crystallite size.

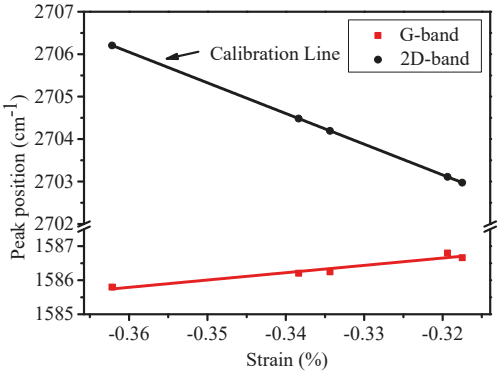

Figure 5. Peak positions of G-band and 2D-band as a function of strain.

Another significant observation in Figure 4a is the linear relation between the 2D-band frequency and $1/L_a$. As mentioned above, the 2D-band keeps constant in stage one of the three-stage amorphization trajectory. So, it could not directly obtain the relation between 2D-band position and crystallite size from the effect of defects, which is attributed to the nonuniform distribution of

compressive strain. In this case, the compressive strain has a larger value in the positions with larger crystallite size. This interesting property of polycrystalline graphene has never been reported before.

It is assumed that the graphene is free of strain when the growth period is over [25]. As the temperature goes down, there will be a compressive strain in the graphene film because of the much greater thermal expansion coefficient of SiC substrate than that of graphene film. Since the crystallite size is small and the type of defects is mainly boundary-like, there will be abundant grain boundaries. The atoms at the grain boundaries can diffuse in two ways [37]:

(1) lattice diffusion directly into the grains and
(2) much faster diffusion along the grain boundary.

The square shape grain model (as shown in Figure 6) is used according to the AFM image in Figure 2 and it is supposed that each grain is isolated with no mechanical interaction between neighboring grains. In steady-state diffusion, the atom distribution caused by lattice diffusion can be described by diffusion Equation (3).

$$D\frac{d^2C(L_a/2-x)}{dx^2} = \frac{C(L_a/2-x)}{\tau}, \tag{3}$$

where D and τ are diffusion coefficient and relaxation time of lattice diffusion, respectively. The solution of Equation (3) has the form of Equation (4).

$$C(x) = A\exp\left(-\frac{L_a/2-x}{L}\right) + B\exp\left(+\frac{L_a/2-x}{L}\right), \tag{4}$$

where $L = \sqrt{D\tau}$ is the diffusion length. The boundary conditions are $C(0) = 0$ and $C(L_a/2) = C_0$. Here, it is assumed that the diffusion length L is much smaller than crystallite size L_a. Thus, $A = C_0$ and $B = 0$. The solution of Equation (3) is written by Equation (5).

$$C(x) = C_0\exp\left(-\frac{L_a/2-x}{L}\right). \tag{5}$$

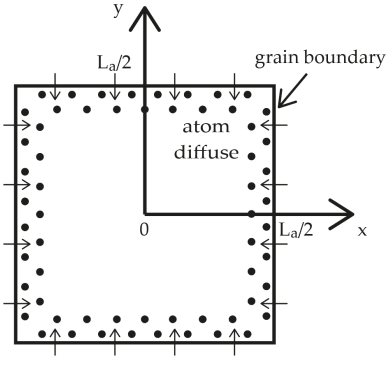

Figure 6. Square shape grain model of graphene.

The diffusion of atoms will cause the relaxation of compressive strain and it could be assumed that the strain reduced is proportional to the number of atoms diffused. Thus, the strain ε has a maximum value at the center of the grain, decays exponentially with distance x from the center point, and reaches zero at the grain boundary because of the much faster diffusion along grain boundaries. The strain at a point (x,y) inside the grain is given by Equation (6).

$$\varepsilon(x,y) = \varepsilon_{max}\left[1 - \exp\left(-\frac{L_a/2 - x}{L}\right) - \exp\left(-\frac{L_a/2 - y}{L}\right)\right], \quad (6)$$

where ε_{max} is the strain at the center of the grain. The average strain $\bar{\varepsilon}$ inside a grain can be calculated by Equation (7).

$$\bar{\varepsilon} = \frac{1}{(L_a/2)^2}\int_0^{L_a/2}\int_0^{L_a/2}\varepsilon(x,y)dxdy. \quad (7)$$

Integrating Equation (7), the average strain $\bar{\varepsilon}$ is given by Equation (8).

$$\bar{\varepsilon} = \varepsilon_{max}\left\{1 - \frac{4L}{L_a}\left[1 - \exp\left(-\frac{L_a/2}{L}\right)\right]\right\} \approx \varepsilon_{max}\left(1 - \frac{4L}{L_a}\right). \quad (8)$$

Equation (8) shows that the relation of the average strain $\bar{\varepsilon}$ with $1/L_a$ is linear, thus the relation of 2D-band frequency shift $\Delta\omega_{2D}$ with $1/L_a$ is also linear according to Equation (2), which explains the Raman results in Figure 4a. The intercept of the fitting line for 2D-band in Figure 4a is 2714 cm^{-1}, which corresponds to a compressive strain of 0.47%. The value of 0.47% well matches with the results in Ref. [8].

4. Conclusions

Raman spectra of CVD-EG show that abundant boundary-like defects exist in the graphene film and a significant blue-shift of 2D-band position is observed. The frequency of the 2D-band decreases linearly as $1/L_a$ increases and the G-band frequency increases linearly as $1/L_a$ increases. The opposite variation direction of G and 2D bands results from the presence of grain boundaries in graphene with small crystallite size. The downshift of 2D-band is caused by strain relaxation due to grain boundary diffusion.

Author Contributions: Conceptualization, L.C.; Data curation, L.C.; Formal analysis, L.C.; Funding acquisition, H.G. and Y.Z. (Yuming Zhang); Investigation, L.C.; Methodology, L.C.; Project administration, H.G.; Resources, H.G.; Supervision, H.G., Y.H. and Y.Z. (Yimen Zhang); Validation, L.C. and Y.H.; Visualization, L.C.; Writing—original draft, L.C.; Writing—review & editing, Y.Z. (Yimen Zhang).

Funding: This research was funded by National Natural Science Foundation of China, Grant Numbers 61575153 and 61675191.

Conflicts of Interest: The authors declare no conflict of interest.

References

1. Wu, J.-B.; Lin, M.-L.; Cong, X.; Liu, H.-N.; Tan, P.-H. Raman spectroscopy of graphene-based materials and its applications in related devices. *Chem. Soc. Rev.* **2018**, *47*, 1822–1873. [CrossRef] [PubMed]
2. Bae, S.; Kim, H.; Lee, Y.; Xu, X.; Park, J.-S.; Zheng, Y.; Balakrishnan, J.; Lei, T.; Ri Kim, H.; Song, Y.I.; et al. Roll-to-Roll Production of 30-inch Graphene Films for Transparent Electrodes. *Nat. Nanotechnol.* **2010**, *5*, 574–578. [CrossRef] [PubMed]
3. Wagner, S.; Dieing, T.; Centeno, A.; Zurutuza, A.; Smith, A.D.; Östling, M.; Kataria, S.; Lemme, M.C. Noninvasive Scanning Raman Spectroscopy and Tomography for Graphene Membrane Characterization. *Nano Lett.* **2017**, *17*, 1504–1511. [CrossRef] [PubMed]
4. Xu, W.; Ling, X.; Xiao, J.; Dresselhaus, M.S.; Kong, J.; Xu, H.; Liu, Z.; Zhang, J. Surface enhanced Raman spectroscopy on a flat graphene surface. *PNAS* **2012**, *109*, 9281–9286. [CrossRef] [PubMed]
5. Ling, X.; Xie, L.; Fang, Y.; Xu, H.; Zhang, H.; Kong, J.; Dresselhaus, M.S.; Zhang, J.; Liu, Z. Can Graphene be used as a Substrate for Raman Enhancement? *Nano Lett.* **2010**, *10*, 553–561. [CrossRef] [PubMed]
6. Mueller, N.S.; Heeg, S.; Alvarez, M.P.; Kusch, P.; Wasserroth, S.; Clark, N.; Schedin, F.; Parthenios, J.; Papagelis, K.; Galiotis, C.; et al. Evaluating arbitrary strain configurations and doping in graphene with Raman spectroscopy. *2D Mater.* **2018**, *5*, 015016. [CrossRef]

7. Kim, S.; Ryu, S. Thickness-dependent native strain in graphene membranes visualized by Raman spectroscopy. *Carbon* **2016**, *100*, 283–290. [CrossRef]
8. Strupinski, W.; Grodecki, K.; Wysmolek, A.; Stepniewski, R.; Szkopek, T.; Gaskell, P.E.; Grüneis, A.; Haberer, D.; Bozek, R.; Krupka, J.; et al. Graphene Epitaxy by Chemical Vapor Deposition on SiC. *Nano Lett.* **2011**, *11*, 1786–1791. [CrossRef] [PubMed]
9. Lim, G.; Kihm, K.D.; Kim, H.G.; Lee, W.; Lee, W.; Pyun, K.R.; Cheon, S.; Lee, P.; Min, J.Y.; Ko, S.H. Enhanced Thermoelectric Conversion Efficiency of CVD Graphene with Reduced Grain Sizes. *Nanomaterials* **2018**, *8*, 557. [CrossRef] [PubMed]
10. Chen, M.Q.; Quek, S.S.; Sha, Z.D.; Chiu, C.H.; Pei, Q.X.; Zhang, Y.W. Effects of grain size, temperature and strain rate on the mechanical properties of polycrystalline graphene—A molecular dynamics study. *Carbon* **2015**, *85*, 135–146. [CrossRef]
11. Wang, B.; Puzyrev, Y.; Pantelides, S.T. Strain enhanced defect reactivity at grain boundaries in polycrystalline graphene. *Carbon* **2011**, *49*, 3983–3988. [CrossRef]
12. Ren, Y.; Cao, G. Effect of geometrical defects on the tensile properties of graphene. *Carbon* **2016**, *103*, 125–133. [CrossRef]
13. Xu, P.; Qi, D.; Schoelz, J.K.; Thompson, J.; Thibado, P.M.; Wheeler, V.D.; Nyakiti, L.O.; Myers-Ward, R.L.; Eddy, C.R., Jr.; Gaskill, D.K.; et al. Multilayer graphene, Moire' patterns, grain boundaries and defects identified by scanning tunneling microscopy on the m-plane, non-polar surface of SiC. *Carbon* **2014**, *80*, 75–81. [CrossRef]
14. Zhou, X.; Ji, S.H.; Chockalingam, S.P.; Hannon, J.B.; Tromp, R.M.; Heinz, T.F.; Pasupathy, A.N.; Ross, F.M. Electrical transport across grain boundaries in graphene monolayers on SiC(0001¯). *2D Mater.* **2018**, *5*, 031004. [CrossRef]
15. Tison, Y.; Lagoute, J.; Repain, V.; Chacon, C.; Girard, Y.; Joucken, F.; Sporken, R.; Gargiulo, F.; Yazyev, O.V.; Rousset, S. Grain Boundaries in Graphene on SiC(0001¯) Substrate. *Nano Lett.* **2014**, *14*, 6382–6386. [CrossRef] [PubMed]
16. Bissett, M.A.; Izumida, W.; Saito, R.; Ago, H. Effect of Domain Boundaries on the Raman Spectra of Mechanically Strained Graphene. *ACS Nano* **2012**, *6*, 10229–10238. [CrossRef] [PubMed]
17. Ferrante, C.; Virga, A.; Benfatto, L.; Martinati, M.; De Fazio, D.; Sassi, U.; Fasolato, C.; Ott, A.K.; Postorino, P.; Yoon, D.; et al. Raman spectroscopy of graphene under ultrafast laser excitation. *Nat. Commun.* **2018**, *9*, 308. [CrossRef] [PubMed]
18. Krishna, R.; Wade, J.; Jones, A.N.; Lasithiotakis, M.; Mummery, P.M.; Marsden, B.J. An understanding of lattice strain, defects and disorder in nuclear graphite. *Carbon* **2017**, *124*, 314–333. [CrossRef]
19. Lafont, F.; Ribeiro-Palau, R.; Kazazis, D.; Michon, A.; Couturaud, O.; Consejo, C.; Chassagne, T.; Zielinski, M.; Portail, M.; Jouault, B.; et al. Quantum Hall resistance standards from graphene grown by chemical vapour deposition on silicon carbide. *Nat. Commun.* **2015**, *6*, 6806. [CrossRef] [PubMed]
20. Conrad, M.; Rault, J.; Utsumi, Y.; Garreau, Y.; Vlad, A.; Coati, A.; Rueff, J.-P.; Miceli, P.F.; Conrad, E.H. Structure and evolution of semiconducting buffer graphene grown on SiC(0001). *Phys. Rev. B* **2017**, *96*, 195304. [CrossRef]
21. Fromm, F.; Oliveira, M.H., Jr.; Molina-S'anchez, A.; Hundhausen, M.; Lopes, J.M.J.; Riechert, H.; Wirtz, L.; Seyller, T. Contribution of the buffer layer to the Raman spectrum of epitaxial graphene on SiC(0001). *New J. Phys.* **2013**, *15*, 043031. [CrossRef]
22. Magaud, L.; Hiebel, F.; Varchon, F.; Mallet, P.; Veuillen, J.-Y. Graphene on the C-terminated SiC (0001¯) surface: An ab initio study. *Phys. Rev. B* **2009**, *79*, 161405. [CrossRef]
23. Hiebel, F.; Mallet, P.; Varchon, F.; Magaud, L.; Veuillen, J.-Y. Graphene-substrate interaction on 6H-SiC(0001¯): A scanning tunneling microscopy study. *Phys. Rev. B* **2008**, *78*, 153412. [CrossRef]
24. Graf, D.; Molitor, F.; Ensslin, K.; Stampfer, C.; Jungen, A.; Hierold, C.; Wirtz, L. Spatially resolved Raman spectroscopy of single- and few-layer graphene. *Nano Lett.* **2007**, *7*, 238–242. [CrossRef] [PubMed]
25. Röhrl, J.; Hundhausen, M.; Emtsev, K.V.; Seyller, T.; Graupner, R.; Ley, L. Raman spectra of epitaxial graphene on SiC(0001). *Appl. Phys. Lett.* **2008**, *92*, 201918. [CrossRef]
26. Strudwick, A.J.; Creeth, G.L.; Johansson, N.A.B.; Marrows, C.H. Probing residual strain in epitaxial graphene layers on with Raman spectroscopy. *Appl. Phys. Lett.* **2011**, *98*, 051910. [CrossRef]
27. Cançado, L.G.; Jorio, A.; Pimenta, M.A. Measuring the absolute Raman cross section of nanographites as a function of laser energy and crystallite size. *Phys. Rev. B* **2007**, *76*, 064304. [CrossRef]

28. Lee, D.S.; Riedl, C.; Krauss, B.; von Klitzing, K.; Starke, U.; Smet, J.H. Raman Spectra of Epitaxial Graphene on SiC and of Epitaxial Graphene Transferred to SiO_2. *Nano Lett.* **2008**, *8*, 4320–4325. [CrossRef] [PubMed]
29. Robinson, J.A.; Puls, C.P.; Staley, N.E.; Stitt, J.P.; Fanton, M.A.; Emtsev, K.V.; Seyller, T.; Liu, Y. Raman Topography and Strain Uniformity of Large-Area Epitaxial Graphene. *Nano Lett.* **2009**, *9*, 964–968. [CrossRef] [PubMed]
30. Ferrari, A.C.; Meyer, J.C.; Scardaci, V.; Casiraghi, C.; Lazzeri, M.; Mauri, F.; Piscanec, S.; Jiang, D.; Novoselov, K.S.; Roth, S.; et al. Raman Spectrum of Graphene and Graphene Layers. *Phys. Rev. Lett.* **2006**, *97*, 187401. [CrossRef] [PubMed]
31. Wang, Y.Y.; Ni, Z.H.; Yu, T.; Wang, H.M.; Wu, Y.H.; Chen, W.; Wee, A.T.S.; Shen, Z.X. Raman studies of monolayer graphene: The substrate effect. *J. Phys. Chem. C* **2008**, *112*, 10637–10640. [CrossRef]
32. Eckmann, A.; Felten, A.; Mishchenko, A.; Britnell, L.; Krupke, R.; Novoselov, K.S.; Casiraghi, C. Probing the Nature of Defects in Graphene by Raman Spectroscopy. *Nano Lett.* **2012**, *12*, 3925–3930. [CrossRef] [PubMed]
33. Ferrari, A.C.; Basko, D.M. Raman spectroscopy as a versatile tool for studying the properties of graphene. *Nat. Nanotechnol.* **2013**, *8*, 235–246. [CrossRef] [PubMed]
34. Eckmann, A.; Felten, A.; Verzhbitskiy, I.; Davey, R.; Casiraghi, C. Raman study on defective graphene: Effect of the excitation energy, type, and amount of defects. *Phys. Rev. B* **2013**, *88*, 035426. [CrossRef]
35. Vantasin, S.; Tanaka, Y.; Uemura, S.; Suzuki, T.; Kutsuma, Y.; Doujima, D.; Kaneko, T.; Ozaki, Y. Characterization of SiC-grown epitaxial graphene microislands using tip-enhanced Raman spectroscopy. *Phys. Chem. Chem. Phys.* **2015**, *17*, 28993–28999. [CrossRef] [PubMed]
36. Das, A.; Pisana, S.; Chakraborty, B.; Piscanec, S.; Saha, S.K.; Waghmare, U.V.; Novoselov, K.S.; Krishnamurthy, H.R.; Geim, A.K.; Ferrari, A.C.; et al. Monitoring dopants by Raman scattering in an electrochemically top-gated graphene transistor. *Nat. Nanotechnol.* **2008**, *3*, 210–215. [CrossRef] [PubMed]
37. Mehrer, H. *Diffusion in Solids*; Springer: Berlin, Germany, 2007; pp. 553–582.

nanomaterials

MDPI

Article

Tunable Electronic Properties of Nitrogen and Sulfur Doped Graphene: Density Functional Theory Approach

Ji Hye Lee [1], Sung Hyun Kwon [1], Soonchul Kwon [2], Min Cho [3], Kwang Ho Kim [4], Tae Hee Han [5,*] and Seung Geol Lee [1,*]

[1] Department of Organic Material Science and Engineering, Pusan National University, 2, Busandaehak-ro 63beon gil, Geumjeong-gu, Busan 46241, Korea; iciti5425@pusan.ac.kr (J.H.L.); rnjstjdgus5@hanmail.net (S.H.K.)
[2] Department of Civil and Environmental Engineering, Pusan National University, 2, Busandaehak-ro 63beon gil, Geumjeong-gu, Busan 46241, Korea; sckwon@pusan.ac.kr
[3] Division of Biotechnology, Advanced institute of Environment and Bioscience, College of Environmental and Bioresource Sciences, Chonbuk National University, Iksan 54596, Korea; cho317@jbnu.ac.kr
[4] School of Materials Science and Engineering, Pusan National University, 2, Busandaehak-ro 63 Beon-gil, Geumjeong-gu, Busan 46241, Korea; khkim@pusan.ac.kr
[5] Department of Organic and Nano Engineering, Hanyang University, Seoul 04763, Korea
* Correspondence: than@hanyang.ac.kr (T.H.H.); seunggeol.lee@pusan.ac.kr (S.G.L.)

Received: 7 January 2019; Accepted: 13 February 2019; Published: 15 February 2019

Abstract: We calculated the band structures of a variety of N- and S-doped graphenes in order to understand the effects of the N and S dopants on the graphene electronic structure using density functional theory (DFT). Band-structure analysis revealed energy band upshifting above the Fermi level compared to pristine graphene following doping with three nitrogen atoms around a mono-vacancy defect, which corresponds to p-type nature. On the other hand, the energy bands were increasingly shifted downward below the Fermi level with increasing numbers of S atoms in N/S-co-doped graphene, which results in n-type behavior. Hence, modulating the structure of graphene through N- and S-doping schemes results in the switching of "p-type" to "n-type" behavior with increasing S concentration. Mulliken population analysis indicates that the N atom doped near a mono-vacancy is negatively charged due to its higher electronegativity compared to C, whereas the S atom doped near a mono-vacancy is positively charged due to its similar electronegativity to C and its additional valence electrons. As a result, doping with N and S significantly influences the unique electronic properties of graphene. Due to their tunable band-structure properties, the resulting N- and S-doped graphenes can be used in energy and electronic-device applications. In conclusion, we expect that doping with N and S will lead to new pathways for tailoring and enhancing the electronic properties of graphene at the atomic level.

Keywords: co-doping; graphene; electronic structure; density functional theory; tunable electronics

1. Introduction

Graphene consists of two-dimensional sheets of sp^2-bonded carbon atoms arranged in a honeycomb lattice [1–3]. It is a zero bandgap semiconductor or semimetal with a large surface area of 2630 $m^2\ g^{-1}$ [4,5], which is larger than other carbon-based materials [5,6]. Graphene also has exceptional charge-carrier mobility of 2×10^5 $cm^2\ V\ s^{-1}$ [7], good thermal conductivity of ~5000 $W\ m^{-1}K^{-1}$ [8] and high mechanical strength with ~1 TPa of Young's modulus [9]. Due to its fascinating properties, graphene is considered to be a promising candidate material for applications in a wide range of fields, such as nanoelectronics [10], optoelectronics [11], energy-storage and conversion

devices [12–14], sensors [15], and catalysts [16]. It is essential that the intrinsic electronic properties of graphene are tailorable for use in a range of nanoelectronics devices. Tremendous effort has been dedicated to the tuning of the electronic properties of graphene, and various techniques have been proposed [17–33]. As the zero bandgap, at the Fermi level, is attributed to the sub-lattice symmetry of the graphene structure, breaking this symmetry will induce bandgap widening. Substitutional doping and the formation of atomistic defects such as vacancies are simple and effective methods for opening the bandgap and altering the band structure of graphene. The band structure can subsequently be tuned by controlling the degree of heteroatom doping or the number of vacancies. The electronic properties of graphene have been found to change considerably when doped with single heteroatoms, such as B, N, O, P, or S [17–19,23,24,28–30,33]. Because of the relative differences in the electronegativities of the atomic dopants with respect to that of C, heteroatom doping is expected to induce changes in the band structure, charge distribution, and magnetic properties of graphene. Both experimental and theoretical studies have revealed that graphitic N atoms lead to n-type behavior, whereas pyridinic and pyrrolic N atoms give rise to p-type behavior [22–24]. Therefore, controlling the bonding configurations of the N atoms in graphene may provide a mechanism for tuning the electronic characteristics from n-type to p-type. Recently, co-doping with multiple heteroatoms has become popular because co-doping creates a unique, synergistically coupled, electronic structure. However, there are few reports that provide a fundamental understanding of the alternating electronic structure and accompanying performance of co-doped graphene [25–28,31–33]. Among the atoms possible as N co-dopants, the S atom is considered to be an attractive doping material due to its similar electronegativity and van der Waals radius to those of C, while possessing two lone pairs of electrons. Herein, we present a spin-polarized density functional theory (DFT) study on the electronic properties of N- and S-doped graphene in which we characterize changes in band structure and charge-density distribution by controlling the concentrations of the N and S dopants.

2. Computational Details

First-principles density functional theory (DFT) calculations were carried out using the Vienna Ab Initio Simulation Package (VASP) [34,35]. Geometries were optimized, and the total energies and forces were calculated using a planewave basis set with the projector augmented wave (PAW) method [36]. The generalized gradient approximation (GGA) with the Perdew–Burke–Ernzerhof (PBE) exchange-correlation functional [37] was used, and the planewave cutoff energy was set to 500 eV; the GGA-PBE functional has been successfully used to describe carbon-based systems [38–43]. All structures were optimized such that the total energy converged to less than 1.0×10^{-6} eV per atom and the maximum force converged to below 0.05 eV Å^{-1}. The graphene model used in our simulation consisted of a $12.3 \times 12.3 \times 15.0$ Å, 5×5 supercell with a vacuum thickness of 15 Å, which avoids interference between adjacent graphene layers. Brillouin-zone integrations were carried out using a $4 \times 4 \times 1$ Monkhorst–Pack K-point grid. The effects of van der Waals (vdW) interactions were included using the empirical DFT-D3 correction within the Grimme scheme [44]. All atomic charge distributions in our study were calculated by Mulliken population analysis from Materials Studio [45,46].

3. Results and Discussion

Various configurations exist for the doped and defective graphene chosen as the anode material in a lithium-ion battery (LIB). For instance, N-doped graphene exists in distinct forms that include graphitic, pyridinic, and pyrrolic N atoms [47]. Among these nitrogen types, pyridinic N-doped graphene is believed to be associated with high electrocatalytic activity and excellent reversible capacity [29,48,49]. Pyridinic Ns are located at the edges of graphene planes, and arise from sp^2-hybridized N atoms bonded to two neighboring sp^2-hybridized C atoms. Using this configuration as the starting point, different configurations of N- and S-doped graphene with mono-vacancy defects were built as simulation models. Three C atoms around a mono-vacancy defect were substituted with

different numbers of atomic N and/or S dopants. Regarding model structures in this investigation, research groups successfully reported the synthesis of N- and S-doped graphene [22,43,50–64]. In order to analyze the effects of the N and S doping levels on electronic properties, we first fixed the doping concentration to three dopant atoms at the mono-vacancy defect. We constructed four configurations with different N and S doping ratios; the graphene doped with three nitrogen atoms is designated as "3N-gra", that doped with two nitrogens and one sulfur as "2N1S-gra", while the graphene doped with one nitrogen and two sulfur atoms is "1N2S-gra", and the three sulfur-doped graphene is "3S-gra". The optimized structures of the N- and S-doped graphenes are displayed in Figure 1, with the calculated band structures shown in Figure 2, which reveal clear changes in electronic structure following doping with N and S. Pristine graphene is a zero bandgap semiconductor with its Dirac point located at the Fermi energy [38].

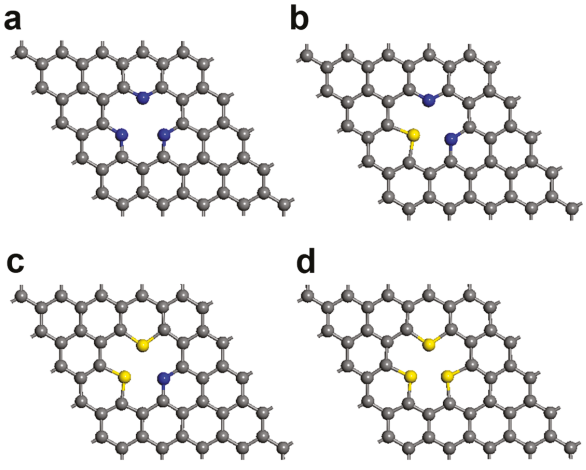

Figure 1. Optimized structures of the (**a**) 3N-gra, (**b**) 2N1S-gra, (**c**) 1N2S-gra, and (**d**) 3S-gra systems. Blue, gray, and yellow denote nitrogen, carbon, and sulfur, respectively.

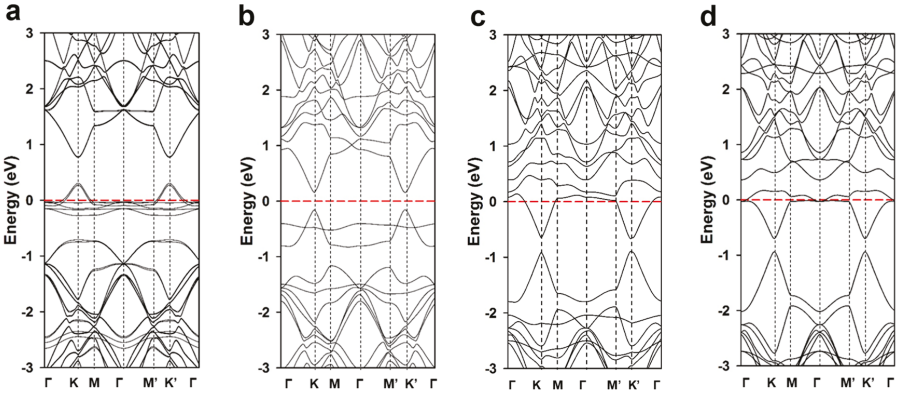

Figure 2. Calculated band structures of the (**a**) 3N-gra, (**b**) 2N1S-gra, (**c**) 1N2S-gra, and (**d**) 3S-gra systems.

The bandgap clearly opens after doping with N or S, and/or the introduction of a mono-vacancy defect, which is ascribable to the effects of the atomic dopant and/or vacancy defect on the π electrons in the hexagonal rings. Mono-vacancy defects lead to shortages of whole charges compared to pristine

graphene, which downshift the Fermi energy, indicating that the mono-vacancy defect acts as a hole dopant with missing π electrons. As shown in Figure S1, the band structure for pristine graphene and graphene with a single vacancy were calculated that the band gap of graphene with a single vacancy is opened at the Dirac point and the Fermi level is downshifted compared to pristine graphene.

On the other hand, N and S atoms have one and two additional valence electrons, respectively; hence, doping with N or S results in an upward shift in the Fermi energy. Table 1 reveals that the bandgap energies also change when the band structures are altered by the atomic dopant and/or vacancy defect. In moving from 3N-gra to 3S-gra, the bandgap energy was observed to gradually decrease with increasing levels of the sulfur dopant. The Fermi level is substantially shifted downward from the Dirac point of pristine graphene in 3N-gra. This downward shift indicates that the 3N-doped graphene exhibits p-type behavior and has an affinity for gaining electron density. In addition, flat bands appeared around the Fermi level. Meanwhile, the Fermi level for 3N-doped graphene is somewhat upshifted compared to the mono-vacancy defective graphene because nitrogen has more available electrons than carbon and can replenish some of the electron deficiency. Nevertheless, doping the mono-vacancy defective graphene with three N atoms is unable to completely compensate for the charge deficiency of the mono-vacancy defect. The energy band gradually becomes narrower, that is to say, the Fermi level is upshifted in moving from 3N-gra to 3S-gra, with increasing levels of the sulfur dopant. Indeed, the energy band for 2N1S-gra is slightly narrower than that of the 3N-gra system. In addition, the band structure of the 1NS2-gra system, which is more doped with sulfur than nitrogen, features visible changes in band energies that are shifted below the Fermi level; hence, this system can be considered to exhibit n-type behavior. Interestingly, the p-type to n-type conversion can be induced through control of the N and S doping levels (e.g., by increasing the S-to-N doping ratio). The 3S-gra system also exhibits n-type character, with slightly downward shifted band energies compared to the 1N2S-gra system; however, the level of downward shift induced by moving from 1N2S-gra to S3-gra is very marginal. The degree in the downward shift in band energy tends to decrease with decreasing nitrogen atom concentration.

Table 1. The band gap energies Eg (in eV) for 3N-gra, 2N1S-gra, 1N2S-gra and 3S-gra systems.

	3N-gra	**2N1S-gra**	**1N2S-gra**	**3S-gra**
Bandgap (eV)	0.473	0.350	0.275	0.255

Finally, we studied the charge-density distribution of each atom around the mono-vacancy defect for each N- and S-doped graphene system by Mulliken population analysis because the charge distributions on the carbon, nitrogen, and sulfur atoms are important for determining the origin of the alternating electronic properties. Figure 3 displays the charge on each atom around the mono-vacancy defect; positive charges are shown in black, while negative charges are shown in red. The difference in the electronegativity of the N atom (3.04) and the C atom (2.55), which is referred to Pauling scale [65], polarizes the hexagonal ring. Therefore, all of the N atoms inside the mono-vacancy for each system are negatively charged. The average charges on the N atoms in these systems were determined to be -0.176e, -0.341e, and -0.401e for 3N-gra, 2N1S-gra, and 1N2S-gra, respectively. Meanwhile, most of the compensating positive charges are distributed on the adjacent C atoms connected to the atomic N dopants. As shown in Figure 2a (3N-gra system), the charges on the three C atoms connected to the N atoms in the range between +0.043 and +0.044e. Unlike the N-doped systems, the C–S bond is negligibly polarized because the electronegativities of the S (2.58) and C (2.55) atoms are similar. Moreover, the S atom has two additional valence electrons compared to carbon, which provide positive charge and lone pairs of electrons. The average charges on the S atoms in these systems were determined to be +0.475e, +0.374e, and +0.302e for 2N1S-gra, 1N2S-gra, and 3S-gra, respectively. In contrast, most of the compensating negative charges are distributed on the adjacent C atoms bonded to the doping S atoms. As displayed in Figure 2b (the 2N1S-gra system), the C atoms bonded to the N atoms bear positive charges, with values of +0.081e and +0.146e on the $C_{N1}{}'$ and

C_{N1}'' atoms, and +0.143e and +0.082e on the C_{N2}' and C_{N2}'' atoms, respectively. The charges on the C atoms on each side of the N atom are almost identical. On the other hand, the C atoms bonded to the S atom exhibit negative charges, at −0.242e on C_{S1}', and −0.246e on C_{S1}''. Likewise, the 1N2S-gra system showed a similar trend. As shown in Figure 2c, the C atoms bonded to the N atoms, namely C_{N1}' and C_{N2}'', bear charges of +0.109e and +0.110e, which are almost identical. The C atoms adjacent to the S atoms exhibit negative charges, with charges of −0.248e and −0.240e on C_{S1}' and C_{S1}'', and −0.238e and −0.250e on the C_{S2}' and C_{S2}'' atoms, respectively. Finally, the 3S-gra system exhibited charges on the C atoms bonded to the S atoms that were in the −0.245e to −0.233e range. It seems that polarization in the doped region increases with increasing S concentration. The transformed charge-density distribution following doping, as well as the vacancy defect, affects the electronic properties of the graphene system.

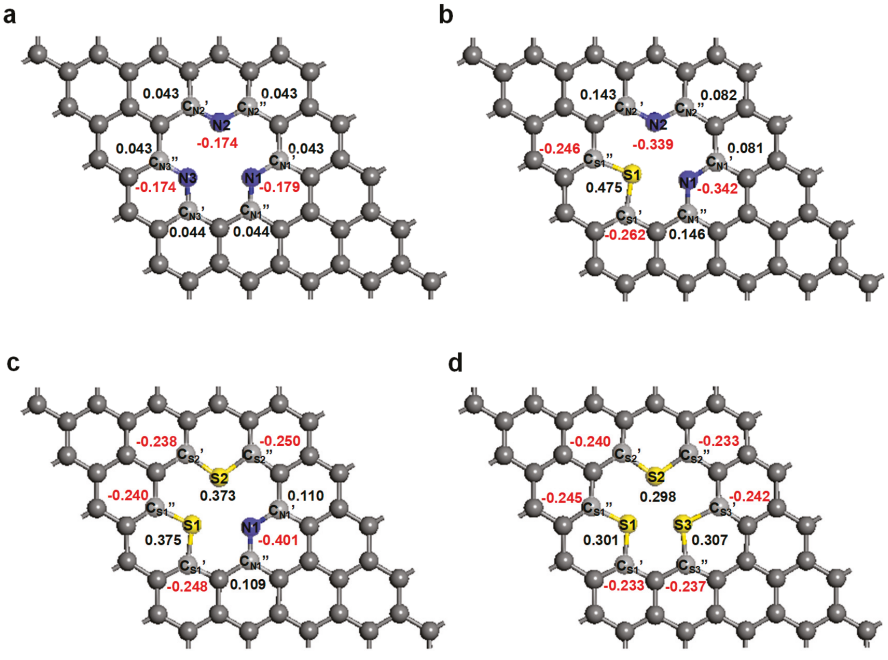

Figure 3. Calculated charge-density distributions on the atoms around the doped mono-vacancy region for the (**a**) 3N-gra, (**b**) 2N1S-gra, (**c**) 1N2S-gra, and (**d**) 3S-gra systems. Blue, gray, and yellow denote nitrogen, carbon, and sulfur, respectively.

4. Conclusions

The present density functional theory study aimed to reveal details of the electronic structures of several N- and S-doped graphenes in order to understand the effects of the N and S dopants on the graphene electronic structure. We found that the band structure of graphene can easily be tuned by doping with N and S atoms. The roles of the atomic N and S dopants on the band energies were clearly revealed; these dopants noticeably perturb the band shapes and open the bandgap at the Dirac point, compared to graphene itself. The band energies of 3N-doped graphene were upward shifted below the Fermi level compared with those of pure graphene, and showed p-type behavior. The band structure exhibits a remarkable electronic transition, from "p-type" to "n-type", in moving from 3N-gra to 3S-gra (with increasing numbers of S atoms) with a downshifting of the band energy below the Fermi level. Moreover, Mulliken population analysis revealed that the atomic N dopants bear negative charges, whereas the atomic S dopants bear positive charges in N- and/or S-co-doped graphene

systems, which is ascribable to differences in the electronegativities and numbers of valence electrons among the C, N, and S atoms. In each N- and/or S-co-doped graphene system, all of the N atoms bear negative charges, whereas all of the S atoms bear positive charges. The average charge on the N atoms gradually increases with decreasing numbers of N atoms in the N- and/or S-co-doped graphene system. In contrast, the average charge on the S atoms decreases with increasing numbers of S atoms in the co-doped graphene system. Due to their tunable band-structure properties, the resulting N- and S-co-doped graphenes can be used in energy and electronic-device applications. In conclusion, we expect that doping with N and S will lead to new pathways for tailoring and enhancing the electronic properties of graphene at the atomic level.

Supplementary Materials: The following are available online at http://www.mdpi.com/2079-4991/9/2/268/s1, Figure S1: Calculated band structures of the (**a**) pristine graphene and (**b**) graphene with mono-vacancy.

Author Contributions: S.G.L., K.H.K., and T.H.H. conceived the research idea. J.H.L, S.K., M.C., and S.G.L. wrote the main manuscript text. J.H.L. and S.H.K. performed the experiments. All authors reviewed the manuscript.

Funding: This research was funded by the National Research Foundation of Korea (NRF) funded by the Ministry of Science, ICT & Future Planning (Nos. NRF-2016M1A2A2937151 and NRF-2016R1A6A1A03013422). This research was funded by the Global Frontier Program through the Global Frontier Hybrid Interface Materials (GFHIM) of the NRF of Korea funded by the Ministry of Science, ICT, and Future Planning (No. 2013M3A6B1078882).

Acknowledgments: This research was supported by the National Research Foundation of Korea (NRF) funded by the Ministry of Science, ICT & Future Planning (Nos. NRF-2016M1A2A2937151 and NRF-2016R1A6A1A03013422). This research was supported by the Global Frontier Program through the Global Frontier Hybrid Interface Materials (GFHIM) of the NRF of Korea funded by the Ministry of Science, ICT, and Future Planning (No. 2013M3A6B1078882).

Conflicts of Interest: The authors declare no conflict of interest.

References

1. Geim, A.K.; Novoselov, K.S. The rise of graphene. *Nat. Mater.* **2007**, *6*, 183–191. [CrossRef] [PubMed]
2. Castro Neto, A.H.; Guinea, F.; Peres, N.M.R.; Novoselov, K.S.; Geim, A.K. The electronic properties of graphene. *Rev. Modern Phys.* **2009**, *81*, 109–162. [CrossRef]
3. Geim, A.K. Graphene: Status and Prospects. *Science* **2009**, *324*, 1530–1534. [CrossRef] [PubMed]
4. Stankovich, S.; Dikin, D.A.; Dommett, G.H.B.; Kohlhaas, K.M.; Zimney, E.J.; Stach, E.A.; Piner, R.D.; Nguyen, S.T.; Ruoff, R.S. Graphene-based composite materials. *Nature* **2006**, *442*, 282–286. [CrossRef] [PubMed]
5. Peigney, A.; Laurent, C.; Flahaut, E.; Bacsa, R.R.; Rousset, A. Specific surface area of carbon nanotubes and bundles of carbon nanotubes. *Carbon* **2001**, *39*, 507–514. [CrossRef]
6. Zhu, Y.W.; Murali, S.; Stoller, M.D.; Ganesh, K.J.; Cai, W.W.; Ferreira, P.J.; Pirkle, A.; Wallace, R.M.; Cychosz, K.A.; Thommes, M.; et al. Carbon-Based Supercapacitors Produced by Activation of Graphene. *Science* **2011**, *332*, 1537–1541. [CrossRef] [PubMed]
7. Bolotin, K.I.; Sikes, K.J.; Jiang, Z.; Klima, M.; Fudenberg, G.; Hone, J.; Kim, P.; Stormer, H.L. Ultrahigh electron mobility in suspended graphene. *Solid State Commun.* **2008**, *146*, 351–355. [CrossRef]
8. Balandin, A.A.; Ghosh, S.; Bao, W.Z.; Calizo, I.; Teweldebrhan, D.; Miao, F.; Lau, C.N. Superior thermal conductivity of single-layer graphene. *Nano Lett.* **2008**, *8*, 902–907. [CrossRef]
9. Lee, C.; Wei, X.D.; Kysar, J.W.; Hone, J. Measurement of the elastic properties and intrinsic strength of monolayer graphene. *Science* **2008**, *321*, 385–388. [CrossRef]
10. Freitag, M. Graphene—Nanoelectronics goes flat out. *Nat. Nanotechnol.* **2008**, *3*, 455–457. [CrossRef]
11. Bonaccorso, F.; Sun, Z.; Hasan, T.; Ferrari, A.C. Graphene photonics and optoelectronics. *Nat. Photon.* **2010**, *4*, 611–622. [CrossRef]
12. Hou, J.B.; Shao, Y.Y.; Ellis, M.W.; Moore, R.B.; Yi, B.L. Graphene-based electrochemical energy conversion and storage: Fuel cells, supercapacitors and lithium ion batteries. *Phys. Chem. Chem. Phys.* **2011**, *13*, 15384–15402. [CrossRef] [PubMed]
13. Choi, H.J.; Jung, S.M.; Seo, J.M.; Chang, D.W.; Dai, L.M.; Baek, J.B. Graphene for energy conversion and storage in fuel cells and supercapacitors. *Nano Energy* **2012**, *1*, 534–551. [CrossRef]

14. Bonaccorso, F.; Colombo, L.; Yu, G.H.; Stoller, M.; Tozzini, V.; Ferrari, A.C.; Ruoff, R.S.; Pellegrini, V. Graphene, related two-dimensional crystals, and hybrid systems for energy conversion and storage. *Science* **2015**, *347*, 1246501. [CrossRef] [PubMed]
15. Shao, Y.Y.; Wang, J.; Wu, H.; Liu, J.; Aksay, I.A.; Lin, Y.H. Graphene Based Electrochemical Sensors and Biosensors: A Review. *Electroanalysis* **2010**, *22*, 1027–1036. [CrossRef]
16. Huang, C.C.; Li, C.; Shi, G.Q. Graphene based catalysts. *Energy Environ. Sci.* **2012**, *5*, 8848–8868. [CrossRef]
17. Liu, H.T.; Liu, Y.Q.; Zhu, D.B. Chemical doping of graphene. *J. Mater. Chem.* **2011**, *21*, 3335–3345. [CrossRef]
18. Nigar, S.; Zhou, Z.F.; Wang, H.; Imtiaz, M. Modulating the electronic and magnetic properties of graphene. *RSC Adv.* **2017**, *7*, 51546–51580. [CrossRef]
19. Wang, X.W.; Sun, G.Z.; Routh, P.; Kim, D.H.; Huang, W.; Chen, P. Heteroatom-doped graphene materials: Syntheses, properties and applications. *Chem. Soc. Rev.* **2014**, *43*, 7067–7098. [CrossRef]
20. Liu, L.L.; Qing, M.Q.; Wang, Y.B.; Chen, S.M. Defects in Graphene: Generation, Healing, and Their Effects on the Properties of Graphene: A Review. *J. Mater. Sci. Technol.* **2015**, *31*, 599–606. [CrossRef]
21. Banhart, F.; Kotakoski, J.; Krasheninnikov, A.V. Structural Defects in Graphene. *ACS Nano* **2011**, *5*, 26–41. [CrossRef] [PubMed]
22. Schiros, T.; Nordlund, D.; Palova, L.; Prezzi, D.; Zhao, L.Y.; Kim, K.S.; Wurstbauer, U.; Gutierrez, C.; Delongchamp, D.; Jaye, C.; et al. Connecting Dopant Bond Type with Electronic Structure in N-Doped Graphene. *Nano Lett.* **2012**, *12*, 4025–4031. [CrossRef] [PubMed]
23. Fujimoto, Y.; Saito, S. Formation, stabilities, and electronic properties of nitrogen defects in graphene. *Phys. Rev. B* **2011**, *84*, 245446. [CrossRef]
24. Hou, Z.F.; Wang, X.L.; Ikeda, T.; Terakura, K.; Oshima, M.; Kakimoto, M. Electronic structure of N-doped graphene with native point defects. *Phys. Rev. B* **2013**, *87*, 165401. [CrossRef]
25. Wang, T.; Wang, L.X.; Wu, D.L.; Xia, W.; Jia, D.Z. Interaction between Nitrogen and Sulfur in Co-Doped Graphene and Synergetic Effect in Supercapacitor. *Sci. Rep.* **2015**, *5*, 9591. [CrossRef]
26. Xu, J.X.; Dong, G.F.; Jin, C.H.; Huang, M.H.; Guan, L.H. Sulfur and Nitrogen Co-Doped, Few-Layered Graphene Oxide as a Highly Efficient Electrocatalyst for the Oxygen-Reduction Reaction. *ChemSusChem* **2013**, *6*, 493–499. [CrossRef]
27. Wu, Z.S.; Winter, A.; Chen, L.; Sun, Y.; Turchanin, A.; Feng, X.L.; Mullen, K. Three-Dimensional Nitrogen and Boron Co-doped Graphene for High-Performance All-Solid-State Supercapacitors. *Adv. Mater.* **2012**, *24*, 5130–5135. [CrossRef]
28. Panchokarla, L.S.; Subrahmanyam, K.S.; Saha, S.K.; Govindaraj, A.; Krishnamurthy, H.R.; Waghmare, U.V.; Rao, C.N.R. Synthesis, Structure, and Properties of Boron- and Nitrogen-Doped Graphene. *Adv. Mater.* **2009**, *21*, 4726–4730. [CrossRef]
29. Reddy, A.L.M.; Srivastava, A.; Gowda, S.R.; Gullapalli, H.; Dubey, M.; Ajayan, P.M. Synthesis Of Nitrogen-Doped Graphene Films For Lithium Battery Application. *ACS Nano* **2010**, *4*, 6337–6342. [CrossRef]
30. Zhang, C.Z.; Mahmood, N.; Yin, H.; Liu, F.; Hou, Y.L. Synthesis of Phosphorus-Doped Graphene and its Multifunctional Applications for Oxygen Reduction Reaction and Lithium Ion Batteries. *Adv. Mater.* **2013**, *25*, 4932–4937. [CrossRef]
31. Choi, C.H.; Chung, M.W.; Kwon, H.C.; Park, S.H.; Woo, S.I. B, N- and P, N-doped graphene as highly active catalysts for oxygen reduction reactions in acidic media. *J. Mater. Chem. A* **2013**, *1*, 3694–3699. [CrossRef]
32. Ma, X.L.; Ning, G.Q.; Qi, C.L.; Xu, C.G.; Gao, J.S. Phosphorus and Nitrogen Dual-Doped Few-Layered Porous Graphene: A High-Performance Anode Material for Lithium-Ion Batteries. *ACS Appl. Mater. Interf.* **2014**, *6*, 14415–14422. [CrossRef] [PubMed]
33. Paraknowitsch, J.P.; Thomas, A. Doping carbons beyond nitrogen: An overview of advanced heteroatom doped carbons with boron, sulphur and phosphorus for energy applications. *Energy Environ. Sci.* **2013**, *6*, 2839–2855. [CrossRef]
34. Kresse, G.; Furthmuller, J. Efficient iterative schemes for ab initio total-energy calculations using a plane-wave basis set. *Phys. Rev. B* **1996**, *54*, 11169–11186. [CrossRef]
35. Kresse, G.; Furthmuller, J. Efficiency of ab-initio total energy calculations for metals and semiconductors using a plane-wave basis set. *Comp. Mater. Sci.* **1996**, *6*, 15–50. [CrossRef]
36. Kresse, G.; Joubert, D. From ultrasoft pseudopotentials to the projector augmented-wave method. *Phys. Rev. B* **1999**, *59*, 1758–1775. [CrossRef]

37. Perdew, J.P.; Burke, K.; Ernzerhof, M. Generalized gradient approximation made simple. *Phys. Rev. Lett.* **1996**, *77*, 3865–3868. [CrossRef]
38. Lee, J.H.; Kang, S.G.; Moon, H.S.; Park, H.; Kim, I.T.; Lee, S.G. Adsorption mechanisms of lithium oxides (LixO2) on a graphene-based electrode: A density functional theory approach. *App. Surf. Sci.* **2015**, *351*, 193–202. [CrossRef]
39. Pham, N.N.T.; Park, J.S.; Kim, H.-T.; Kim, H.-J.; Son, Y.-A.; Kang, S.G.; Lee, S.G. Catalytic performance of graphene quantum dot supported manganese phthalocyanine for highly efficient oxygen reduction: A DFT+U approach. *New J. Chem.* **2019**, *43*, 348–355. [CrossRef]
40. Lee, H.W.; Moon, H.S.; Hur, J.; Kim, I.T.; Park, M.S.; Yun, J.M.; Kim, K.H.; Lee, S.G. Mechanism of sodium adsorption on N-doped graphene nanoribbons for sodium ion battery applications: A density functional theory approach. *Carbon* **2017**, *119*, 492–501. [CrossRef]
41. Hwang, D.G.; Jeong, E.; Lee, S.G. Density functional theory study of CH4 and CO2 adsorption by fluorinated graphene. *Carbon Lett.* **2016**, *20*, 81–85. [CrossRef]
42. Moon, H.S.; Yun, J.M.; Kim, K.H.; Jang, S.S.; Lee, S.G. Investigations of the band structures of edge-defect zigzag graphene nanoribbons using density functional theory. *RSC Adv.* **2016**, *6*, 39587–39594. [CrossRef]
43. Zhang, J.; Yang, Z.X.; Qiu, J.Y.C.; Lee, H.W. Design and synthesis of nitrogen and sulfur co-doped porous carbon via two-dimensional interlayer confinement for a high-performance anode material for lithium-ion batteries. *J. Mater. Chem. A* **2016**, *4*, 5802–5809. [CrossRef]
44. Grimme, S.; Antony, J.; Ehrlich, S.; Krieg, H. A consistent and accurate ab initio parametrization of density functional dispersion correction (DFT-D) for the 94 elements H-Pu. *J. Chem. Phys.* **2010**, *132*, 154104. [CrossRef] [PubMed]
45. *Materials Studio*; BIOVIA: San Diego, CA, USA, 2018.
46. Mulliken, R.S. Citation Classic—Electronic Population Analysis on Lcao-Mo Molecular Wave-Functions. *Curr. Contents/Eng. Technol. Appl. Sci.* **1985**, 18.
47. Wang, H.B.; Maiyalagan, T.; Wang, X. Review on Recent Progress in Nitrogen-Doped Graphene: Synthesis, Characterization, and Its Potential Applications. *ACS Catal.* **2012**, *2*, 781–794. [CrossRef]
48. Wu, J.J.; Ma, L.L.; Yadav, R.M.; Yang, Y.C.; Zhang, X.; Vajtai, R.; Lou, J.; Ajayan, P.M. Nitrogen-Doped Graphene with Pyridinic Dominance as a Highly Active and Stable Electrocatalyst for Oxygen Reduction. *ACS Appl. Mater. Interf.* **2015**, *7*, 14763–14769. [CrossRef]
49. Li, L.J.; Dai, P.C.; Gu, X.; Wang, Y.; Yan, L.T.; Zhao, X.B. High oxygen reduction activity on a metal-organic framework derived carbon combined with high degree of graphitization and pyridinic-N dopants. *J. Mater. Chem. A* **2017**, *5*, 789–795. [CrossRef]
50. Sun, D.F.; Yang, J.; Yan, X.B. Hierarchically porous and nitrogen, sulfur-codoped graphene-like microspheres as a high capacity anode for lithium ion batteries. *Chem. Commun.* **2015**, *51*, 2134–2137. [CrossRef]
51. Wohlgemuth, S.A.; Vilela, F.; Titirici, M.M.; Antonietti, M. A one-pot hydrothermal synthesis of tunable dual heteroatom-doped carbon microspheres. *Green Chem.* **2012**, *14*, 741–749. [CrossRef]
52. Qiu, Z.Z.; Lin, Y.M.; Xin, H.L.; Han, P.; Li, D.Z.; Yang, B.; Li, P.C.; Ullah, S.; Fan, H.S.; Zhu, C.Z.; et al. Ultrahigh level nitrogen/sulfur co-doped carbon as high performance anode materials for lithium-ion batteries. *Carbon* **2018**, *126*, 85–92. [CrossRef]
53. Xiong, J.W.; Pan, Q.C.; Zheng, F.H.; Xiong, X.H.; Yang, C.H.; Hu, D.L.; Huang, C.L. N/S Co-doped Carbon Derived From Cotton as High Performance Anode Materials for Lithium Ion Batteries. *Front. Chem.* **2018**, *6*, 78. [CrossRef] [PubMed]
54. Ruan, J.F.; Yuan, T.; Pang, Y.P.; Luo, S.N.; Peng, C.X.; Yang, J.H.; Zheng, S.Y. Nitrogen and sulfur dual-doped carbon films as flexible free-standing anodes for Li-ion and Na-ion batteries. *Carbon* **2018**, *126*, 9–16. [CrossRef]
55. Wei, T.Y.; Wei, X.L.; Yang, L.W.; Xiao, H.P.; Gao, Y.; Li, H.M. A one-step moderate-explosion assisted carbonization strategy to sulfur and nitrogen dual-doped porous carbon nanosheets derived from camellia petals for energy storage. *J. Power Sources* **2016**, *331*, 373–381. [CrossRef]
56. Cai, D.D.; Wang, C.S.; Shi, C.Y.; Tan, N. Facile synthesis of N and S co-doped graphene sheets as anode materials for high-performance lithium-ion batteries. *J. Alloys Compd.* **2018**, *731*, 235–242. [CrossRef]
57. Ai, W.; Luo, Z.M.; Jiang, J.; Zhu, J.H.; Du, Z.Z.; Fan, Z.X.; Xie, L.H.; Zhang, H.; Huang, W.; Yu, T. Nitrogen and Sulfur Codoped Graphene: Multifunctional Electrode Materials for High-Performance Li-Ion Batteries and Oxygen Reduction Reaction. *Adv. Mater.* **2014**, *26*, 6186–6192. [CrossRef]

58. Xing, L.B.; Xi, K.; Li, Q.Y.; Su, Z.; Lai, C.; Zhao, X.S.; Kumar, R.V. Nitrogen, sulfur-codoped graphene sponge as electroactive carbon interlayer for high-energy and -power lithium-sulfur batteries. *J. Power Sources* **2016**, *303*, 22–28. [CrossRef]
59. Usachov, D.; Vilkov, O.; Gruneis, A.; Haberer, D.; Fedorov, A.; Adamchuk, V.K.; Preobrajenski, A.B.; Dudin, P.; Barinov, A.; Oehzelt, M.; et al. Nitrogen-Doped Graphene: Efficient Growth, Structure, and Electronic Properties. *Nano Lett.* **2011**, *11*, 5401–5407. [CrossRef]
60. Yang, Y.F.; Jin, S.; Zhang, Z.; Du, Z.Z.; Liu, H.R.; Yang, J.; Xu, H.X.; Ji, H.X. Nitrogen-Doped Hollow Carbon Nanospheres for High-Performance Li-Ion Batteries. *ACS Appl. Mater. Interf.* **2017**, *9*, 14180–14186. [CrossRef]
61. Guo, P.P.; Xiao, F.; Liu, Q.; Liu, H.F.; Guo, Y.L.; Gong, J.R.; Wang, S.; Liu, Y.Q. One-Pot Microbial Method to Synthesize Dual-Doped Graphene and Its Use as High-Performance Electrocatalyst. *Sci. Rep.* **2013**, *3*, 3499. [CrossRef]
62. Yang, Z.; Nie, H.G.; Zhou, X.M.; Yao, Z.; Huang, S.M.; Chen, X.H. Investigation of Homologous Series as Precursory Hydrocarbons for Aligned Carbon Nanotube Formation by the Spray Pyrolysis Method. *Nano* **2011**, *6*, 205–213. [CrossRef]
63. Ji, J.Y.; Zhang, G.H.; Chen, H.Y.; Wang, S.L.; Zhang, G.L.; Zhang, F.B.; Fan, X.B. Sulfonated graphene as water-tolerant solid acid catalyst. *Chem. Sci.* **2011**, *2*, 484–487. [CrossRef]
64. Park, J.E.; Jang, Y.J.; Kim, Y.J.; Song, M.S.; Yoon, S.; Kim, D.H.; Kim, S.J. Sulfur-doped graphene as a potential alternative metal-free electrocatalyst and Pt-catalyst supporting material for oxygen reduction reaction. *Phys. Chem. Chem. Phys.* **2014**, *16*, 103–109. [CrossRef] [PubMed]
65. Pauling, L. Citation Classic—The Nature of the Chemical-Bond and the Structure of Molecules and Crystals—An Introduction to Modern Structural Chemistry. *Curr. Contents/Phys. Chem. Earth Sci.* **1985**, 16.

nanomaterials

MDPI

Article

Drain Current Model for Double Gate Tunnel-FETs with InAs/Si Heterojunction and Source-Pocket Architecture

Hongliang Lu *, Bin Lu *, Yuming Zhang, Yimen Zhang and Zhijun Lv

Key Laboratory of Wide Band-Gap Semiconductor technology, School of Microelectronics, Xidian University, Xi'an 710071, China; zhangym@xidian.edu.cn (Y.Z.); ymzhang@xidian.edu.cn (Y.Z.); zhijjunlv@163.com (Z.L.)
* Correspondence: hllv@mail.xidian.edu.cn (H.L.); lubinxidian@sina.cn (B.L.); Tel.: +86-029-8820-1644 (H.L.)

Received: 21 December 2018; Accepted: 28 January 2019; Published: 1 February 2019

Abstract: The practical use of tunnel field-effect transistors is retarded by the low on-state current. In this paper, the energy-band engineering of InAs/Si heterojunction and novel device structure of source-pocket concept are combined in a single tunnel field-effect transistor to extensively boost the device performance. The proposed device shows improved tunnel on-state current and subthreshold swing. In addition, analytical potential model for the proposed device is developed and tunneling current is also calculated. Good agreement of the modeled results with numerical simulations verifies the validation of our model. With significantly reduced simulation time while acceptable accuracy, the model would be helpful for the further investigation of TFET-based circuit simulations.

Keywords: TFET; BTBT; InAs/Si; heterojunction; staggered-bandgap; source-pocket; 2D Poisson equations; parabolic approximation; Kane's model; current model

1. Introduction

Owing to the band-to-band tunneling (BTBT) mechanism, Tunnel field-effect transistors (TFETs) allow further scaling of operation voltages, which makes them the most promising alternatives to the conventional metal oxide semiconductor field-effect transistors (MOSFETs) for low-power applications [1–4]. However, the All-silicon TFET suffers from unacceptably low on-state current, which is even lower than the demand reported by the International Technology Roadmap for Semiconductors (ITRS) [5,6], due to the indirect and large bandgap and thus its practical use is retarded.

To address this issue, various design improvements [7–9] and 2D materials [10,11] have been proposed and heterojunction TFET (HTFET) made of III-V/Si have been studied as promising solution. Among all the III-V/Si structures, InAs/Si HTFET has been proposed for the highest tunneling current for the p-TFET due to its much lower tunneling mass [12], staggered band lineup and the direct tunneling process [13]. Besides that, with an ultra-thin doping pocket inserted between the heavily doped source and the intrinsic channel region [14,15], the source-pocket TFET (SP-TFET) was proposed for more abrupt tunnel junction and steeper energy band bending, resulting in reduced tunneling distance and improved on-state tunneling current. The energy-band engineering of InAs/Si heterojunction and the novel device structure of SP concept improving the device performance have motivated us to combine both the techniques in a single device to further boost up the characteristics and the InAs/Si HSP-TFET is proposed in this paper. The proposed InAs/Si HSP-TFETs can significantly enhance the device performance.

On the other hand, TFET devices so far are mainly studied by the aid of TCAD simulator, an analytical model which is helpful to provide fast results for circuit simulations is still in ample necessity. Some models [16–18] are developed for conventional TFET structures. However, in order to simplify the integration process, the tunneling volume is assumed to be the device volume which is unchanged

with the gate voltage. Although the electric field is very large near the source/channel interface, the energy band do not overlap in the region where the distance from the source/channel interface is less than the shortest tunneling distance. Namely, the tunneling window is not open. Thus no BTBT happens. Considering that the BTBT rate changes very rapidly, integrating the BTBT rate over the unchanged device volume sums extremely large but actually non-existent BTBT rate and the current would be overestimated. These models present a brief insight for the design of TFETs, but the simplification is not exactly suitable for the actual physical situation, which would lead to improper results sometimes.

In this paper, we proposed the InAs/Si HSP-TFETs combing InAs/Si heterojunction and the SP technique to improve device performance and study their impact in a single device. Furthermore, an analytical potential model for the proposed device is developed. Based on the potential model, the shortest tunnel distance considering the variation of the tunneling volume with the gate voltage is also presented and the current is calculated by numerically integrating the carrier tunneling rate over the varied tunnel volume. The paper is arranged as follows: Section 2 exhibits the mechanism of the proposed InAs/Si HSP-TFET. The model derivation of this work is shown in Section 3. The results and discussions are shown in Sect 4 and Sect 5 gives the conclusion of this work.

2. Heterojunction Source-Pocket DGTFET

The cross section view of the studied InAs/Si HSP-TFET and the coordinate system adopted in this work are shown in Figure 1. The tunneling junction between the N++ source region and the narrow P+ pocket acts as a carrier source for the channel. The device channel can include two regions, as shown in Figure 1, which are the source pocket region denoted as R_1 and the rest of channel denoted as R_2. Typical values of the device and material parameters used are listed in Tables A1 and A2 if not otherwise stated.

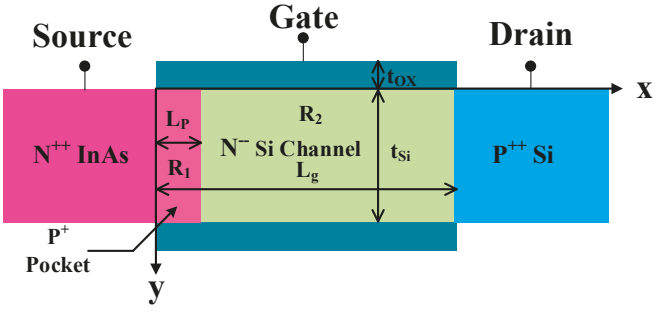

Figure 1. Schematic cross-sectional view of a p-type HSP-TFET.

The effect of the staggered bandgap of InAs/Si heterojunction and the thin fully depleted pocket reduce the tunneling distance and result in more efficient carrier injection from the source region to the channel body. Figure 2 shows the comparison in terms of transfer characteristics, on-state current and average subthreshold swing (SS). The on-state current is extracted at $|V_{GS}\text{-}V_{tunnel}| = 1$ V, where V_{GS} is the gate-to-source voltage, and V_{tunnel} is the gate voltage at which the drain current starts to be higher than the reverse leakage current [19]. The average SS is evaluated between V_{tunnel} and $|V_{GS}\text{-}V_{tunnel}| = 1$ V. It is shown that the All-Si TFET has an extremely low off-state current (<0.5 fA/μm), but its on-state current is less than 0.5 pA/μm at V_{GS} of 2 V. By applying the staggered bandgap of InAs/Si heterojunction, extraordinary device improvement about a 14000-fold can be obtained in the on-state current with much smaller average SS for the InAs/Si HTFET, compared with the All-Si TFET counterpart. Moreover, by the aid of the heavily doped pocket, the drain current of the HSP-TFET can be further improved by 2.2 times higher than that of the HTFET without SP. It should be pointed out

that despite of HSP-TFET simultaneously increased off-state current, it is still much smaller than that of a state-of-the-art 65-nm CMOS transistor which is about 10^{-11} A/μm [20].

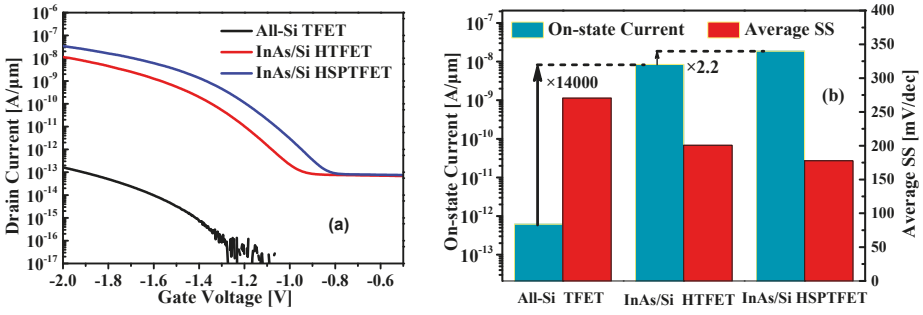

Figure 2. (**a**) Simulated I_D-V_G curves for different TFET configurations. (**b**) Plots for comparison of the on-state current and SS. The HSP-TFET is with the pocket doping $N_P = 1 \times 10^{19}$ cm^{-3} and the pocket length is $L_P = 6$ nm. The gate work function is 4.3 eV and drain bias is −0.5 V.

Figure 3 shows the simulated band diagram of InAs/Si HSP-TFET compared with InAs/Si HTFET and All-Si TFET counterparts. The energy band of All-Si TFET has been moved up-forward for the band alignment in drain region with that of InAs/Si HSP-TFET. The large negative gate voltage drop results in an overlap between the channel valence band and the source conductance band. Thus, carriers in the interval of channel valence band edge and source conductance band edge, namely the tunnel window Δφ, can be tunneled from the source conductance band to the channel valence band. As only the carriers in Δφ can tunnel from the source into the channel, the carrier energy distribution is limited and the high energy carriers are effectively filtered. Thus the electronic system is much more immune to the hot carriers compared with a conventional MOSFET [18].

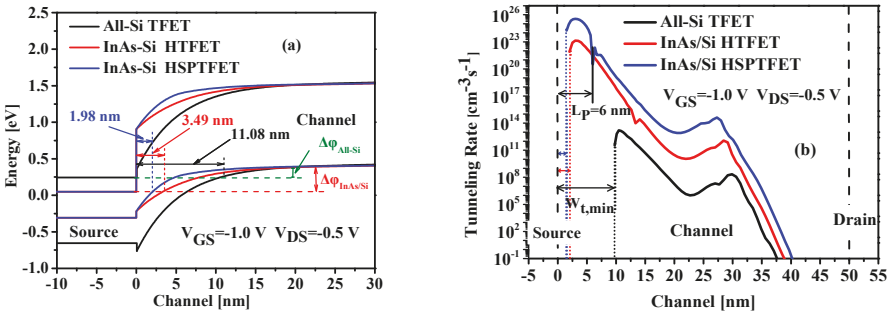

Figure 3. (**a**) Illustration of the energy band diagrams and (**b**) carrier band to band tunneling rate profile along the channel/oxide interface.

The shortest tunnel distance $W_{t,min}$ between available source conduction band states and channel valence band states must appear nearby the highest electric field and is one of the most significant parameters in Figure 3a. $W_{t,min}$ determines the lower bound of the tunnel volume. The more smaller $W_{t,min}$, the larger the tunnel volume. Owing to the smaller bandgap of InAs and the large conduction band offset at InAs/Si interface, InAs/Si HTFETs shows much smaller $W_{t,min}$ (3.49 nm) compared with that (11.08 nm) of All-Si TFETs. Thus much higher tunneling rate and larger tunnel volume are obtained for InAs/Si HTFETs, as shown in Figure 3b, which is consistent with the extraordinary improvement of the on-state current. The $W_{t,min}$ of InAs/Si HTFET can be further reduced from 3.49 nm to 1.98 nm by applying the heavily doped SP structure as plotted in Figure 3a. Figure 3b shows

that the InAs/Si HSP-TFET has greatly elevated tunneling rate, especially over the pocket region, compared with InAs/Si HTFETs and this is the reason of the highest tunnel on-state current for the InAs/Si HSP-TFET as shown in Figure 2.

3. Model Derivation for InAs/Si HSP-TFET

3.1. Channel Potential Model

With the assumption of a fully depleted channel in the subthreshold operation domain, the charge density in the channel region is equal to the ionized doping concentration. Thus the 2D Poisson equations can be used to describe the potential distribution across the regions R_1 and R_2 as Equation (1) [21].

$$\frac{\partial^2 \Phi_j(x,y)}{\partial x^2} + \frac{\partial^2 \Phi_j(x,y)}{\partial y^2} = \frac{qN_{i,j}}{\varepsilon_{Si}}, \tag{1}$$

where $\Phi_j(x,y)$ is the overall channel potential and $N_{i,j}$ is the doping concentration. The subscript j = 1, 2 for regions R_1 and R_2, respectively.

The parabolic approximation [22,23] of the potential in the direction normal to the channel surface is adopted, so that the channel potential can be described as an analytical Equation (2).

$$\Phi_j(x,y) = \varphi_j(x) + C_{j,1}(x)y + C_{j,2}(x)y^2, \tag{2}$$

Here the $C_{1,j}(x)$ and $C_{2,j}(x)$ are arbitrary functions of the surface potential $\varphi_j(x)$. At the interface between the channel and the oxide, the electric flux must be continuous. In addition, the electric field in the middle position of the channel along the y-direction equals to zero due to the structure symmetry of device.

$$\begin{cases} \left.\frac{d\Phi_j(x,y)}{dy}\right|_{y=0} = -\frac{\varepsilon_{OX}}{\varepsilon_{Si}}\left(\frac{V_{gs,j}-\varphi_j(x)}{t_{OX}}\right), \\ \left.\frac{d\Phi_j(x,y)}{dy}\right|_{y=\frac{t_{Si}}{2}} = 0, \end{cases} \tag{3}$$

where $V_{gs,j} = V_{GS} - V_{FB,j}$. $V_{FB,j}$ is the gate flat band voltage. With Equation (3), the coefficient $C_{1,j}(x)$ and $C_{2,j}(x)$ can be expressed as functions of the surface potential $\varphi_j(x)$.

$$\begin{cases} C_{1,j}(x) = -\dfrac{\varepsilon_{OX}}{\varepsilon_{Si}t_{OX}}\left(V_{gs,j} - \varphi_j(x)\right), \\ C_{2,j}(x) = +\dfrac{\varepsilon_{OX}}{\varepsilon_{Si}t_{OX}t_{Si}}\left(V_{gs,j} - \varphi_j(x)\right), \end{cases} \tag{4}$$

By substituting Equation (4), and Equation (2) into Equation (1), the 2D Poisson equations can be reduced to the well-known form.

$$\frac{\partial^2 \varphi_j(x)}{\partial x^2} - \beta^2 \varphi_j(x) = \alpha_j, \tag{5}$$

where $\beta = (2\varepsilon_{ox}/t_{ox}t_{si}\varepsilon_{si})^{1/2}$, $\alpha_j = qN_{i,j}/\varepsilon_{si} - \beta^2 V_{gs,j}$.

The general solutions for Equation (5) can be expressed as Equation (6).

$$\varphi_j(x) = A_j \exp(+\beta x) + B_j \exp(-\beta x) - \frac{\alpha_j}{\beta^2}, \tag{6}$$

Undetermined parameters A_j and B_j in Equation (6) can be solved by the boundary conditions, i.e., the potential and electric displacement continuities at the Source/R_1, R_1/R_2 and R_2/Drain interfaces.

$$\begin{cases} \varphi_1(0) = V_S + V_t In\left(N_S/n_{i,Source}\right) + \Delta E_C/q + \Delta V_{\text{Ref}}, \\ \varphi_1(L_P) = \varphi_2(L_P), \\ \frac{\partial \varphi_1(x)}{\partial x}\Big|_{x=L_P} = \frac{\partial \varphi_2(x)}{\partial x}\Big|_{x=L_P}, \\ \varphi_2\left(L_g\right) = V_D - V_t In\left(N_D/n_{i,Drain}\right), \end{cases} \tag{7}$$

where $\Delta V_{Ref} = (E_{g,Channel} - E_{g,Source})/2q$ and $\Delta E_C = \chi_{Channel} - \chi_{Source}$ is the conductance band offset of the InAs/Si heterojunction interface. $n_{i,Source}$ and $n_{i,Drain}$ are the intrinsic carrier density of source and drain regions, respectively. V_t is the thermal voltage. V_S and V_D are source and drain bias respectively. The A_j and B_j are solved by substituting Equation (7) into Equation (6), and the results are given in Equation (8).

$$\begin{cases} A_1 = & (1-M)\times\gamma_1 + N\times\gamma_2 - C_{A1}\times\gamma_3, \\ B_1 = & M\times\gamma_1 - N\times\gamma_2 + C_{B1}\times\gamma_3, \\ A_2 = & (1-M)\times\gamma_1 + N\times\gamma_2 - C_{A2}\times\gamma_3, \\ B_2 = & M\times\gamma_1 - N\times\gamma_2 + C_{B2}\times\gamma_3, \end{cases} \tag{8}$$

With

$$\begin{cases} C_{A1} = \left(\theta_1^2 + \theta_2^2\right)/FM, \\ C_{B1} = C_{A1}, \\ C_{A2} = \left(1+\theta_2^2\right)/FM, \\ C_{B2} = \left(1+\theta_2^2\right)\theta_1^2/FM, \\ FM = 2\theta_2\left(1-\theta_1^2\right), \end{cases} \quad \begin{cases} \gamma_1 = \frac{\alpha_1}{\beta^2} + \Phi_1(0,0), \\ \gamma_2 = \frac{\alpha_2}{\beta^2} + \Phi_2\left(L_g,0\right), \\ \gamma_3 = \frac{\alpha_1-\alpha_2}{\beta^2}, \end{cases} \quad \begin{cases} M = \frac{\theta_1^2}{\theta_1^2-1}, \\ N = \frac{\theta_1}{\theta_1^2-1}, \end{cases} \tag{9}$$

where $\theta_1 = \exp(\beta\times L_g)$ and $\theta_2 = \exp(\beta\times L_P)$. $\Phi_1(0,0)$ and $\Phi_2(L_g,0)$ are surface potential at x = 0 and x = L_g respectively.

With the obtained surface potential $\varphi_j(x)$, the overall channel potential $\Phi_j(x,y)$ can be obtained by Equation (2). Differentiating the channel potential, the electric-field distribution in the channel region can be obtained.

$$\begin{cases} E(x,y) = \sqrt{E_{jx}^2 + E_{jy}^2}, \\ E_{jx} = \frac{\partial \Phi_j(x,y)}{\partial x} = \left[-\frac{\beta^2}{2}y^2 + \frac{\beta^2 t_{Si}}{2}y + 1\right]\frac{\partial \varphi_j(x)}{\partial x}, \\ E_{jy} = \frac{\partial \Phi_j(x,y)}{\partial y} = \beta^2\left[y - \frac{t_{Si}}{2}\right]\left[V_{gs,j} - \varphi_j(x)\right], \end{cases} \tag{10}$$

where E(x,y) is the magnitude of the electric field. E_x and E_y are electric field along the x and y directions, respectively. The energy bands are derived from the potential expression Equation (11).

$$\begin{cases} E_{C,Source} & = (-q)\times\Phi_1(0,0), \\ E_{C,j} & = (-q)\times\Phi_j(x,y) + (\chi_{Source} - \chi_{Channel}), \\ E_{C,Drain} & = (-q)\times\Phi_2\left(L_g,0\right) + (\chi_{Source} - \chi_{Drain}), \\ E_{V,Source} & = E_{C,Source} - E_{g,Source}, \\ E_{V,j} & = E_{C,j} - E_{g,Channel}, \\ E_{V,Drain} & = E_{C,Drain} - E_{g,Drain}, \end{cases} \tag{11}$$

3.2. Drain Current Model

The $W_{t,min}$ can be used to determine the tunnel volume and calculate the device tunneling current. The carrier tunnel into the channel as the source conduction band and the channel valence band are in-line to each other. Hence, the $W_{t,min}$ can be obtained as $E_{C,Source} = E_{Vj}(W_{t,min},y)$.

$$W_{t,\min} = \frac{1}{\beta}\ln\left(Cons + \alpha_j/\beta^2 - \sqrt{\left(Cons + \alpha_j/\beta^2\right)^2 - 4A_jB_j}/2A_j\right), \tag{12}$$

With

$$Cons = \frac{\left(\Phi_1(0,0) + \chi_{Source} - \chi_{Channel} - E_{g,Channel}\right) - 0.5\beta^2\left(y^2 - t_{Si}y\right)V_{gs,j}}{1 - 0.5\beta^2(y^2 - t_{Si}y)}, \tag{13}$$

The $W_{t,min}$ reduction caused by the increased gate bias boosts the tunneling current due to the larger tunneling volume. Instead of a full quantum treatment, the tunneling carriers are modeled by a generation-recombination process. For a given tunneling path of length L which starts at x = 0 and ends at x = L, holes are generated at x = 0 and electrons are generated at x = L [24]. Thus, the carrier tunneling rate can be equivalently processed by the generation rate and the tunnel current density of carriers tunneling from the source to the channel equals to electron charge times the integral of the generation rate G_{BTBT}. Then the tunnel current can be computed by integrating the tunnel current density over tunnel volume.

Considering the exponential decrease of the tunneling rate with the tunnel distance [25], the BTBT process from source to channel is assumed to be extended up to the channel center and the BTBT process from channel to drain usually known as the ambipolar effect [26] is limited in the right part of the channel. Thus the tunnel current can be described by Equation (14).

$$\begin{cases} I_{BTBT,S-C} = q\int_0^{t_{Si}} \left(\int_{W_{t,\min}}^{\frac{L_g}{2}} G_{BTBT}(x,y)dx \right) dy, \\ I_{BTBT,C-D} = q\int_0^{t_{Si}} \left(\int_{\frac{L_g}{2}}^{L_g} G_{BTBT}(x,y)dx \right) dy, \\ I_{BTBT} = I_{BTBT,S-C} + I_{BTBT,C-D}, \end{cases} \tag{14}$$

The well-known Kane's Model [27] is used to calculate the generation rate as Equation (15).

$$G_{BTBT}(x,y) = A_K \left| \frac{E}{E_0} \right|^2 \exp\left(-\frac{B_K}{|E|} \right), \tag{15}$$

In Equation (15), E_0 = 1 V/cm and |E| is the electric field magnitude given by Equation (10). The A_K and B_K are the Kane's tunneling parameters.

4. Results and Discussion

In this part, the numerical simulations by ISE TCAD tool from Synopsys were carried out to verify the validity of our model. In this work, a non-local path BTBT model along with SRH recombination and bandgap narrowing has been employed for carrier transport.

4.1. Channel Potential

Calculating with the proposed model, the channel surface potential and electric field versus gate voltage along the x-direction are plotted in Figure 4, in which the comparison with the results simulated by TCAD tool are also shown in this figure, and the excellent agreement demonstrates the validation of our model. Owing to the non-uniform modulation of the gate voltage on the channel potential, the potential near the tunneling junction becomes steeper with the increased gate voltage, leading to much larger electric field, which can be seen in Figure 4b. Furthermore, the potential change with the increased gate voltage greatly narrows the tunneling distance for the charge carriers, thus resulting in elevating tunnel probability.

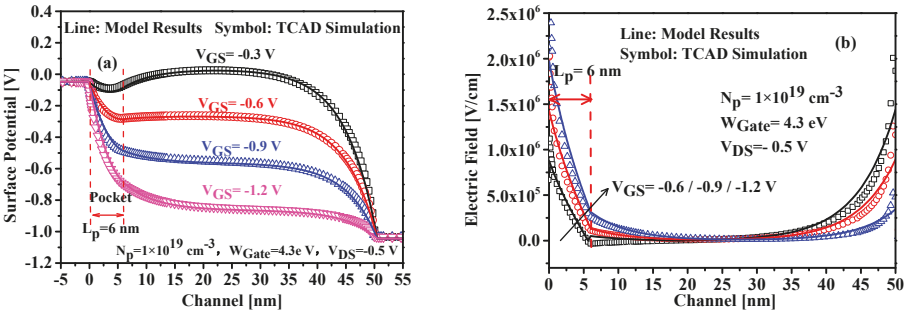

Figure 4. Variation of (**a**) the surface potential and (**b**) the lateral electric field with V_{GS}.

The surface potential distributions of InAs/Si HSP-TFET with different SP doping concentrations are plotted in Figure 5a. Increasing the SP doping concentration results in much more steeper surface potential distribution close to the source end and thus leads to improved electric field and higher drain tunnel current. But the carrier would be injected by diffusion over the barrier with a too heavily doped pocket structure. Thus, the SP doping concentration is fixed at 1×10^{19} cm^{-3} to guarantee that the carrier transport based on BTBT mechanism. Another critical parameter for the device design is the pocket length and Figure 5b shows the variation of the surface potential with pocket lengths. It can be seen that longer length is helpful to increase the steepness of the potential profile near the source end and therefore will lead to improved on-state tunnel current. The pocket length should be carefully designed because the pocket region with a fixed pocket doping density no longer remains fully depleted if it is too long and in this case, the subthreshold characteristics would be drastically degraded.

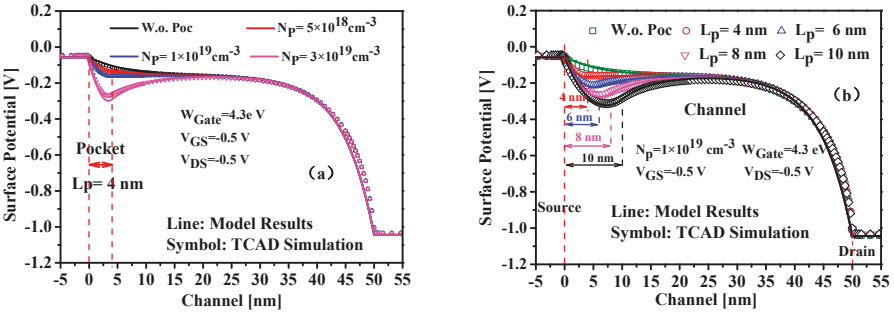

Figure 5. Surface Potential along the channel with (**a**) the pocket doping concentrations and (**b**) the pocket lengths.

Excellent agreement of modeled potential results with the TCAD simulation exhibited in Figure 5 reveals that the presented potential model can predict the impact of pocket doping concentration and pocket length on the potential distribution with good accuracy. It should be noted that although the model is derived for the proposed InAs/Si HSP-TFET, it can also be extended to the homojunction DG-TFET, with correct parameters in Table A2.

4.2. Drain Current

The variation of the shortest tunnel distance with the gate voltage is illustrated in Figure 6. The TCAD simulation results have been extracted by measuring the alignment points between the source conductance band and the channel valence band, and are very sensitive to the meshing strategy. In our simulation, a very fine mesh grid across the tunneling junction is used. The good agreement

obtained between the modeled results and the numerical simulations validates the proposed model. It is evident that the tunnel path is reduced significantly as the gate voltage increases. Due to larger tunneling volume and improved electric field, the reduction of $W_{t,min}$ with gate voltage improves tunneling current.

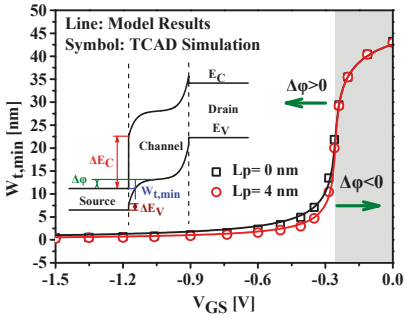

Figure 6. Shortest tunneling distance versus gate voltage. The pocket doping density for HSP-TFET is 1×10^{19} cm^{-3}. The gate work function is 4.7 eV and the drain bias is 0.5 V.

The pocket length equal to zero in Figure 6 corresponds to the case of HTFET without SP structure. The HSP-TFET with SP structure shows smaller shortest tunneling distance over a large gate-to-source voltage range in the positive tunneling widow, compared with that of HTFET and leads to higher tunnel on-state current. However, in the off-state, corresponding to the region of negative tunneling window indicated by shading, the HSP-TFET exhibits the same tunneling distance with that of HTFET, which predicts almost the same off-state tunnel current.

Figure 7 shows the transfer characteristics calculated from our model for different pocket doping concentrations and pocket lengths. It is obvious that good agreement is obtained between the model results and the numerical simulations in the on-state where the BTBT current dominates. The large deviation in the off-state results from the neglect of the SRH thermal generation which dominates the off-state leakage current. Due to the heavily doped pocket structure, the InAs/Si HSP-TFET exhibits improved drain tunneling current compared with that of InAs/Si HTFETs without SP. This can be understood from Figure 5 in which the HSP-TFET shows a potential minimum near the source-to-channel tunneling junction caused by the inserted SP structure compared with HTFET without SP structure. The reduction of $W_{t,min}$ and the increase of electric field due to the sharper potential profile help to boost the on-state tunnel current.

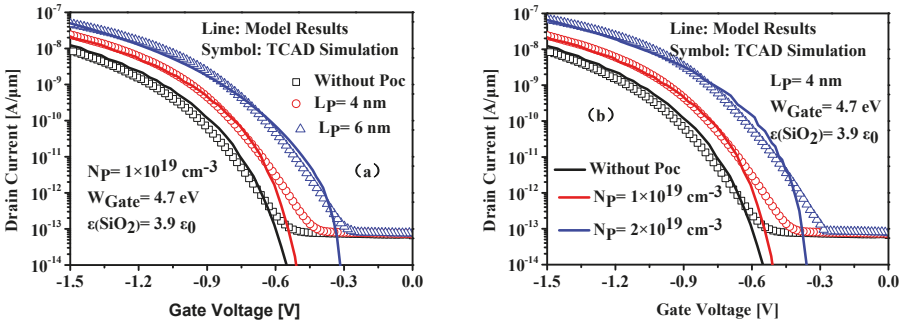

Figure 7. Transfer characteristics versus different (**a**) pocket doping concentrations and (**b**) pocket lengths.

The extracted on-state current and average SS, as functions of the source pocket doping and pocket length, are illustrated in Figure 8. Increasing the pocket doping concentration would cause the energy band to change more abruptly near the tunneling junction, as shown in Figure 5. and thus leads to elevated tunneling current and improved average SS. However, different behaviors of the on-state current and average SS versus the pocket length is exhibited in Figure 8b. It shows an optimum pocket length about 6 nm where the on-state current reaches maximum and the average SS reduces to minimum. For a fixed pocket doping, if the pocket length is increased and larger than the optimum value, the pocket no longer remains fully depleted and the mobile carriers in the pocket region screen the gate electric field, which would degrade the on-state current and also the subthreshold swing.

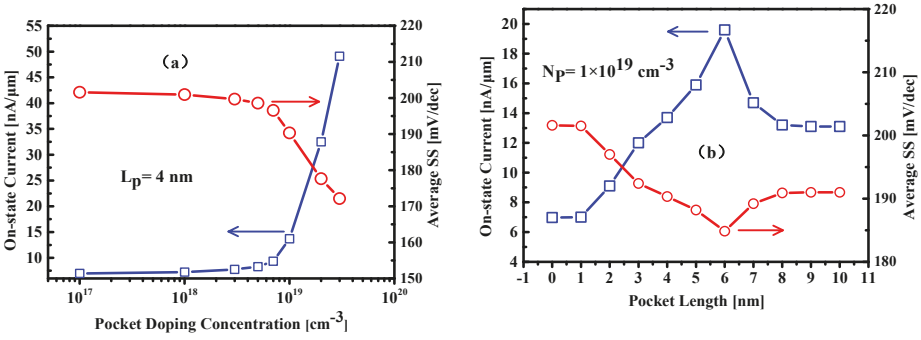

Figure 8. Plot of simulated on-state current and average SS as functions of (**a**) pocket doping concentration and (**b**) pocket length. The $N_P = 1 \times 10^{17}$ cm^{-3} and $L_P = 0$ nm correspond to the case of HTFET without SP structure.

Finally, it is should be noted that although an ideally abrupt and defect/trap-free heterojunction between InAs and Si is assumed in this work to focus on a clear presentation of current model, they are important for the analysis of TFETs. The electrons can be excited from the valence band to the trap states arising from the very high lattice mismatch of about 11.6% between InAs and Si, and subsequent be emitted to the conduction band or vice versa, which leads to increased leakage current of TFETs [13,28]. In addition, this situation can be further degraded by the phonon-assisted tunneling via the trap sates in the bandgap and enhanced recombination process resulted from the traps at or close to the InAs/Si heterojunction [29]. Fortunately, these effects should not significantly affect our discussion, thus, the exclusion is reasonable in the initial stage of the model development. It also should be pointed out that this model is structure-dependent. It can be applied for TFETs made of double gate architecture even inclding other channel materials like germanium, as long as with correct parameters in Table A2.

5. Conclusions

In conclusion, a novel InAs/Si HSP-TFET is proposed to greatly enhance the device performance. The TCAD simulations reveal that the proposed structure shows an on-state current 28000 times higher than that of All-Si TFET and 2.2 times higher than that of InAs/Si HTFET with simultaneously improved subthreshold swing. An analytical potential model with numerically calculated drain current for the InAs/Si HSP-TFET is also developed. The proposed model provides very faster results with acceptable accuracy compared with TCAD simulations and would be helpful to the investigation of TFETs.

Author Contributions: Conceptualization, B.L.; Funding acquisition, Y.Z. (Yuming Zhang); Methodology, H.L.; Project administration, Y.Z. (Yuming Zhang) and Y.Z. (Yimen Zhang); Software, Z.L.; Supervision, H.L.; Validation, Z.L.; Writing—original draft, B.L.; Writing—review & editing, Y.Z. (Yimen Zhang).

Funding: This work was supported by Advance Research Foundation of China (Grant No. 9140Axxx501), National Defense Advance Research project (Grant No. 3151xxxx301) and Frontier innovation program (Grant No. 48xx4).

Conflicts of Interest: The authors declare no conflict of interest.

Appendix A

Table A1. Device parameters used in the calculation and simulation.

Quantity	Value
Channel length, L_g (nm)	50
Pocket length, L_P (nm)	6
Source/Drain length, L_{SD} (nm)	50
Silicon layer thickness, t_{Si} (nm)	10
Gate dielectric thickness, t_{ox} (nm)	2
Source doping, N_s (cm^{-3})	1×10^{20}
Pocket doping, N_P (cm^{-3})	1×10^{19}
Channel doping, N_i (cm^{-3})	1×10^{17}
Drain doping, N_D (cm^{-3})	1×10^{21}

Table A2. Material parameters used in this work.

Quantity	Value
Vacuum permittivity	ε_0
Silicon permittivity, ε_{Si}	$11.9\varepsilon_0$
Oxide permittivity, ε_{OX}	$3.9\varepsilon_0$
Source Energy band gap (InAs), $E_{g,Source}$ (eV)	0.36
Channel Energy band gap (Si), $E_{g,Channel}$ (eV)	1.12
Drain Energy band gap (Si), $E_{g,Drain}$ (eV)	0.89
Source Affinity, χ_{Source} (eV)	4.93
Channel Affinity, $\chi_{Channel}$ (eV)	4.07
Drain Affinity, χ_{Drain} (eV)	4.18
Silicon Conduction density of states, $N_{C,Si}$ (cm^{-3})	2.58×10^{19}
Silicon Valance density of states, $N_{V,Si}$ (cm^{-3})	1.94×10^{19}
InAs Conduction density of states, $N_{C,InAs}$ (cm^{-3})	8.72×10^{16}
InAs Valance density of states, $N_{V,InAs}$ (cm^{-3})	6.66×10^{18}

References

1. Lu, B.; Lu, H.L.; Zhang, Y.; Zhang, Y.; Cui, X.R.; Lv, Z.J.; Liu, C. Fully Analytical Carrier-Based Charge and Capacitance Model for Hetero-Gate-Dielectric Tunneling Field-Effect Transistors. *IEEE Trans. Electron Devices* **2018**, *65*, 3555–3561. [CrossRef]
2. Chen, F.; Ilatikhameneh, H.; Tan, Y.; Gerhard, K.; Rajib, R. Switching Mechanism and the Scalability of vertical-TFETs. *IEEE Trans. Electron Devices* **2018**, *65*, 3065–3068. [CrossRef]
3. Strangio, S.; Palestri, P.; Lan, M. Benchmarks of a III-V TFET technology platform against the 10-nm CMOS FinFET technology node considering basic arithmetic circuits. *Solid-State Electron.* **2017**, *128*, 37–42. [CrossRef]
4. Liu, J.S.; Clavel, M.B.; Hudait, M.K. An Energy-Efficient Tensile-Strained Ge/InGaAs TFET 7T SRAM Cell Architecture for Ultralow-Voltage Applications. *IEEE Trans. Electron Devices* **2017**, *64*, 2193–2200. [CrossRef]
5. Noor, S.L.; Safa, S.; Khan, Z.R. Dual-material double-gate tunnel FET: Gate threshold voltage modeling and extraction. *J. Comput. Electron.* **2016**, *15*, 763–769. [CrossRef]
6. Semiconductor Industry Association (SIA). International Technology Roadmap for Semiconductors 2015. Available online: https://www.semiconductors.org/wp-content/uploads/2018/06/6_2015-ITRS-2.0-Beyond-CMOS.pdf (accessed on 1 February 2019)
7. Ameen, T.A.; Ilatikhameneh, H.; Fay, P. Alloy Engineered Nitride Tunneling Field-Effect Transistor: A Solution for the Challenge of Heterojunction TFETs. *IEEE Trans. Electron Devices* **2018**, *66*, 736–742. [CrossRef]

8. Ambika, R.; Keerthana, N.; Srinivasan, R. Realization of Silicon nanotube tunneling FET on junctionless structure using single and multiple gate workfunction. *Solid-State Electron.* **2017**, *127*, 45–50. [CrossRef]
9. Lu, B.; Lu, H.; Zhang, Y.; Zhang, Y.; Lv, Z.; Zhao, Y. A Novel Planar InAs/Si Hetero-TFET with Buried Drain Design and Face-tunneling Technique. In Proceedings of the 2018 14th IEEE International Conference on Solid-State and Integrated Circuit Technology (ICSICT), Qingdao, China, 31 October–3 November 2018.
10. Giannazzo, F.; Greco, G.; Roccaforte, F.; Sushant, S.S. Vertical transistors based on 2D materials: Status and prospects. *Crystals* **2018**, *8*, 70. [CrossRef]
11. Sarkar, D.; Xie, X.; Liu, W.; Cao, W.; Kang, J.; Gong, Y.; Kraemer, S.; Pulickel, M.A.; Kaustav, B. A subthermionic tunnel field-effect transistor with an atomically thin channel. *Nature* **2015**, *526*, 91. [CrossRef] [PubMed]
12. Mookerjea, S.; Krishnan, R.; Datta, S.; Narayanan, V. Effective capacitance and drive current for tunnel FET (TFET) CV/I estimation. *IEEE Trans. Electron Devices* **2009**, *56*, 2092–2098. [CrossRef]
13. Das, G.D.; Mishra, G.P.; Dash, S. Impact of source-pocket engineering on device performance of dielectric modulated tunnel FET. *Superlattices Microstruct.* **2018**, *124*, 131–138. [CrossRef]
14. Chang, H.Y.; Adams, B.; Chien, P.Y.; Li, J.; Woo, J.C. Improved subthreshold and output characteristics of source-pocket Si tunnel FET by the application of laser annealing. *IEEE Trans. Electron Devices* **2013**, *60*, 92–96. [CrossRef]
15. Mahajan, A.; Dash, D.K.; Banerjee, P.; Sarkar, S.K. Analytical Modeling of Triple-Metal Hetero-Dielectric DG SON TFET. *J. Mater. Eng. Perform.* **2018**, *27*, 2693–2700. [CrossRef]
16. Wang, P.; Zhuang, Y.; Li, C.; Jiang, Z.; Liu, Y. Drain current model for double-gate tunnel field-effect transistor with hetero-gate-dielectric and source-pocket. *Microelectron. Reliab.* **2016**, *59*, 30–36. [CrossRef]
17. Samuel, T.A.; Balamurugan, N.B. Analytical modeling and simulation of germanium single gate silicon on insulator TFET. *J. Semicond.* **2014**, *35*, 034002. [CrossRef]
18. Xu, W.; Wong, H.; Iwai, H. Analytical model of drain current of cylindrical surrounding gate pnin TFET. *Solid-State Electron.* **2015**, *111*, 171–179. [CrossRef]
19. Ionescu, A.M.; Riel, H. Tunnel field-effect transistors as energy-efficient electronic switches. *Nature* **2011**, *479*, 329–337. [CrossRef] [PubMed]
20. Lu, B.; Lu, H.; Zhang, Y.; Zhang, Y.; Cui, X.; Jin, C.; Liu, C. Improved analytical model of surface potentialwith modifiedboundary conditions for double gate tunnel FETs. *Microelectron. Reliab.* **2017**, *79*, 231–238.
21. Madan, J.; Gupta, R.S.; Chaujar, R. Analytical drain current formulation for gate dielectric engineered dual material gate-gate all around-tunneling field effect transistor. *Jpn. J. Appl. Phys.* **2015**, *54*, 094202. [CrossRef]
22. Meshkin, R.; Ziabari, S.A.S.; Jordehi, A.R. A Novel Analytical Approach to Optimize the Work Functions of Dual-Material Double-Gate Tunneling-FETs. *Superlattices Microstruct.* **2018**, *126*, 63–71. [CrossRef]
23. *Sentaurus Device User Guide*, version H-2013.03; Synopsys, Inc.: Mountain View, CA, USA, 2013; pp. 400–401.
24. Wang, C.; Wu, C.; Wang, J.; Huang, Q.; Huang, R. Analytical current model of tunneling field-effect transistor considering the impacts of both gate and drain voltages on tunneling. *Sci. China Inf. Sci.* **2015**, *58*, 1–8. [CrossRef]
25. Nigam, K.; Pandey, S.; Kondekar, N. A Barrier Controlled Charge Plasma-Based TFET With Gate Engineering for Ambipolar Suppression and RF/Linearity Performance Improvement. *IEEE Trans. Electron Devices* **2017**, *64*, 2751–2757. [CrossRef]
26. Kwon, D.W.; Kim, J.H.; Park, E.; Lee, J.; Park, T.; Lee, R.; Park, G. Reduction method of gate-to-drain capacitance by oxide spacer formation in tunnel field-effect transistor with elevated drain. *Jpn. J. Appl. Phys.* **2016**, *55*, 06GG04. [CrossRef]
27. Bessire, C.D.; Bjoörk, M.T.; Schmid, H.; Andreas, S.; Kathleen, B.R.; Heike, R. Trap-assisted tunneling in Si-InAs nanowire heterojunction tunnel diodes. *Nano Lett.* **2011**, *11*, 4195–4199. [CrossRef] [PubMed]
28. Sant, S.; Moselund, K.; Cutaia, D.; Schmid, H.; Mattias, B.; Heike, R.; Andreas, S. Lateral InAs/Si p-type tunnel FETs integrated on Si—Part 2: Simulation study of the impact of interface traps. *IEEE Trans. Electron Devices* **2016**, *63*, 4240–4247. [CrossRef]
29. Björk, M.T.; Schmid, H.; Bessire, C.D.; Moselund, K.E.; Ghoneim, H.; Karg, S.; Lonscher, E.; Riel, H. Si–InAs heterojunction Esaki tunnel diodes with high current densities. *Appl. Phys. Lett.* **2010**, *97*, 163501. [CrossRef]

nanomaterials

MDPI

Article

Tin, The Enabler—Hydrogen Diffusion into Ruthenium

Chidozie Onwudinanti [1], Ionuţ Tranca [2], Thomas Morgan [3] and Shuxia Tao [4,*]

[1] Center for Computational Energy Research, DIFFER—Dutch Institute for Fundamental Energy Research, 5612 AJ Eindhoven, The Netherlands; c.k.onwudinanti@differ.nl
[2] Department of Mechanical Engineering, Eindhoven University of Technology, 5600 MB Eindhoven, The Netherlands; i.tranca@tue.nl
[3] Plasma Material Interactions, DIFFER—Dutch Institute for Fundamental Energy Research, 5612 AJ Eindhoven, The Netherlands; t.w.morgan@differ.nl
[4] Center for Computational Energy Research, Department of Applied Physics, Eindhoven University of Technology, 5600 MB Eindhoven, The Netherlands
* Correspondence: s.x.tao@tue.nl

Received: 21 December 2018; Accepted: 16 January 2019; Published: 21 January 2019

Abstract: Hydrogen interaction with ruthenium is of particular importance for the ruthenium-capped multilayer reflectors used in extreme ultraviolet (EUV) lithography. Hydrogen causes blistering, which leads to a loss of reflectivity. This problem is aggravated by tin. This study aims to uncover the mechanism via which tin affects the hydrogen uptake, with a view to mitigation. We report here the results of a study of hydrogen interaction with the ruthenium surface in the presence of tin using Density Functional Theory and charge density analyses. Our calculations show a significant drop in the energy barrier to hydrogen penetration when a tin atom or a tin hydride molecule (SnH_x) is adsorbed on the ruthenium surface; the barrier has been found to drop in all tested cases with tin, from 1.06 eV to as low as 0.28 eV in the case of stannane (SnH_4). Analyses show that, due to charge transfer from the less electronegative tin to hydrogen and ruthenium, charge accumulates around the diffusing hydrogen atom and near the ruthenium surface atoms. The reduced atomic volume of hydrogen, together with the effect of electron–electron repulsion from the ruthenium surface charge, facilitates subsurface penetration. Understanding the nature of tin's influence on hydrogen penetration will guide efforts to mitigate blistering damage of EUV optics. It also holds great interest for applications where hydrogen penetration is desirable, such as hydrogen storage.

Keywords: DFT; surface; hydrogen; ruthenium; tin; transition state; electronegativity; bond order

1. Introduction

Hydrogen interacts with metal surfaces in many varied and important technological applications. This occurs in catalysis [1,2], as well as hydrogen separation [3,4], storage [5], and sensors [6]. The ability of the small atom to permeate metals and change their properties gives hydrogen–metal systems added significance; for instance, embrittlement of metals remains an obstacle to the transport and storage of hydrogen [7,8]. In this case, as in separation and purification, diffusion into the subsurface and bulk of the metal is quite important [9]. This interaction has been studied extensively, particularly with transition metals, and the field maintains a high level of scientific interest and relevance [10–13]. The addition of a second metal creates a so-called bimetallic surface. This often introduces significant changes to the electronic structure and characteristics of that surface relative to the single metal [14–17], with consequences for its technological applications.

The use of ruthenium on reflective optics is one such application, with a bimetallic system interacting with hydrogen. The multi-layer reflectors used in the optical systems of extreme ultraviolet

(EUV) lithography employ a ruthenium capping layer [18,19]; this surface may be contaminated by tin debris from the laser-pulsed tin plasma, the source of the EUV photons. Hydrogen used for cleaning the optics comes into contact with the surface and debris. It may penetrate the surface and diffuse to the interfaces of the multi-layer structure, where it recombines to form pockets of gas. When these pockets reach a critical pressure, the layers separate, which results in blistering of the mirror and loss of reflectivity [20,21]. This process appears to be facilitated by tin [22].

Ruthenium has been the subject of many studies [23], as it is used in diverse chemical processes. The Ru-Sn bimetallic catalyst has been studied as a promising option for selective hydrogenation of the carbonyl group [24,25], which is important in the production of unsaturated alcohols [26]. It is also a candidate for hydrogen production via glycerol steam reforming [27]. Hydrogen does not readily permeate ruthenium [28], but the existence of subsurface hydrogen has been demonstrated in ruthenium [29,30] and other metals [31], and it may be considered a precursor to dissolved or hydridic hydrogen in the bulk.

On the one hand, the undesirable effects of hydrogen penetration, i.e., blistering of the reflector, make it necessary to study the penetration process and possible solutions. On the other, the facilitation of diffusion into the ruthenium crystal opens the door to potential applications such as separation and purification. The latter is made especially attractive by the significantly lower cost of ruthenium and tin relative to palladium.

In this study, we focus on the tin-mediated hydrogen penetration of the Ru(0001) surface. Using Density Functional Theory (DFT), we demonstrate that tin affects the energy barriers to diffusion in a manner that facilitates penetration into the ruthenium. We show that adsorbed tin atoms and tin hydrides cause hydrogen to bond to the surface with a more compactly distributed charge, and also cause charge accumulation on the metal surface. The result is a lower energy barrier to subsurface diffusion.

The article is organised as follows: in the next section, we present details of the computational methodology employed. Thereafter, we report the results of calculations for hydrogen on the Ru(0001) surface, and in the ruthenium subsurface and bulk. A number of relevant ruthenium-tin-hydrogen interactions are then considered, and we discuss the changes observed upon introducing tin. Finally, we present a comprehensive analysis of the electronic charge density distributions in the examined interactions, and discuss the implications of the results.

2. Computational Methods

2.1. DFT Calculations

The results presented in this work are based on computations performed within the framework of DFT, as implemented in the Vienna Ab Initio Simulation Package (VASP) [32–34]. The calculations were performed with the generalized gradient approach as proposed by Perdew, Burke, and Ernzerhof (PBE) [35], with the following key convergence parameters: a kinetic energy cutoff of 400 eV, residual force criterion of 1×10^{-2} eV/Å, and a 1×10^{-5} eV energy convergence criterion. Slab calculations were performed with a $(9 \times 9 \times 1)$ Γ-centred *k*-points grid, while bulk calculations were done with a $(9 \times 9 \times 9)$ grid; all atoms were allowed to relax in the optimization process. In order to account for long-range dispersive interactions, all calculations were performed with the DFT-D3 dispersion correction proposed by Grimme et al. [36]. Transition state calculations were carried out using the Climbing Image Nudged Elastic Band (CINEB) algorithm [37], with a force criterion of 1×10^{-2} eV/Å and three (3) intermediate geometries for the transition state search.

The calculated lattice parameters for hexagonal close-packed (hcp) ruthenium are $a = 2.69$ Å and $c/a = 1.58$, which are in good agreement with experimental results, 2.71 Å and 1.58, respectively [38]. The surface is modelled by a slab of seven layers using a (2×2) cell, with ~ 15 Å of vacuum between the periodic images in the *z*-direction. The number of layers and the vacuum height were found to

give accurate results at reasonable computational cost—the calculated surface energy for the (2×2) cell changes by less than 2% from 5 layers to 11 layers.

Lattice parameters $a = 5.82$ Å and $b = 3.17$ Å for solid tin in the β-Sn crystal structure were found to be in good agreement with measured values, 5.83 Å and 3.18 Å, respectively [38]. Slab calculations for Sn(001) and Sn(010) surfaces were performed with $(1 \times 1 \times 3)$ and $(1 \times 3 \times 1)$ cells of 7-layer slabs, with ~15 Å vacuum.

For hydrogen, the energy of adsorption is computed per the definition

$$E_{ads} = \frac{1}{n}\left(E_{nH,surf} - E_{surf} - \frac{n}{2}E_{H_2}\right), \quad (1)$$

where $E_{nH,surf}$, E_{surf}, and E_{H_2} stand respectively for the total energies of the ruthenium slab with n adsorbed hydrogen atoms, clean ruthenium slab, and the energy of the hydrogen molecule. The formation energy of interstitial hydrogen, normalised to the hydrogen concentration, is calculated according to the definition

$$\Delta E_{H_2} = \left(E_{M_xH_y} - xE_M - \frac{y}{2}E_{H_2}\right) / \frac{y}{2}, \quad (2)$$

where x, y are respectively the number of metal atoms and the number of hydrogen atoms, while $E_{M_xH_y}$, E_M, and E_{H_2} stand respectively for the total energy of the metal hydride, the energy of each bulk metal atom, and the energy of a hydrogen molecule.

Jump frequencies for the hydrogen diffusion were extracted from the transition state calculations. The jump rate for a diffusing hydrogen atom may be expressed as

$$v = v_0 e^{-E_b/k_B T}, \quad (3)$$

where E_b is the energy difference between the transition state and ground state. For bulk diffusion, the pre-exponential factor v_0 in Equation (3) may be approximated by the expression [39]

$$v_0 = \frac{\prod_{i=1}^{N} \omega_i}{\prod_{i=1}^{N-1} \omega_i^*}, \quad (4)$$

where ω_i and ω_i^* are the vibrational frequencies in the initial and transition states respectively, obtained by determining the the Hessian matrix (matrix of the second derivatives of the energy with respect to atomic positions).

Due to the low mass of the hydrogen atom, its adsorption and diffusion behaviour is, in general, influenced by zero-point energy (ZPE). The ZPE is calculated by the relation

$$ZPE = \frac{\sum_i h v_i}{2}, \quad (5)$$

where v_i is a real normal mode frequency. The zero point energy for a hydrogen molecule (H_2) calculated thus is 0.27 eV (0.135 eV per H atom), corresponding to a vibrational mode of 4354 cm^{-1}, in good agreement with the experimentally-determined value of 4401 cm^{-1} [40]. However, ZPE contributions are not explicitly included in this work, as they do not affect the computed energies and barriers to a significant degree, particularly in relation to one another.

2.2. Electronic Structure and Bonding Analysis

In addition to the energy calculations, we have carried out an in-depth analysis of the chemical bonding for a thorough understanding of the interaction between species. The bonds of main interest are those between the diffusing hydrogen atom and the surface ruthenium atoms. We investigated the Bader atomic charges and volumes [41–44], the Density Derived Electrostatic and Chemical (DDEC6) bond orders and net atomic charges [45,46], the electron density and Laplacian at bond critical points

(BCP) [47], and also the Crystal Orbital Hamilton Population (COHP) and Crystal Orbital Overlap Population (COOP) functions [48–51].

The Bader charge is a measure of the electron occupation on an atom, and indicates charge transfer, while the Bader volume is an indication of how closely the charge associated with each atom is localised around the nucleus. The bond-critical points (BCPs) were assigned to saddle-points of electron density along the bond-paths. The electron density value at the BCP shows the covalent energy contribution to the chemical bond. The covalent nature of the bond is reflected in the bond order, with a higher value showing a stronger covalent bond. The sum of bond orders for each atom, its total bond order, is an indication of the activity of the atom in that particular configuration. The ionic contribution of a bond can be characterized by net atomic charge, which quantifies the charge transfer between atoms. The Laplacian, the scalar derivative of the gradient vector field of the electron density, indicates where the electronic charge is locally concentrated or depleted. The sign and value of the Laplacian at the BCP provide information on the nature of a bond, with a negative sign indicating a shared interaction (e.g., covalent bonding), while a positive sign indicates a non-covalent interaction such as ionic, hydrogen, or van der Waals [52,53].

The COOP and COHP enable the extraction of information about bonding in the system on the basis of Partial Density of States (PDOS) and Bond Order Overlap Population density. They allow us to identify bonding, non-bonding, and anti-bonding interaction domains for pairs of atoms (or orbitals). The COOP is defined according to the formula:

$$\mathrm{COOP}_{ij}(E) = S_{ij}\Sigma_n c_i^n c_j^{*n}\delta(E - E_n), \tag{6}$$

where $S_{ij} = \langle \varphi_i | \varphi_j \rangle$ is the overlap of atomic orbitals φ_i and φ_j, and c_i and c_j are respectively the coefficients of these atomic orbitals in the molecular orbital ψ_n. Positive and negative COOP values indicate bonding and anti-bonding interactions, respectively, while a zero value represents a non-bonding interaction. The closely-related COHP is defined thus:

$$-\mathrm{COHP}_{ij}(E) = H_{ij}\Sigma_n c_i^n c_j^{*n}\delta(E - E_n), \tag{7}$$

where H_{ij} represents the Hamiltonian matrix element between atomic orbitals φ_i and φ_j. In replacing the S_{ij} matrix with the H_{ij}, the COHP values are reversed: negative for bonding and positive for anti-bonding, with zero values again representing a non-bonding interaction. More thorough discussions of the COOP and COHP techniques can be found in the cited literature [48–51].

Combining these analytical tools allows us to carry out a comprehensive examination of the relevant bonds in each modelled system and reveal the underlining reaction mechanisms. Recently, computational studies using a combination of these electronic structure analysis techniques have led to an improved understanding of the reactivity and scaling laws on transition metal surfaces [13].

3. Results

In this section, we present the results of DFT calculations of hydrogen adsorption and diffusion. In the first two subsections, we report the results for hydrogen interaction with ruthenium and tin, respectively. For the former, we show the stable configurations and their energies of formation, and also present the results of CINEB transition state calculations for hydrogen diffusion and the corresponding energy barriers. In Section 3.3, to show the influence of the tin on the H–Ru interaction, we present the range of calculations performed for hydrogen–ruthenium-tin interactions on the Ru(0001) surface. The calculations cover adsorption, surface diffusion, and subsurface penetration of hydrogen.

3.1. Hydrogen and Ruthenium

3.1.1. Surface, Subsurface, and Bulk

We calculated adsorption energies of hydrogen atoms on the ruthenium surface to identify the relative stability of different adsorption sites. The Ru(0001) surface is chosen as it has the lowest surface energy γ and is therefore the most commonly-exposed; it is well-studied and represented in the literature. We calculated the energy of adsorption of hydrogen at ¼ monolayer (ML), i.e., one hydrogen atom for four surface ruthenium atoms in our (2 × 2) cell. Four sites are considered for adsorbed hydrogen atoms on the pure Ru(0001) surface, as shown in Figure 1: *top*, *bridge*, *hcp*, and *fcc* sites. We have also identified the subsurface and bulk interstitial sites for hydrogen in ruthenium. The results of the calculations are summarised in Table 1.

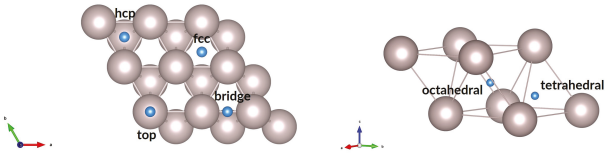

Figure 1. Surface adsorption and bulk interstitial sites for hydrogen on Ru(0001) and in Ru bulk. Blue spheres represent hydrogen atoms.

For Ru(0001), the *fcc* site was found to be most favourable with $E_{ads} = -0.64$ eV, a slight energy advantage of 0.06 eV relative to the *hcp* site. The top site is the least favourable at −0.15 eV. Nonetheless, the overall result for the four adsorption modes indicates that adsorption readily occurs on the ruthenium surface, as all sites have negative values for E_{ads}. The trend in energies and the preference for the *fcc* site is in agreement with the results reported in the literature [54,55]; the differences can be attributed to the different software, functionals, parameters, and convergence criteria used in the computations.

Table 1. Energies and structure parameters for adsorbed and interstitial hydrogen on Ru(0001) and in ruthenium bulk. Adsorption energies correspond to ¼ ML hydrogen coverage, while hydride formation energies are for hydrogen concentration (H/Ru) equal to ⅛ . Sites marked "*" correspond to calculations done with one (1) Sn adatom in an *hcp* site; *fcc_Sn* is the *fcc* site closest to the Sn adatom in an hcp site.

	E_{ads} [eV]			ΔE_{H_2} [eV]	
	This Work	**Other**		**This Work**	**Other**
top	−0.15	−0.14 [55], −0.09 [54]	T_{bulk}	0.76	
bridge	−0.45	−0.44 [55], −0.43 [54]	O_{bulk}	0.21	
hcp	−0.58	−0.50 [55], −0.52 [54]	T_{sub}	0.90	1.04 [55]
fcc	−0.64	−0.59 [55], −0.55 [54]	O_{sub}	0.15	0.37 [55]
top *	0.01				
hcp *	−0.52				
fcc *	−0.58				
fcc_Sn *	−0.33				

An interstitial hydrogen atom in ruthenium bulk can occupy one of the two sites shown in Figure 1, octahedral or tetrahedral, within the voids found in the hcp crystal structure. The results presented in Table 1 show that the interstitial sites have positive energies of formation with relative to H_2; therefore, interstitial hydride formation is unfavourable in ruthenium at this concentration

(eight ruthenium atoms per hydrogen atom). This aligns with experimental data, which show very low hydrogen solubility in ruthenium due to the highly endothermic nature of the reaction [28].

Overall, hydrogen readily adsorbs on the Ru(0001) surface, as shown by the calculated adsorption energies. According to Luppi et al., the H_2 molecule does not face a large barrier to dissociation on the ruthenium surface: from 0.013 eV to 0.436 eV, depending on the initial configuration and exchange-correlation functional used in the computations [56]. Therefore, dissociative adsorption of molecular hydrogen on ruthenium occurs easily. However, our results show that interstitial hydrogen in the ruthenium bulk is not thermodynamically favoured.

3.1.2. Diffusion

In order to acquire a more complete picture of the hydrogen–ruthenium interaction on the surface and in the bulk of the metal, we performed transition state calculations using the CINEB method. For a number of diffusion scenarios, we calculated transition states and energy barriers to hydrogen diffusion, covering (i) surface diffusion, (ii) bulk diffusion, and (iii) subsurface penetration.

For surface diffusion, we have found the transition state for diffusion of an adsorbed hydrogen atom from an *fcc* site to a neighbouring *hcp* site, and vice versa. Both transition states are found to be more or less the bridge adsorption mode, in which the hydrogen atom is equidistant from two neighbouring surface Ru atoms, above the axis joining the atoms. We found the energy barrier to be 0.18 eV for the *fcc* to *hcp* jump; the barrier for the reverse transition (*hcp* to *fcc*) is even lower, at 0.12 eV, due to the 0.06 eV difference in adsorption energies of the *hcp* and *fcc* sites. These values indicate a largely favourable energy landscape for diffusion of adsorbed hydrogen across the Ru(0001) surface, and this conclusion agrees with the findings reported elsewhere [57,58].

The picture for bulk diffusion is somewhat more complicated. As Figure 2 illustrates, the two stable interstitial sites (octahedral and tetrahedral sites) imply four diffusion paths: (i) tetrahedral to octahedral (TO), (ii) tetrahedral to tetrahedral (TT), (iii) octahedral to octahedral (OO), and (iv) octahedral to tetrahedral (OT). The transition state for each path has the diffusing atom passing through a triangle formed by three ruthenium atoms. The energy barriers for all four paths are listed in Figure 2, as are the jump frequencies derived from the vibrational analyses of the interstitial hydrogen states and the transition states. The energy barriers for the jumps (0.21–0.75 eV) and the jump frequencies suggest that hydrogen diffusion in the ruthenium bulk is quite rapid. For the most important diffusion event, subsurface penetration, we have looked at one key diffusion path: from the *fcc* site on the surface to the octahedral interstitial site in the subsurface. As these sites represent the most favourable locations for hydrogen on the surface and in the subsurface void, we believe that this is the most likely path for hydrogen penetration into the metal. The energy barrier is found to be 1.06 eV, which indicates that this diffusion step is unfavourable from a thermodynamic standpoint, although it remains accessible. Most importantly, this is the largest energy barrier faced by a hydrogen atom in going from the molecule in vacuum to the metal surface, across the surface, and into the metal bulk.

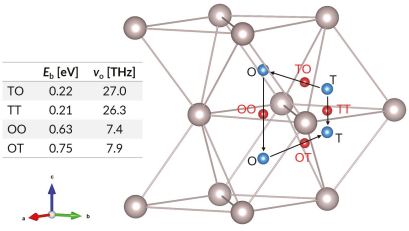

Figure 2. Interstitial hydrogen diffusion paths and transition states. Blue spheres represent interstitial sites, while red spheres indicate transition states. O and T correspond to octahedral and tetrahedral sites; OO, OT, TO, and TT show the corresponding diffusion path ways between these sites. The accompanying table shows energy barriers and jump frequencies (per Equation (4)) for the interstitial diffusion paths, for hydrogen concentration (H/Ru) equal to 1/16 .

3.2. Hydrogen and Tin

We evaluated hydrogen adsorption on tin surfaces by calculating adsorption energies for a number of sites on the Sn(100) and Sn(010) surfaces. The tin slab for both surfaces is a 1×1 cell of a β-Sn structure with seven layers. At ¼ ML and ⅕ ML hydrogen coverage for the Sn(100) and Sn(010) surfaces respectively, all adsorption sites without exception have positive energies relative to H_2, i.e., dissociation on these tin surfaces is entirely unfavourable. This points to the conclusion that tin deposited on the ruthenium surface does not provide a site of increased dissociation/adsorption of hydrogen molecules.

Tin, however, forms volatile hydrides. Stannane (SnH_4) and possibly other hydride compounds are formed when tin is etched from a ruthenium surface by hydrogen. Stannane readily evaporates, adsorbs, and dissociates on the ruthenium surface, which results in the persistence of tin on the ruthenium surface [22,59,60].

3.3. The Effect of Tin

We continue our investigation of the hydrogen-tin-ruthenium interaction on the Ru(0001) surface by calculating the adsorption energies for ¼ ML of tin on the Ru(0001) surface, finding that the *hcp* site is thermodynamically most favoured at this coverage, with $E_{ads} = -1.49$ eV. The adsorption energy for the *fcc* site differs by 0.09 eV from that of the *hcp* site, while the *top* site is 0.55 eV higher in energy. We found the energy barrier for tin migration from the *hcp* to the *fcc* site to be 0.13 eV. The barrier for the reverse jump is 0.04 eV; the difference is entirely due to the relative adsorption energies of the sites. Therefore, neither tin nor hydrogen faces a large energy barrier to diffusion on the Ru(0001) surface.

We consider the adsorption and diffusion of hydrogen on the Ru(0001) surface with tin present. A tin atom is located at its preferred *hcp* site on a 2×2 Ru(0001) slab, and the adsorption energies are calculated for the subsequent adsorption of hydrogen to the surface. In addition to the earlier-described *top*, *hcp*, and *fcc* sites, a second type of *fcc* site (*fcc_Sn*) is found, which has the hydrogen atom in the *fcc* site closest to the Sn atom. The calculated adsorption energies are given in Table 1. As with the clean ruthenium surface, the *fcc* site is lowest in energy ($E_{ads} = -0.58$ eV); the *top* site is least favoured, with its slightly positive adsorption energy of 0.01 eV. Overall, the hydrogen atom tends to occupy sites which are not in close proximity to the tin atom. These surface adsorption results are similar to findings for PtSn surface alloys [61], on which hydrogen adsorption sites near tin are higher in energy. The *fcc_Sn* site (−0.33 eV) is higher in energy than the *hcp* and *fcc* sites, and the barrier faced by hydrogen in jumping to this site is higher than the barrier when jumping to a site not next to the tin atom. This preference for ruthenium has important consequences for hydrogen diffusion across the Ru(0001) surface in the presence of tin, as the hydrogen jump trajectory becomes more convoluted (see Figure 3) due to the change in the energy landscape and blockage of sites by tin atoms. It follows

that the surface mobility of hydrogen is reduced by this obstacle, with consequences for hydrogen diffusion into the subsurface.

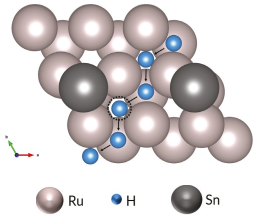

Figure 3. Example jump trajectory of H atom on Ru(0001) with ¼ ML Sn. The highlighted site (dashed circle) is the *fcc* site next to an Sn atom (*fcc_Sn*).

The presence of tin also results in a substantial change in the energy barrier to subsurface penetration. Figure 4 shows a comparison of the energy barriers for the migration of a hydrogen atom from the *fcc* site on the surface to a subsurface octahedral site in the presence and absence of tin. These cases correspond to adsorption and dissociation of progressively more hydrogenated tin hydrides (SnH, SnH_2, SnH_3, SnH_4) or co-adsorption of tin and varying quantities of hydrogen. The energy barrier drops to 0.28 eV when the stannane molecule is the source of the diffusing atom.

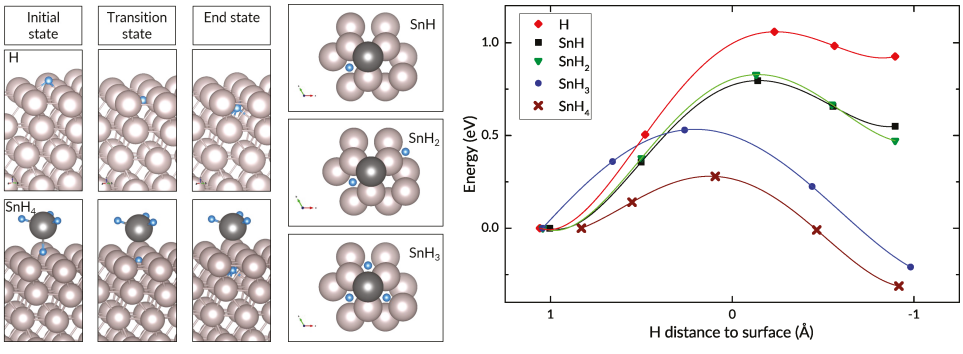

Figure 4. (**a**) initial, transition, and end states of hydrogen subsurface diffusion for a hydrogen atom (top row) and for SnH_4 (bottom row) on Ru(0001); (**b**) top view of adsorbed SnH, SnH_2, and SnH_3 configurations; (**c**) energy profiles for diffusion of a hydrogen atom from an *fcc* site to a subsurface octahedral site. Negative distance values indicate that the H atom is beneath the ruthenium surface.

It is important to note that the studied scenarios are not a simple progression from low hydrogen levels to high. The cases for SnH and SnH_2 are very similar, differing only in the presence of a second hydrogen atom at a considerable distance from the tin atom. Their transition states are similar, with the diffusing hydrogen atom located in the centre of a triangle formed by three Ru surface atoms. The relative position of the tin atom is unchanged. However, the SnH_3 case is different from the previous two in that its transition state and final state have the tin atom at the *fcc* site, above the penetrating hydrogen atom. In this, it is similar to the transition state of the case with the stannane molecule. Despite the clear differences in geometry and energies for all the scenarios, the initial and final positions of the diffusing hydrogen atom are the same in all cases: *fcc* site and octahedral site, respectively (see Figure 4). In all cases, the penetrating atom is found in the midst of three surface atoms in the transition state.

One other modelled case, which differs from all of those described in the preceding paragraph, is the case for a vertically-oriented SnH_2 molecule (SnH_2*), with a hydrogen atom above the *fcc* site.

As shown in Figure 5, the molecule does not adsorb on the Ru(0001) surface; rather, at the end of the relaxation calculation, the hydrogen atom which is initially closer to the metal surface is located in the octahedral subsurface site. The tin atom ends up at the *fcc* site, with the second hydrogen atom adsorbed on top of the tin atom. Therefore, what our calculations show is a more or less barrier-less penetration through the surface when the molecule approaches the surface in this configuration.

As mentioned earlier, the energy barrier to subsurface penetration for hydrogen on an otherwise clean Ru(0001) surface equals 1.06 eV. When tin is present, the energy barrier is lower in all the different test cases: 0.80 eV for SnH, 0.83 eV for SnH_2, 0.53 eV for SnH_3, and 0.28 eV when the hydrogen atom is taken from the adsorbed SnH_4 molecule, which is a considerable drop from the value for hydrogen on Ru(0001) with no tin present. For subsurface penetration at sites far from the tin atom, the energy barrier is essentially unchanged. In other words, the diffusion of a hydrogen atom from the *fcc* site on the Ru(0001) surface to the underlying octahedral void in the subsurface is made significantly easier by the proximity of a tin atom.

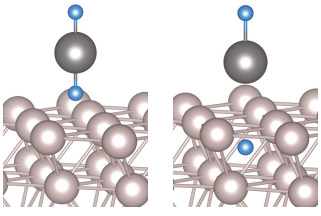

(**a**) (**b**)

Figure 5. (**a**) Initial and (**b**) end states for SnH_2* (vertically-oriented SnH_2 molecule) on Ru.

3.4. Charge Density Analysis

A deeper look into the effect of tin on the subsurface penetration is obtained by analysing the electronic charge density, based on the output of the DFT calculations. In the various penetration scenarios, the bonds which are formed and broken affect the energy barrier to H penetration, and so do the electronic configurations of the participating H, Sn, and Ru surface atoms. Via bond order, Bader charge, and topological analyses, we examined the changes in charge density which accompany the changes in the energy barriers. The main focus is on the bonds between the diffusing hydrogen atom and the three surrounding ruthenium atoms, because of their direct relevance to the transition from the surface *fcc* site to the subsurface site, and the analyses reveal trends in various characteristics of the Ru–H bonds in the initial adsorbed state (Table 2). The salient ones—energy barrier, reaction energy, atomic volume and bond order of the hydrogen atom—are plotted in Figure 6 for each diffusion scenario we explored. We find that the sum of bond orders for hydrogen is inversely proportional to the barrier to diffusion, while a smaller H atomic volume and more negative reaction energy correspond to lower diffusion barriers. We consider these trends and their implications in more detail in the Discussion section.

An illustration of one of the differences in bonding is provided in Figure 7. The topological analysis of the electron density distribution shows a symmetrical allocation of bonds between the H atom in the *fcc* position and three surrounding Ru atoms on the Ru(0001) surface (Figure 7a). The central triangle shows the extent of the electron density associated with the adsorbed H atom. When an SnH_4 molecule is adsorbed on the surface, with one hydrogen atom oriented downwards, the bonds formed between the ruthenium atoms and the hydrogen atom are nearly identical to those formed by the lone H atom, with the important difference being the bond critical points' location closer to the hydrogen atom; the triangle demarcating the H atom's basin is perceptibly smaller in area in Figure 7c (SnH_4 on Ru) than in Figure 7a (H on Ru). This indicates that the charge associated with the hydrogen atom is located in a smaller region, and this is confirmed by the calculated atomic volume of hydrogen (Table 2, Figure 6). In the transition state, in which the hydrogen atom is surrounded

by three (3) Ru atoms in the plane of the Ru(0001) surface, the electron density concentrated around the diffusing hydrogen atom is confined within similar size volumes, irrespective of the structure considered (Figure 7d–f).

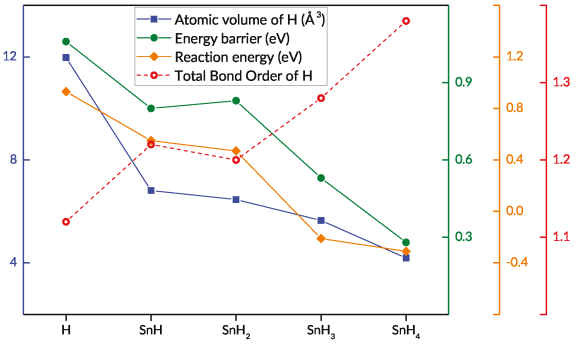

Figure 6. Energy barrier, formation energy, atomic volume and sum of the bond orders of the diffusing hydrogen atom in the initial state for each modelled diffusion scenario.

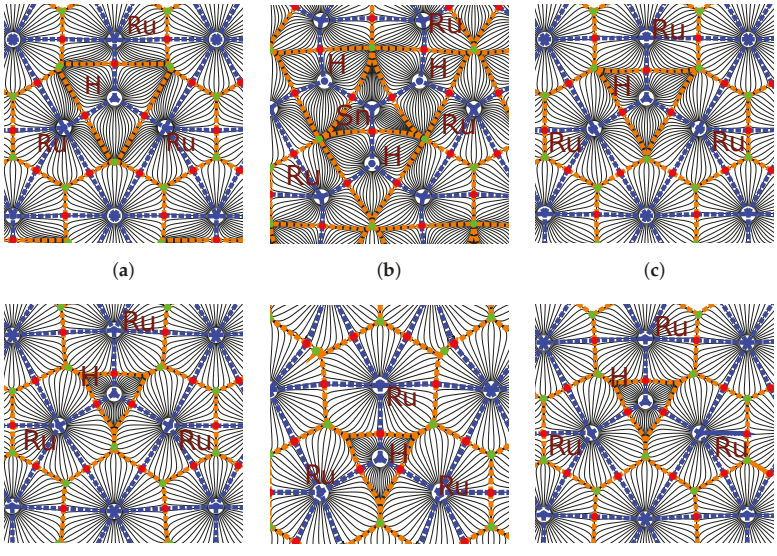

Figure 7. Topological analysis of the electron density for (**a**–**c**) H on Ru(0001), SnH_3 on Ru, and SnH_4 on Ru, respectively; (**d**–**f**) transition states with H from the adsorbate (H, SnH_3, and SnH_4 respectively) between three ruthenium surface atoms. The figures show the horizontal plane through the diffusing hydrogen atom. Atomic basins are circumscribed by dashed orange lines. Within each atomic basin, the blue dot marks the position of the nucleus. Bond paths are shown with dashed blue lines. Along each bond path, the red dot represents the bond critical point (BCP). The green dots represent the ring critical points.

Table 2. Characteristics of diffusing H atom and bonds between H atom and surrounding Ru surface atoms in the initial state. Values for SnH_2* do not correspond to clearly-defined initial and transition states (see text). Inter-atomic distances (d_{H-Ru}), bond critical point (BCP) distances (d_{H-BCP}), electron density and its Laplacian at BCPs are average values for 3 Ru–H bonds. Net atomic charge (NAC) for Ru is sum over 4 surface Ru atoms in (2×2) unit cell.

	d_{H-Ru}/ d_{H-BCP} [Å]	Total Bond Order	Electron Density	Laplacian	Bader Volume [Å^3]	NAC			Reaction Energy [eV]	Barrier [eV]
						H	Ru	Sn		
H	1.90/0.69	1.12	0.50	2.79	11.98	−0.051	−0.01	-	0.93	1.06
SnH	1.89/0.68	1.22	0.50	3.59	6.81	−0.059	−0.26	0.22	0.55	0.80
SnH_2	1.88/0.68	1.20	0.52	3.56	6.46	−0.061	−0.20	0.25	0.47	0.83
SnH_3	1.89/0.68	1.28	0.51	3.53	5.65	−0.075	−0.14	0.33	−0.21	0.53
SnH_4	1.82/0.63	1.38	0.56	3.86	4.19	−0.062	−0.23	0.57	−0.31	0.28
SnH_2 *	1.93/0.70	1.54	0.45	3.54	3.54	−0.061	−0.20	0.25	-	-

Charge density difference ($\Delta\rho$) plots paint a three-dimensional picture of the influence of tin on the charge density distribution. Figure 8 shows the charge difference for the initial and transition states for the H, SnH_3, and SnH_4 cases. In Figure 8a, which shows an adsorbed H atom at the *fcc* site on the Ru(0001) surface, the H atom is surrounded by a region of accumulation; this indicates a net transfer of charge density to the hydrogen from the areas of depletion around the three surrounding Ru atoms. There are also small regions of increased density near the Ru atoms, beneath the surface. The transition state in Figure8d is quite similar, with smaller regions of depletion on the Ru atoms. For the SnH_4 case (Figure 8c,d), the charge density donated to the hydrogen's 1*s* orbital is taken not only from the ruthenium, but in large part from the region between the H and Sn atoms. This points to the transfer of charge to the more electronegative hydrogen. Furthermore, the small regions of charge accumulation on the Ru atoms are now positioned above the ruthenium surface. The transition state shows redistribution of the charge to regions between the Ru atoms and the Sn atom, with a large depletion region above the penetrating H atom.

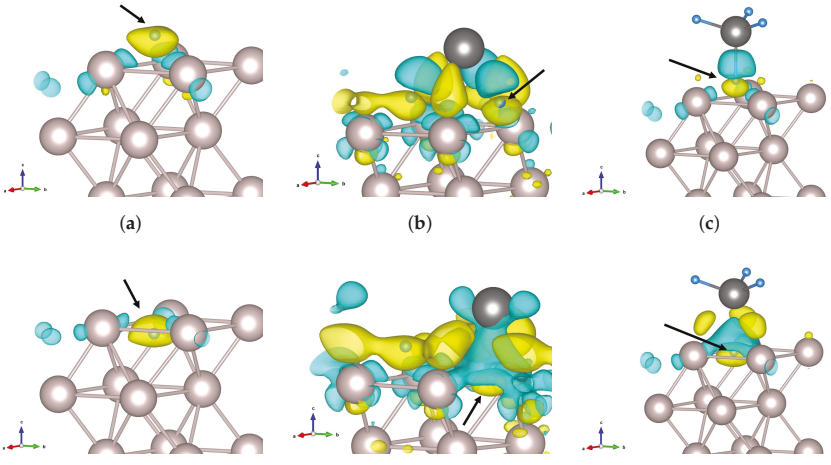

(**a**) (**b**) (**c**)

(**d**) (**e**) (**f**)

Figure 8. Charge difference for (**a**–**c**) H on Ru(0001), SnH_3 on Ru, and SnH_4 on Ru, respectively; (**d**–**f**) transition states with H from the adsorbate (H, SnH_3, and SnH_4, respectively) between three ruthenium surface atoms. In all the figures, the yellow isosurface is for charge density −0.004 e Å^{-3}, and shows regions of charge accumulation, while the cyan is for +0.004 e Å^{-3}, and shows regions of charge depletion. The black arrow shows the location of the diffusing hydrogen atom.

Due to the number of atoms on the ruthenium surface, SnH_3 on Ru presents the most complex interactions, which is evident from Figure 8b,e. The donation to the hydrogen is again present, but the source of the transferred charge is different. Each ruthenium atom on the surface has several small depletion zones, but the charge redistribution has resulted in large accumulation zones between the Sn atom and the surrounding Ru atoms, interleaved with depletion zones above the adsorbed hydrogen atoms, which are also surrounded by areas of increased charge density. There appears to be significant charge transfer from the Sn atom, both to the hydrogen atoms and the surface ruthenium atoms. In the transition state, a large depletion zone similar to that found in Figure 8f is found above the diffusing hydrogen atom, also surrounded by zones of increased charge density. The implication is that electron–electron repulsion in the SnH_3 and SnH_4 cases makes the transition state more accessible, and makes the end state more energetically favourable, which is reflected in the exothermic nature of the reactions.

Using the LOBSTER code [51], we performed density-of-states and COHP/COOP calculations. We extracted the total and projected densities of states for the various cases and computed the orbitalwise COHP and COOP for the hydrogen atom and the surface ruthenium atoms. In Figure 9, we present the projected densities of states (PDOS) curves for the *d*-band electrons of the ruthenium atoms on the surface, with different adsorbates; the COHP for the interaction between the key hydrogen atom and one of the three surrounding ruthenium atoms are also given.

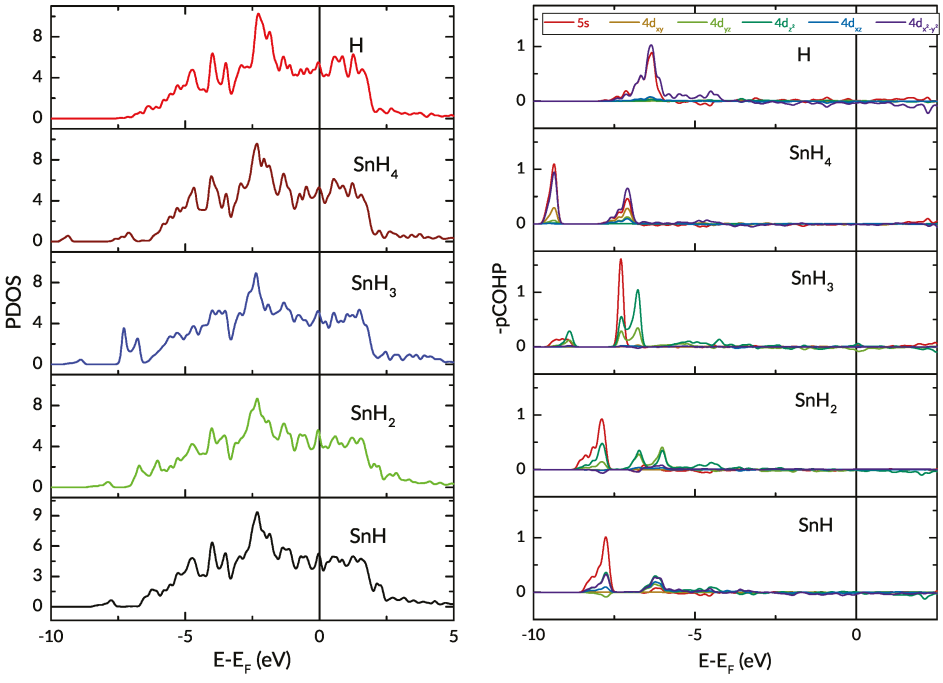

(**a**) (**b**)

Figure 9. (**a**) projected Density of States for *d*-band of ruthenium surface atoms with different adsorbates; and (**b**) projected COHP for Ru–H interaction. i.e., one ruthenium atom and the adsorbed hydrogen atom. For clarity, the COHP for the weakest interactions are not shown. In all cases, the initial structure is considered.

The main differences in the density-of-states can be observed in the lowest energy levels (below −5 eV), where the adsorbed hydrogen and tin atoms cause the appearance and/or shift of peaks. The centre of the *d* band distribution is lower when the Sn atom is adsorbed on the Ru(0001) surface,

and moves progressively lower with the adsorption of more hydrogen atoms. The *d* band width increases as the band centre is shifted downward. In the COHP plots (–pCOHP, to be precise), significant differences can be seen in the orbitals which contribute to the bonding between the atoms. We show in Figure 9 the COHP for the key hydrogen atom and one of the surface Ru atoms surrounding it. Whereas both the 5*s* and $4d_{x^2-y^2}$ orbitals dominate the bonding and very slight anti-bonding populations for the H and SnH_4 adsorbates, the 5*s* contribution is much reduced for the other cases with a tin atom on the ruthenium surface, in which the $4d_{z^2}$ interaction with the hydrogen comes to prominence as more hydrogen atoms are added. The COHP for the other Ru–H pairs in the same scenario are not necessarily identical to those in Figure 9 because the tin affects the surrounding Ru atoms to different degrees, based on their distance and arrangement. Taken together, the COHP and the $\Delta\rho$ plots of Figure 8 confirm that the electrons participating in the bonding generally originate from different orbitals for different adsorbates. This is especially apparent when the SnH_3 case is compared to the others.

4. Discussion

A number of observations can be made upon comparing the results of the charge density analyses with the results of the NEB calculations (Table 2). First, it can be seen that the energy barrier is higher when the distance between the adsorbed H atom and each of the surface Ru atoms is greater; topological analyses show that the same is true for the distance between the H atom and the bond critical point. The difference is not stark: the adsorbed SnH_4 has the hydrogen atom in the *fcc* site at an average distance 4% smaller than the average distance between a lone H atom and the surrounding Ru atoms; the difference in the H-BCP distance is 9%. The barrier–distance relationship is not necessarily enough to predict a difference in energy barriers, since the three cases with Sn coadsorbed with H on the surface (SnH, SnH_2, and SnH_3 in Table 2) have the same bond lengths and BCP distances, but different barriers to penetration.

A second, clearer correlation can be observed between the total bond order of the hydrogen atom and the calculated energy barrier. Taking into account all of the bonds in which the hydrogen atom of interest participates, we have calculated the sum of bond orders, and find that the changes in this value correspond to the changes in energy barrier quite neatly: a larger total bond order for H corresponds to a lower subsurface penetration barrier. The total bond order of the hydrogen atom in the SnH and SnH_2 cases are quite close, 1.22 and 1.20, respectively, as are the energy barriers, 0.80 and 0.83 eV, respectively. Moreover, the inverse proportionality is maintained. The trend holds for all the examined scenarios, suggesting that a key factor in the observed barrier differences is the state of the adsorbed and subsequently diffusing hydrogen atom itself, as characterised by its bonds and associated electron density.

The results of Bader charge analysis on the charge density shows a third trend, which relates the charge density distribution and the energy barrier. Recall that Bader's definition of an atom uses zero-flux surfaces to divide atoms, thereby associating a certain region of the electronic charge density with each atom in the system. In our system, the atomic volume computed for the adsorbed H atom of interest is generally larger for the cases with higher energy barriers, with the smallest volume corresponding to the lowest energy barrier. This supports the inference that the smaller atomic volume of H in a certain adsorption mode leads to a lower energy barrier to subsequent diffusion into the subsurface. We can discern yet another link when comparing the energy barriers to the reaction energies, i.e., the total energy difference between the initial adsorbed state and the final state with hydrogen in the subsurface. Whereas the subsurface penetration event is endothermic for a hydrogen atom on Ru(0001), it is made progressively less so in the presence of tin, and is ultimately exothermic when the hydrogen is taken from a stannane molecule. Moreover, as seen in Figure 4, the SnH_3 and SnH_4 cases have early transition states, which contrasts with the late transition states of the other cases.

We note that some of the other characteristics we examined do not show such a clear trend when taken in isolation. For instance, the charge on the H atom as calculated by the Bader method does

not match the trend in energy barriers. The trend of net atomic charges (NAC) calculated via the DDEC6 approach is also inconclusive, as are the trends of electronic density (ED) and charge density Laplacians at the bond critical point. Nevertheless, viewed together with the trends found in the hydrogen BCP, bond order, and atomic volume, these characteristics indicate that the hydrogen atom is in a state with more localised charge in the scenarios with lower penetration barriers. In the transition states, the area of the triangle formed by the surrounding ruthenium atoms is in fact smaller for the SnH_4 case than for the lone hydrogen atom. It appears that the localisation of the charge around the H nucleus is of more importance than the actual charge on the atom.

We speculate that the lower electronegativity of tin (1.96) relative to hydrogen (2.2) leads to the more compact localisation of charge around the hydrogen nucleus, i.e., the shared electrons are drawn closer to the hydrogen atom, which results in the reduced atomic volume found in our calculations. The introduction of tin results in charge transfer to the hydrogen atom, which can be seen in the more negative values of net atomic charge (NAC in Table 2) of the hydrogen atom in the scenarios with tin. Ruthenium's electronegativity is 2.2, equal to that of hydrogen, and the ruthenium atoms also show a more negative net atomic charge when tin is present. The tin atom therefore donates charge to the hydrogen and ruthenium atoms, as made evident by its positive NAC, and the charge accumulation above the ruthenium surface pushes the hydrogen into the surface due to electron–electron repulsion. The charge accumulation and repulsion also account for the preference of hydrogen for adsorption sites farther from tin, as seen in Section 3.3. The lower electronegativity of tin has also been put forward as the key factor in the difficulty of tin removal from ruthenium using hydrogen [60].

The barrier-less penetration of the Ru(0001) surface by the hydrogen atom from the vertically-oriented SnH_2 appears to support the conclusion that the hydrogen atom is in a decisively different state of bonding and charge localisation when the subsurface penetration is more facile. Both the total bond order and Bader volume (see Table 2) suggest that the energy barrier would be lower in this case than in the SnH_4 scenario; the bond order is 1.54, the highest value, while the Bader volume is 3.54, the lowest value. The charge difference ($\Delta\rho$) in the initial geometry of the relaxation also shows charge accumulation around the hydrogen and above the ruthenium surface, in a manner similar to the transition state for SnH_4. Indeed, this calculation finds its local minimum with the hydrogen atom below the surface, showing that the hydrogen atom attached to tin is in a most advantageous state for passing through the surface ruthenium atoms.

These results together indicate that a closer, shorter bond exists between the hydrogen atom and the surface ruthenium atoms in the presence of tin, with a smaller atomic volume for the H atom in the adsorbed state, which is corroborated by the trend in calculated Bader volumes. The surrounding ruthenium atoms are moved apart to a lesser extent (smaller change in area of the triangle, see Table 2) to arrive at the transition state, i.e., at a lower energy cost. The reduced atomic volume is likely due to the asymmetric charge distribution relative to the less electronegative tin. The charge transfer from tin to hydrogen and ruthenium creates areas of charge accumulation around the hydrogen atom and on the ruthenium surface, and makes the subsurface interstitial site more energetically favourable. These conditions are most advantageous for the adsorbed SnH_3 and SnH_4, with the result that the penetration of hydrogen is easiest in these cases.

5. Conclusions

In this work, we have investigated hydrogen penetration of the Ru(0001) surface in the presence and absence of tin, by means of DFT computations, chemical bonding, and charge density analysis. We showed that hydrogen faces a significant barrier to subsurface penetration in the absence of tin. We find that the energy barrier drops significantly in the presence of tin, be it as an adatom or as part of an adsorbed tin hydride molecule. The lowest energy barriers are found when a hydride molecule adsorbs on the Ru(0001) surface and subsequently loses a hydrogen atom. We performed charge density analyses on systems with and without tin, which revealed changes in the bonds formed between ruthenium and hydrogen under the influence of tin, as well as a change in charge distribution

around the diffusing hydrogen atom, resulting in reduced energy barriers to penetration. The much higher barrier found for a hydrogen atom with no tin present allows us to conclude that tin hydrides play an important role in the increased blistering of EUV reflectors with tin debris on the surface.

These insights into the effect of charge transfer from tin have important implications for the development of blistering mitigation techniques, and prolonging the operational lifetime of EUV optics. Our findings may also have value in cases where hydrogen penetration needs to be improved, such as hydrogen storage or separation and purification.

Author Contributions: Conceptualization, S.T.; Methodology, I.T., S.T.; Analysis, C.O. and I.T.; Investigation, C.O.; Writing—Original Draft Preparation, C.O.; Writing—Review and Editing, C.O., I.T., T.M., and S.T.; Supervision, T.M. and S.T.

Funding: S.T. acknowledges funding by the Computational Sciences for Energy Research (CSER) tenure track program of Shell and NWO (Project number 15CST04-2).

Acknowledgments: This research was carried out under project number T16010a in the framework of the Research Program of the Materials Innovation Institute (M2i) (www.m2i.nl) supported by the Dutch government. DIFFER is part of the Netherlands Organisation for Scientific Research (NWO). The authors thank the NWO for access to the national high-performance computing facilities (Cartesius).

Conflicts of Interest: The authors declare no conflict of interest.

References

1. Bond, G.C.; Webb, G.; Wells, P.B.; Winterbottom, J.M. Patterns of behavior in catalysis by metals. *J. Catal.* **1962**, *1*, 74–84. doi:10.1016/0021-9517(62)90011-8. [CrossRef]
2. Sinfelt, J.H. Heterogeneous catalysis by metals. *Prog. Solid-State Chem.* **1975**, *10*, 55–69. [CrossRef]
3. Knapton, A.G. Palladium Alloys for Hydrogen Diffusion Membranes. *Platinum Met. Rev.* **1977**, *21*, 44–50.
4. Al-Mufachi, N.A.; Rees, N.V.; Steinberger-Wilkens, R. Hydrogen selective membranes: A review of palladium-based dense metal membranes. *Renew. Sustain. Energy Rev.* **2015**, *47*, 540–551. doi:10.1016/j.rser.2015.03.026. [CrossRef]
5. Sakintuna, B.; Lamari-Darkrim, F.; Hirscher, M. Metal hydride materials for solid hydrogen storage: A review. *Int. J. Hydrog. Energy* **2007**, *32*, 1121–1140. doi:10.1016/j.ijhydene.2006.11.022. [CrossRef]
6. Hübert, T.; Boon-Brett, L.; Black, G.; Banach, U. Hydrogen sensors—A review. *Sens. Actuators B Chem.* **2011**, *157*, 329–352. doi:10.1016/j.snb.2011.04.070. [CrossRef]
7. Herlach, D.; Kottler, C.; Wider, T.; Maier, K. Hydrogen embrittlement of metals. *Phys. B Condens. Matter* **2000**, *290*, 443–446. doi:10.1016/S0921-4526(00)00431-2. [CrossRef]
8. Nanninga, N.E.; Levy, Y.S.; Drexler, E.S.; Condon, R.T.; Stevenson, A.E.; Slifka, A.J. Comparison of hydrogen embrittlement in three pipeline steels in high pressure gaseous hydrogen environments. *Corros. Sci.* **2012**, *59*, 1–9. doi:10.1016/j.corsci.2012.01.028. [CrossRef]
9. Muschiol, U.; Schmidt, P.K.; Christmann, K. Adsorption and absorption of hydrogen on a palladium (210) surface: A combined LEEDS, TDS, $\Delta\Phi$ and HREELS study. *Surf. Sci.* **1998**, *395*, 182–204. doi:10.1016/S0039-6028(97)00624-9. [CrossRef]
10. Nordlander, P.; Holloway, S.; Nørskov, J.K. Hydrogen adsorption on metal surfaces. *Surf. Sci.* **1984**, *136*, 59–81. doi:10.1016/0039-6028(84)90655-1. [CrossRef]
11. Pick, M.A.; Sonnenberg, K. A model for atomic hydrogen-metal interactions—Application to recycling, recombination and permeation. *J. Nucl. Mater.* **1985**, *131*, 208–220. doi:10.1016/0022-3115(85)90459-3. [CrossRef]
12. Myers, S.M.; Richards, P.M.; Wampler, W.R.; Besenbacher, F. Ion-beam studies of hydrogen-metal interactions. *J. Nucl. Mater.* **1989**, *165*, 9–64. doi:10.1016/0022-3115(89)90502-3. [CrossRef]
13. Van Santen, R.A.; Tranca, I. How molecular is the chemisorptive bond? *Phys. Chem. Chem. Phys.* **2016**, *18*, 20868–20894. doi:10.1039/c6cp01394e. [CrossRef] [PubMed]
14. Sinfelt, J.H. Catalysis by Alloys and Bimetallic Clusters. *Acc. Chem. Res.* **1977**, *10*, 15–20. doi:10.1021/ar50109a003. [CrossRef]
15. Rodriguez, J.A. Electronic and chemical properties of Pt, Pd and Ni in bimetallic surfaces. *Surf. Sci.* **1996**, *345*, 347–362. doi:10.1016/0039-6028(95)00903-5. [CrossRef]

16. Ruban, A.; Hammer, B.; Stoltze, P.; Skriver, H.L.; Nørskov, J.K. Surface electronic structure and reactivity of transition and noble metals. *J. Mol. Catal. A Chem.* **1997**, *115*, 421–429. doi:10.1016/S1381-1169(96)00348-2. [CrossRef]
17. Chen, J.G.; Menning, C.A.; Zellner, M.B. Monolayer bimetallic surfaces: Experimental and theoretical studies of trends in electronic and chemical properties. *Surf. Sci. Rep.* **2008**, *63*, 201–254. doi:10.1016/j.surfrep.2008.02.001. [CrossRef]
18. He, Y.B.; Goriachko, A.; Korte, C.; Farkas, A.; Mellau, G.; Dudin, P.; Gregoratti, L.; Barinov, A.; Kiskinova, M.; Stierle, A.; et al. Oxidation and reduction of ultrathin nanocrystalline Ru films on silicon: Model system for Ru-capped extreme ultraviolet lithography optics. *J. Phys. Chem. C* **2007**, *111*, 10988–10992. doi:10.1021/jp071339b. [CrossRef]
19. Bajt, S.; Chapman, H.N.; Nguyen, N.; Alameda, J.B.; Robinson, J.C.; Malinowski, M.E.; Gullikson, E.; Aquila, A.; Tarrio, C.; Grantham, S. Design and performance of capping layers for EUV multilayer mirrors. *Proc. SPIE* **2003**, *5037*, 236–248. doi:10.1117/12.484966. [CrossRef]
20. Kuznetsov, A.S.; van de Kruijs, R.W.E.; Gleeson, M.A.; Schmid, K.; Bijkerk, F. Hydrogen interaction with EUVL-relevant optical materials. *J. Surf. Investig. X-ray Synchrotron Neutron Tech.* **2010**, *4*, 563–566. doi:10.1134/S1027451010040026. [CrossRef]
21. Kuznetsov, A.S.; Gleeson, M.A.; Bijkerk, F. Temperature dependencies of hydrogen-induced blistering of thin film multilayers. *J. Appl. Phys.* **2014**, *115*, 173510. doi:10.1063/1.4875484. [CrossRef]
22. Faradzhev, N.; Sidorkin, V. Hydrogen mediated transport of Sn to Ru film surface. *J. Vac. Sci. Technol. A Vac. Surf. Films* **2009**, *27*, 306–314. doi:10.1116/1.3081968. [CrossRef]
23. Bruneau, C.; Dixneuf, P.H. Volume 48, Topics in Organometallic Chemistry. In *Ruthenium in Catalysis*; Springer International Publishing: Berlin/Heidelberg, Germany, 2014. doi:10.1007/978-3-319-08482-4.
24. Adams, R.D.; Trufan, E. Ruthenium-tin cluster complexes and their applications as bimetallic nanoscale heterogeneous hydrogenation catalysts. *Philos. Trans. R. Soc. A Math. Phys. Eng. Sci.* **2010**, *368*, 1473–1493. doi:10.1098/rsta.2009.0277. [CrossRef]
25. Bonnefille, E.; Novio, F.; Gutmann, T.; Poteau, R.; Lecante, P.; Jumas, J.C.; Philippot, K.; Chaudret, B. Tin-decorated ruthenium nanoparticles: A way to tune selectivity in hydrogenation reaction. *Nanoscale* **2014**, *6*, 9806–9816. doi:10.1039/c4nr00791c. [CrossRef]
26. Galvagno, S.; Donato, A.; Neri, G.; Pietropaolo, R.; Capannelli, G. Selective hydrogenation of cinnamaldehyde over Ru-Sn catalysts. *J. Mol. Catal.* **1993**, *78*, 227–236. doi:10.1016/0304-5102(93)85041-Q. [CrossRef]
27. Gallo, A.; Pirovano, C.; Marelli, M.; Psaro, R.; Dal Santo, V. Hydrogen production by glycerol steam reforming with ru-based catalysts: A study on sn doping. *Chem. Vap. Depos.* **2010**, *16*, 305–310. doi:10.1002/cvde.201006864. [CrossRef]
28. Driessen, A.; Sanger, P.; Hemmes, H.; Griessen, R. Metal hydride formation at pressures up to 1 Mbar. *J. Phys. Condens. Matter* **1990**, *2*, 9797–9814. doi:10.1088/0953-8984/2/49/007. [CrossRef]
29. Yates, J.T.; Peden, C.H.; Houston, J.E.; Goodman, D.W. Subsurface penetration of chemisorbed hydrogen isotopes into the Ru(0001) crystal surface. *Surf. Sci.* **1985**, *160*, 37–45. doi:10.1016/0039-6028(85)91024-6. [CrossRef]
30. Peden, C.H.F.; Goodman, D.W.; Houston, J.E.; Yates, J.T. Subsurface hydrogen on Ru(0001): Quantification by Cu titration. *Surf. Sci.* **1988**, *194*, 92–100. doi:10.1016/0039-6028(94)91246-7. [CrossRef]
31. Lagos, M. Subsurface bonding of hydrogen to metallic surfaces. *Surf. Sci.* **1982**, *122*, L601–L607. doi:10.1016/0039-6028(82)90067-X. [CrossRef]
32. Kresse, G.; Hafner, J. Ab initio molecular-dynamics simulation of the liquid-metalamorphous- semiconductor transition in germanium. *Phys. Rev. B* **1994**, *49*, 14251–14269. doi:10.1103/PhysRevB.49.14251. [CrossRef]
33. Kresse, G.; Furthmüller, J. Efficiency of ab-initio total energy calculations for metals and semiconductors using a plane-wave basis set. *Comput. Mater. Sci.* **1996**, *6*, 15–50. doi:10.1016/0927-0256(96)00008-0. [CrossRef]
34. Joubert, D. From ultrasoft pseudopotentials to the projector augmented-wave method. *Phys. Rev. B Condens. Matter Mater. Phys.* **1999**, *59*, 1758–1775. doi:10.1103/PhysRevB.59.1758. [CrossRef]
35. Perdew, J.D.; Burke, K.; Ernzerhof, M. Generalized Gradient Approximation Made Simple. *Phys. Rev. Lett.* **1996**, *77*, 3865–3868. [CrossRef] [PubMed]

36. Grimme, S.; Antony, J.; Ehrlich, S.; Krieg, H. A consistent and accurate ab initio parametrization of density functional dispersion correction (DFT-D) for the 94 elements H-Pu. *J. Chem. Phys.* **2010**, *132*, 154104. doi:10.1063/1.3382344. [CrossRef] [PubMed]
37. Henkelman, G.; Uberuaga, B.P.; Jónsson, H. Climbing image nudged elastic band method for finding saddle points and minimum energy paths. *J. Chem. Phys.* **2000**, *113*, 9901–9904. doi:10.1063/1.1329672. [CrossRef]
38. King, H.W. Crystal structures and lattice parameters of allotropes of the elements. In *CRC Handbook of Chemistry and Physics*; CRC: Boca Raton, FL, USA, 2012; pp. 15–18.
39. Vineyard, G.H. Frequency factors and isotope effects in solid state rate processes. *J. Phys. Chem. Solids* **1957**, *3*, 121–127. doi:10.1016/0022-3697(57)90059-8. [CrossRef]
40. Irikura, K.K. Experimental Vibrational Zero-Point Energies: Diatomic Molecules. *J. Phys. Chem. Ref. Data* **2007**, *36*, 389–397. doi:10.1063/1.2436891. [CrossRef]
41. Tang, W.; Sanville, E.; Henkelman, G. A grid-based Bader analysis algorithm without lattice bias. *J. Phys. Condens. Matter* **2009**, *21*, 084204. doi:10.1088/0953-8984/21/8/084204. [CrossRef]
42. Sanville, E.; Kenny, S.D.; Smith, R.; Henkelman, G. Improved grid-based algorithm for Bader charge allocation. *J. Comput. Chem.* **2007**, *28*, 899–908. doi:10.1002/jcc.20575. [CrossRef]
43. Henkelman, G.; Arnaldsson, A.; Jónsson, H. A fast and robust algorithm for Bader decomposition of charge density. *Comput. Mater. Sci.* **2006**, *36*, 354–360. doi:10.1016/j.commatsci.2005.04.010. [CrossRef]
44. Yu, M.; Trinkle, D.R. Accurate and efficient algorithm for Bader charge integration. *J. Chem. Phys.* **2011**, *134*, 064111. doi:10.1063/1.3553716. [CrossRef] [PubMed]
45. Manz, T.A.; Limas, N.G. Introducing DDEC6 atomic population analysis: Part 1. Charge partitioning theory and methodology. *RSC Adv.* **2016**, *6*, 47771–47801. doi:10.1039/c6ra04656h. [CrossRef]
46. Manz, T.A. Introducing DDEC6 atomic population analysis: Part 3. Comprehensive method to compute bond orders. *RSC Adv.* **2017**, *7*, 45552–45581. doi:10.1039/c7ra07400j. [CrossRef]
47. Vega, D.; Almeida, D. AIM-UC: An application for QTAIM analysis. *J. Comput. Methods Sci. Eng.* **2014**, *14*, 131–136. doi:10.3233/JCM-140491. [CrossRef]
48. Hoffmann, R. Interaction of Orbitals through Space and through Bonds. *Acc. Chem. Res.* **1971**, *4*, 1–9. doi:10.1021/ar50037a001. [CrossRef]
49. Dronskowski, R.; Blöchl, P.E. Crystal orbital hamilton populations (COHP). Energy-resolved visualization of chemical bonding in solids based on density-functional calculations. *J. Phys. Chem.* **1993**, *97*, 8617–8624. doi:10.1021/j100135a014. [CrossRef]
50. Deringer, V.L.; Tchougréeff, A.L.; Dronskowski, R. Crystal orbital Hamilton population (COHP) analysis as projected from plane-wave basis sets. *J. Phys. Chem. A* **2011**, *115*, 5461–5466. doi:10.1021/jp202489s. [CrossRef]
51. Maintz, S.; Deringer, V.L.; Tchougréeff, A.L.; Dronskowski, R. LOBSTER: A tool to extract chemical bonding from plane-wave based DFT. *J. Comput. Chem.* **2016**, *37*, 1030–1035. doi:10.1002/jcc.24300. [CrossRef]
52. Matta, C.F.; Boyd, R.J. *An Introduction to the Quantum Theory of Atoms in Molecules*; Wiley-VCH Verlag GmbH & Co. KGaA: Weinheim, Germany, 2007; pp. 1–34. doi:10.1002/9783527610709.ch1.
53. Bader, R.F.W. A quantum theory of molecular structure and its applications. *Chem. Rev.* **1991**, *91*, 893–928. doi:10.1021/cr00005a013. [CrossRef]
54. Ciobica, I.M.; Kleyn, A.W.; Van Santen, R.A. Adsorption and coadsorption of CO and H on ruthenium surfaces. *J. Phys. Chem. B* **2003**, *107*, 164–172. doi:10.1021/jp0201478. [CrossRef]
55. Del Rosal, I.; Truflandier, L.; Poteau, R.; Gerber, I.C. A density functional theory study of spectroscopic and thermodynamic properties of surfacic hydrides on Ru (0001) model surface: The influence of the coordination modes and the coverage. *J. Phys. Chem. C* **2011**, *115*, 2169–2178. doi:10.1021/jp110090e. [CrossRef]
56. Luppi, M.; Olsen, R.A.; Baerends, E.J. Six-dimensional potential energy surface for H_2 at Ru(0001). *Phys. Chem. Chem. Phys.* **2006**, *8*, 688–696. doi:10.1039/B513033F. [CrossRef] [PubMed]
57. Kristinsdóttir, L.; Skúlason, E. A systematic DFT study of hydrogen diffusion on transition metal surfaces. *Surf. Sci.* **2012**, *606*, 1400–1404. doi:10.1016/j.susc.2012.04.028. [CrossRef]
58. McIntosh, E.M.; Wikfeldt, K.T.; Ellis, J.; Michaelides, A.; Allison, W. Quantum Effects in the Diffusion of Hydrogen on Ru(0001). *J. Phys. Chem. Lett.* **2013**, *4*, 1565–1569. doi:10.1021/jz400622v. [CrossRef] [PubMed]
59. Van Herpen, M.M.J.W.; Klunder, D.J.W.; Soer, W.A.; Moors, R.; Banine, V. Sn etching with hydrogen radicals to clean EUV optics. *Chem. Phys. Lett.* **2010**, *484*, 197–199. doi:10.1016/j.cplett.2009.11.030. [CrossRef]

60. Pachecka, M.; Sturm, J.M.; van de Kruijs, R.W.E.; Lee, C.J.; Bijkerk, F. Electronegativity-dependent tin etching from thin films. *AIP Adv.* **2016**, *6*, 075222. doi:10.1063/1.4960429. [CrossRef]
61. Fearon, J.; Watson, G.W. Hydrogen adsorption and diffusion on Pt {111} and PtSn {111}. *J. Mater. Chem.* **2006**, *16*, 1989–1996. doi:10.1039/b600250c. [CrossRef]

nanomaterials

MDPI

Article

Quantum-Mechanical Study of Nanocomposites with Low and Ultra-Low Interface Energies

Martin Friák [1,*], David Holec [2] and Mojmír Šob [3,1,4]

[1] Institute of Physics of Materials, Academy of Sciences of the Czech Republic, Žižkova 22, CZ-616 62 Brno, Czech Republic; mojmir@ipm.cz
[2] Department of Materials Science, Montanuniversität Leoben, Franz-Josef-Strasse 18, A-8700 Leoben, Austria; david.holec@unileoben.ac.at
[3] Department of Chemistry, Faculty of Science, Masaryk University, Kotlářská 2, CZ-611 37 Brno, Czech Republic
[4] Central European Institute of Technology, CEITEC MU, Masaryk University, Kamenice 5, CZ-625 00 Brno, Czech Republic
* Correspondence: friak@ipm.cz; Tel.: +420-532-290-400

Received: 27 November 2018; Accepted: 12 December 2018; Published: 15 December 2018

Abstract: We applied first-principles electronic structure calculations to study structural, thermodynamic and elastic properties of nanocomposites exhibiting nearly perfect match of constituting phases. In particular, two combinations of transition-metal disilicides and one pair of magnetic phases containing the Fe and Al atoms with different atomic ordering were considered. Regarding the disilicides, nanocomposites $MoSi_2/WSi_2$ with constituents crystallizing in the tetragonal $C11_b$ structure and $TaSi_2/NbSi_2$ with individual phases crystallizing in the hexagonal C40 structure were simulated. Constituents within each pair of materials exhibit very similar structural and elastic properties and for their nanocomposites we obtained ultra-low (nearly zero) interface energy (within the error bar of our calculations, i.e., about 0.005 J/m^2). The interface energy was found to be nearly independent on the width of individual constituents within the nanocomposites and/or crystallographic orientation of the interfaces. As far as the nanocomposites containing Fe and Al were concerned, we simulated coherent superlattices formed by an ordered Fe_3Al intermetallic compound and a disordered Fe-Al phase with 18.75 at.% Al, the α-phase. Both phases were structurally and elastically quite similar but the disordered α-phase lacked a long-range periodicity. To determine the interface energy in these nanocomposites, we simulated seven different distributions of atoms in the α-phase interfacing the Fe_3Al intermetallic compound. The resulting interface energies ranged from ultra low to low values, i.e., from 0.005 to 0.139 J/m^2. The impact of atomic distribution on the elastic properties was found insignificant but local magnetic moments of the iron atoms depend sensitively on the type and distribution of surrounding atoms.

Keywords: $MoSi_2$; WSi_2; $TaSi_2$; $NbSi_2$; elasticity; ab initio; interface energies; Fe_3Al; disorder

1. Introduction

Ever increasing demand for energy-conversion units exhibiting a higher efficiency leads to increasing operating temperatures in these systems and, therefore, new materials, which would sustain such conditions, are needed. Because the development of these materials is highly complex and multi-faceted, combinations of often mutually-conflicting properties are rarely found in a single-phase structures. Composites then represent a critically important class of materials. In particular, coherent nanocomposites require optimum matching of constituting phases for their stability and rather low interface energies. In our study, we addressed three nanocomposites combining materials intended for high or elevated temperature applications: two pairs of transition-metal disilicides that are predicted

to possess ultra-low interface energies and then a pair of two different phases from the Fe-Al system, which are expected to have the interface energies ranging from ultra low to low values.

Regarding the transition-metal silicides, they are currently considered as very promising bases for future high-temperature structural materials (see, e.g., Refs. [1–4]), in particular for operational temperatures above those of Ni-based superalloys. At high temperatures, transition-metal silicides are known to combine the ductility and thermal conductivity of metals with high strength and corrosion resistance of ceramics. As far as composites combining them are concerned, $MoSi_2/WSi_2$ composite powders with different phase compositions are fabricated via a self-propagating high-temperature synthesis (SHS) method [5]. This approach is widely recognized as an effective manufacturing strategy for the fabrication of materials applied in high-temperature fields, in particular for refractories such as transition-metal carbides, nitrides, silicides, and borides [6]. Preparation of $MoSi_2/WSi_2$ composites using elemental powders of Mo, W and Si by the thermal explosion mode of SHS have been theoretically calculated and investigated by experiments in Ref. [7]. Phase composition and microchemical area analyses were conducted by XRD, SEM and EDAX methods. Pure $MoSi_2/WSi_2$ composites are fabricated by the thermal explosion mode of SHS, and $MoSi_2/WSi_2$ exists as a solid solution of $(Mo_x,W_{1-x})Si_2$ but the chemical elements inside of individual grains are not uniformly distributed. As an alternative processing route, five kinds of $WSi_2/MoSi_2$ composites are fabricated by mechanical alloying in [8]. WSi_2-reinforced $MoSi_2$ composites are successfully prepared also by mechanical activation followed by in situ reactive spark plasma sintering of Mo, Si, and W elemental powders in [9]. The addition of W to the reactants leads to a finer microstructure than that obtained using pure $MoSi_2$, resulting in a significant improvement of mechanical properties. The Vicker's hardness of 20 vol % $WSi_2/MoSi_2$ is as high as 16.47 GPa. Nanocomposite of $(Mo,W)Si_2/WSi_2$ was synthesized via mechanical alloying (MA) and heat treatment in Ref. [10]. Increasing the milling time to 80 h followed by the post-annealing at 1000 °C caused the complete formation of $(Mo,W)Si_2/WSi_2$ nanocomposite. $MoSi_2/WSi_2$ composites were successfully prepared by pressureless sintering from mechanically-assisted combustion synthesized powders in [11].

Motivated by the above-mentioned studies of $MoSi_2/WSi_2$ (nano)composites containing structurally and elastically very similar pair of materials crystallizing in the $C11_b$ structure, we also assessed another pair of matching materials, $TaSi_2$ and $NbSi_2$, which are crystallizing in the C40 structure.

Finally, as a system with rather low interface energy, we studied nanocomposites formed by two phases from the Fe-Al binary system [12–15]. These materials are also considered as promising for elevated-temperature applications and as such they are intensively studied [16–40]. A sub-class of Fe-Al-based materials is represented by composites consisting of an ordered Fe_3Al with the $D0_3$ structure and a disordered Fe-Al solid solution with about 18-19 at.% Al. The existence of these composites can be experimentally proved using, for example, Mössbauer spectroscopy [41] or transmission electron microscopy (TEM) techniques. The latter are sensitive to anti-phase boundaries (APBs), which have a different character in Fe_3Al and the Fe-Al phase [42–45].

2. Methods

Our quantum-mechanical calculations were performed within the framework of density functional theory [46,47] using the Vienna Ab initio Simulation Package (VASP) [48,49] and projector augmented wave (PAW) pseudopotentials [50,51]. When studying the transition-metal disilicides, the exchange and correlation energy was treated in the local density approximation (LDA) [52] but, in the case of phases containing the Fe and Al atoms, the generalized gradient approximation (GGA) parameterized by Perdew and Wang [53] (PW91) with the Vosko–Wilk–Nusair correction [54] was necessary to correctly reproduce the ground-state $D0_3$ structure of Fe_3Al. Regarding the $MoSi_2$ and WSi_2, we used a plane-wave energy cut-off of 400 eV and the k-point Monkhorst–Pack [55] meshes contained $20 \times 20 \times 2$ ($10 \times 10 \times 8$) k-points in the case of 24-atom supercells modeling the superlattices with stacking along the [001] ([100] and [110]) directions. The calculations for $TaSi_2$ and $NbSi_2$ required the

cut-off energy of 480 eV and the 12 × 12 × 4 k-point mesh in the case of 18-atom supercells. When computing Fe-Al-based nanocomposites, the cut-off energy was equal to 350 eV and the sampling of the Brillouin zone was done using Monkhorst–Pack grids with 10 × 10 × 6 k-points in the case of computational supercells containing 32 atoms. All calculations had an estimated error-bar of about 0.001 eV/atom. Finally, the second-order elastic constants were determined using the stress-strain method [56].

3. Results

The first type of studied nanocomposite containing transition-metal disilicides is visualized in Figure 1a. WSi_2 and $MoSi_2$, which crystallize in the tetragonal $C11_b$ structure, form a coherent nanocomposite where two conventional cells of each materials are stacked one on top of the other along the [001] direction (the interfaces are perpendicular to this direction) and alternate. It should be emphasized that, due to the periodic boundary conditions, which are applied to all nanocomposites in our calculations, the simulated nanocomposites form so-called superlattices [57–78] when the atomic planes continue from one phase into another.

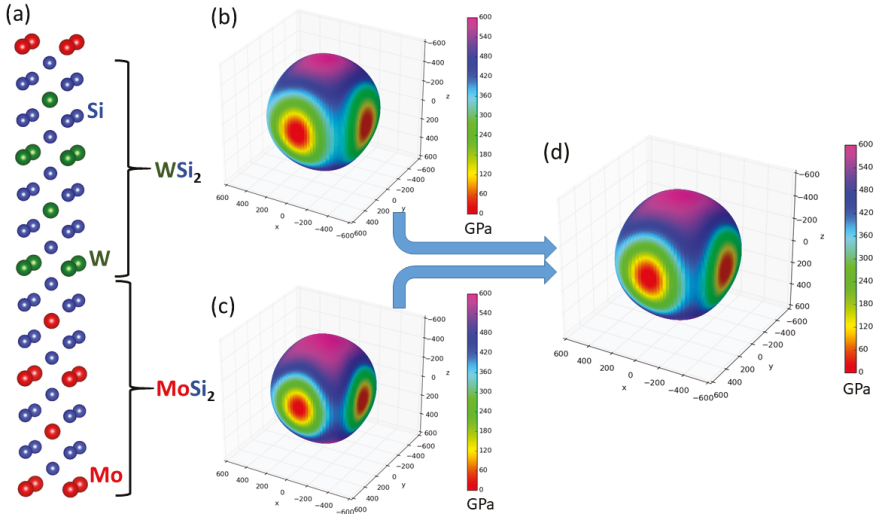

Figure 1. Visualization of a $WSi_2/MoSi_2$ nanocomposite (a superlattice) with the stacking along (and the interfaces perpendicular to) the [001] direction within the $C11_b$ lattice (**a**) accompanied with directional dependences of the Young's modulus of bulk WSi_2 (**b**), bulk $MoSi_2$ (**c**) and the composite $WSi_2/MoSi_2$ (**d**) formed out of them. The parts (**b**–**d**) were visualized by the SC-EMA [79–81] library (scema.mpie.de) based on ab initio computed elastic constants.

As seen in Table 1, both disilicides have very similar lattice parameters a and c describing their tetragonal structure and also quite similar elastic properties. Our theoretical values are in excellent agreement with both experimental data and previous calculations. The elasticity of bulk phases is conveniently visualized in Figure 1b,c in the form of directional dependences of the Young's modulus. The values for this composite with an equal amount of both phases are listed in Table 1 at the line for the composition $(WSi_2)_4(MoSi_2)_4$.

Table 1. Calculated structural characteristics and elastic constants of bulk $MoSi_2$ and WSi_2 as well as of their composite $MoSi_2/WSi_2$ with the stacking along (and the interfaces perpendicular to) the [001] direction within the $C11_b$ lattice. The computed values are complemented by experimental data from the literature. As far as the lattice parameters a and c of the $C11_b$ structure are concerned, the values for the c lattice parameters of the nanocomposites are marked by the symbol of an asterisk * because they are divided by a factor of 4 to be compared with the values for the bulk unit cells of the individual constituents (bulk $MoSi_2$ and WSi_2). The simulated nanocomposites are shown in Figure 2 and, specifically for the equal amount of both phases, in Figure 1a. Experimental elastic constants of $MoSi_2$ and WSi_2 were taken from Refs. [82,83].

Composition	a (Å)	c (Å)	C_{11} (GPa)	C_{12} (GPa)	C_{13} (GPa)	C_{33} (GPa)	C_{44} (GPa)	C_{66} (GPa)
$MoSi_2$	3.176	7.781	428	125	101	537	208	207
	3.202 [83]	7.855 [83]	417.0 [82]	104.2 [82]	83.8 [82]	514.5 [82]	204.2 [82]	193.6 [82]
$(WSi_2)_1/(MoSi_2)_7$	3.178	7.782 *	433	126	101	542	210	209
$(WSi_2)_2/(MoSi_2)_6$	3.180	7.781 *	437	127	102	546	210	210
$(WSi_2)_3/(MoSi_2)_5$	3.181	7.781 *	440	127	102	551	211	212
$(WSi_2)_4/(MoSi_2)_4$	3.183	7.780 *	444	127	103	555	212	213
$(WSi_2)_5/(MoSi_2)_3$	3.185	7.780 *	447	127	103	560	212	214
$(WSi_2)_6/(MoSi_2)_2$	3.186	7.780 *	450	128	106	565	213	216
$(WSi_2)_7/(MoSi_2)_1$	3.188	7.780 *	453	128	106	570	213	217
WSi_2	3.188	7.778	456	131	105	576	214	217
	3.211 [83]	7.835 [83]	442.8 [82]	121.7 [82]	81.0 [82]	552.3 [82]	211.6 [82]	217.5 [82]

As a consequence of the similarity of the elastic constants of both constituents, the overall elastic properties of their nanocomposites are quite similar, too.

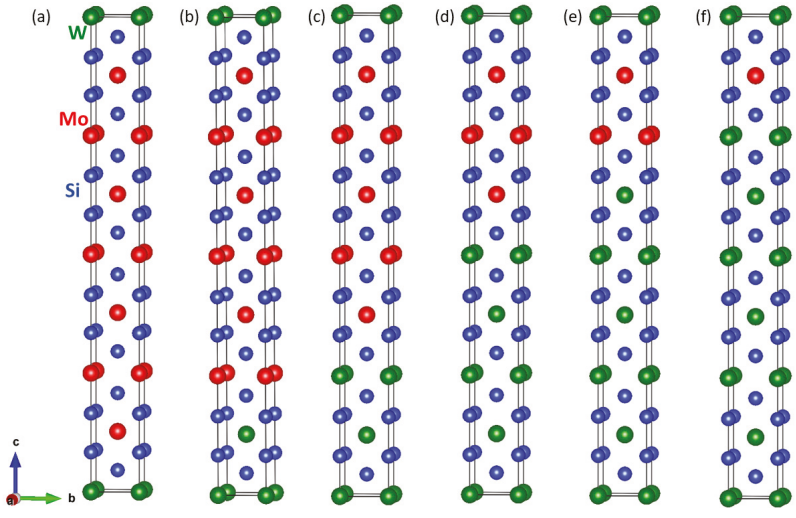

Figure 2. Schematic visualization of supercells modeling various nanocomposites with the stacking along (and the interfaces perpendicular to) the [001] direction. The mutual ratio of the constituents varies from 1:7, i.e., $(WSi_2)_1(MoSi_2)_7$, in the case of sub-figure (**a**), via 2:6 (**b**) and 3:5 (**c**) further for the opposite ratios 5:3 (**d**) and 6:2 (**e**) to 7:1, i.e., $(WSi_2)_7(MoSi_2)_1$, in the case of sub-figure (**f**).

Next, we evaluated the interface energy of the nanocomposites according to the formula:

$$\gamma((WSi_2)_m/(MoSi_2)_n) = \frac{E((WSi_2)_m/(MoSi_2)_n) - m \cdot E(WSi_2) - n \cdot E(MoSi_2)}{(2 \cdot A)} \quad (1)$$

using the energy $E((WSi_2)_m/(MoSi_2)_n)$ of the supercell modeling the nanocomposite $(WSi_2)_m/(MoSi_2)_n$, which contains m formula units of WSi_2 and n formula units of $MoSi_2$, the energies of bulk phases of each constituent $E(WSi_2)$ and $E(MoSi_2)$ and the area of the interface A. Importantly, very probably due to the similarity of both constituents, the interface energy was found to be ultra low, essentially zero within the error bar of our calculations, i.e., the energy differences in Equation (1) are smaller than 0.001 eV/atom and the interface energies are then smaller than about 0.005 J/m^2.

To examine how the ultra-low interface energies depend on the width of the layers containing individual constituents within the nanocomposite as well as on the ratio of amount of both materials, we simulated a series of seven other superlattices with varying width of the constituents, as visualized in Figure 2. The calculated structural and elastic parameters are summarized in Table 1. The lattice parameter a increased quite monotonously from the value calculated for bulk $MoSi_2$ to that obtained for bulk WSi_2. The changes of the lattice parameter c are much smaller because the values found for bulk $MoSi_2$ and WSi_2 are only very slightly different. Rather monotonous changes appear also for the elastic constants with all of them increasing when increasing the amount of elastically stiffer WSi_2. Importantly, all the studied nanocomposites have again ultra low interface energies, which are essentially zero within the error-bar of our calculations. Next, as seen in the Appendix, the ultra low interface energies were nearly independent of the crystallographic orientation of the interface.

After examining the $WSi_2/MoSi_2$ nanocomposites, which were experimentally reported to exist, we next drew our attention to another class of nanocomposites containing transition-metal disilicides, which were structurally and elastically very similar. The studied $TaSi_2$ and $NbSi_2$ crystallize in the hexagonal C40 structure and, therefore, we simulated a superlattice based on this structure (see Figure 3).

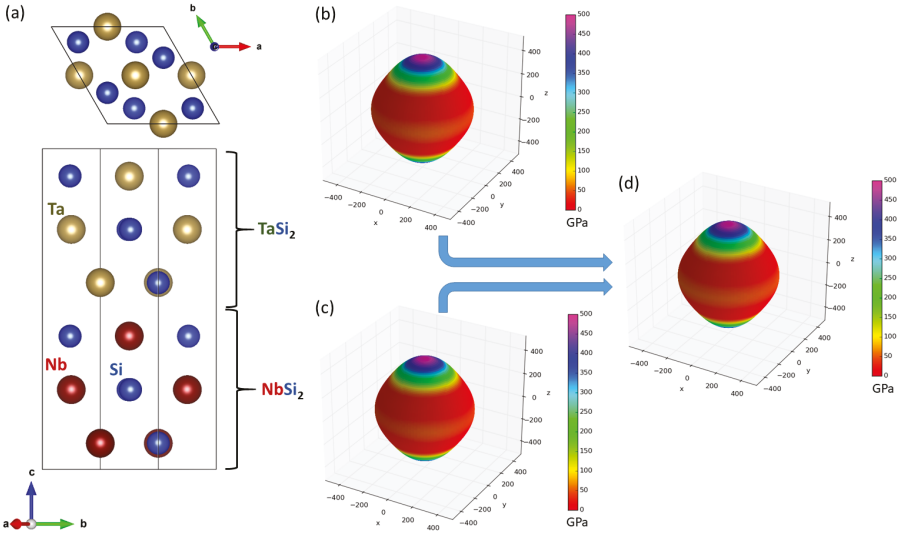

Figure 3. A top-view and a side-view of the computational supercell used in our calculations as a model of $TaSi_2/NbSi_2$ nanocomposite (a superlattice) with the stacking along (and the interfaces perpendicular to) the [0001] direction within the C40 lattice (**a**) accompanied with directional dependences of the Young's modulus of bulk $TaSi_2$ (**b**), bulk $NbSi_2$ (**c**) and their composite $TaSi_2/NbSi_2$ (**d**).

The nanocomposites have the interfaces perpendicular to the [0001] crystallographic direction. The lattice parameters a and c and elastic constants of both constituents in their bulk phases are summarized in Table 2. Our theoretical values are in an excellent agreement with both experimental data and previous calculations. Both disilicides have all the parameters very similar. The elasticity of bulk phases is conveniently visualized in Figure 3b,c in the form of directional dependences of the Young's modulus. As the elastic properties are quite similar, the elasticity of the studied nanocomposite is not too different from that of the constituting phases (see Figure 3d). Importantly, the interface energy is ultra low for this superlattice, again zero within the error-bar of our calculations.

Similar to the case of the $WSi_2/MoSi_2$ nanocomposites studied above, we examined how the ultra-low interface energies depend on the molar ratio of the constituting phases as well as on the width of the phases forming the superlattice (see Figure 4). We performed our calculations for a series of six other nanocomposites with different ratio of the $TaSi_2$ and $NbSi_2$ (see Figure 4a–f). Out of the six calculated superlattices shown in Figure 4, those shown in Figure 4c,d have the same ratio of the amount of both materials but a higher number of internal interfaces, six and four, respectively.

When evaluating the interface energies, they were again found to be ultra low, namely zero within the error-bar of our calculations. The lattice parameters a and c of the C40-based structure are concerned were rather monotonously increasing from their lower values in $TaSi_2$ to higher values in $NbSi_2$. In contrast to this trend, the elastic constants rather monotonously decreased from their higher values in $TaSi_2$ to lower values in $NbSi_2$.

Table 2. Calculated structural characteristics and elastic constants of bulk $TaSi_2$ and $NbSi_2$ as well as of their nanocomposites $TaSi_2/NbSi_2$ with the stacking along (and the interfaces perpendicular to) the [0001] direction within the C40 lattice. The computed values are complemented by both experimental data as well as by other theoretical results from literature. As far as the lattice parameters *a* and *c* of the C40 structure are concerned, the values of the lattice parameter *c* for the nanocomposites are marked by an asterisk * because they are divided by factor of 2 to be compared with the values for the bulk unit cells of the individual constituents (bulk $TaSi_2$ and $NbSi_2$). Experimental elastic constants of $TaSi_2$ and $NbSi_2$ were taken from Ref. [84] and theoretical ones from Refs. [85,86].

Composition	*a* (Å)	*c* (Å)	C_{11} (GPa)	C_{12} (GPa)	C_{13} (GPa)	C_{33} (GPa)	C_{44} (GPa)
$TaSi_2$	4.736	6.530	394	85	101	487	143
	4.77 [84]	6.55 [84]	375.3 [84]	78.4 [84]	90.1 [84]	467.7 [84]	143.7 [84]
	4.731 [85]	6.501 [85]	392.2 [85]	78.3 [85]	98.2 [85]	484.6 [85]	148.8 [85]
	–	–	351.0 [86]	84.0 [86]	73.0 [86]	461.0 [86]	123.0 [86]
$(NbSi_2)_1/(TaSi_2)_5$—Figure 4a	4.739	6.534 *	392	84	99	483	143
$(NbSi_2)_2/(TaSi_2)_4$—Figure 4b	4.742	6.539 *	390	83	98	479	142
$(NbSi_2)_3/(TaSi_2)_3$—Figure 3a	4.745	6.543 *	387	82	96	475	142
$(NbSi_2)_3/(TaSi_2)_3$—Figure 4c	4.745	6.543 *	387	82	96	476	142
$(NbSi_2)_3/(TaSi_2)_3$—Figure 4d	4.745	6.543 *	388	82	96	476	142
$(NbSi_2)_4/(TaSi_2)_2$—Figure 4e	4.748	6.547 *	385	81	95	472	142
$(NbSi_2)_5/(TaSi_2)_1$—Figure 4f	4.751	6.551 *	383	80	94	469	141
$NbSi_2$	4.754	6.555	380	79	92	465	141
	4.79 [84]	6.59 [84]	380.2 [84]	75.9 [84]	88.3 [84]	468.0 [84]	145.3 [84]
	4.747 [85]	6.529 [85]	378.9 [85]	73.0 [85]	90.2 [85]	462.5 [85]	144.6 [85]
	–	–	344.0 [86]	85.0 [86]	69.0 [86]	456.0 [86]	115.0 [86]

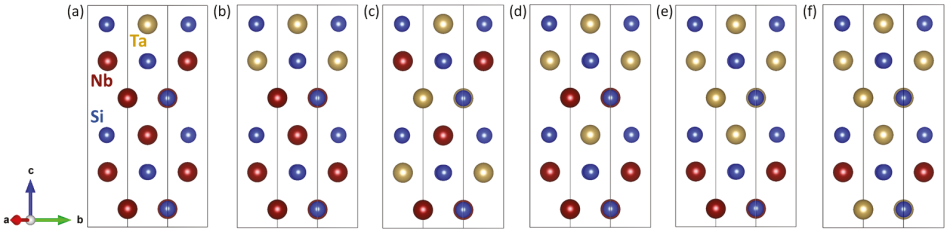

Figure 4. Schematic visualization of simulated $NbSi_2/TaSi_2$ nanocomposites with the stacking along (and the interfaces perpendicular to) the [0001] direction. The mutual ratio of the amount of constituents varies from 1:5, i.e., $(NbSi_2)_1(TaSi_2)_5$ in the case of (**a**) via 2:4 (**b**), 3:3 (**c**,**d**) to 4:2 (**e**) and 5:1, i.e., $(NbSi_2)_5(TaSi_2)_1$ in the case of (**f**). Variants shown in (**c**,**d**) have an equal amount of both constituting phases (similar to the case of Figure 3a) but a different arrangement of atomic layers. Consequently, there is a higher number of internal interfaces (6 and 4 in the case of (**c**,**d**), respectively) and the layers with different constituents have different widths.

The last systems studied here is that containing two different phases from the binary iron-aluminium system, in particular, an ordered Fe_3Al intermetallic compound crystallizing in the $D0_3$ structure and a disordered solid solution of 18.75 at.% of Al with a body-centered cubic (bcc) ferromagnetic (FM) matrix, so-called α-or B2 phase. The structure of the former was is derived from the bcc lattice and, therefore, both materials structurally match each other. The studied nanocomposite is schematically visualized in Figure 5a. Fe_3Al was modeled by a 16-atom conventional cell depicted in the upper part of in Figure 5a. The α-phase represents a challenge for quantum-mechanical calculations because it lacks any long-range periodicity. We used a 16-atom supercell with atoms distributed according to so-called special quasi-random structure (SQS) concept.

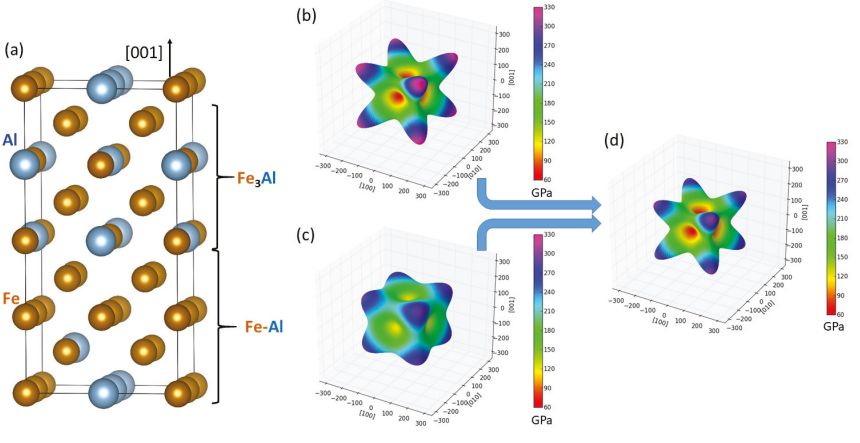

Figure 5. Visualization of a Fe_3Al/Fe-Al nanocomposite (a superlattice) with the stacking along (and the interfaces perpendicular to) the [001] direction (**a**) accompanied with directional dependences of the Young's modulus of bulk Fe_3Al (**b**), bulk Fe-Al (**c**) and the nanocomposite Fe_3Al/Fe-Al (**d**) formed out of them. Parts (**b**–**d**) were visualized by the SC-EMA [79–81] library (scema.mpie.de) based on ab initio computed elastic constants.

The nanocomposite was formed by stacking the Fe_3Al on top of the α-phase along the [001] direction (the interfaces are perpendicular to this direction). In contrast to the above-discussed cases of

superlattices formed by pairs of ordered transition-metal disilicides, when the both interfaces in the simulation supercell were identical, the supercells modeling the Fe-Al-based nanocomposites have different interfaces due to different distribution of atoms in the disordered α-phase. The interface energies were then averaged values related to the two interfaces. As another difference between the pairs of structurally and elastically nearly identical disilicides discussed above, the two constituting phases have clearly distinguishable elastic properties. Again, they are conveniently visualized in the form of directional dependences of the Young's modulus in Figure 5b,c for the Fe_3Al and the Fe-Al α-phase, respectively. The calculated values of elastic constants for Fe_3Al compound are C_{11} = 211 GPa, C_{12} = 161 GPa and C_{44} = 139 GPa. The elastic constants calculated for the disordered Fe-Al α-phase were projected onto a set of elastic constants possessing a cubic symmetry according to the rigorous mathematical theory by Moakher and Norris [87]. Similar concepts are often used in case of systems with any form of disorder (see, e.g., Refs. [59,88–91]). The resulting cubic-symmetry elastic constants are C_{11} = 217 GPa, C_{12} = 131 GPa and C_{44} = 120 GPa. Both phases exhibit $\langle 001 \rangle$ directions as elastically soft and $\langle 111 \rangle$ directions as elastically hard (i.e., with the minimum and maximum values of the Young's modulus, respectively). The Fe_3Al is also apparently elastically more anisotropic. The overall elasticity of their composite is then shown in Figure 5d.

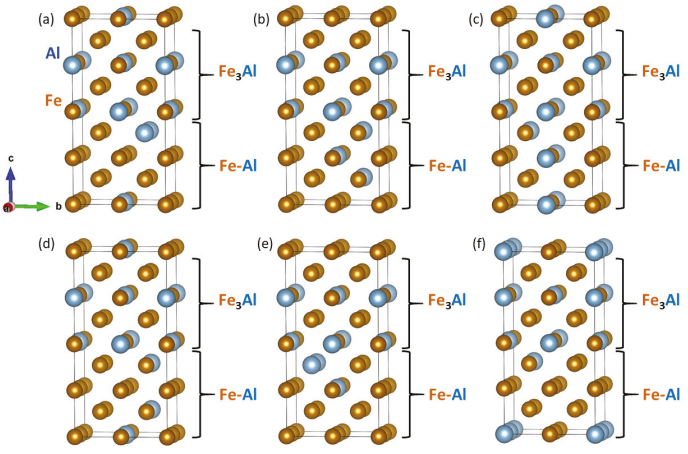

Figure 6. Schematic visualizations of different computed Fe_3Al/Fe-Al nanocomposites. The computed variants shown in sub-figures (**a**–**f**) differ by the distribution of atoms in the disordered Fe-Al phase.

Importantly, the interface energy was found to be ultra low again, only 0.005 J/m^2, which represents an energy difference appearing in Equation ((1)) smaller than 0.001 eV/atom, i.e., within the error-bar of our calculations. To determine an impact of distribution of atoms in the disordered Fe-Al α-phase on the interface energies, we performed a series of six additional calculations for supercells which have the same stoichiometry but differ in distributions of atoms in the Fe-Al α-phase (see Figure 6). In fact, the structure of coordination shells of atoms remain the same. For example, considering the Al atoms, their distribution in the part corresponding to the Fe-Al α-phase in the structural variants in Figure 6 are the same but the part of the supercell corresponding to the Fe-Al α-phase is either rotated and/or the atomic planes are permuted. As far as the latter process is concerned, if the atomic planes perpendicular to the [001] direction in the α-phase part of Figure 5a would be numbered 1, 2, 3, 4, then by a permutation is meant, e.g., an arrangement 2, 3, 4, 1. Importantly, if being in a single-phase bulk, such permutation of atomic planes within the periodically repeated cell or rotations of the whole cell would not change the energy because the position of the origin

of coordinates (and the attached coordinate frame) can be arbitrarily shifted with respect to the crystal lattice.

Table 3. Calculated elastic constants of Fe_3Al/Fe-Al nanocomposites with the stacking along (and the interfaces perpendicular to) the [001] direction. The nanocomposites are visualized in Figure 6.

Variant	C_{11} (GPa)	C_{12} (GPa)	C_{13} (GPa)	C_{22} (GPa)	C_{23} (GPa)	C_{33} (GPa)	C_{44} (GPa)	C_{55} (GPa)	C_{66} (GPa)
Fe_3Al/Fe-Al Figure 6a	188	143	134	201	139	199	120	126	124
Fe_3Al/Fe-Al Figure 6b	186	134	142	185	141	199	123	123	123
Fe_3Al/Fe-Al Figure 6c	197	146	145	196	145	184	129	129	124
Fe_3Al/Fe-Al Figure 6d	200	151	143	199	143	200	125	125	122
Fe_3Al/Fe-Al Figure 6e	183	135	138	189	136	202	117	124	123
Fe_3Al/Fe-Al Figure 6f	175	141	137	189	145	200	121	126	127

The situation is, on the other hand, different in nanocomposites because the interface represents a reference point not existing in the single-phase bulk. The calculated energies are covering a broader range: 0.055 J/m^2 (Figure 6a), 0.021 J/m^2 (Figure 6b), 0.032 J/m^2 (Figure 6c), 0.006 J/m^2 (Figure 6d), 0.139 J/m^2 (Figure 6e), and 0.014 J/m^2 (Figure 6f). While this sensitivity on the atomic distribution is rather significant, the elastic properties of nanocomposites shown in Figure 6 are very similar. The computed values of elastic constants are summarized in Table 3.

As both phases appearing in the studied nanocomposites are magnetic, we further examined local magnetic moments of the iron atoms in configurations visualized in Figure 6a–f. The magnitude of local magnetic moments are shown in Figure 7 by the diameter of the spheres representing the Fe atoms. The lowest and the highest value (1.8 μ_B and 2.44 μ_B) are explicitly mentioned in Figure 7a to demonstrate a scaling, by which the magnitude of the local magnetic moment is indicated by the diameter of the spheres. Importantly, the magnetic properties of the Fe atoms turned out to be very sensitive to the distribution of atoms (they are reduced when the Al atoms are nearby).

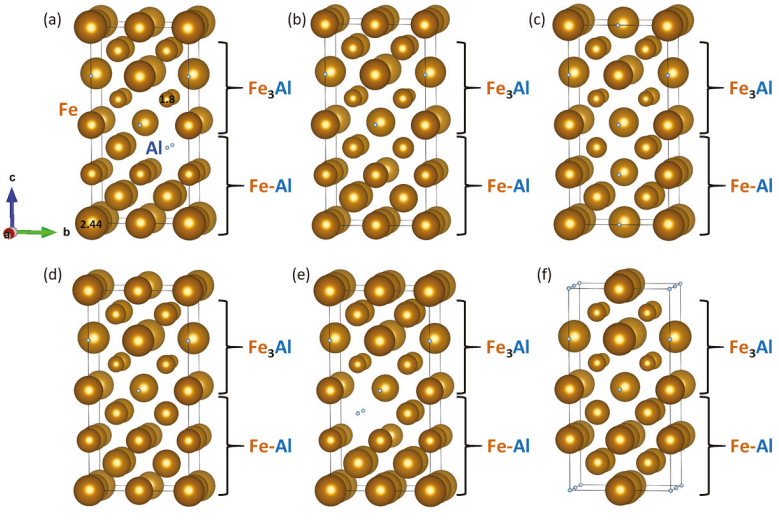

Figure 7. Calculated local magnetic moments of iron atoms (the magnitude is indicated by the diameter of the spheres representing the Fe atoms). The local magnetic moments shown in sub-figures (**a**–**f**) correspond to atomic distributions of nanocomposites visualized in sub-figures (**a**–**f**) of Figure 6, respectively.

4. Discussion

The above-discussed ultra low interface energies in the $MoSi_2/WSi_2$ nanocomposites may also indicate that both constituents are prone to mixing even at the atomic level. Indeed, it seems that longer annealing times lead to formation of solid-solution phases rather than (nano)composites. For example, $MoSi_2/WSi_2$ powders are synthesized by means of self-propagating high temperature combustion in [92] but solid solutions of $MoSi_2/WSi_2$ and Mo_5Si_3/W_5Si_3 are found. In [93], it is also reported that it is hard to distinguish $MoSi_2$ and WSi_2 phases and $(W,Mo)Si_2$ mainly in solid solution is found in Ref. [94]. The difficulties to distinguish $MoSi_2$ and WSi_2 Bragg peaks can be attributed to tetragonal $MoSi_2$ and WSi_2 phase having a long-range structure with very similar lattice constants (a is equal to 0.3202 nm and 0.3211, c amounts to 0.7855nm and 0.7835nm, respectively) [83]. It is also confirmed that $MoSi_2/WSi_2$ solid solution powder with nanometric $(Mo,W)Si_2$ structure forms via combustion synthesis method from the mechanical activated powder mixture [95].

To test the scenario of a random solid solution of Mo and W within a $C11_b$ lattice, we performed a series of calculations for supercells modeling these states (see Figure 8a–d). The corresponding enthalpies of mixing (evaluated with respect to the energy of $MoSi_2$ and WSi_2 as reference end-members) are shown in Figure 8e and all of them are between zero and -0.001 eV/atom, i.e., within the error-bar of our calculations and comparable to the energy differences obtained when simulating the $MoSi_2/WSi_2$ nanocomposites.

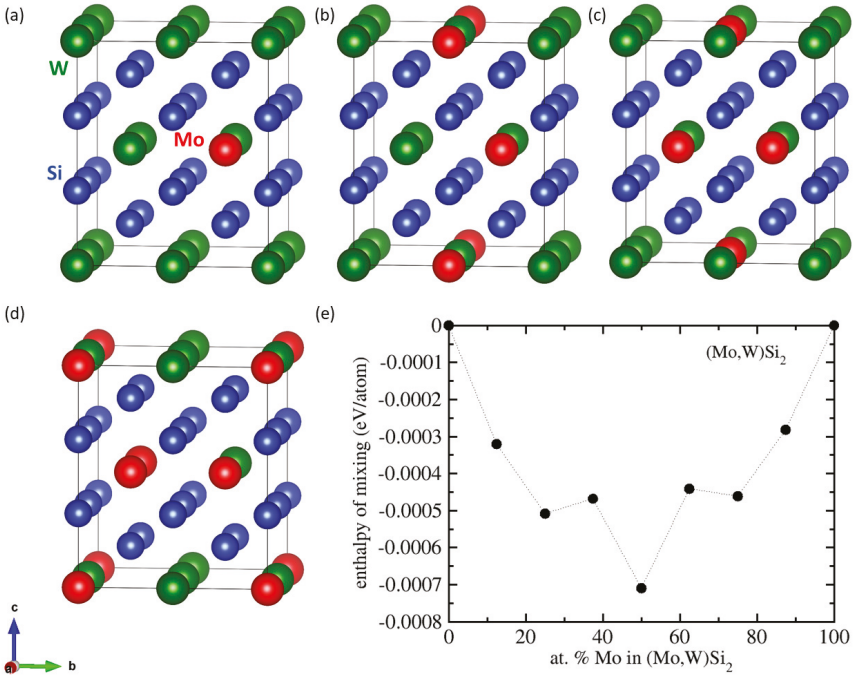

Figure 8. Schematic visualization of the supercells modeling random solid solutions of Mo and W within a $C11_b$ lattice in the case of Mo:W ratio equal to 1:7 (**a**), 2:6 (**b**), 3:5 (**c**), and 4:4 (**d**) together with the correspondingenthalpies of mixing (**e**). The supercells for the Mo:W ratios equal to 5:3, 6:2 and 7:1 were obtained by swapping Mo and W atoms in the supercells shown in sub-figures (**a**–**c**). The atoms in the 32-atom supercells ($2 \times 2 \times 1$ multiple of 6-atom conventional cell of the $C11_b$ structure) were distributed according to the special quasi-random structure (SQS) concept [96].

The above-discussed competition between formation of two-phase nanocomposites on the one hand and single-phase solid solutions on the other hand probably explains why a suitable preparation route is still being searched for in the case of $TaSi_2/NbSi_2$ nanocomposites when Nb solubility in $TaSi_2$ extremely large [97]. Our results related to the $TaSi_2/NbSi_2$ nanocomposites are intended as a motivation for future studies of this interesting system.

5. Conclusions

We performed a first-principles study of structural, thermodynamic and elastic properties of nanocomposites exhibiting ultra low or low interface energies. As examples of systems with predominantly covalent interatomic bonds, we studied two combinations of transition-metal disilicides: (i) $MoSi_2/WSi_2$ nanocomposites with individual constituents crystallizing in the tetragonal $C11_b$ structure; and (ii) $TaSi_2/NbSi_2$ with the two components crystallizing in the hexagonal C40 structure. The constituents within each pair of materials exhibit very similar structural and elastic properties and we obtained ultra low (nearly zero) interface energy for their nanocomposites (within the error bar of our calculations, i.e., about 0.005 J/m^2). The interface energy was found to be nearly independent on the width of individual constituents within the nanocomposites and/or crystallographic orientation of the interfaces.

As an example of a magnetic system, a pair of metallic phases containing from the Fe-Al system with different atomic ordering was considered. In particular, we simulated coherent superlattices formed by an ordered Fe_3Al intermetallic compound and a disordered Fe-Al phase with 18.75 at.% Al, the α-phase. Both constituents are structurally and elastically rather similar (but less than the two pairs of studied disilicides). To estimate the interface energy in the nanocomposite containing the disordered α-phase, which lacks a long-range periodicity, we simulated seven different distributions of atoms in the α-phase interfacing the Fe_3Al intermetallic compound. The resulting interface energies were again either ultra low or low, from 0.005 to 0.139 J/m^2. While the impact of atomic distribution on the elastic properties was found insignificant, the local magnetic moments of the iron atoms sensitively depended on the type and the distribution of surrounding atoms.

Author Contributions: Conceptualization, M.F.; Methodology, D.H.; Resources, M.Š. and M.F.; Writing—Original Draft Preparation, M.F.; Writing—Review and Editing, D.H. and M.Š.; Visualization, M.F.; Supervision, M.Š.; Project Administration, M.Š. and M.F.; and Funding Acquisition, M.Š. and M.F.

Funding: The authors acknowledge the Czech Science Foundation for the financial support received under the Project Nos. 16-24711S (M.Š.) and 17-22139S (M.F.). Additional resources were provided by the Academy of Sciences of the Czech Republic through the Fellowship of J. E. Purkyně (M.F.) and by the Ministry of Education, Youth and Sports of the Czech Republic under the Project CEITEC 2020, LQ1601 (M.Š). D.H. acknowledges financial support from the Austrian Science Fund (FWF), Project Number P30341-N36. The computational results presented have been achieved in part using the Vienna Scientific Cluster (VSC).

Acknowledgments: M.F. and M.Š. acknowledge the support from the Academy of Sciences of the Czech Republic (Institutional Project No. RVO:68081723) and from the Ministry of Education, Youth and Sports of the Czech Republic via the research infrastructure IPMINFRA, LM2015069. Computational resources were made available by the Ministry of Education, Youth and Sports of the Czech Republic under the Projects CESNET (Project No. LM2015042), CERIT-Scientific Cloud (Project No. LM2015085) and IT4Innovations National Supercomputer Center (Project No. LM2015070) within the program Projects of Large Research, Development and Innovations Infrastructures. Figures 1a, 2, 3a, 4, 5a, 6, 8a–d, and A1a,b were visualized using the VESTA package [98].

Conflicts of Interest: The authors declare no conflict of interest.

Appendix A

To analyze the dependence of the ultra-low interface energies in the $MoSi_2/WSi_2$ nanocomposites on the crystallographic orientation of the interface, we computed properties of two other superlattices with the interfaces perpendicular to the [010] and [110] directions, respectively. The corresponding supercells modeling these nanocomposites are shown in Figure A1a,b, respectively. The elastic properties of these superlattices are visualized in the form of directional dependences of the Young's

modulus in Figure A1c,d. It is obvious that they are again very similar to each other and also very similar to that of the superlattice with the interfaces perpendicular to the [001] direction.

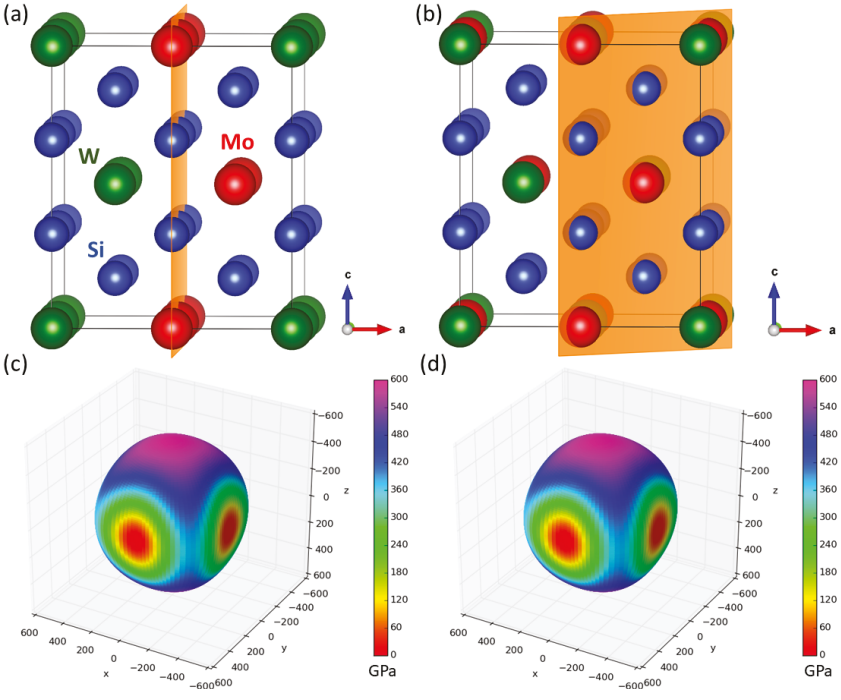

Figure A1. Schematics of computational supercells of $MoSi_2/WSi_2$ nanocomposites (superlattices) with the stacking along (and the interfaces perpendicular to) the [010] (**a**) and [110] (**b**) directions within the $C11_b$ lattice, respectively. The interface planes are marked by orange color. The calculated elastic constants for these superlattices are shown as directional dependences of the Young's modulus for the composite with the [010] stacking direction (**c**) as well as that with the [110] stacking direction (**d**). Parts (**c**,**d**) were visualized by the SC-EMA [79–81] library (scema.mpie.de) based on ab initio computed elastic constants.

References

1. Yamaguchi, M.; Inui, H.; Ito, K. High-temperature structural intermetallics. *Acta Mater.* **2000**, *48*, 307–322. [CrossRef]
2. Umakoshi, Y.; Nakano, T.; Kishimoto, K.; Furuta, D.; Hagihara, K.; Azuma, M. Strength and deformation mechanism of C40-based single crystal and polycrystalline silicides. *Mater. Sci. Eng. A* **1999**, *261*, 113–121. [CrossRef]
3. Petrovic, J.; Vasudevan, A. Key developments in high temperature structural silicides. *Mater. Sci. Eng. A* **1999**, *261*, 1–5. [CrossRef]
4. Inui, H.; Moriwaki, M.; Yamaguchi, M. Plastic deformation of single crystals of VSi_2 and $TaSi_2$with the C40 structure. *Intermetallics* **1998**, *6*, 723–728. [CrossRef]
5. Zhou, Y.; Zhang, Z.; Jin, X.; Ye, G.; Liu, C. Fabrication and Composition Investigation of $WSi_2/MoSi_2$ Composite Powders Obtained by a Self-Propagating High-Temperature Synthesis Method. *Arabian J. Sci. Eng.* **2016**, *41*, 2583–2587. [CrossRef]
6. Deevi, S.C. Self-propagating high-temperature synthesis of molybdenum disilicide. *J. Mater. Sci.* **1991**, *26*, 3343–3353. [CrossRef]

7. Ke, P.; Yi, M.; Ran, L. Reaction thermodynamics of $MoSi_2$-WSi_2 composites in the thermal explosion mode of SHS. *Rare Met. Mater. Eng.* **2006**, *35*, 554–558.
8. Zhang, H.; Chen, P.; Wang, M.; Liu, X. Room-temperature mechanical properties of $WSi_2/MoSi_2$ composites. *Rare Met.* **2002**, *21*, 304–307.
9. Chen, F.; Xu, J.; Liu, Y.; Cai, L. In situ reactive spark plasma sintering of WSi2/$MoSi_2$ composites. *Ceram. Int.* **2016**, *42*, 11165–11169. [CrossRef]
10. Zamani, S.; Bakhsheshi-Rad, H.R.; Kadir, M.R.A.; Shafiee, M.R.M. Synthesis and kinetic study of (Mo,W)Si_2-WSi_2 nanocomposite by mechanical alloying. *J. Alloys Compd.* **2012**, *540*, 248–259. [CrossRef]
11. Xu, J.; Wang, Y.; Weng, B.; Chen, F. Preparation and Characterization of $MoSi_2/WSi_2$Composites from MASHSed Powder. *Mater. Trans.* **2015**, *56*, 313–316. [CrossRef]
12. Kattner, U.; Burton, B. Al-Fe (Aluminium-Iron). In *Phase Diagrams of Binary Iron Alloys*; Okamoto, H., Ed.; ASM International: Materials Park, OH, USA, 1993; pp. 12–28.
13. Sauthoff, G. *Intermetallics*; VCH Verlagsgesellschaft: Weinheim, Germany, 1995.
14. Liu, C.T.; Stringer, J.; Mundy, J.N.; Horton, L.L.; Angelini, P. Ordered intermetallic alloys: An assessment. *Intermetallics* **1997**, *5*, 579–596. [CrossRef]
15. Stoloff, N.S. Iron aluminides: Present status and future prospects. *Mater. Sci. Eng. A* **1998**, *258*, 1–14. [CrossRef]
16. Palm, M.; Inden, G.; Thomas, N. The Fe-Al-Ti system. *J. Phase Equilib.* **1995**, *16*, 209–222. [CrossRef]
17. Palm, M.; Lacaze, J. Assessment of the Al-Fe-Ti system. *Intermetallics* **2006**, *14*, 1291–1303. [CrossRef]
18. Palm, M.; Sauthoff, G. Deformation behaviour and oxidation resistance of single-phase and two-phase $L2_1$-ordered Fe-Al-Ti alloys. *Intermetallics* **2004**, *12*, 1345–1359. [CrossRef]
19. Sundman, B.; Ohnuma, I.; Dupin, N.; Kattner, U.R.; Fries, S.G. An assessment of the entire Al-Fe system including D0(3) ordering. *Acta Mater.* **2009**, *57*, 2896–2908. [CrossRef]
20. Stein, F.; Palm, M. Re-determination of transition temperatures in the Fe-Al system by differential thermal analysis. *Int. J. Mater. Res.* **2007**, *98*, 580–588. [CrossRef]
21. Palm, M. Fe-Al materials for structural applications at high temperatures: Current research at MPIE. *Int. J. Mater. Res.* **2009**, *100*, 277–287. [CrossRef]
22. Watson, R.E.; Weinert, M. Transition-metal aluminide formation: Ti, V, Fe, and Ni aluminides. *Phys. Rev. B* **1998**, *58*, 5981–5988. [CrossRef]
23. Gonzales-Ormeno, P.; Petrilli, H.; Schon, C. Ab-initio calculations of the formation energies of BCC-based superlattices in the Fe-Al system. *Calphad* **2002**, *26*, 573. [CrossRef]
24. Friák, M.; Neugebauer, J. Ab initio study of the anomalous volume-composition dependence in Fe-Al alloys. *Intermetallics* **2010**, *18*, 1316–1321. [CrossRef]
25. Amara, H.; Fu, C.C.; Soisson, F.; Maugis, P. Aluminum and vacancies in α-iron: Dissolution, diffusion, and clustering. *Phys. Rev. B* **2010**, *81*, 174101. [CrossRef]
26. Liu, S.; Duan, S.; Ma, B. First-principles calculation of vibrational entropy for Fe-Al compounds. *Phys. Rev. B* **1998**, *58*, 9705–9709.
27. Kulikov, N.I.; Postnikov, A.V.; Borstel, G.; Braun, J. Onset of magnetism in B2 transition-metal aluminides. *Phys. Rev. B* **1999**, *59*, 6824–6833. [CrossRef]
28. Fähnle, M.; Drautz, R.; Lechermann, F.; Singer, R.; Diaz-Ortiz, A.; Dosch, H. Thermodynamic properties from ab-initio calculations: New theoretical developments, and applications to various materials systems. *Phys. Status Solidi B-Basic Solid State Phys.* **2005**, *242*, 1159–1173. [CrossRef]
29. Friák, M.; Deges, J.; Krein, R.; Frommeyer, G.; Neugebauer, J. Combined ab initio and experimental study of structural and elastic properties of Fe_3Al-based ternaries. *Intermetallics* **2010**, *18*, 1310. [CrossRef]
30. Kirklin, S.; Saal, J.E.; Hegde, V.I.; Wolverton, C. High-throughput computational search for strengthening precipitates in alloys. *Acta Mater.* **2016**, *102*, 125–135. [CrossRef]
31. Airiskallio, E.; Nurmi, E.; Heinonen, M.H.; Vayrynen, I.J.; Kokko, K.; Ropo, M.; Punkkinen, M.P.J.; Pitkanen, H.; Alatalo, M.; Kollar, J.; Johansson, B.; Vitos, L. High temperature oxidation of Fe-Al and Fe-Cr-Al alloys: The role of Cr as a chemically active element. *Corros. Sci.* **2010**, *52*, 3394–3404. [CrossRef]
32. Medvedeva, N.I.; Park, M.S.; Van Aken, D.C.; Medvedeva, J.E. First-principles study of Mn, Al and C distribution and their effect on stacking fault energies in fcc Fe. *J. Alloy. Compd.* **2014**, *582*, 475–482. [CrossRef]
33. Čížek, J.; Lukáč, F.; Procházka, I.; Kužel, R.; Jirásková, Y.; Janičkovič, D.; Anwand, W.; Brauer, G. Characterization of quenched-in vacancies in Fe-Al alloys. *Physica B* **2012**, *407*, 2659–2664. [CrossRef]

34. Ipser, H.; Semenova, O.; Krachler, R. Intermetallic phases with DO_3-structure: A statistical-thermodynamic model. *J. Alloy. Compd.* **2002**, *338*, 20–25. [CrossRef]
35. Miháliková, I.; Slávik, A.; Friák, M.; Všianská, M.; Koutná, N.; Holec, D.; Šob, M. First-principles study of interface energies in Fe-Al-based superalloy nanocomposites. In *NANOCON 2017 Conference Proceedings (9th International Conference on Nanomaterials—Research & Application, Brno, Oct. 18–20, 2017)*; Tanger Ltd.: Ostrava, Czech Republic; 2017; pp. 69–74.
36. Šesták, P.; Friák, M.; Holec, D.; Všianská, M.; Šob, M. Strength and Brittleness of Interfaces in Fe-Al Superalloy Nanocomposites under Multiaxial Loading: An ab initio and Atomistic Study. *Nanomaterials* **2018**, *8*, 873. [CrossRef] [PubMed]
37. Lechermann, F.; Welsch, F.; Elsässer, C.; Ederer, C.; Fähnle, M.; Sanchez, J.; Meyer, B. Density-functional study of Fe_3Al: LSDA versus GGA. *Phys. Rev. B* **2002**, *65*, 132104. [CrossRef]
38. Connetable, D.; Maugis, P. First principle calculations of the kappa-Fe_3AlC perovskite and iron-aluminium intermetallics. *Intermetallics* **2008**, *16*, 345–352. [CrossRef]
39. Lechermann, F.; Fähnle, M.; Meyer, B.; Elsässer, C. Electronic correlations, magnetism, and structure of Fe-Al subsystems: An LDA+U study. *Phys. Rev. B* **2004**, *69*, 165116. [CrossRef]
40. Kellou, A.; Grosdidier, T.; Raulot, J.M.; Aourag, H. Atomistic study of magnetism effect on structural stability in Fe_3Al and Fe_3AlX (X = H, B, C, N, O) alloys. *Phys. Status Solidi B-Basic Solid State Phys.* **2008**, *245*, 750–755. [CrossRef]
41. Jiraskova, Y.; Pizurova, N.; Titov, A.; Janickovic, D.; Friak, M. Phase separation in Fe-Ti-Al alloy—Structural, magnetic, and Moessbauer study. *J. Magn. Magn. Mater.* **2018**, *468*, 91–99. [CrossRef]
42. Wang, K.; Wang, Y.; Cheng, Y. The Formation and Dynamic Evolution of Antiphase Domain Boundary in FeAl Alloy: Computational Simulation in Atomic Scale. *Mater. Res. Ibero-Am. J. Mater.* **2018**, *21*, e20171048. [CrossRef]
43. Balagurov, A.M.; Bobrikov, I.A.; Sumnikov, V.S.; Golovin, I.S. Antiphase domains or dispersed clusters? Neutron diffraction study of coherent atomic ordering in Fe_3Al-type alloys. *Acta Mater.* **2018**, *153*, 45–52. [CrossRef]
44. Murakami, Y.; Niitsu, K.; Tanigaki, T.; Kainuma, R.; Park, H.S.; Shindo, D. Magnetization amplified by structural disorder within nanometre-scale interface region. *Nat. Commun.* **2014**, *5*, 4133. [CrossRef] [PubMed]
45. Oguma, R.; Matsumura, S.; Eguchi, T. Kinetics of B2-and $D0_3$ type ordering and formation of domain structures in Fe-Al alloys. *J. Phys. Cond. Matter* **2008**, *20*, 275225. [CrossRef] [PubMed]
46. Hohenberg, P.; Kohn, W. Inhomogeneous electron gas. *Phys. Rev.* **1964**, *136*, B864–B871. [CrossRef]
47. Kohn, W.; Sham, L.J. Self-consistent equations including exchange and correlation effects. *Phys. Rev.* **1965**, *140*, A1133–A1138. [CrossRef]
48. Kresse, G.; Hafner, J. Ab initio molecular dynamics for liquid metals. *Phys. Rev. B* **1993**, *47*, 558–561. [CrossRef]
49. Kresse, G.; Furthmüller, J. Efficient iterative schemes for ab initio total-energy calculations using a plane-wave basis set. *Phys. Rev. B* **1996**, *54*, 11169–11186. [CrossRef]
50. Blöchl, P.E. Projector augmented-wave method. *Phys. Rev. B* **1994**, *50*, 17953–17979. [CrossRef]
51. Kresse, G.; Joubert, D. From ultrasoft pseudopotentials to the projector augmented-wave method. *Phys. Rev. B* **1999**, *59*, 1758. [CrossRef]
52. Ceperley, D.M.; Alder, B.J. Ground State of the Electron Gas by a Stochastic Method. *Phys. Rev. Lett.* **1980**, *45*, 566–569. [CrossRef]
53. Perdew, J.P.; Wang, Y. Accurate and simple analytic representation of the electron-gas correlation energy. *Phys. Rev. B* **1992**, *45*, 13244–13249. [CrossRef]
54. Vosko, S.H.; Wilk, L.; Nusair, M. Accurate spin-dependent electron liquid correlation energies for local spin density calculations: A critical analysis. *Can. J. Phys.* **1980**, *58*, 1200. [CrossRef]
55. Monkhorst, H.J.; Pack, J.D. Special points for Brillouin-zone integrations. *Phys. Rev. B* **1976**, *13*, 5188–5192. [CrossRef]
56. Zhou, L.; Holec, D.; Mayrhofer, P.H. First-principles study of elastic properties of Cr-Al-N. *J. Appl. Phys.* **2013**, *113*, 043511. [CrossRef]
57. Mayrhofer, P.H.; Fischer, F.D.; Boehm, H.J.; Mitterer, C.; Schneider, J.M. Energetic balance and kinetics for the decomposition of supersaturated $Ti_{1-x}Al_xN$. *Acta Mater.* **2007**, *55*, 1441–1446. [CrossRef]

58. Wu, L.; Chen, M.; Li, C.; Zhou, J.; Shen, L.; Wang, Y.; Zhong, Z.; Feng, M.; Zhang, Y.; Han, K.; et al. Ferromagnetism and matrix-dependent charge transfer in strained $LaMnO_3$-$LaCoO_3$ superlattices. *Mater. Res. Lett.* **2018**, *6*, 501–507. [CrossRef]
59. Koutná, N.; Holec, D.; Friák, M.; Mayrhofer, P.H.; Šob, M. Stability and elasticity of metastable solid solutions and superlattices in the MoN-TaN system: First-principles calculations. *Mater. Des.* **2018**, *144*, 310–322. [CrossRef]
60. Jiang, M.; Xiao, H.Y.; Peng, S.M.; Yang, G.X.; Liu, Z.J.; Zu, X.T. A comparative study of low energy radiation response of AlAs, GaAs and GaAs/AlAs superlattice and the damage effects on their electronic structures. *Sci. Rep.* **2018**, *8*, 2012. [CrossRef]
61. Wen, Y.N.; Gao, P.F.; Xia, M.G.; Zhang, S.L. Half-metallic ferromagnetism prediction in MoS_2-based two-dimensional superlattice from first-principles. *Mod. Phys. Lett. B* **2018**, *32*, 1850098. [CrossRef]
62. Friák, M.; Tytko, D.; Holec, D.; Choi, P.P.; Eisenlohr, P.; Raabe, D.; Neugebauer, J. Synergy of atom-probe structural data and quantum-mechanical calculations in a theory-guided design of extreme-stiffness superlattices containing metastable phases. *New J. Phys.* **2015**, *17*, 093004. [CrossRef]
63. Dai, Q.; Eckern, U.; Schwingenschlog, U. Effects of oxygen vacancies on the electronic structure of the $(LaVO3)_6/SrVO_3$ superlattice: A computational study. *New J. Phys.* **2018**, *20*, 073011. [CrossRef]
64. Jiang, M.; Xiao, H.; Peng, S.; Qiao, L.; Yang, G.; Liu, Z.; Zu, X. First-Principles Study of Point Defects in GaAs/AlAs Superlattice: the Phase Stability and the Effects on the Band Structure and Carrier Mobility. *Nanoscale Res. Lett.* **2018**, *13*, 301. [CrossRef]
65. Chen, H.; Millis, A.J.; Marianetti, C.A. Engineering Correlation Effects via Artificially Designed Oxide Superlattices. *Phys. Rev. Lett.* **2013**, *111*, 116403. [CrossRef] [PubMed]
66. Mottura, A.; Janotti, A.; Pollock, T.M. A first-principles study of the effect of Ta on the superlattice intrinsic stacking fault energy of $L1_2$-Co_3(Al,W). *Intermetallics* **2012**, *28*, 138–143. [CrossRef]
67. Rosengaard, N.; Skriver, H. Ab-initio study of antiphase boundaries and stacking-faults in $L1_2$ and $D0_{22}$ compounds. *Phys. Rev. B* **1994**, *50*, 4848–4858. [CrossRef]
68. Torres-Pardo, A.; Gloter, A.; Zubko, P.; Jecklin, N.; Lichtensteiger, C.; Colliex, C.; Triscone, J.M.; Stephan, O. Spectroscopic mapping of local structural distortions in ferroelectric $PbTiO_3/SrTiO_3$ superlattices at the unit-cell scale. *Phys. Rev. B* **2011**, *84*, 220102. [CrossRef]
69. Chawla, V.; Holec, D.; Mayrhofer, P.H. Stabilization criteria for cubic AlN in TiN/AlN and CrN/AlN bi-layer systems. *J. Phys. D* **2013**, *46*, 045305. [CrossRef]
70. Cooper, V.R.; Rabe, K.M. Enhancing piezoelectricity through polarization-strain coupling in ferroelectric superlattices. *Phys. Rev. B* **2009**, *79*, 180101. [CrossRef]
71. Chen, B.; Zhang, Q.; Bernholc, J. Si diffusion in GaAs and Si-induced interdiffusion in GaAs/AlAs superlattices. *Phys. Rev. B* **1994**, *49*, 2985–2988. [CrossRef]
72. Schmid, U.; Christensen, N.; Cardona, M.; Lukes, F.; Ploog, K. Optical anisotropy in GaAs/AlSs(110) superlattices. *Phys. Rev. B* **1992**, *45*, 3546–3551. [CrossRef]
73. Gibson, Q.D.; Schoop, L.M.; Weber, A.P.; Ji, H.; Nadj-Perge, S.; Drozdov, I.K.; Beidenkopf, H.; Sadowski, J.T.; Fedorov, A.; Yazdani, A.; Valla, T.; Cava, R.J. Termination-dependent topological surface states of the natural superlattice phase Bi_4Se_3. *Phys. Rev. B* **2013**, *88*, 081108R. [CrossRef]
74. Park, C.; Chang, K. Structural and electronic-properties of GaP-AlP (001) superlattices. *Phys. Rev. B* **1993**, *47*, 12709–12715. [CrossRef]
75. Romanyuk, O.; Hannappel, T.; Grosse, F. Atomic and electronic structure of GaP/Si(111), GaP/Si(110), and GaP/Si(113) interfaces and superlattices studied by density functional theory. *Phys. Rev. B* **2013**, *88*, 115312. [CrossRef]
76. Abdulsattar, M.A. SiGe superlattice nanocrystal pure and doped with substitutional phosphorus single atom: Density functional theory study. *Superlattices Microstruct.* **2011**, *50*, 377–385. [CrossRef]
77. Botti, S.; Vast, N.; Reining, L.; Olevano, V.; Andreani, L. Ab initio and semiempirical dielectric response of superlattices. *Phys. Rev. B* **2004**, *70*, 045301. [CrossRef]
78. Rondinelli, J.M.; Spaldin, N.A. Electron-lattice instabilities suppress cuprate-like electronic structures in $SrFeO_3/OSrTiO_3$ superlattices. *Phys. Rev. B* **2010**, *81*, 085109. [CrossRef]
79. Titrian, H.; Aydin, U.; Friák, M.; Ma, D.; Raabe, D.; Neugebauer, J. Self-consistent Scale-bridging Approach to Compute the Elasticity of Multi-phase Polycrystalline Materials. *MRS Proc.* **2013**, *1524*, rr06. [CrossRef]

80. Friák, M.; Counts, W.; Ma, D.; Sander, B.; Holec, D.; Raabe, D.; Neugebauer, J. Theory-Guided Materials Design of Multi-Phase Ti-Nb Alloys with Bone-Matching Elastic Properties. *Materials* **2012**, *5*, 1853–1872. [CrossRef]
81. Zhu, L.F.; Friák, M.; Lymperakis, L.; Titrian, H.; Aydin, U.; Janus, A.; Fabritius, H.O.; Ziegler, A.; Nikolov, S.; Hemzalová, P.; Raabe, D.; Neugebauer, J. Ab initio study of single-crystalline and polycrystalline elastic properties of Mg-substituted calcite crystals. *J. Mech. Behav. Biomed. Mater.* **2013**, *20*, 296–304. [CrossRef]
82. Nakamura, M.; Matsumoto, S.; Hirano, T. Elastic constants of $MoSi_2$and WSi_2 single crystals. *J. Mater. Sci.* **1990**, *25*, 3309–3313. [CrossRef]
83. Zhang, H.; Chen, P.; Yan, J.; Tang, S. Fabrication and wear characteristics of $MoSi_2$ matrix composite reinforced by $WSi_2$and La_2O_3. *Int. J. Refract. Met. Hard Mater.* **2004**, *22*, 271–275. [CrossRef]
84. Chu, F.; Ming, L.; Maloy, S.A.; Mitchell, T.E.; Migliori, A.; Garrett, J. Single crystal elastic constants of $NbSi_2$. *Philos. Mag. B* **1995**, *71*, 373–382. [CrossRef]
85. Erturk, E.; Gurel, T. Ab initio study of structural, elastic, and vibrational properties of transition-metal disilicides $NbSi_2$ and $TaSi_2$ in hexagonal C40 structure. *Phys. B Cond. Matter* **2018**, *537*, 188–193. [CrossRef]
86. Wan, B.; Xiao, F.; Zhang, Y.; Zhao, Y.; Wu, L.; Zhang, J.; Gou, H. Theoretical study of structural characteristics, mechanical properties and electronic structure of metal (TM=V, Nb and Ta) silicides. *J. Alloys Compd.* **2016**, *681*, 412–420. [CrossRef]
87. Moakher, M.; Norris, A.N. The closest elastic tensor of arbitrary symmetry to an elasticity tensor of lower symmetry. *J. Elast.* **2006**, *85*, 215–263. [CrossRef]
88. Tasnádi, F.; Abrikosov, I.A.; Rogström, L.; Almer, J.; Johansson, M.P.; Oden, M. Significant elastic anisotropy in Ti1-xAlxN alloys. *Appl. Phys. Lett.* **2010**, *97*, 231902. [CrossRef]
89. Tasnádi, F.; Odén, M.; Abrikosov, I. Ab initio elastic tensor of cubic $Ti_{0.5}Al_{0.5}N$ alloys: Dependence of elastic constants on size and shape of the supercell model and their convergence. *Phys. Rev. B* **2012**, *85*, 144112. [CrossRef]
90. Von Pezold, J.; Dick, A.; Friák, M.; Neugebauer, J. Generation and performance of special quasirandom structures for studying the elastic properties of random alloys: Application to Al-Ti. *Phys. Rev. B* **2010**, *81*, 094203. [CrossRef]
91. Holec, D.; Tasnádi, F.; Wagner, P.; Friák, M.; Neugebauer, J.; Mayrhofer, P.; Keckes, J. Macroscopic elastic properties of textured ZrN-AlN polycrystalline aggregates: From ab initio calculations to grainscale interactions. *Phys. Rev. B* **2014**, *90*, 184106. [CrossRef]
92. Kou, K.; Yang, Y.; Ai, Y.; Chen, Y.; Kang, M. Self-propagating high-temperature combustion synthesis of $MoSi_2$-WSi_2 composite. *Rare Met. Mater. Eng.* **2000**, *29*, 190–192.
93. Zhang, Y.; Zhang, P.; Ren, J.; Zhang, L.; Zhang, J. SiC nanowire-toughened $MoSi_2$-WSi_2-SiC-Si multiphase coating for improved oxidation resistance of C C composites. *Ceram. Int.* **2016**, *42*, 12573–12580. [CrossRef]
94. Ai, Y.; Cheng, Y.; Yang, Y.; Kang, M.; Liu, C. Preparation and microstructure of WSi_2/$MoSi_2$composite heat element. *Rare Met. Mater. Eng.* **2005**, *34*, 962–965.
95. Xu, J.; Wu, H.; Li, B. Synthesis of $MoSi_2$/WSi_2nanocrystalline powder by mechanical-assistant combustion synthesis method. *Int. J. Refract. Met. Hard Mater.* **2010**, *28*, 217–220. [CrossRef]
96. Zunger, A.; Wei, S.; Ferreira, L.; Bernard, J. Special quasirandom structures. *Phys. Rev. Lett.* **1990**, *65*, 353–356. [CrossRef] [PubMed]
97. Li, J.; Wang, C.; Yao, J.; Yang, S.; Kang, Y.; Shi, Z.; Liu, X. Experimental investigation of phase equilibria in the Nb-Si-Ta ternary system. *Int. J. Mater. Res.* **2016**, *107*, 1112–1120. [CrossRef]
98. Momma, K.; Izumi, F. VESTA 3 for three-dimensional visualization of crystal, volumetric and morphology data. *J. Appl. Crystallogr.* **2011**, *44*, 1272–1276. [CrossRef]

MDPI
St. Alban-Anlage 66
4052 Basel
Switzerland
Tel. +41 61 683 77 34
Fax +41 61 302 89 18
www.mdpi.com

Nanomaterials Editorial Office
E-mail: nanomaterials@mdpi.com
www.mdpi.com/journal/nanomaterials

MDPI
St. Alban-Anlage 66
4052 Basel
Switzerland

Tel: +41 61 683 77 34
Fax: +41 61 302 89 18

www.mdpi.com

ISBN 978-3-03936-195-3